İSTANBUL TECHNICAL UNIVERSITY ★ GRADUATE SCHOOL OF SCIENCE ENGINEERING AND TECHNOLOGY

GENESIS OF THE GOLD MINERALIZATION AT ATUD AREA, CENTRAL EASTERN DESERT OF EGYPT: GEOLOGICAL, ORE MINERALOGICAL AND GEOCHEMICAL APPROACHES

Ph.D. THESIS

Amr Abdelnasser Ali KHALIL

Department of Geological Engineering

Geological Engineering Programme

JULY 2016

İSTANBUL TECHNICAL UNIVERSITY ★ GRADUATE SCHOOL OF SCIENCE ENGINEERING AND TECHNOLOGY

GENESIS OF THE GOLD MINERALIZATION AT ATUD AREA, CENTRAL EASTERN DESERT OF EGYPT: GEOLOGICAL, ORE MINERALOGICAL AND GEOCHEMICAL APPROACHES

Ph.D. THESIS

Amr Abdelnasser Ali KHALIL
(505122304)

Department of Geological Engineering

Geological Engineering Programme

Thesis Advisor: Assoc. Prof. Dr. Mustafa KUMRAL

JULY 2016

İSTANBUL TEKNİK ÜNİVERSİTESİ ★ FEN BİLİMLERİ ENSTİTÜSÜ

ATUD BÖLGESİ, MISIR'IN ORTA DOĞU ÇÖLÜ'NDEKİ ALTIN CEVHERLEŞMESİNİN KÖKENİ: JEOLOJİK, CEVHER MİNERALOJİK VE JEOKİMYASAL YAKLAŞIMLAR

DOKTORA TEZI

Amr Abdelnasser Ali KHALIL
(505122304)

Jeoloji Mühendisliği Anabilim Dalı

Jeoloji Mühendisliği Programı

Tez Danışmanı: Doç. Dr. Mustafa KUMRAL

TEMMUZ 2016

Amr Abdelnasser Ali Khalil, a Ph.D. student of İTU Graduate School of Science Engineering and Technology student ID 505122304, successfully defended the thesis/dissertation entitled "GENESIS OF THE GOLD MINERALIZATION AT ATUD AREA, CENTRAL EASTERN DESERT OF EGYPT: GEOLOGICAL, ORE MINERALOGICAL AND GEOCHEMICAL APPROACHES", which he prepared after fulfilling the requirements specified in the associated legislations, before the jury whose signatures are below.

Thesis Advisor:	**Assoc. Prof. Dr. Mustafa KUMRAL** İstanbul Technical University	.....
Jury Members:	**Assoc. Prof. Dr. Emin Çiftçi** İstanbul Technical University	.....
	Prof. Dr. Mehmet Sezai Kırıkoğlu İstanbul Technical University	.....
	Assoc. Prof. Dr. Nurullah Hanilçi Istanbul University	.....
	Prof. Dr. Yusuf Kağan Kadıoğlu Ankara University	.....

Date of Submission : 28 June 2016
Date of Defense : 15 July 2016

To my parents, lovely wife (Fatma), and nice kids (Ali & Moaaz),

To my brother and sisters,

To my advisor (Assoc. Prof. Dr. M. Kumral),

FOREWORD

This thesis is written as a completion to the Ph.D. in the field of Ore Deposits and Geochemistry in the Geological Engineering department from the Graduate School of Science and Technology at Istanbul Technical University (ITU), Istanbul, Turkey. It focuses on the genesis of intrusion-related gold mineralization at Atud area, Central Eastern Desert of Egypt. Therefore, this thesis provides field relationships, geologic, petrographic, ore mineralogic, and geochemical data of the gold-bearing quartz veins and associated hydrothermally altered host rocks. As well as it provides electron microprobe and stable isotopic data of the different alteration and ore minerals associated with this gold deposit.

More than one manuscript was extracted from this thesis, one of them was published in Ore Geology Reviews which represents chapter 2 in the thesis, and the other two manuscripts are under reviewing in the peer-reviewed international journals which represent chapter 3 and 4. Furthermore, chapter 1 and 5 in this thesis represent general introduction and general conclusions, respectively. Also, about six conference papers were also extracted and presented in different international conferences.

This PhD thesis is completed in the frame of a scholarship offered from the Egyptian Government (Cultural Affairs and Mission Sector) in cooperation with the Turkish Government (YTB, Turkey), and was financially supported by the BAP Project (No. 39183) for graduate students by Istanbul Technical University (ITU), Turkey.

I would like to express my sincere thanks to my advisor Assoc. Prof. Dr. Mustafa KUMRAL for his kind supervision, his efforts and helps during all the different stages of the thesis workings, and for revising the ealier versions of the thesis and finally for teaching me how to think freely and critically. Many thanks go to Prof. B. Zoheir (Benha University, Egypt), Dr. M. Afife (Benha University, Egypt), L. Gumus (ITU, Turkey) for their helps during field work. I also thank the helps of the research group of ITU/JAL, Turkey; Prof. M. Budakoğlu, Dr. D. Kıran Yıldırım, Mr. M. Karaman, Mr. O. Taş, Mrs. S. Sultanyan, Ms. Z. Döner, Mr. A. T. Ünlüer, Mr. H. Kocatürk, Mr. M. Kaya, Ms. B. Tanç, Mr. S. Öztürk, Mr. Ridvan, Ms. M. Uyğur, and Mr. M. Kaibru. In addition, great thanks go to the juries of thesis; Prof. M. Sezai Kırıkoğlu (ITU), Prof. Yusuf K. Kadıoğlu (Ankara University), Dr. E. Çiftçi (ITU) and Dr. N. Hanilçi (Istanbul University) for their constructive comments, corrections and helpful suggestions which greatly improved the thesis.

At last but not least my deep gratitude to my parents and lovely wife (Fatma Shaker) for encourage and support me during the different stages of the thesis and for my nice kids (Ali and Moaaz), my brother (Ali) and lovely sisters.

27 June 2016

Amr Abdelnasser

(B.Sc., M.Sc. Geology)

(Ore deposits and Geochemistry)

TABLE OF CONTENTS

ABBREVIATIONS

Ab : Albite
Act : Actinolite
A.I. : Alteration index
An : Anorthite
Ank : Ankerite
ANS : Arabian-Nubian Shield
Ant : Antigorite
apy : Arsenopyrite
ath : Anthophyllite
Au : Gold
ASL : Above sea level
ASTER : Advanced Spaceborne Thermal Emission and Reflection Radiometer
BC : Before Christ
BIF : Banded Iron Formation
BR : Band Ratio
Bt : Biotite
cal : Calcite
ccp : Chalcopyrite
chl : Chlorite
chm : chamosite
chr : Chromite
clc : Clinochlore
CLI : Calcite index
Cpx : Clinopyroxene
dol : Dolomite
EA-IRMS : Elemental Analysis-Isotope Ratio Mass Spectrometry
EAO : East African Orogen
EGSMA : Egyptian Geologic Survey and Mining Authority
EMPA : Electron microprobe analyses
Eng : Enargite

ep : Epidote

FCC : False-Color Composite

Goe : Goethite

gr : Graphite

ICP-MS : Inductively Coupled Plasma-Mass Spectrometry

ITU : Istanbul Technical University

JAL : Jeokimya Araştirmalari Laboratuvari (Geochemistry Research Laboratories)

Kfs : K-feldspar-or-microperthite

K.I. : K_2O index

KLI : Kaolinite index

Kln : Kaolinite

mag : Magnetite

MG Metagabbro-diorite complex

Mgs : Magnesite

M.I. : MgO index

MT : Metatuffs

Ms : Muscovite

OG : Olivine gabbronorite

OHI : OH-bearing altered mineral index

Ol : Olivine

Opx : Orthopyroxene

or : Orthoclase

PCA : Principal Component Analysis

Pht : Phlogopite

plag : Plagioclase

Px : Pyroxene

Py : Pyrite

qz : Quartz

RBD : Relative absorption Band Depth

SEM : Scanning electron microscope

Ser : Sericite

SP : Serpentinite rocks

Sp : Sphalerite

SRI : Sericite index

TC **:** Talc-carbonate rocks

Tlc **:** Talc

tr **:** Tremolite

ttn **:** Titanite

vol **:** Volume

XRD **:** X-ray diffractometer

XRF **:** X-ray fluorescence

Zeo **:** Zeolite

LIST OF TABLES

Page

LIST OF FIGURES

Page

GENESIS OF THE GOLD MINERALIZATION AT ATUD AREA, CENTRAL EASTERN DESERT OF EGYPT: GEOLOGICAL, ORE MINERALOGICAL AND GEOCHEMICAL APPROACHES

SUMMARY

This thesis provides comprehensive geological, petrographical, mineralogical, and geochemical studies of the gold deposit at Atud area at the Central block of the Egyptian Eastern Desert. It aims to provide a better understanding of the genesis of this vein-type mesothermal gold deposit and its relation to the tectonic evolution of the Arabian-Nubian Shield at East Africa. Electron microprobe (EMPA) and stable isotope analyses are also carried on to identify the conditions of the gold deposition and the mineralizing fluid according to the appropriate geothermometers, as well as to determine the temperature of the ore systems and the source, evolution, and nature of the ore-bearing fluids. Moreover, ASTER imagery data are used to delineate and detect the main alteration types associated with the gold mineralization at Atud area.

The study area (Atud area) that located in the Central Eastern Desert of Egypt is made up of a gabbro-diorite intrusion emplaced into the pre-existing rocks; serpentinite and metatuffs and is cut by a younger intrusion of olivine gabbronorite. The vein-type gold deposits in the Atud area are related to the metagabbro-diorite complex that occurred in Gabal Atud in the Central Eastern Desert of Egypt.

The dispersed talc-carbonate, dolomitic marble and calc-silicate rocks are derivatives of serpentinite around Gabal Atud. They represent the Pan-African dismembered ophiolitic rocks exposed in the study area. Metatuffs cover a vast area of the area around Gabal Atud where they form low-lying outcrops associated with serpentinite rocks. They are microscopically differentiated into different varieties; mafic lapilli metatuffs, intermediate metatuffs, metacherts, and quartz-biotite schists. The metagabbro-diorite complex covers a large proportion of the mapped area and exists as a semicircular body of Gabal Atud. It represents one of the early orogenic gabbro-diorite complexes in the Arabian-Nubian Sheild and its age ranges from 987 to 830 Ma. It had an obvious intrusive contact against serpentinites and metatuffs and later was invaded by olivine gabbronorite. It also was cut by numerous mineralized and barren quartz veins and dikes at its eastern and southeastern slopes, where NW-SE brittle-ductile shear zone cuts through this complex. Slightly metamorphosed gabbro and diorite rocks and hybrid leucocratic gabbro zone in between are exposed at the study area. Olivine gabbronorite forms a small intrusion cutting the gabbro-diorite complex of Gabal Atud. There are different types of dikes cut through the country rocks in the mine area, trend mainly in two directions. The oldest one is NNE-SSW and the youngest is NW-SE. Lamprophyre dikes occupy commonly the old direction (NNE-SSW) and cut through the serpentinite rocks, while porphyritic andesite and aplitic dikes occupy the NW-SE direction and cut through the gabbro-diorite intrusion.

This gold mineralization is associated with quartz veins and intense hydrothermal alteration haloes along the NW-SE brittle-ductile shear zone, as well as along the contacts between them. Two generations of quartz veins include the mineralized grayish-to-white color old vein (trending NW-SE), and the younger, non-mineralized milky white vein (trending NE-SW). The ore minerals associated with gold are essentially arsenopyrite and pyrite (type-I and II), with subordinate chalcopyrite, sphalerite, tetrahedrite, and pyrrhotite with goethite forming in three stages of mineralization: first, second (main ore), and third (supergene) stages.

Three main subsurface hydrothermal alteration zones were determined around the quartz veins in the main Atud area: zone 1: sericitic alteration (mainly sericite/muscovite and kaolinite with subordinate quartz and pyrite), zone 2: phyllic alterations (mainly quartz and sericite with pyrite and subordinate albite quartz-chlorite-carbonate), and zone 3: carbonate propylitic alterations (mainly carbonate (ankerite/calcite) and chlorite (chamosite/clinochlore) with albite and arsenopyrite). Concentrations of Au, Ag, and Cu are different from zone to zone by having 25-790 ppb, 0.7-69.6 ppm, and 6-93.8 ppm; 48.6-176.1 ppb, 0.9-12.3 ppm, and 39.6-118.2 ppm; and 53.9-155.4 ppb, 0.7-3.4 ppm, and 0.2-79 ppm for zone 1, 2, and 3, respectively. By using the mass balance calculations (calculated using the GEOISO-Windows program), the mass/volume gains and losses of the chemical components during the hydrothermal alteration processes in these different zones were studied revealing that the gold to be highly associated with the main mineralized zone as well as sericite/kaolinite and muscovite alterations in zone 1 more than in zones 2 and 3. Also, the REE pattern of these alteration zones suggested that La, Eu, and K added to the rocks from hydrothermal solution during the sericitization in zones (1) and (2), while in zone (3) HREE anomalies are with Mg-enrichments indicating low solubility of these elements in alkaline hydrothermal solutions during chloritization and carbonatization.

Microprobe data of the alteration minerals revealed that the sericite had a higher muscovite component in all analyzed flakes (average X_{Ms}= 0.89), with 0.10%-0.55% phengite content in wall rocks and 0.13%-0.29% phengite content in mineralized quartz veins. The wall rocks had higher calcite ($CaCO_3$) contents and lower $MgCO_3$ and $FeCO_3$ contents than the quartz veins. The chlorite flakes in the altered wall rocks were composed of pycnochlorite and ripidolite, with estimated formation temperatures of 289-295°C and 301-312°C, respectively. Albite had higher albite content (95.08%-99.20%) which occurs with chlorite in zone 3. While the microprobe studies of ore minerals reveal that gold can be classified as electrum (52.2-60.7 atom % Au & 36.7-39.1 atom % Ag) and is associated with arsenopyrite and As-bearing pyrite in the main mineralization phase within the main mineralized quartz veins and altered host rocks. Based on the arsenopyrite geothermometer, As-contents (29.3-32.7 atom %) in arsenopyrite point to deposition in the f_{S2} and T ranges of -10.5 to -5.5 and 305-450 °C, respectively during the main mineralizing stage. This indicates that the gold is transported and precipitated due to increasing lack of the hydrosulphide complexes AuHS° and $Au(HS)^-_2$.

Based on the $\delta^{34}S$ isotopic compositions of the sulfides (2.8 – 9.5 ‰ from mineralized quartz veins and 0.7 – 7.8 ‰ from the altered host rocks), they are originated from magmatic fluids in which the sulfur is sourced either directly from magma or remobilized from the magmatic rocks. On the other hand, calcite formed from fluids having magmatic mixed with metamorphic signatures based on its $\delta^{13}C$ (-10.6 to -8.0 $‰_{VPDB}$) and $\delta^{18}O$ (13.1 to 14.5 $‰_{SMOW}$) values.

ASTER-imagery band rationing (BR), relative absorption band depth (RBD), principal component analysis (PCA), false-color composite (FCC), and mineral indices suggest the sericitic and argillic (kaolinite) alterations are the main alteration types detected at the main Atud mine area, while the calcite alteration is confined to the serpentinite and talc-carbonate around the mine area.

This work concluded that the gold-bearing ores at Atud deposit have magmatic sources leaching from the country intrusive rocks during water/rock interactions then remobilized during a metamorphic event. Therefore, the Atud gold deposit is classified as an intrusion-related gold deposit, in which the host intrusion acted as the source of metals, which were later mobilized and deposited as a result of NW-SE shearing. This also refers to the gold mineralization at the study area was structurally controlled.

ATUD BÖLGESİ, MISIR'IN ORTA DOĞU ÇÖLÜ'NDEKİ ALTIN CEVHERLEŞMESİNİN KÖKENİ: JEOLOJİK, CEVHER MİNERALOJİK VE JEOKİMYASAL YAKLAŞIMLAR

ÖZET

Bu tez Mısır Doğu Çölü'nün Orta bloğundaki Atud bölgesinde intrüzyonla ilişkili altın yatağının kapsamlı jeolojik, petrografik, mineralojik ve jeokimyasal çalışmaları kapsamaktadır. Tezin amacı, damar tipi mezotermal altın yatağının kökeninin ve onun Doğu Afrika'daki Arap Nubian Kalkanı'nın tektonik gelişimi ile ilişkisinin daha iyi anlaşılmasını sağlamaktır. Elektron mikroprob (EMPA) ve duraylı izotop analizleri, altın yatağının durumunu ve uygun jeotermometrelere göre hidrotermal akışkanı belirlemenin yanı sıra cevher sistemlerinin sıcaklığını, kaynağını, gelişimini ve cevher-taşıyan akışkanların doğasını belirlemek için kullanılmıştır. Bir de ASTER görüntü verisi ile de Atud bölgesindeki altın cevherleşmesi ile ilişkili ana alterasyon tipleri betimlenmiş ve tespit edilmiştir.

Mısır'ın Orta Doğu Çölü'nde yer alan çalışma alanı (Atud bölgesi) önceden var olan serpantinit ve metatüf kayaçlarının içine sokulan metagabro-diyorit intrüzyonundan oluşur ve olivin gabronoritlerin daha genç intrüzyonu tarafından kesilmektedir. Atud bölgesindeki damar tipi altın yatakları Mısır'ın Orta Doğu Çölü'ndeki Gabal Atud'da oluşmuş metagabro-diyorit kompleks ile ilişkilidir.

Talk karbonat, dolomitik mermer ve kalk-silikatik kayaçlar Gabal-Atud civarında bulunan serpantinitlerden türemişlerdir ve çalışma alanında gözlemlenen Pan-Afrikan ofiyolit segmentlerini temsil eder. Metatüfler Gabal Atud etrafında büyük bir alanı kapsamakta olup serpantinitler ile birlikte mostra vermektedirler. Meta-tüfler mikroskopik olarak mafik-lapilli tüfler, ortaç tüfler, meta-çörtler ve kuvars-biyotit şistler olarak tanımlanabilmektedir. Metagabro-diyorit kompleksi ise haritalanmış alanın büyük bir kısmını kapsamakta ve yarı-dairesel bir şekilde Gabal-Atud'un gövdesini oluşturmaktadır. Metagabro-diyorit kompleksinin yaşı 987-830 Ma arasındadır ve Arabo-Nubian kalkanının erken dönem orojenik komplekslerinden biridir. Serpantinitler ve Metatüfler ile intrüzif dokanağı bulunan kayaç daha sonra olivin gabro-norit karakterli bir sokulum tarafından kesilmiştir. Kayaç ayrıca cevherleşmeler içeren oldukça fazla sayıda kuvars damaraları ve dayklar tarafından doğu ve güneydoğu yamaçlarında gözlemlenen Kuzeybatı-Güneydoğu gidişli gevrek-sünek makaslama zonunda kesilmiştir. Düşük derece metamorfizma geçirmiş gabro ve diyorit kayaçları ve bu kayaçların arasındaki zonda gözlemlenen hibrit lökokratik gabro kayaçları çalışma alanında mostra vermektedir. Olivin gabro-norit karakterli küçük intrüzif kütle Gabal-Atud Gabro diyorit kompleksini kesmektedir. Farklı tipteki dayklar bölgedeki temel kayaçları kesmekte olup genellikle daha yaşlı olanlar KKD-GGB ve daha genç olanlar KB-GD gidişlidir. Daha yaşlı dayklar Lamproifirik karakterli olmakla bereaber serpantitleri kesmektedir. Daha genç dayklar ise andezit porfir karakterli veya aplitik dokulu olup gabro-diyorit kompleksini kesmektedir.

Bu altın cevherleşmesi kuvars damarları ve KB-GD kırılgan-sünek makaslama zonu boyunca yoğun hidrotermal alterasyon haleleri içerisinde aynı zamanda bunlar arasındaki kontaklar boyunca yer alır. Kuvars damarları, cevherleşmiş griimsiden beyaza eski damar (KB-GD doğrultulu) ve daha genç, cevherleşmemiş süt beyaz damar (KD-GB) olmak üzere iki gelişimi içermektedir. Altınla ilişkili cevher mineralleri; alt kalkopirit, sfalerit, tetrahedrit ile beraber başlıca arsenopirit ve pirit (tip-I ve II), ilk, ikinci (ana cevher) ve üçüncü (süperjen) fazları olmak üzere cevherleşmenin üç fazı boyunca götitle beraber pirotindir.

Üç ana yeraltı hidrotermal alterasyon zonları ana Atud bölgesindeki kuvars damarları boyunca gözlenmiştir; zon 1: kuvars-serisit-pirit, zon 2: kuvars-klorit-karbonat ve zon 3: kalsit-albit-klorit. Au, Ag ve Cu konsantrasyonları zondan zona değişmektedir. Zon 1, 2 ve 3 için sırasıyla bu konsantrasyonlar; 25-790 ppb, 0.7-69.6 ppm ve 6-93.8 ppm; 48.6-176.1 ppb, 0.9-12.3 ppm ve 39.6-118.2 ppm; 53.9-155.4 ppb, 0.7-3.4 ppm ve 0.2-79 ppm'dir. Kütle balansı hesaplamaları (GEOISO-Windows programı kullanılarak hesaplanmış) kullanılarak bu farklı üç zondaki hidrotermal alterasyon süreçleri boyunca kimyasal bileşimlerin kütle/hacim kazanımları ve kayıpları çalışılmış, buna göre altının ana cevherleşme zonu ile, aynı zamanda serisit/kaolinit ve muskovit alterasyonlarının da zon 2 ve 3'ten daha çok zon 1 ile yüksek ilişkili olduğu tespit edilmiştir. Bir de bu alterasyon zonlarının NTE paternleri, La, Eu ve K'nın zon (1) ve (2)'de serisit alterasyonu boyunca hidrotermal solüsyondan kayaçlara eklendiğini, zon (3)'te HNTE anomalilerinin klorit ve karbonat alterasyonları boyunca alkalin hidrotermal solüsyonlarındaki bu elemetlerin düşük çözünürlüklerine işaret eden Mg-zenginleşmeleri ile olduğunu önermektedir.

Alterasyon minerallerinin mikroprob verileri, tüm analiz edilmiş pulcuklarda serisitin yüksek muskovit bileşenine sahip olduğunu (ortalama X_{Ms}= 0.89), yan kayaçlarda fengit içeriğinin %0.10-0.55 olduğunu ve cevherli kuvars damarlarında fengit içeriğinin %0.13-0.29 olduğunu açığa çıkarmıştır. Yan kayaçlar kuvars damarlarından daha yüksek kalsit ($CaCO_3$) içeriklerine ve daha düşük $MgCO_3$ ve $FeCO_3$ içeriklerine sahiptir. Altere yan kayaçlardaki klorit pulcukları pinoklorit ve ripidolitten oluşmuştur, tahmini oluşum sıcaklıkları sırasıyla 289-295°C ve 301-312°C'dir. Albit, zon 3'teki klorit ile beraber oluşmuş daha yüksek albit içeriğine (%95.08-99.20) sahiptir. Cevher minerallerinin mikroprob çalışmaları, altının electrum (52.2-60.7 atom % Au & 36.7-39.1 atom % Ag) olarak sınıflandırıldığını ve ana cevherli kuvars damarları ve altere ana kayaçlar içerisindeki ana cevherleşme fazındaki arsenopirit ve As-taşıyan pirit ile ilişkili olduğunu ortaya koymuştur. Arsenopirit jeotermometresine dayanarak, arsenopiritteki As-içerikleri (29.3-32.7 atom %), ana cevherleşme fazı boyunca f_{S2} ve T sırasıyla,; -10.5 to -5.5 arasında ve 305-450 °C'deki depolanmaya işaret etmektedir. Bu da altının taşındığına, hidrosülfid kompleksleri AuHS° ve $Au(HS)^-_2$'nin artan eksikliğinden dolayı çökeldiğine işaret etmektedir.

Sülfidlerin $\delta^{34}S$ izotopik kompozisyonlarına dayanarak, bunlar magmatik akışkanlardan kaynaklıdır ki burada sülfür ya direkt magmadan ya da magmatik kayaçlardan yeniden taşınmasından kaynaklanmıştır. Diğer bir deyişle, kalsit, $\delta^{13}C$ ve $\delta^{18}O$ değerleri baz alındığında, değişken metamorfik izler ile karışık başlıca magmatikleri içeren akışkanlardan oluşmuştur.

ASTER-görüntü bant oranlaması (BR), bağıl absorpsiyon bant derinliği (RBD), esas bileşen analizi (PCA), yanlış-renk kompoziti (FCC) ve mineral indeksleri, serisit ve arjilik (kaolinit) alterasyonlarının Atud maden bölgesindeki ana alterasyon tipleri

olduğunu, kalsit alterasyonunun maden bölgesi etrafında serpantinit ve talk-karbonat ile sınırlı olduğunu önermiştir.

Bu çalışmada Atud yatağındaki altın-taşıyan cevherlerin magmatik kaynaklı olduğu, su/kayaç etkileşimleri boyunca çevre intrüzif kayaçlardan çözünerek, sonrasında metamorfik olaylar boyunca yeniden hareketlendiği sonucuna varılmıştır. Bu yüzden Atud altın yatağı intrüzyonla ilişkili altın yatağı olarak sınıflandırılmaktadır, ana intrüzyon, KB-GD makaslama etkileri sonucu olarak taşınan ve depolanan metallerin kaynağı olarak davranmıştır, bu durum ise çalışma alanındaki altın cevherleşmesinin yapısal kontrollü olduğu anlamına gelir.

1. INTRODUCTION

1.1 General overview

The gold deposits and occurrences were located in the Precambrian basement rocks of the Arabian-Nubian Shield (ANS) (Figure 1.1). This ANS represented the northern extension of the East African Orogen (EAO), and extends from the river Nile at the east towards the Arabian Peninsula and continued to the south to the Mozambique Belt (Vail, 1988) (Figure 1.1). It is formed during the Neoproterozoic (Kröner, 1979) by a complex accretion of terranes onto a pre-existing pre-Panafrican Basement (Nile Craton or East Sahara Craton; Bertrand and Caby (1978); Stern (1994)) through progressive oblique convergence of East- and West-Gondwana lands (Stern, 1994). Also, the ANS comprises the ophiolite, intra-oceanic island arc, and back-arc assemblages that act as a preserved remnant of the ancient Mozambique Ocean (Burke and Sengör, 1986). The gold occurrences at the ANS are mainly confined to quartz-mineralized shear zones that occurred in different terrenes; ophiolitic sequences, island arc assemblages, Hammamat and Dokhan Groups, and post-orogenic granitoids (Pohl, 1982; El-Gaby et al., 1988). Moreover, the gold mineralization that related to the post-orogenic granitoid is very important as productive shear zones and quartz veins. During the compressional or transpressional late stage events of the orogeny, these shear zones and quartz veins were structurally formed and postdated the post-orogenic intrusions which provided the heat sources leading to the formation of the hydrothermal convention cells (Klemm et al., 2001). As well as, the available minerals at the host rocks were dissolved by the interstitial waters due to high temperature and pressure, also by which little concentrations of gold were originated from the deformed host rocks (Klemm et al., 2001).

In the Eastern Desert of Egypt, more than 110 gold deposits and occurrences are distributed over the whole area of the Precambrian basement of the Nubian Shield (Figure 1.2). The gold mining activity in Egypt was started from the pre-dynastic times (Gabra, 1986) passing through different ancient periods up to now. The ancient Egyptians extracted the gold from the auriferous quartz veins with various

dimensions in the underground and open-pits mining works (Botros, 2004). Therefore, these auriferous quartz veins have represented the main target for gold in Egypt since ancient times with some gold-bearing other deposits (Botros, 2004).

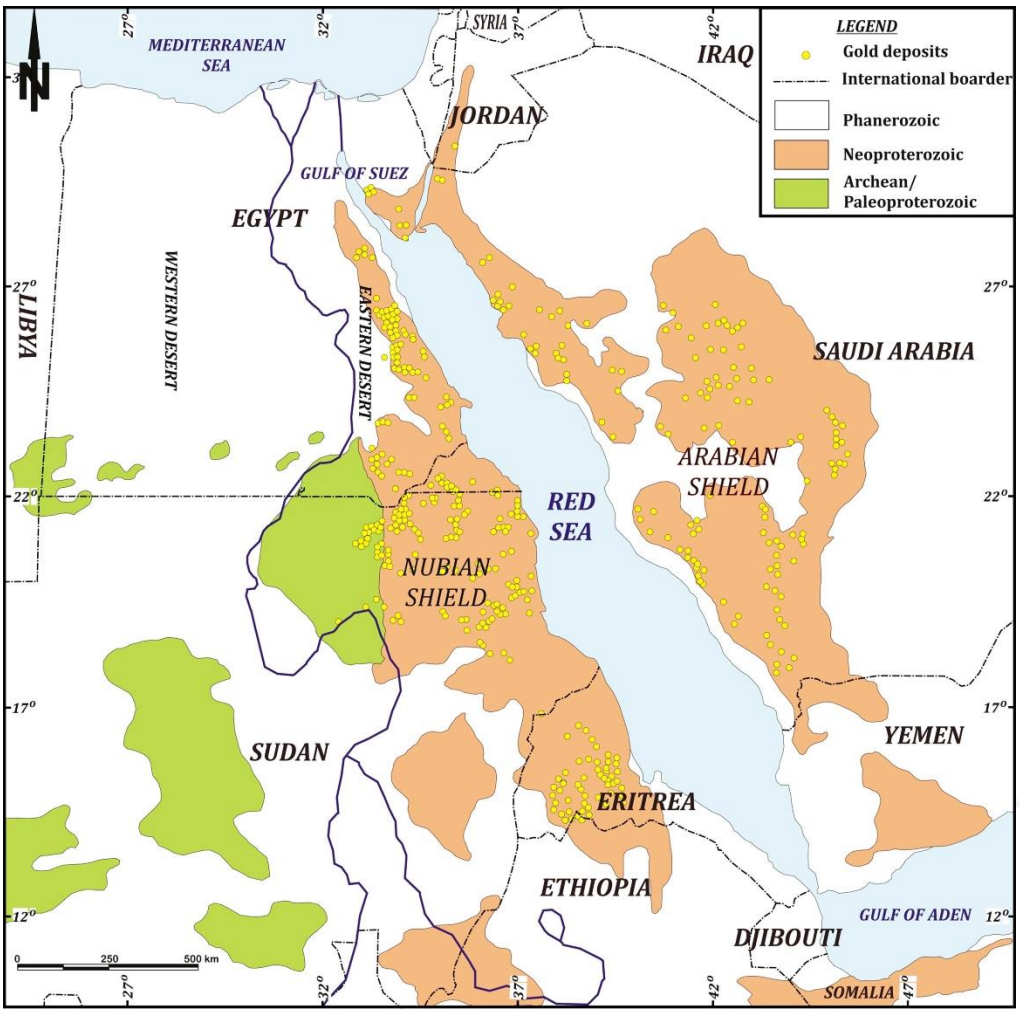

Figure 1.1 : Gold occurrences in Arabian-Nubian Shield (ANS), compiled from Kochine and Bassyuni (1968) with distribution of the Archean–Paleoproterozoic and Neoproterozoic rocks.

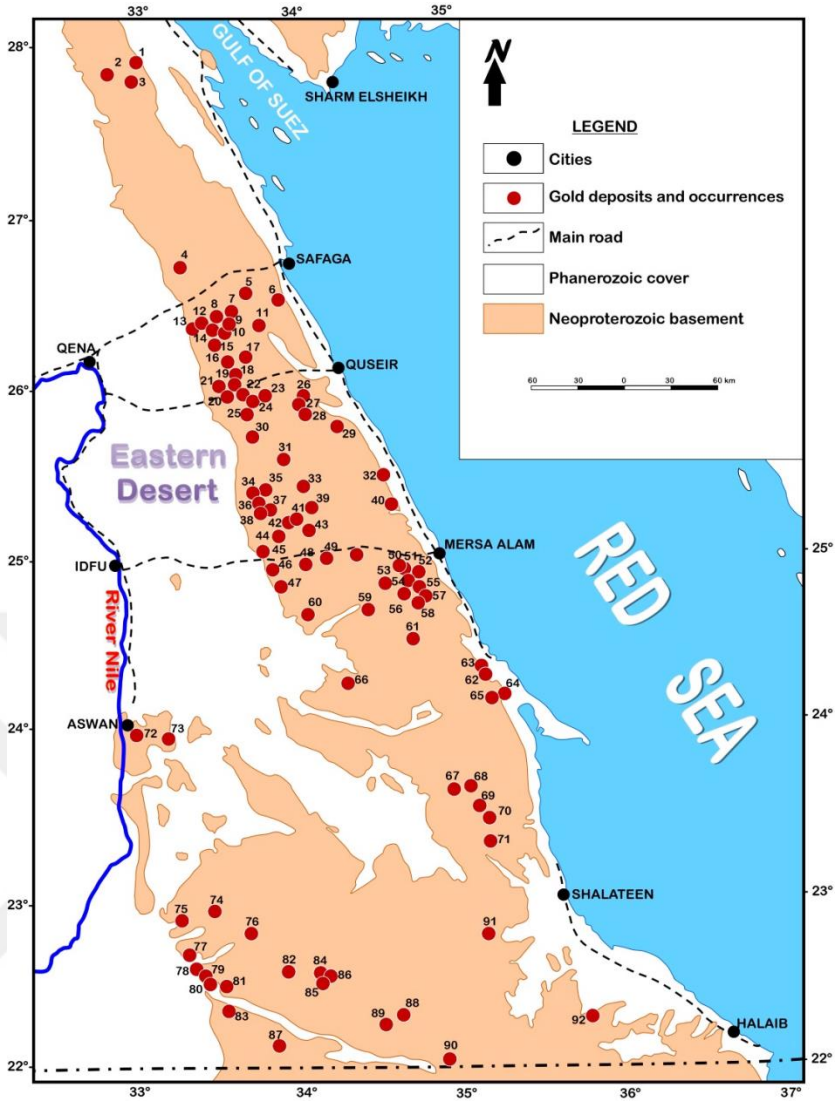

Figure 1.2 : Gold deposits and occurrences in the Eastern Desert of Egypt, compiled from Kochine and Bassyuni (1968); Botros (2004). (1) Umm Mongul; (2) Umm Balad; (3) Wadi Dib; (4) Fatira; (5) Abu Marawat; (6) Wadi Gasus; (7) Semma; (8) Gebel Semna; (9) Abu Qarahish; (10) Kab Amiri; (11) Sagi; (12) Gidami; (13) Hamana; (14) Erediya; (15) Abu Had; (16) Atalla; (17) Rebshi; (18) Umm Esh; (19) Fawakhir; (20) Hammamat; (21) Umm Had; (22) El Sid; (23) Umm Selimat; (24) Hammuda; (25) El Nur; (26) Kareim; (27) Kab El Abyad; (28) Tarfawi; (29) Sherm El Bahaari; (30) Zeidum; (31) Wadi Zeidum; (32) Umm Rus; (33) Sigdit; (34) Talat Gadalla; (35) Abu Muawaad; (36) Daghbag; (37) El Hisimat; (38) Bokari; (39) Umm Samra; (40) Abu Dabbad; (41) Abu Qaria; (42) Umm Saltit; (43) Bezah; (44) Umm Selim; (45) Barramiya; (46) Dungash; (47) Samut; (48) Umm Hugab; (49) Urf El Fahid; (50) Atud; (51) Sukkari; (52) Umm Tundeba; (53) Hanglaliya; (54) Kurdeman; (55) Sabahia; (56) Umm Ud; (57) Allawi; (58) Lewewi; (59) Dweig; (60) Hamash; (61) Geli; (62) Qulan; (63) Kab El Rayan; (64) Sheialik; (65) Abu Rahaya; (66) Wadi Khashb; (67) Umm Eleiga; (68) Betan; (69) Qurga Rayan; (70) Hutit; (71) Kalib; (72) Kurtunos; (73) El Hudi; (74) Hariari; (75) Um Shira; (76) Neqib; (77) Haimur; (78) The Nile Valley (Block E); (79) Umm Garaiart; (80) Marahib; (81) Atshani; (82) Murra; (83) Filat; (84) Seiga I; (85) Seiga II; (86) Umm Shashoba; (87) Abu Fass; (88) Umm Tuyur; (89) Betam; (90) Umm Egat; (91) Kurbiai; (92) Romit.

1.1.1 Overview of the classification of the Egyptian gold deposits

There are many studies classified the gold deposits in Egypt based on different styles (e.g. the nature, occurrences, and tectonic environment of mineralization) as well as according to the types and tectonic setting of the host rocks and types of metal association. Three types of gold were distinguished based on the nature and mode of occurrences of mineralization; (1) dyke-type, (2) vein-type, and (3) placer-type (Kochine and Bassyuni, 1968). Based on the time of mineralization and formation of gold, Sabet et al. (1976) identified four main epochs; (1) Pre-orogenic epoch, (2) Syn to late-orogenic epoch, (3) Riphean-lower Paleozoic epoch, and (4) Mesozoic-Cenozoic epoch. Sabet and Bordonosov (1984) classified the gold-ore formations into three types namely as; (1) gold–sulphide, (2) skarn gold-ferruginous quartzite, and (3) gold quartz veins formations. In the named gold quartz vein formation, it was subdivided according to the metal and mineral associations into; gold-arsenic, gold-pyrite, gold-polymetal, gold-copper, gold-mercury, and gold-antimony types (Sabet and Bordonosov, 1984). Also based on the mode of occurrences, AbdelTawab (1992) suggested three mode of occurrences for gold; (1) vein-type disseminated gold, (2) algoma-type, and (3) gold in thermal domes. The vein-type disseminated gold formed as a result of several gold-bearing hydrothermal solutions' pulses that circulated in the open fractures and active shear zones (AbdelTawab, 1992). Algoma-type gold that associated with the Banded Iron Formation (BIF) has a volcanogenic origin (AbdelTawab, 1992). While, the gold in thermal domes that restricted to the shear zones cutting through the gabbroic to granitic rocks and some Dokhan volcanics surrounded the thermal domes (AbdelTawab, 1992). Hassaan and El Mezayen (1995) subdivided the gold mineralization in the Egyptian Eastern Desert according its genesis into three genetic groups; (1) ophiolitic group at which the gold is associated with graphites and the quartz-carbonates (listwaenites) in the serpentinite rocks, (2) island-arc group that is represented by the calc-alkaline metavolcanics and metavolcanosediments, metagabbro-diorites, quartzdiorites and tonalities in which Au is associated with different metals (e.g. Cr, Co, Cu, Pb, Zn, Sn, Mo, Ba, As, Ag, Be, Fe, and Mn), and (3) cordilleran group at which gold was occurred in the calc-alkaline older granites, Dokhan volcanics and Hammamat molasse sediments, felsite porphyry younger granites and younger ultrabasic-basic rocks.

Botros (2004), based on the tectonic-magmatic evolution of the Nubian shield, was newly classified the Egyptian gold deposit into three types; (1) stratabound, (2) non-stratabound, and (3) placer gold deposits. Each type has a subdivision types that are shown in Table 1.1.

Table 1.1 : The Egyptian gold deposits' classification and tectonic environment (Botros, 2004).

Class	Types of mineralization	Tectonic environment	Remarks
(1) Stratabound deposits	(1.1) Gold hosted in Algoma-type BIF	-Immature island-arc	-Syngenetic
	(1.2) Gold hosted in tuffaceous sediments		
	(1.3) Gold hosted in volcanogenic massive sulphide deposits	-Mature island arc	
(2) Non-stratabound deposits	(2.1) Vein-type mineralization	-Continental margin	-Epigenetic
	(2.1.1) Auriferous quartz veins hosted in metamorphic rocks and/or the granitic rocks surrounding them		
	(2.1.2) Auriferous quartz veins in sheared ophiolitic ultramafic rocks		
	(2.1.3) Auriferous quartz veins associated with porphyry copper mineralization		
	(2.1.4) Auriferous quartz veins at the contact between younger gabbros and granites	-Intra-plate	
	(2.1.5) Small amounts of the element in quartz veins of Sn- W- Ta- Nb- mineralization		
	(2.2) Disseminated-type mineralization hosted in hydrothermally altered rocks (alteration zones)	-Continental margin and intra-plate	-Epigenetic
(3) Placer deposits	(3.1) Modern placers	-Intra-plate sedimentation	
	(3.1.1) Alluvial gold in wadis and gullies		
	(3.1.2) Beach placers		
	(3.2) Lithified placers		

The stratabound gold deposits that are hosted in the island arc volcanic and volcaniclastic rocks are considered as syngenetic mineralization (Botros, 2004). They have gold-bearing Algoma-type BIF and -tuffaceous sediments that were formed in the early stage of the formation of the island-arc (Immature), whereas the gold-bearing volcanogenic massive deposits were formed in the mature island-arc stage (Botros, 2004). On the other hand, The non-stratabound deposits that were occurred during the periods of the Pan-African orogeny and post-cratonization stage have two major subtypes; vein-type and disseminated-type mineralization confined to the hydrothermally alteration zones in the host rocks and considered as epigenetic mineralization (Botros, 2004). The vein-type mineralization was hosted in different

lithologies; metamorphic rocks and/or the surrounded granitic rocks, sheared ophiolitic ultramafic rocks, porphyry intrusive rocks, and younger gabbros and granitic contacts (Botros, 2004). Many authors (e.g. Garson and Shalaby (1976); Pohl (1982); El-Bouseily et al. (1985); El-Gaby et al. (1988); Hilmy and Osman (1989); Hussein and El Sharkawi (1990); Harraz et al. (1992); Harraz and Ashmawy (1994); Harraz (1999); Harraz (2002); Zoheir (2012b); Zoheir (2012a); Abdelnasser et al. (2014a); Abdelnasser et al. (2014b); Abdelnasser and Kumral (2016)) studied the vein type gold deposits in Eastern Egypt up to date.

While, the placer gold deposit was occurred as a result of thermal and mechanical weathering of the nearby gold mineralization over long time by which gold concentrates in the valleys and drainages (Botros, 2004). Modern placer and paleoplacer gold deposits are the main categories of this type. The modern type is represented by beach placer in black beach sands in Egypt, whereas auriferous conglomerates occurring near ancient eroded surfaces belong to the paleoplacer type (Botros, 2004).

1.1.2 Overview of the mining and production history of the Egyptian gold.

The historical time of the earliest gold production and mining in Egypt is dated by the remains of the sites of its production by the “Earliest Hunters” who mostly are the nomadic population (Mond and Winkler, 1940). This production was started with accumulation of the nugget gold from the grounds of some wadis in the middle of the fourth millennium BC (Mond and Winkler, 1940). Klemm et al. (2001) classified the gold production periods in Egypt and Nubia into seven periods; (1) pre- and early dynastic times, (2) old and middle kingdom times, (3) New Kingdom times, (4) Ptolemaic (Greek) times, (5) Kushitic times, (6) Roman and Byzantine times, and (7) Arab times.

The gold production in the Pre-dynastic times (~ 3500 BC) was represented by the explorations of the gold artifacts (Kroeper and Wildung, 1994) that were concentrated in quartz veins within Neoproterozoic granitic intrusions (Klemm et al., 2001). At this period, the gold mining started with open pits with moderate underground workings. The oldest tools of mining that were discovered in the old mining sites refer to the gold was associated with altered quartz vein systems within Cu-sulfide mineralization. Moreover, the gold-bearing quartz veins were crushed in

situ to fine powders by large stone hummers (6-10 kg weight), later gold fragments were separated for other processing (Klemm et al., 2001).

The production of gold in old (2700–2160 BC) and middle kingdom times (2119–1794 BC) was depended on looking for the malachite staining and hematite enrichments in the host rock where gold-bearing quartz veins were associated (Klemm et al., 2001). The mining tools used during the in situ crushing at the old kingdom are oval stone hummer with 2-5 kg weight, while at the middle kingdom; they used stone mortar with the hummer giving pea-sized grains of gold-bearing quartz then grinding to powder portions. During the period of Sesostris-I (king of ancient Egypt at the middle kingdom; 1908-1875 BC), the first military campaign was established to highly produce the Nubian gold (Newberry, 1893).

The gold in New Kingdom times (1550–1070 BC) was produced mainly from the old mines at the Central Eastern Desert of Egypt (South Qena-Safaga road) with some mines from the South Egypt (Wadi Allaqi area) and Northeast Sudan. The gold mining at this period set up on the prospecting of the structural control of gold-bearing quartz veins free of hematite and green copper aureoles, as well as following the strike and orientation directions of these vein systems and identify their geological environments (Klemm et al., 2001). Because the mining activities were enlarged at this period, a new milling technique had been used represented by a flat and oval-shaped grinding surface millstone having 30-50cm wide and 80cm long that similar to the flour mills used at the region of the Nile Valley (Roubet, 1989). The gold was separated from the fine-milled quartz powder portion by the washing processes. At these kingdom times, during the region of Ramesses IV (1151-1145 BC), the world oldest surviving geological map was drawn exhibiting the topography and geology of Wadi Hammamat area at the Central block of the Egyptian Eastern Desert as well as illustrating the gold-working settlement at Bir Umm Fawakhir (Harrell and Brown, 1992). This map was discovered as papyrus around 1820 and now found in the Egyptian Museum in Turin, Italy (Figure 1.3).

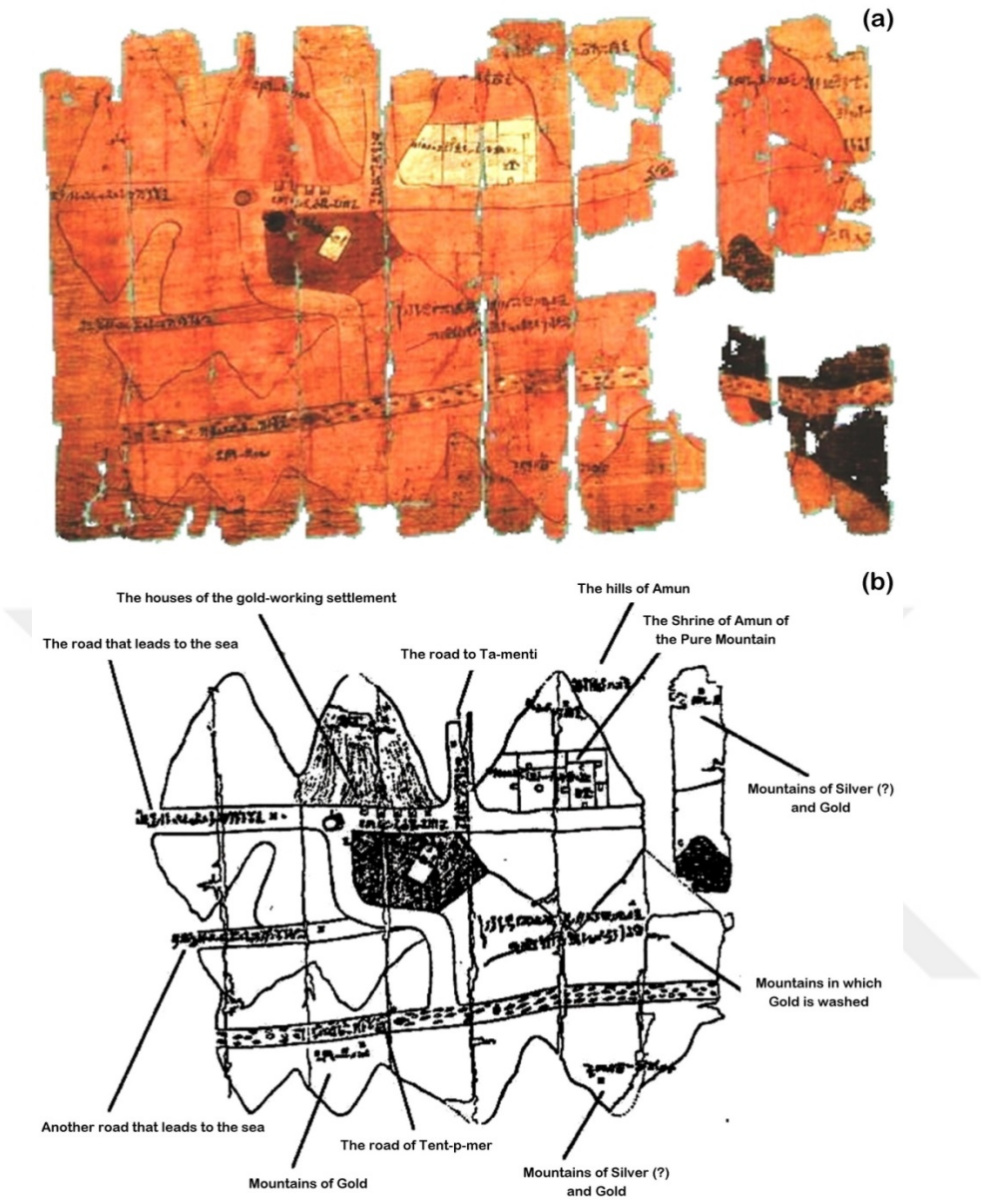

Figure 1.3 : a) Papyrus showing the world's oldest surviving geological map; b) Descriptions of this papyrus map after Harrell and Brown (1992).

Gold in Ptolemaic (Greek) and Roman times was produced from the underground mining activities that were located close to the Desert roads (Murray, 1925). The mining in Wadi Allaqi district was also reported during the Ptolemaic times with different localities cluster around different main roads in the Central Eastern Desert; Qena-Safaga, Quft-Qoseir, Edfu-Berenice and Laqeita-Berenice roads that have least some safety (Klemm et al., 2001).

Gold production during Kushitic times (800–400 BC) was not highly reported just in few sites in Nubia. The milling tools were represented by handle oval and tough-shaped stone mills having deeper secondary concavity (Klemm et al., 2001).

Gold production in Roman and Byzantine times decreased largely because of the attacks by the desert tribes of the Blemmyes. Therefore, the existence of the Roman and gold mining activities was highly restricted to the highly protected Eastern Desert's roads. The used mills were changed from oval-shape in the past to round mills having 30-45 cm diameter that improve the gold recovery (Klemm et al., 2001). While, at the Byzantine times, no more archeological evidences for the mining activities of gold worked out expect in Bir Umm Fawakhir has some evidences (Meyer and Heidorn, 1998).

During the Arab times, the ancient gold mining sites were reopened and reactivated in the Egyptian Eastern Desert with no evidence for primary underground workings, while in NE Sudan; the gold production was depended on the wadi working close to the River Nile (Klemm et al., 2001).

1.2 Location of the study area

The study area -namely Atud area- is located in the central part of the Egyptian Eastern Desert and lies between latitudes 24°59'30" – 25°02'15" N and longitudes 34°22'30" – 34°25'30" E covering 20 km^2 (Figure 1.4).

Geographically, the Atud area is characterized by various topographic features such as low lands, moderately elevated outcrops and high mountains. It has main peak represented by Gabal Atud with 885 m (above sea level) elevation and traversed by Wadi Atud at the southern part.

The Atud gold mine is about 58 km west of Mersa Alam city on the Red Sea Coast and 170 km east of Idfu city in the Nile Valley, and south of the Idfu-Mersa Alam highway about five km (Figure 1.4). The closest settlements are the ports of Quseir and Abu Ghusun cities on the Red Sea. The source of water for the mite site is closely supplied from Bir Umm Kariga (~ 40 km east of Gabal Atud on the Idfu-Mersa Alam paved road), while the source of drinking water is either from 1dfu or Mersa Alam cities.

Climate at the study area is typically arid being hot in summer and mild to cold in winter with scarcity rainfalls. Plants are scarce and inhabitants are very few. Some sporadic flash torrents may be take place in October-November.

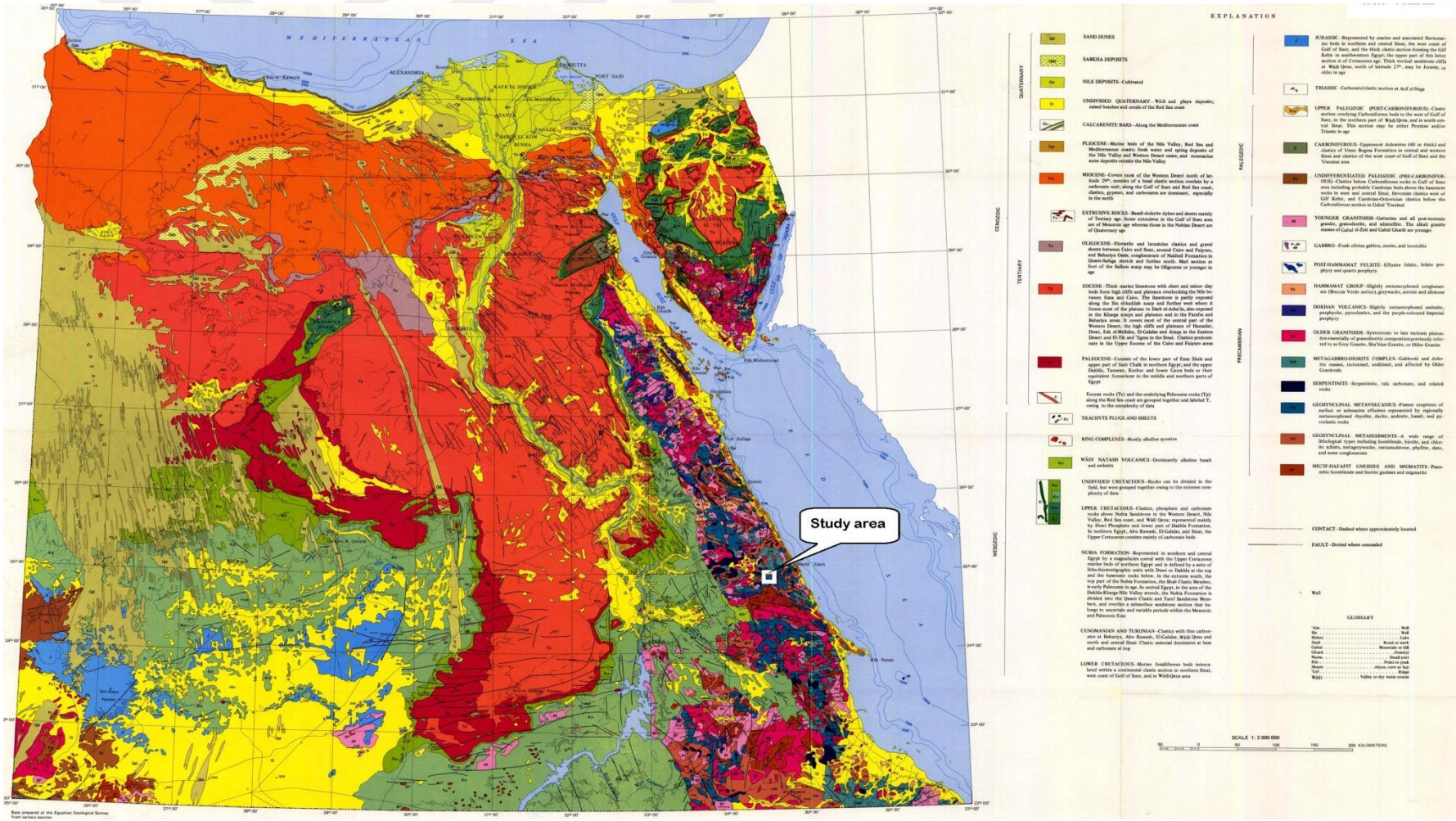

Figure 1.4 : Location map of the study area (Atud area) at the Central Eastern Desert of Egypt. The geolgic map of Egypt after EGSMA (1981).

1.3 Historic gold mining at Atud area

The Atud gold mine is one of many in the Egyptian Eastern Desert that was exploited during Pharaonic times, but no ore has been produced since then (Gabra, 1986). A little more detail, based on the old mining tools in the Atud area (Figure 1.5a-b), the Atud gold mining was done during New Kingdom times (1550–1070 BC) as a result of presence oval-shaped grinding surface millstone having 30-50cm wide and 80cm long (Figure 1.5a), and during the Roman and Byzantine times due to existence of round mills having 30-45 cm diameter (Figure 1.5b). Detailed work was done at the Atud gold mine by the Egyptian Geologic Survey and Mining Authority (EGSMA) between 1953 and 1969, including surface and subsurface geological studies, drilling, mapping, mine workings and sampling of the altered rocks, quartz veins and country rocks (Gabra, 1986).

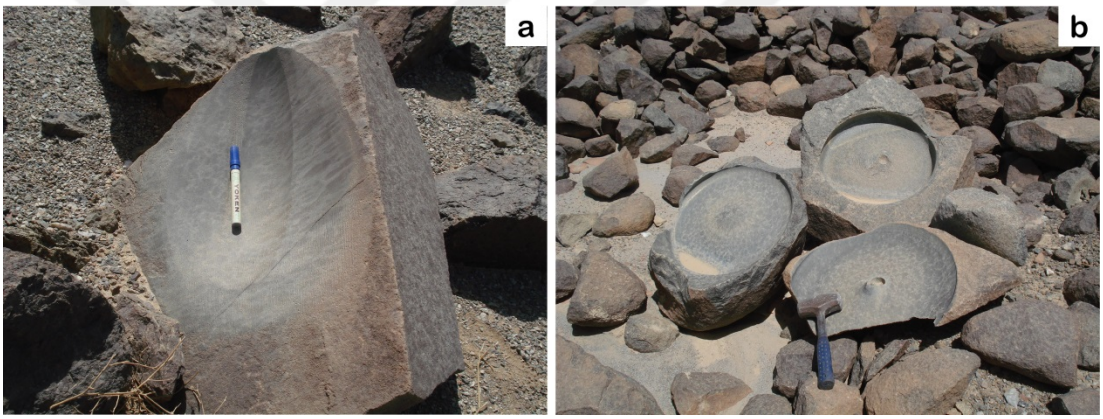

Figure 1.5 : Old gold mining tools at Atud area: a) Oval-shaped grinding surface millstone; b) Round mills.

1.4 Purpose of the thesis

As the title indicates, the objectives of this thesis include initiation of comprehensive studies on the intrusion-related gold deposit at Atud area for providing a better understanding of the genesis of these gold deposits at the Eastern desert in relation to the tectonic evolution of the Arabian-Nubian Shield. This is recognized by using the petrographic and mineralogical examinations, geochemical analyses, electron microprobe analyses (EMPA), and stable isotope analyses, as well as remote sensing techniques.

The geological, field relationships, petrographic, and mineralogical studies are to be able to determine the least altered and highly altered host rocks associated with the

Atud gold deposits as well as classify the subsurface hydrothermal alteration into three alteration zones (zone-1, 2, and 3) around the mineralized and non-mineralization quartz veins. The geochemical studies are to study the whole rock geochemistry of the different rocks unit at Atud area as well as determine the chemical exchanges between host rocks and hydrothermal fluids during hydrothermal alteration processes by applying mass/volume gains and losses of chemical components along with the mass balance calculations.

Electron microprobe analyses (EMPA) of alteration and ore minerals and gold were performed to determine the conditions of gold deposition and the mineralizing fluid according to the appropriate geothermometers. In addition, the stable isotope analyses were carried out on sulfur (^{34}S), oxygen (^{18}O) and carbon (^{13}C) isotopes of sulfide (pyrite and arsenopyrite) and carbonate minerals in order to determine the temperature of the ore systems and the sources of the ore materials (sulfur and carbon) as well as the origin, evolution, and nature of ore-bearing fluids.

The remote sensing techniques were carried out on a Cloud free ASTER images of the Atud mine area are processed for geologic and surface alteration mapping as well as detection of the alteration minerals at the study area.

1.5 Methodology

The following methods are carrying out in attempting to achieve the objectives of this thesis:

a) Sample collections and detailed geologic mapping of the study area (Atud gold deposit): A total of 150 host rock, altered rock, and mineralized samples were collected during a number of field works. Geological mapping at regional, local and mine scales is to provide information about the distribution and controls on mineralization, and to distinguish rocks that are the most favorable hosts to gold resources.

b) Petrographical and mineralogical studies: Petrographic works allow the identification of the minerals in the host rocks and determine the mineralogical changes associated with the gold mineralization. While, the ore microscopy reveals the ore mineralogy and textures that reflect their depositional conditions. It also allows the determination of the gold distribution and associations among the different

ore minerals. Therefore, sixty thin-sections and polished sections were examined petrographically represent the host rock and gold-bearing ore samples at the study area.

c) Ore Genesis: includes ore microscopy and electron microprobe analyses. The electron microprobe (EMPA) and scanning electron microscope (SEM) backscattered electron imaging techniques were used to reveal the detailed interrelationships among the ore and gangue minerals in order to obtain a good understanding of the genesis of studied deposit. The alteration mineralogy and ore mineral chemistry were also studied by wavelength-dispersive X-ray spectrometry at TU-Clausthal, Germany, using a Cameca SX100 four spectrometer and a fully automated electron microprobe at TU-Clausthal, Germany. The sulfide minerals were analyzed under the conditions of an accelerating voltage of 20 keV and a beam current of 40 nA and 10 sto 60 s counting times using a 2 μm beam diameter with references to natural and synthetic sulfides. The analyses were corrected for electron beam/matrix effects, instrumental drift, and dead time using a Phi-Rho-Z (CITZAF; Armstrong (1995)) scheme, as supplied with the Cameca SX100 electron microprobe. Based on the comparison between measured and published compositions of standard reference materials, the relative accuracy of the analyses is ~1–2% for concentrations >1 wt. % and ~5–10% for concentrations b1 wt. %.

d) Geochemical studies: Whole-rock (major and trace) and rare earth element analyses were conducted on 41 rock samples in the Geochemistry Research Laboratories of Istanbul Technical University (ITU/JAL). The samples were ground using a Tungsten Carbide milling device. Major elements of the samples were analyzed using a BRUKER S8 TIGER model X-ray fluorescence spectrometer with a wavelength range from 0.01-12 nm. Trace elements were analyzed by Inductively Coupled Plasma-Mass Spectrometry using an ELAN DRC-e Perkin Elmer model. Approximately 100 mg of powdered sample was digested in two steps. The first step was completed with 6 ml of 37% HCl, 2 ml of 65% HNO3 and 1 ml of 38-40% HF in a pressure- and temperature-controlled Teflon beaker using a Berghoff Microwave at 135°C. The second step was completed with the addition of 6 ml of 5% boric acid solution. The altered rocks were also analyzed for mineralogy using a BRUKER X-ray diffractometer (XRD). Diagrams of rare earth elements were created using Igpet version 2.3 (Carr, 2007). Mass balance/volume changes were calculated and plotted

using GEOISO-Windows (Coelho, 2006) by determining the absolute mobility of the elements using equations from Gresens (1967) and drawing isocon diagrams from Grant (1986); Grant (2005).

e) Stable isotopes studies: Sulfide minerals for the sulfur isotope analysis were separated from lightly crushed (40–60 mesh) lode samples; then, they were washed and hand-picked under a binocular microscope as well as calcite separates for oxygen and carbon isotope measurements in the SIRFER Stable Isotope Ratio Facility for Environmental Research laboratory at University of Utah by using EA-IRMS (Elemental Analysis-Isotope Ratio Mass Spectrometry) Techniques.

f) Remote sensing application (image processing): A Cloud free ASTER level 1B (AST_L1B 00304012005082957 and 20120119100432) images of the Atud mine area are processed for geologic and hydrothermal alteration mapping and detection of the alteration minerals at the study area.

1.6 Equipment, Software and Service Acquisition

The equipment and software that were used to be achieving the targets of this thesis are listed in the following Table (1.2):

Table 1.2 : Equipment and software used in the thesis

	Methods	**Equipment will be used**	**Software will be used**
1	Geological mapping		ArcGIS v. 10.2.2
2	Structural analyses		Stereonet v. 8
3	Petrographical studies	- Polarized microscope (Leica-DM4500P) - Ore microscope (Leica-DM4500P)	
4	Ore genesis	- Scanning electron microscope (SEM) - electron microprobe (EMPA)	
5	Geochemical studies	- XRF (Bruker S8 Tiger) -AAS (PerkinElmer AAnalyst 700) - ICP-MS (PerkinElmer Elan DRC-e) -XRD (Bruker D8 Advance)	- Igneous petrology software® Igpet (version 2.3) (Carr, 2007) - GEOISO-Windows™ program (Coelho, 2006) - X'Pert HighScore Plus software for XRD mineralogical data
6	Stable isotopes studies	- ^{34}S, ^{18}O & ^{13}C stable isotope equipment (EAIRMS)	
6	Remote sensing application (ASTER image processing)		ENVI v. 4.8

2. MINERAL CHEMISTRY AND GEOCHEMICAL BEHAVIOR OF HYDROTHERMAL ALTERATIONS ASSOCIATED WITH MAFIC INTRUSIVE-RELATED AU DEPOSITS AT THE ATUD AREA, CENTRAL EASTERN DESERT, EGYPT

2.1 Introduction

Mineralogical and bulk chemical changes reveal differences in the geochemical composition of hydrothermally altered and unaltered rocks. Reed (1997) stated that hydrothermal alteration processes refer to the physicochemical conditions in the hydrothermal system and ore precipitation results from the chemical interactions between rocks and hydrothermal solutions (Rose and Burt, 1979; Susak, 1994). These processes are typically associated with the gain and loss of components of the entire rock mass (Middelburg et al., 1988). Alteration zones regularly occur around mineralized veins and have definite fluid compositions based on the time and/or extent of interaction with the host rocks (Meyer and Hemley, 1967). The hydrothermal alteration zones around the ore and/or vein arrays are determined by the extent to which the original wall rocks were out of chemical equilibrium with the mineralizing fluids (Lindgren, 1894).

In the intrusion-related hydrothermal mineral systems, oxidised, I-type alkaline, and calc-alkaline magmas are considered to have a large capacity to carry and concentrate the base metals Au, Cu and Mo (Pirajno, 2009). The hydrothermal alteration minerals associated with intrusion-related gold deposits are formed during magmatic-hydrothermal processes by breakdown of host minerals by interaction with magmatic-hydrothermal fluids (Pirajno, 2009). In addition, the hydrothermal alteration associated with brittle-ductile shear zones suggests the presence of chemical ion exchange between wall rocks and hydrothermal fluids.

In Egypt, gold occurs in the Precambrian basement rocks of the Arabian-Nubian shield (ANS) that extends from the river Nile eastwards towards the Arabian Peninsula and southwards to the Mozambique Belt (Vail, 1988). Gold deposits are

mainly confined to quartz-mineralized shear zones, which occur in the ophiolitic sequences, the island arc assemblages, the Hammamat and Dokhan Groups, and in the post-orogenic granitoids (Pohl, 1982; El-Gaby et al., 1988). Gold mineralization related to post-orogenic granitoids is very important as productive shear zones and quartz veins. Structurally, these shear zones were formed during compressional or transpressional late-stage events of the orogeny. Thus, the post-orogenic intrusions predated the quartz veins or shear zones and provided heat sources that resulted in the formation of hydrothermal convection cells. Interstitial waters dissolved available mineral species, and low concentrations of gold were derived from the strained rocks due to elevated temperature and pressure (Klemm et al., 2001).

The Atud gold deposit is located in the central part of the Egyptian Eastern Desert of Egypt (Figure 2.1a) and represents one of the vein-type gold deposits in the ANS. Furthermore, this gold mineralization was largely distributed and controlled by two prominent fracture systems in the Eastern Desert of Egypt (Sabet and Bordonosov, 1984; Harraz and Ashmawy, 1994) and was closely associated with intense hydrothermal alteration haloes along the NW-SE brittle-ductile shear zone in the mined area (Harraz, 1999). El-Taher et al. (2003) determined the average concentration of gold in the Atud deposit to be 25.7 g/t using instrumental neutron activation analysis.

This chapter focuses on the geochemical characteristics of least-altered host rock and hydrothermal alterations of the Atud gold deposit. I evaluated chemical exchanges between host rocks and hydrothermal fluids during hydrothermal alteration processes by applying mass/volume gains and losses of chemical components along with the mass balance calculations (Gresens, 1967; Grant, 1986; Middelburg et al., 1988; Leitch and Lentz, 1994; Grant, 2005). Electron microprobe analyses of alteration minerals were performed to determine the conditions of gold deposition and the mineralizing fluid according to the appropriate geothermometers.

2.2 Sampling and analytical methods

A total of 150 host rock, altered rock, and mineralized samples were collected during a number of field workings. Sixty thin-sections and polished sections were examined petrographically, and a subset were analyzed by scanning electron microscope (SEM) back-scattered electron imaging. Whole-rock (major and trace) and rare earth

element analyses were conducted on 29 rock samples in the Geochemistry Research Laboratories of Istanbul Technical University (ITU/JAL). The samples were ground using a tungsten carbide milling device. Major elements of the samples were analyzed using a BRUKER S8 TIGER model X-ray fluorescence spectrometer with a wavelength range from 0.01-12 nm. Trace elements were analyzed by Inductively Coupled Plasma-Mass Spectrometry using an ELAN DRC-e Perkin Elmer model. Approximately 100 mg of powdered sample was digested in two steps. The first step was completed with 6 ml of 37% HCl, 2 ml of 65% HNO_3 and 1 ml of 38-40% HF in a pressure- and temperature-controlled Teflon beaker using a Berghoff Microwave at 135°C. The second step was completed with the addition of 6 ml of 5% boric acid solution. The altered rocks were also analyzed for mineralogy using a BRUKER X-ray diffractometer (XRD). Discriminated diagrams for rare earth elements were created using Igpet version 2.3 (Carr, 2007). Mass balance/volume changes were calculated and plotted using GEOISO-Windows (Coelho, 2006) by determining the absolute mobility of the elements using equations from Gresens (1967) and drawing isocon diagrams from Grant (1986); Grant (2005). Mineral chemistry of hydrothermal alteration products was performed by wavelength-dispersive X-ray spectrometry at TU-Clausthal, Germany, using a fully automated Cameca SX100 four spectrometer.

2.3 Geology of the study area

The Atud area is located at the extreme southern part of the Central Eastern Desert of Egypt (Figure 2.1a). Atud lies within a region of low-grade metagabbro-diorite complex, ophiolitic rocks and a mélange of Neoproterozoic age and younger gabbro (Figure 2.1b).

A detailed field study revealed that the study area covers about 18 km^2 and is composed mainly of metagabbro-diorite complex emplaced into serpentinites and their derivatives and metatuffs (Figure 2.1b). This complex is later intruded by olivine gabbro norite rocks. The Atud gold deposit area is traversed by many quartz veins and dykes of different compositions and directions, which are concentrated in the eastern, northeastern and southeastern parts of the area (Figure 2.1b). Structurally, the Atud area was affected by brittle-ductile shear zone that showed in altered metagabbro-diorite rocks trending in the NW-SE direction (Figure 2.1b).

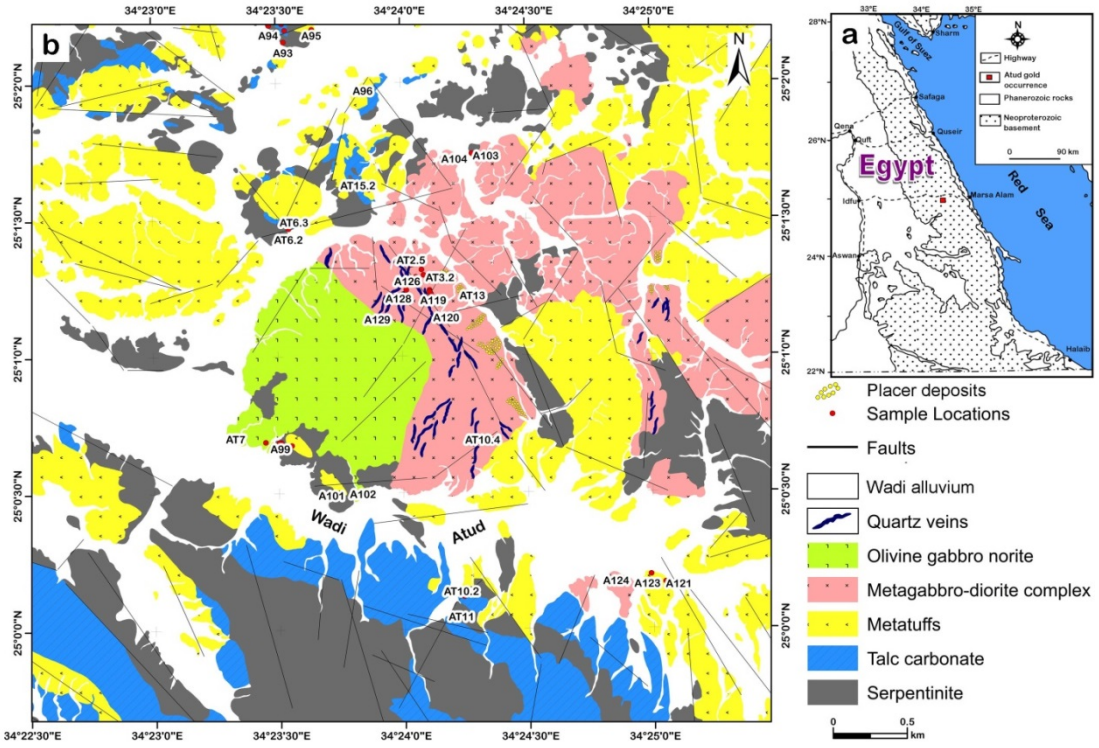

Figure 2.1 : a) Location map of Atud gold mine in the Central Eastern Desert of Egypt; b) Geological map of the study area; modified from Gabra (1986); Harraz (1999); Abdelnasser and Kumral (2016).

The serpentinites and their derivatives represent the Pan-African dismembered ophiolitic rocks exposed in the Atud area. These rocks occupy a large area which is distributed around Gabal Atud (Figures 2.1b & 2.2a). The rocks are geologically and petrographically differentiated into serpentinite, talc-carbonate, dolomitic marble, and calc-silicate rocks. Serpentinite rocks are highly deformed and shearing; their foliation directions are N 60 W dipping 70° toward SW (Figure 2.2b). The serpentinites are composed of antigorite and chrysotile, with minor amounts of tremolite, actinolite, dolomite, and chromite (Figure 2.2c). They are also rich in graphite in the northern part of the study area that occurred along with the talc serpentinite and the calc silicate rocks (Figure 2.2d). Talc-carbonate rocks are exposed at the southern part of the study area, and are closely associated with serpentinite rocks and metatuffs (Figures 2.1b & 2.2e). These rocks are mainly composed of talc (45-55 vol. %) and carbonate (dolomite; 40-50 vol. %), with minor amount of antigorite, actinolite, and chromite (Figure 2.2f). Dolomitic marble is exposed only in the southern slope of Gabal Atud, occurring as small isolated masses of dark greyish medium-to-fine-grained rocks (Figure 2.1b). The marble consists essentially of dolomite (90 vol. %) with subordinate amounts of magnesite and

chromite (Figure 2.2g). Calc-silicate rocks occur at the northern part of the study area and are composed essentially of ankerite, dolomite, and quartz, with minor amounts of calcite, clinochlore, epidote, and chromite (Figure 2.2h).

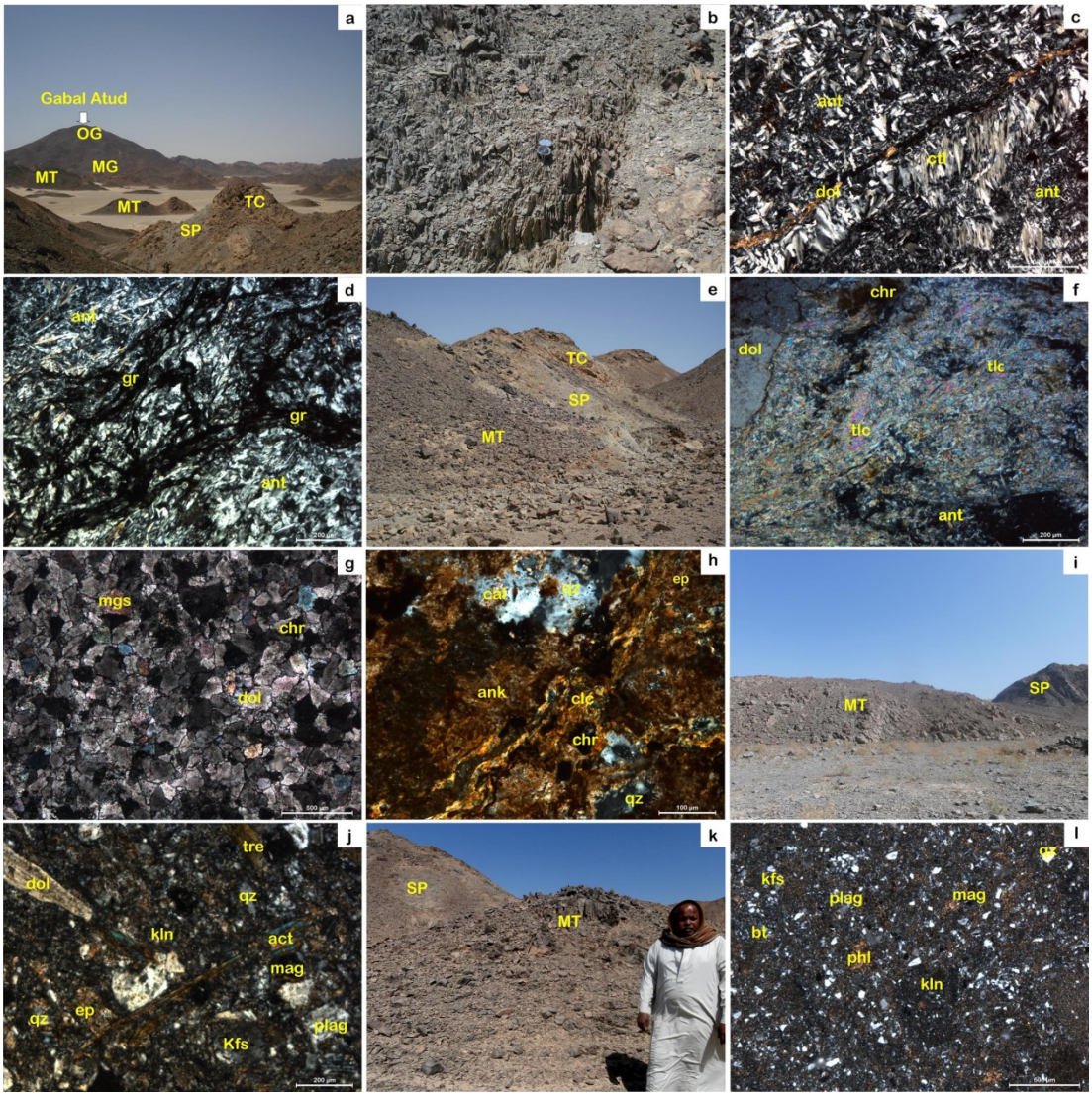

Figure 2.2 : a) Field view of metagabbro-diorite complex (MG) of Gabal Atud intruded into ther serpenitites and metatuffs and latterly intruded by olivine gabbronorite (OG); b) Deformation and shearing in serpentinite rocks (SP); c) Photomicrograph shows the mineral compositions of serpentinite rocks; d) Graphite (gr) with antigorite (ant) in serpentinite rocks; e) Talc-carbonate rocks (TC) are associated with serpentinite rocks (SP) and metatuffs (MT); f) Talc (tlc) with dolomite (dol) and antigorite (ant) in Talc-carbonate rocks; g) Dolomite (dol) with subordinate amounts of magnesite (mgs) and chromite (chr) in dolomitic marble; h) Mineral compositions of calc-silicate rocks; i) Basic Lapilli metatuffs (MT) thrust over the serpentinites (SP) at Wadi Atud; j) Mineral compositions of Basic Lapilli metatuffs; k) Intermediate metatuffs (MT) occur serpentinite rocks (SP) at the northern part of the study area; l) Kaolinitized microperthite (kfs), biotite (bt), phlogopite (pht), and quartz (qz) represent the main constituents of Intermediate metatuffs.

Metatuffs are exposed associated with serpentinite rocks and form low-lying outcrops distributed around Gabal Atud (Figures 2.1b & 2.2a). Metatuffs are microscopically differentiated into different varieties; mafic lapilli metatuffs, intermediate metatuffs, metacherts, and quartz biotite schists. All are slightly layered, and were subjected to low-grade metamorphism within the greenschist facies. Mafic lapilli metatuffs are exposed as an elongate body trending NW-SE and thrust over the serpentinites at the southern part of the study area, at Wadi Atud (Figure 2.2i). These metatuffs are fine-grained dark grey-to-greenish grey in color and are composed of carbonatized plagioclase with actinolite, tremolite, epidote, and dolomite set in a microcrystalline tuffaceous matrix of microcrystalline aggregates of kaolinitized feldspar, tremolite-actinolite, zoisite, quartz, and dusty iron oxide (Figure 2.2j). Intermediate metatuffs, which occur at the northern part of the study area with serpentinite rocks (Figure 2.2k), are composed of kaolinitized microperthite, biotite, plagopite, and quartz with minor amounts of plagioclase and iron oxide in a much finer tuffaceous matrix of microcrystalline aggregates of kaolinitized feldspar, quartz, biotite and dusty iron oxide (Figure 2.2l). Metacherts occupy a small area on the southern slope of Gabal Atud, interposed with serpentinite rock. They are slightly laminated, consisting of irregularly banded quartz- and feldspar-containing laminae containing muscovite, carbonate, and iron oxide (Figure 2.3a). Quartz biotite schists, which form low-lying foliated outcrops, are composed mainly of quartz and feldspar with biotite and subordinate muscovite, carbonate, and opaque minerals (Figure 2.3b).

The metagabbro-diorite complex forms the main part of Gabal Atud, occurring as a semicircular body, and has an obvious intrusive contact against serpentinites and metatuffs (Figures 2.1b, 2.2a & 2.3c). This complex is one of the early orogenic gabbro-diorite complexes in the Egyptian part of the Nubian shield, with an age ranging from 987 Ma to 830 Ma (Abdelrahman and Doig, 1987; Hashad, 2015). It was invaded by olivine gabbro norite of group III of Ghoneim (1989). At the study area, this complex consists of metamorphosed gabbros and diorite, with quartzo-feldspathic veined hybrid leucocratic metagabbros between them (Figure 2.3c). The complex, which is affected by many types of alterations, represents the main host rocks of the gold-bearing quartz veins occurring along the shear zone trending NW-SE at the eastern and southeastern slopes of Gabal Atud (Figure 2.1b). The metagabbros are medium-to-coarse-grained and have hypidiomorphic granular

textures with poikilitic or ophitic-to-subophitic textures composed of plagioclase, actinolite, and tremolite together with variable amounts of secondary quartz, chlorite, clinopyroxene, orthopyroxene, and opaque minerals (hematitic iron oxides) (Figures 2.3d-e). Plagioclase is labradorite in composition (An_{50-65}), zoned (Figure 2.3d), and affected by sericitization, kaolinitization, and carbonatization (Figure 2.3e). In contrast, the diorite is affected by shearing (Figure 2.3f) and is composed essentially of altered plagioclase and hornblende with minor amounts of quartz, tremolite-actinolite, chlorite and iron oxide (Figure 2.3g).

Olivine gabbronorites are non-deformed rocks equivalent to younger gabbro of group III of Ghoneim (1989), that intrude into the metagabbro-diorite complex of Gabal Atud (Figures 2.1b & 2.3a). Therefore, these rocks have intrusive contact with the metagabbro diorite complex and are different from it because they have very little and/or no alteration relative to the metagabbro-diorite complex that represent the host rocks of Atud gold deposit which are typically altered. In addition, they are massive, dark grey and coarse-to-medium-grained, with no signs of mineral foliation and no evidence of ductile and/or brittle deformation, emphasizing the rocks' post-tectonic emplacement. They also show as small boulders along the western slope of Gabal Atud (Figure 2.3h). They consist mainly of plagioclase (labradorite to bytownite; 35-40 vol. %), hypersthene (15-20 vol. %), diopside (25-30 vol. %) partially altered to tremolite-actinolite (~5 vol. %), cumulate olivine (partly altered into serpentine minerals, 15-20 vol. %) and opaque minerals (~ 3 vol. %) (Figure 2.3i). Based on modal mineralogical studies, these rocks are olivine gabbronorite (Figure 2.4).

Dykes, in the study area, trend mostly in the NW-SE direction. Porphyritic andesite and aplitic dykes (trending N 40 W dipping at 50° toward SW) cut through the metagabbro-dioritic rocks at Gabal Atud (Figure 2.3j), but few dykes run roughly NNE-SSW except for an ankerite dyke which is the oldest one and cuts through the serpentinite rocks at the northern part of the study area (Figure 2.3k). The samples of the aplite dyke are yellowish, fine-grained rocks with porphyritic textures composed mainly of phenocrysts of carbonatized plagioclase, biotite and/or phlogopite (partly altered to chlorite) in a carbonate-rich groundmass with potassium feldspar, quartz, sericite, and iron oxide (Figure 2.3l).

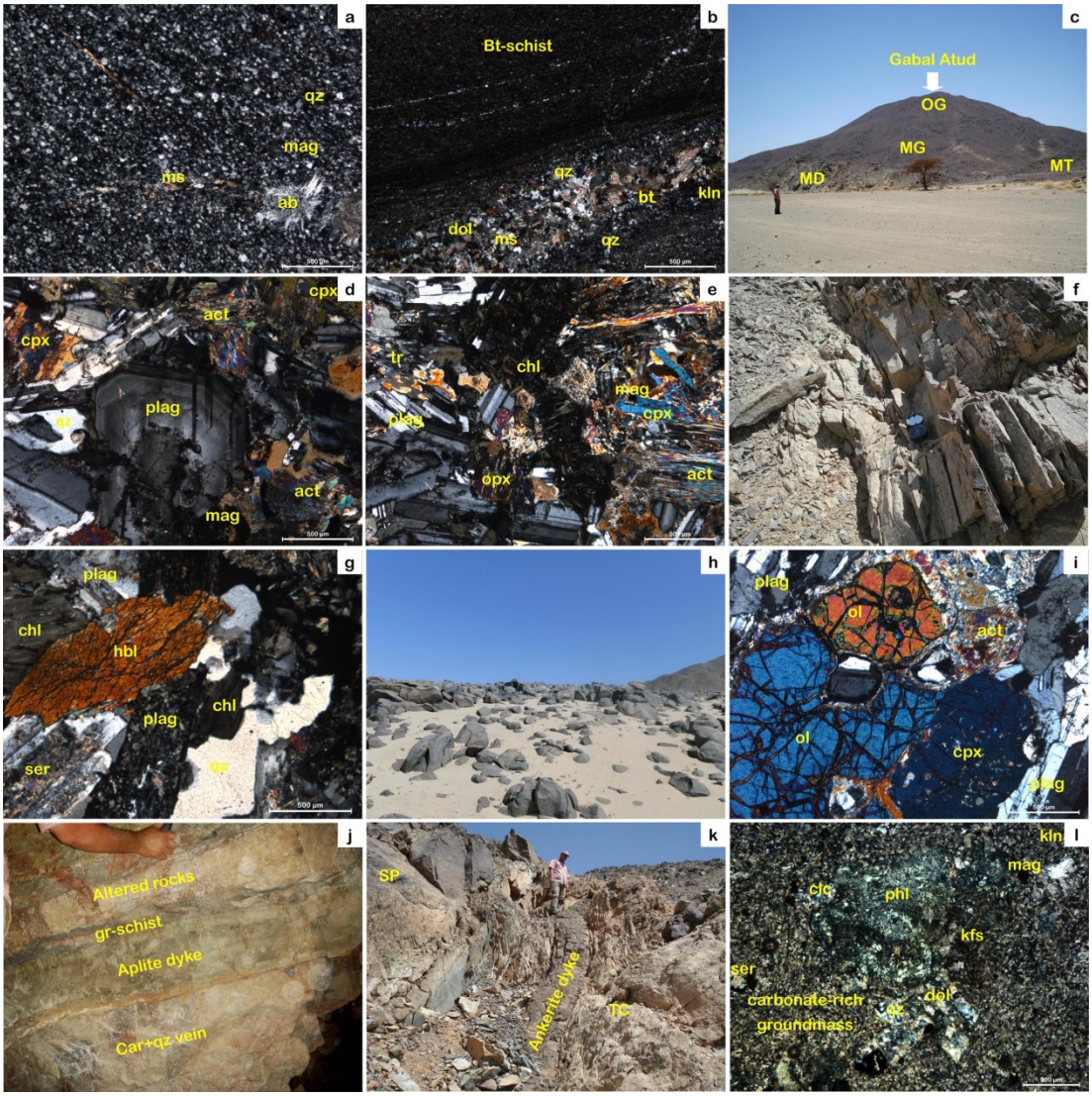

Figure 2.3 : a); b) Photomicrographs of metachert and quartz biotite schist, respectively; c) Metagabbro-diorite complex represents the main body of Gabal Atud; d), e) Plagioclase (plag), actinolite (act), and tremolite (tr) with quartz (qz), chlorite (chl), clinopyroxene (cpx), orthopyroxene (opx) in the metagabbros (MG); f) Diorite is affected by shearing; g) Photomicrograph of dioritic rocks; h) Boulder weathering of olivine gabbro norite (OG); i) Olivine (ol) with plagioclase (plag), clinopyroxene (cpx), and orthopyroxene (opx) in olivine gabbro norite; j) Aplitic dyke cut through the metagabbro-dioritic rocks at Gabal Atud; k) Ankeritic dyke cut through the serpentinite rocks (SP) at the northern part of the study area; l) Mineral compositions of Aplite dyke.

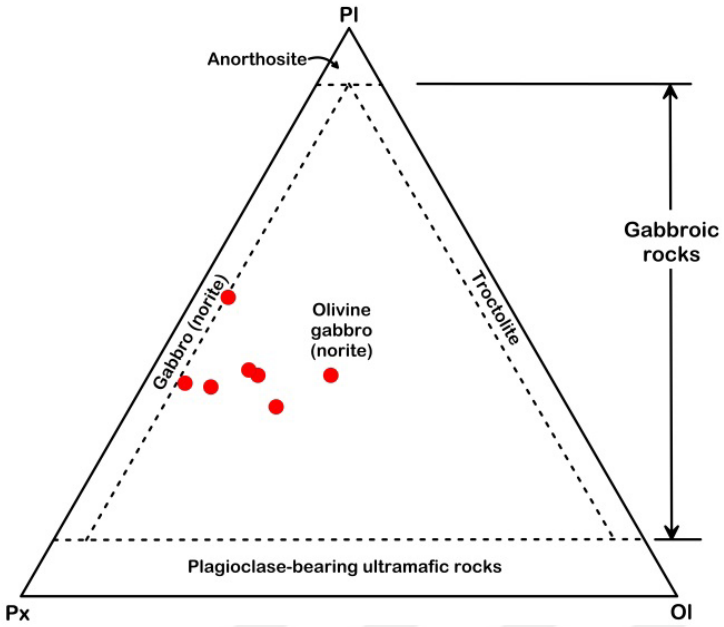

Figure 2.4 : Modal mineralogy of olivine gabbronorite, after Streckeisen (1976), Pl= plagioclase; Px= pyroxene; Ol= olivine.

2.4 Intrusion-related gold mineralization in the Atud area

Gold mineralization occurred in three areas: the main Atud occurring on the eastern and northeastern slopes of Gabal Atud, Atud East-I (NE of the Atud area), and Atud East-II (SE of the Atud area) (Harraz, 1999), (Figure 2.1b). The main Atud mineralization was genetically related to the metagabbro-diorite complex that was intruded by quartz veins (Figure 2.1b). The mineralization was associated with a NNW-SSE brittle-ductile shear zone within hydrothermal alteration zones and quartz veins that occupy the pre-existing fractures. Furthermore, this mineralization represents a structurally-controlled mesothermal vein-type gold mineralization of the Arabian-Nubian Shield (Harraz, 1999; Harraz, 2002).

The Atud gold mine is one of many in the Egyptian Eastern Desert that was exploited during Pharaonic times, but no ore has been produced since then (Gabra, 1986). Detailed work was done at the Atud gold mine by the Egyptian Geologic Survey and Mining Authorities (EGSMA) between 1953 and 1969, including surface and subsurface geological studies, drilling, mapping, mine workings and sampling of the altered rocks, quartz veins and country rocks (Gabra, 1986). In the main Atud mine, EGSMA performed underground prospecting and drifting on three levels along the strike of the main lode (NNW-SSE brittle-ductile shear zone) for a total length of 690 m (Figure 2.5). The inclined shafts connected these levels and winzes down the

dip of the lode for a total length of 230 m. The levels are about 30 m, along the dip, below one another, and four main shafts are recognized (Figure 2.5). The characteristics of these levels are shown in Table 2.1. In addition, EGSMA excavated 135 surface trenches in the main Atud mine area. Six quartz veins were exposed on the eastern slope of Gabal Atud and 12 quartz veins were exposed on the southeastern slope. The gold content varied from <0.l to 31 g/t (average: 16.28 g/t), with 19,000 tons of rock and 348 kg of pure gold in the principal lode (Gabra, 1986). In addition, 1600 tons of dumps with 12.4 g/t of gold are present in the area (Hussein and El Sharkawi, 1990). More information can be found in unpublished EGSMA reports in the Information Center.

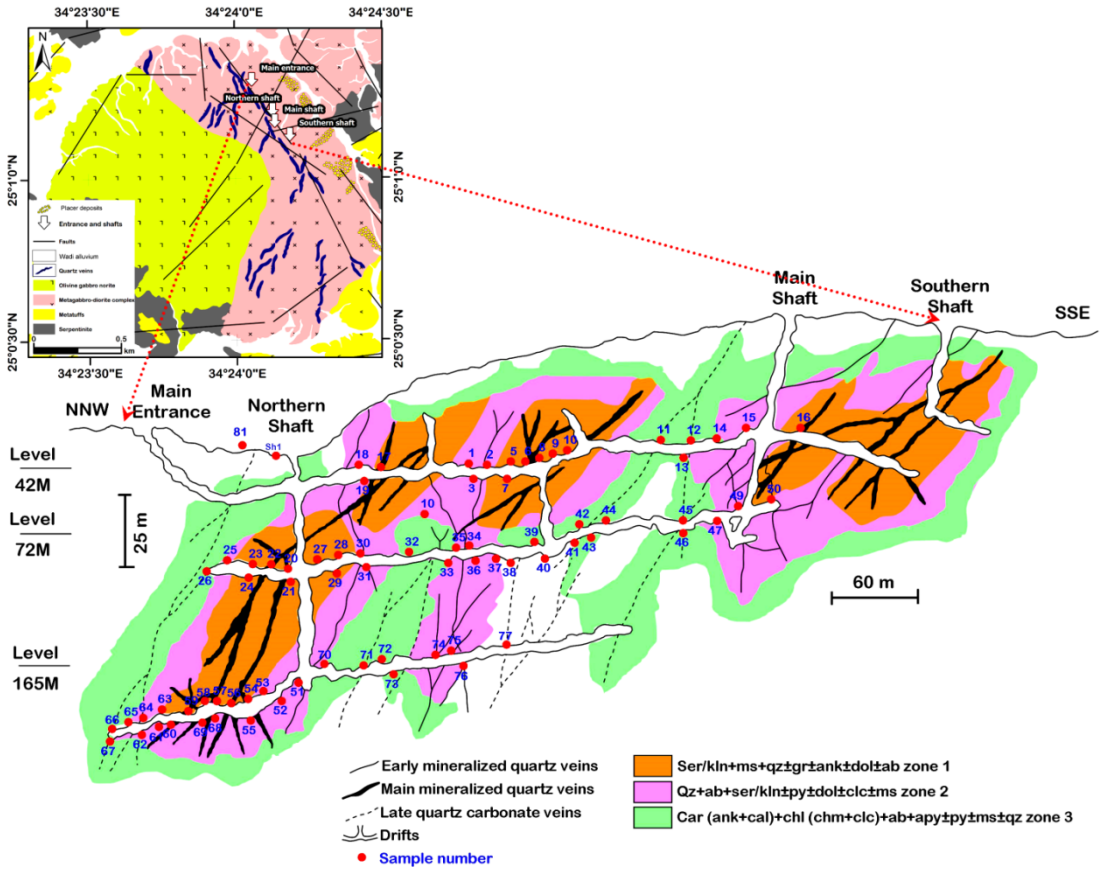

Figure 2.5 : Longitudinal section shows drifting of underground working of the Atud gold mine, (Traced quartz vein stages and alteration zones, after Gabra (1986); Harraz (1999); Abdelnasser and Kumral (2016)).

Table 2.1 : Description of three levels of the underground working of main Atud deposits.

	1st level	2nd level	3rd level
Depth	~ 40 m	~ 70 m	~ 160 m
Alteration	- Sericitization -Carbonatization (Ankerite) - Argillic	- Sericitization -Carbonation (Ankerite & calcite) - Silicification - Agillic - Sulfidation	- Sericitization - Agillic (Kaolinite) -Carbonatization (Ankerite & calcite)
Quartz veins	- Mostly grey quartz (N20W/45W) with variable amount of milky quartz (N30W/50SW) and very little of smoky quartz.	- Mostly milky quartz and grey quartz with laminated quartz (N40W/50W).	- Mostly milky quartz with grey quartz (N40W/50SW) and laminated quartz.
Deformation	- N-S / 55 W. - N 40 W / 70 NE. - N 20 W / 60 NE. - N 20 E / 10 SE.	- N-S / 55 W.	- N 25 W / 50 SW.

2.4.1 Quartz veins

Field and optical microscopy observations suggest that there are two generations of quartz veins; the older one is grayish-to-white, mineralized trending N 30°-40° W dipping 45° toward SW. The younger vein is non-mineralized, milky-white, trending NE-SW dipping 15° toward NW (Figures 2.6a-b). These veins are differentiated in the different underground levels. In the first level (42 m depth), the main quartz vein is composed of bluish or greyish quartz and is frequently associated with variable amounts of milky quartz (Figure 2.6c). In the second level (72 m depth), the main quartz veins are milky quartz trending N 30°-40° W dipping 55° SW with variable amounts of bluish or greyish quartz. The quartz veins extend discontinuously up to 270 m and are nearly 70 cm-thick (Figure 2.6d). Pinching, swelling and bifurcation into small veins and veinlets are observed in this level (Figure 2.6e). The third level (165 m depth) contains large amounts of milky quartz with subordinate bluish or greyish quartz, directed N 40° W, and is cut by carbonate veinlets (Figure 2.6f).

2.4.2 Ore mineralogy

The ore mineralogical studies revealed that the sulfides associated with gold mineralization include arsenopyrite, pyrite, chalcopyrite, sphalerite, and enargite with goethite as iron oxide minerals. These ore minerals occur as disseminations within the metasomatic hydrothermal alteration zones (Figures 2.6g-i), as well as along the borders between the zones and the quartz veins (Figure 2.6h), cutting

through the altered metagabbro-diorite complex. Gangue minerals include quartz, sericite/kaolinite, carbonate (calcite, dolomite, and ankerite), and chlorite.

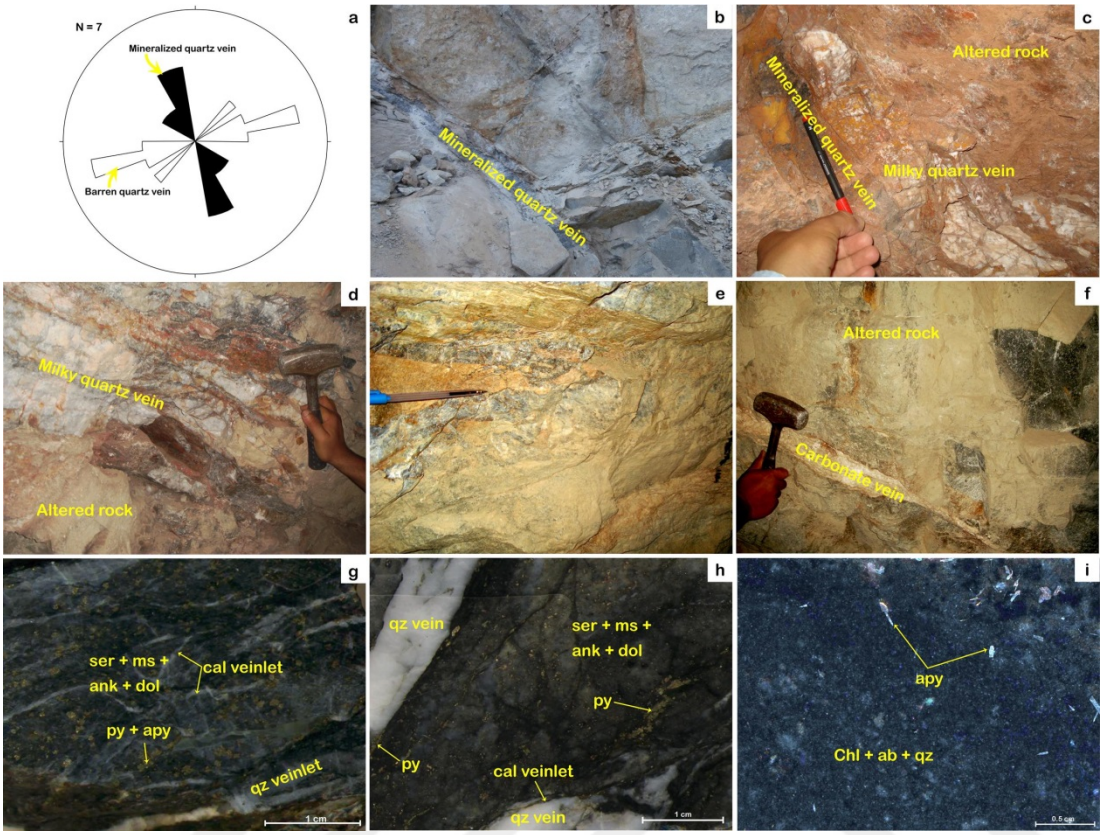

Figure 2.6 : a) Rose diagram showing for two type of quartz veins; b) Mineralized grey quartz vein cut through altered rocks; c) Grey quartz vein with variable amounts of milky one in the first underground level (42 m depth); d) milky quartz veins mainly placed in the second underground level (72 m depth); e) Pinching, swelling and bifurcation into small veins and veinlets in level 2 f) Carbonate veinlets cut through the third underground level (165 m depth) with milky quartz; g) High amount of pyrite (py) and arsenopyrite (apy) within the alteration minerals in zone 1; h) Milky quartz vein and calcite (cal) veinlets cut through the wall rocks at sulfidized zone 2; i) Reflected light centimeter-scale view of chloritization (chl), albitization (ab), and silicification (qz) with arsenopyrite (apy) in zone 3.

Arsenopyrite occurs as individual rhombic or prismatic zoned grains disseminated in the quartz veins and wall rock (Figure 2.7a) and is intergrown with euhedral arsenian-pyrite (with ~ 2 atoms. % As; unpublished data) (Figure 2.7b). Pyrite occurs as arsenic-bearing pyrite associated with arsenopyrite (Figure 2.7c) and also occurs as disseminated subhedral or anhedral zoned grains replacing by chalcopyrite in some samples (Figure 2.7d). Inclusions of sphalerite and enargite are common in the large pyrite and arsenopyrite grains, respectively (Figures 2.7e-f). Goethite occurs mainly as alteration products replacing the iron-bearing sulfide minerals in the quartz veins and alteration zones (Figures 2.7b-d). Gold is mostly associated with

arsenopyrite, arsenic-bearing pyrite and sphalerite, with an average ~70 wt.% Au (+26 wt.% Ag) (unpublished data). Gold occurs along microfractures of arsenopyrite (Figure 2.7b) and pyrite (Figure 2.7g) in altered wall rocks and mineralized quartz veins. Gold also occurs either as inclusions in large pyrite crystals (Figure 2.7h) or as disseminated grains with chalcopyrite and pyrite in the alteration zones (Figure 2.7i).

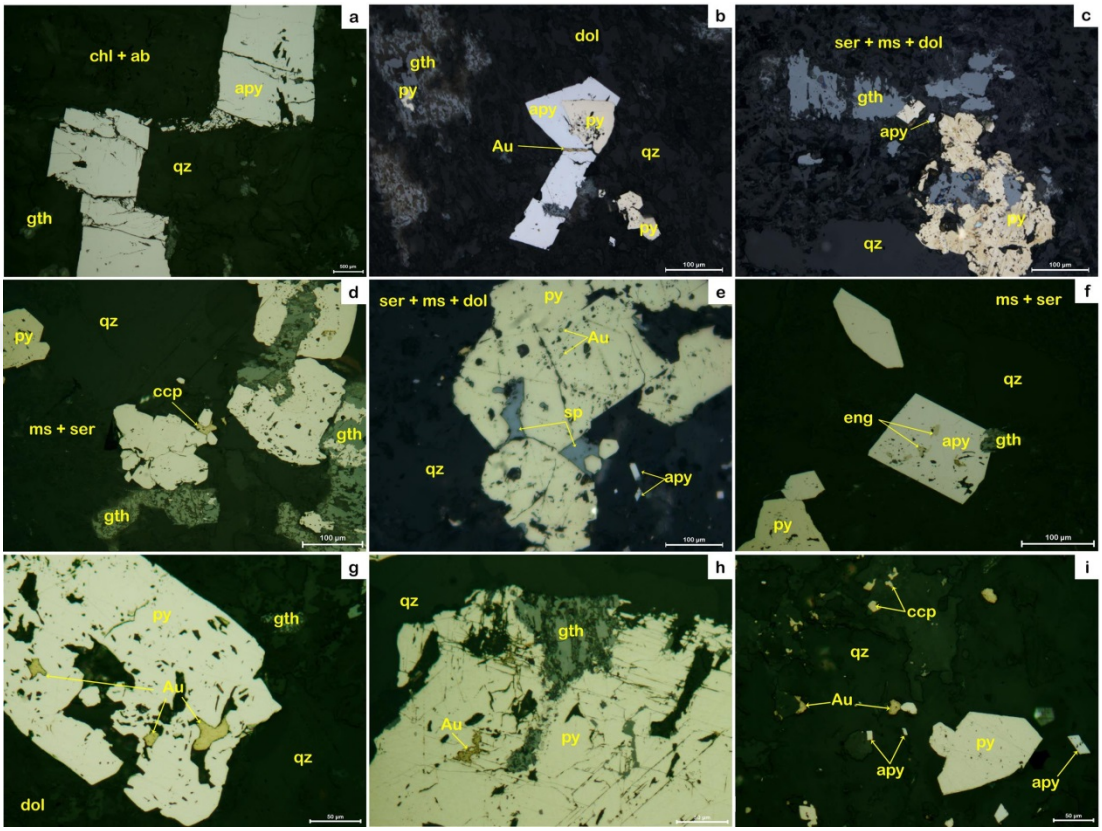

Figure 2.7 : Photomicrographs of reflected light microscopy: a) Deformed arsenopyrite (apy) in the altered rocks; b) Gold (Au) filled the cracks in arsenopyrite (apy) that associated with pyrite (py); c) Pyrite (py) with arsenopyrite (apy) and goethite (goe); d) Chalcopyrite (ccp) associated with pyrite (py); e) Inclusions of sphalerite (sp) in the large pyrite (py); f) Enargite (eng) occurred as inclusion in arsenopyrite grains (apy); g) Microfractures of pyrite (py) filled by gold (Au); h) Inclusions of gold (Au) in pyrite crystals (py); i) Gold (Au) occurred as disseminated grains with chalcopyrite (ccp) and pyrite (py) in the alteration zones.

The contact relationships of the minerals in the paragenesis revealed the three mineralization phases at the Atud Au deposit (Figure 2.8). The first phase is represented by disseminated euhedral pyrite and arsenopyrite, as well as quartz that are observed as large anhedral crystals. The second (main ore) phase is represented by chalcopyrite, sphalerite, and enargite, with gold enclosed as inclusions in pyrite and arsenopyrite. During this stage, small polygonal crystals of a second type of

quartz were deposited, forming thin veinlest. The third phase is represented by goethite mineral occurred under the supergene condition.

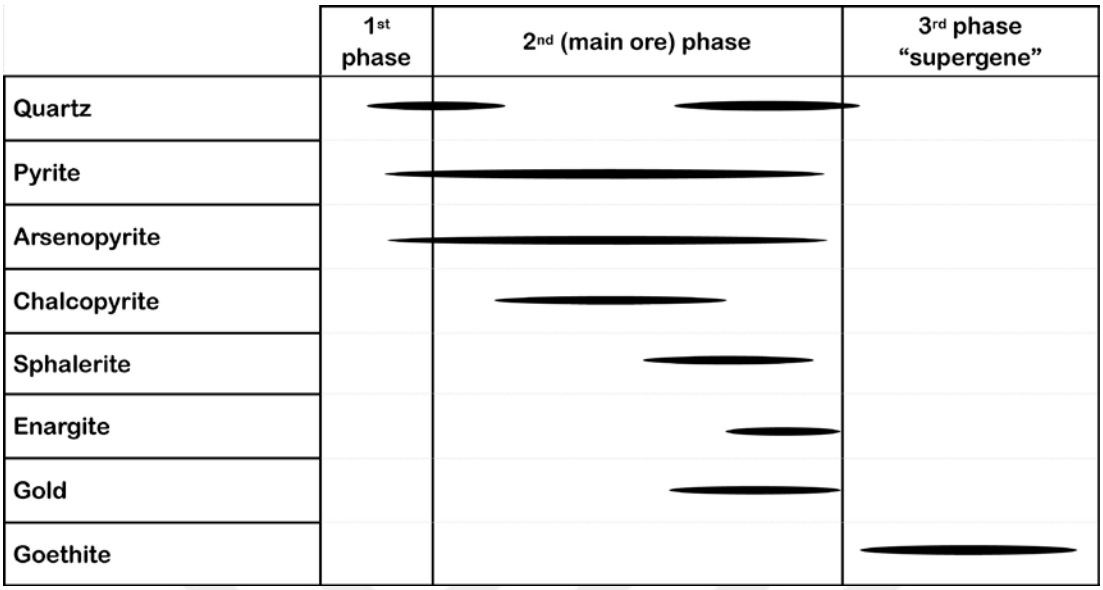

Figure 2.8 : Paragenetic sequence of quartz, sulfide minerals, and supergene minerals as defined by mineral assemblages.

2.4.3 Hydrothermal alteration types

The Atud gold mineralization is closely associated with intense hydrothermal alteration in the metagabbro-diorite complex along the NNW-SSE shear zones at the eastern and northeastern slopes of Gabal Atud, with typical greenschist facies alteration assemblages (Harraz, 1999; Harraz, 2002).

The hydrothermal alteration is divided into three zones: Zone-1, Zone-2 and Zone-3 according to field, petrographic and XRD data. They occur around quartz veins and are associated with the main shear/fault zone trending NNW-SSE (Figure 2.5).

Zone 1 occurs around the main mineralized quartz veins distributed in all underground levels (Figure 2.5). The zone is characterized by greyish/reddish color (Figure 2.9a), highly sulfidized (Figure 2.9b), cut by mostly grey quartz veins (Figure 2.9c) with variable amounts of milky and smoky quartz veins (Figure 2.9d), and is affected by faulting (N30W/80SW) (Figure 2.9a). Based on the petrographic and XRD studies, the samples of this zone are composed mainly of sericite and muscovite with quartz and pyrite and minor amounts of ankerite, dolomite, albite, and graphite (Figures 2.9e-f & Figures 2.10a-b). Mineralogical studies revealed large amounts of pyrite and arsenopyrite with the alteration minerals (Figure 2.6g).

Zone 2 represents the outer halo of zone 1 (Figure 2.5) and is cut by a milky quartz vein and calcite veinlets (Figures 2.9g & 2.6i). The zone is characterized by a large amount of quartz, albite, and sericite/kaolinite with pyrite, dolomite, clinochlore, and muscovite (Figures 2.9h-i and Figure 2.10c). Zone 2 is rich in pyrite (Figure 2.6i).

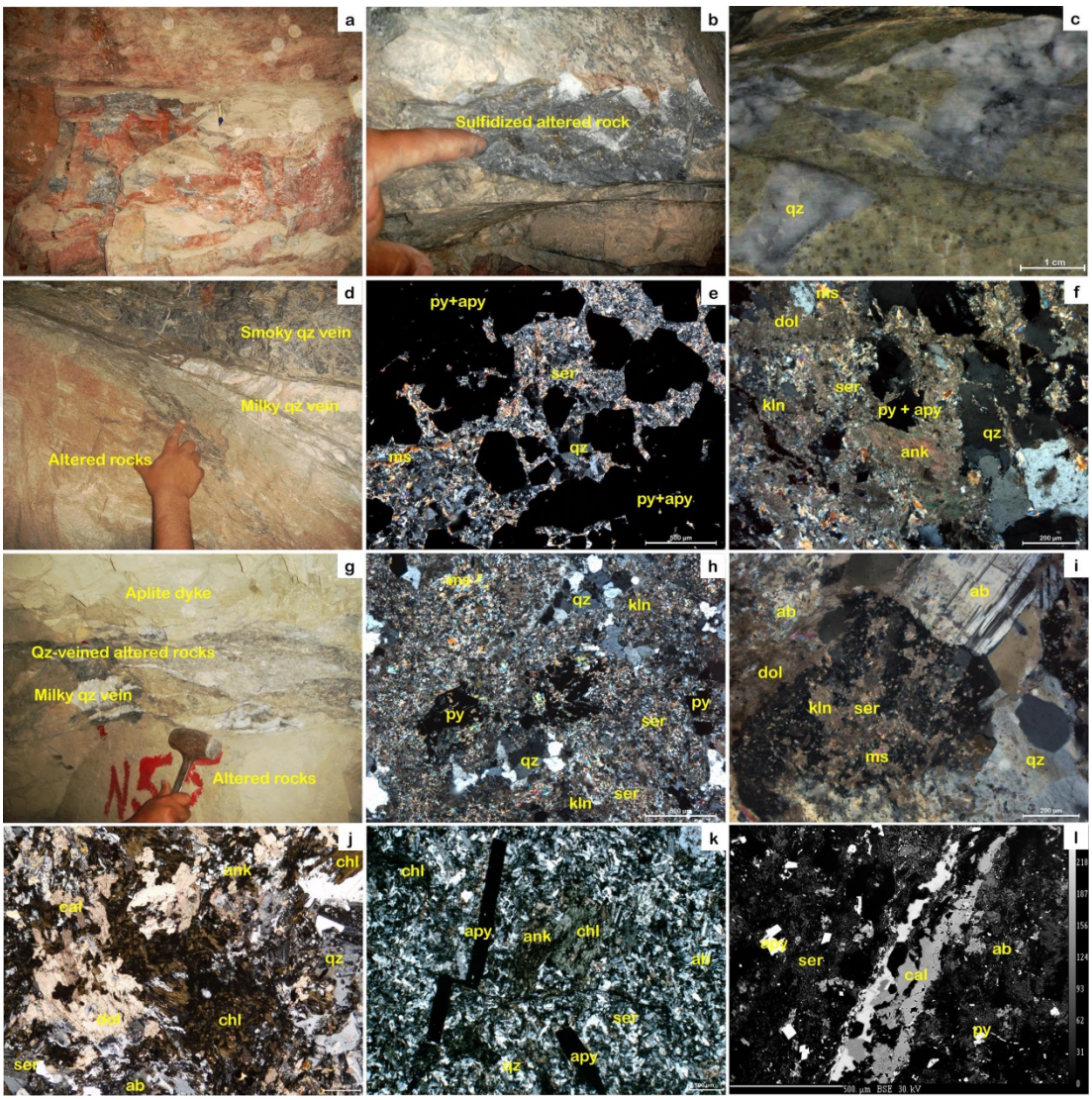

Figure 2.9 : a) Main mineralized quartz (qz) in veins greyish/reddish wall rocks of zone 1 affected by faulting; b) Highly sulfidized wall rocks in zone 1; c) Grey quartz (qz) vein cut through wall rocks; d) Variable amounts of milky and smoky quartz veins in zone 1; e), f) photomicrographs show the alteration products at zone 1; g) Milky quartz vein (qz) and calcite veinlets cut through the wall rocks at sulfidized zone 2; h), i) Quartz (qz), albite (ab), and sericite (ser) /kaolinite (kln) with pyrite (py), dolomite (dol), clinochlore (clc), and muscovite (ms) in zone 2; j); k) photomicrographs show the alteration products with arsenopyrite (apy) in zone 3; l) Backscattered images of the calcite (cal), quartz (qz), and albite (ab) with sericite (ser) in zone 3.

Zone 3 occurs along the outer contact of zone 2 (Figure 2.5) and is represented by rocks enriched in carbonate (dolomite and ankerite) and chlorite along with

arsenopyrite (Figure 2.6h). The zone consists of ankerite, calcite, dolomite, chlorite, chamosite (XRD results), chlinochlore, and albite, with minor amounts of muscovite and quartz (Figures 2.9j-l & Figure 2.10d).

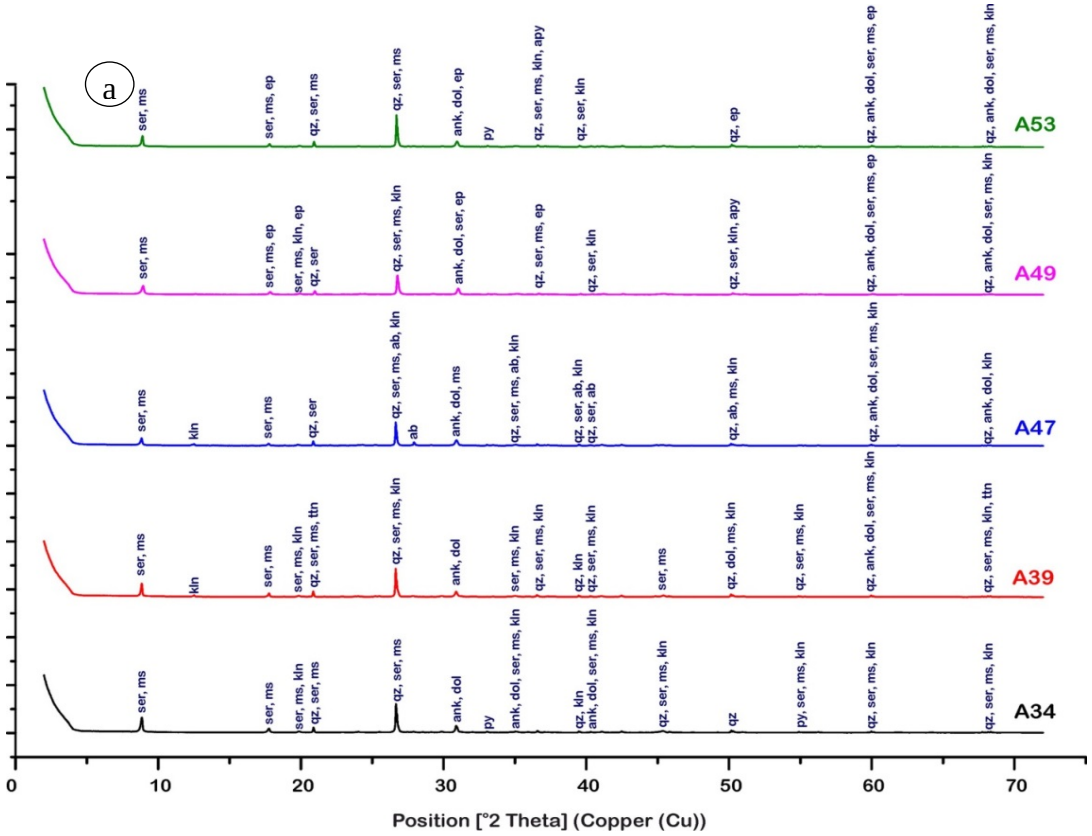

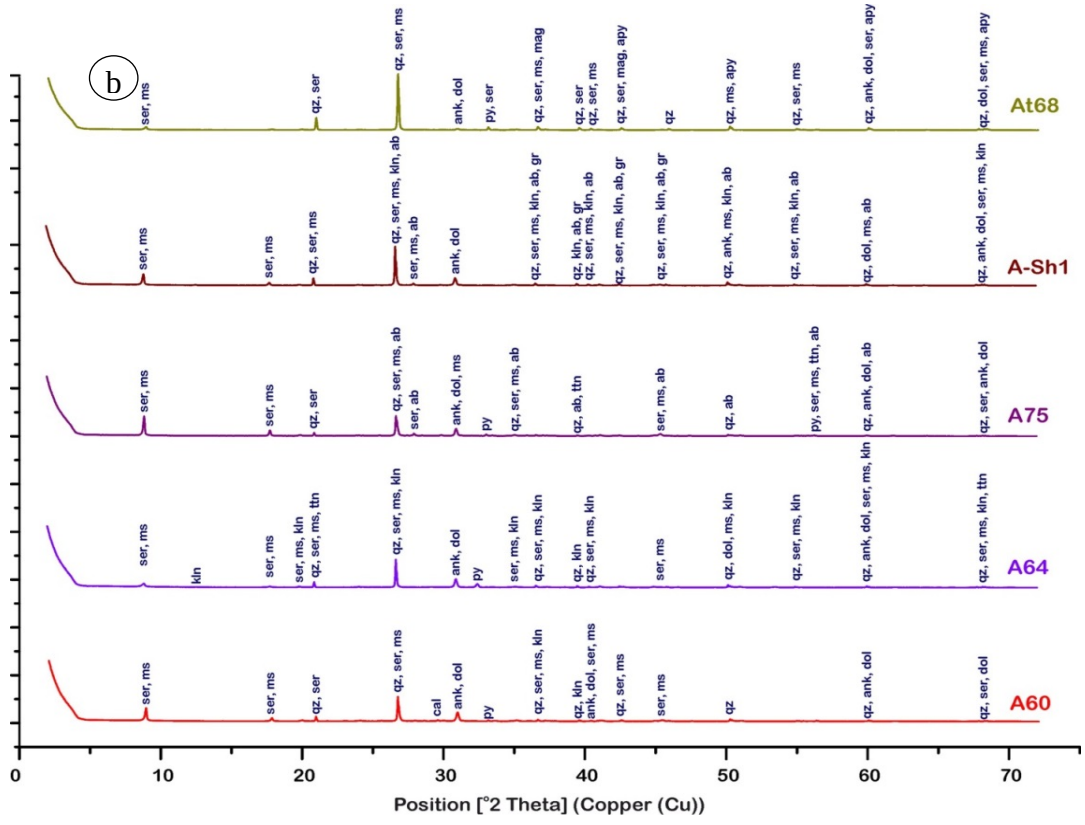

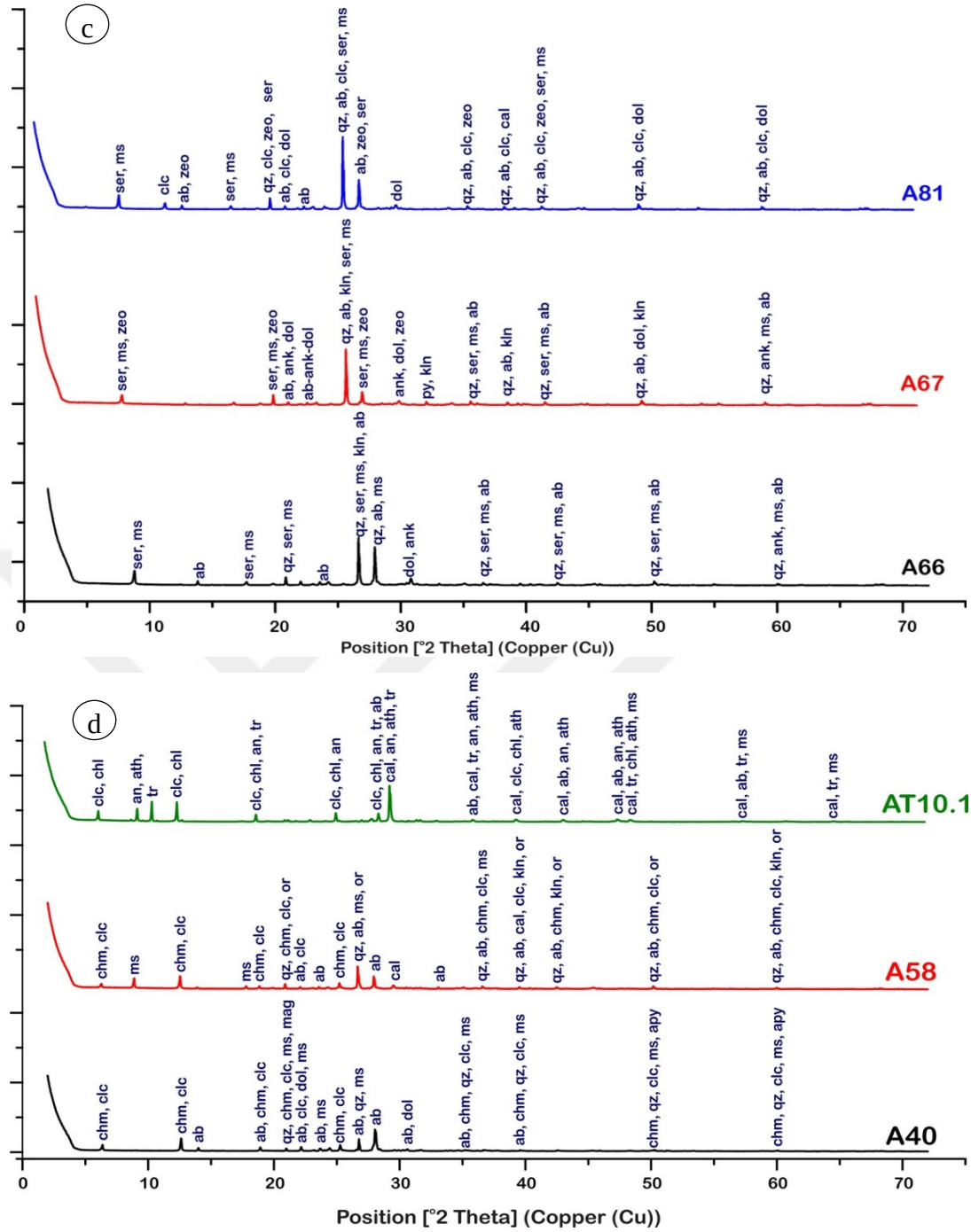

Figure 2.10 : XRD patterns of altered samples collected from the different alteration zones around the Atud mineralization: a), b) zone 1; c) zone 2; d) zone 3. Abbreviation: ankerite (ank), anorthite (an), anthophyllite (ath), arsenopyrite (apy), calcite (cal), chamosite (chm), chlorite (chl), clinochlore (clc), dolomite (dol), epidote (ep), graphite (gr), kaolinite (kln), magnetite (mag), muscovite (ms), orthoclase (or), pyrite (py), quartz (qz), sericite (ser), titanite (ttn), tremolite (tr), zeolite (zeo).

2.5 Geochemical Characteristics

The metagabbro-diorite complex, which includes the Atud gold mineralization, was divided into least-altered and altered rocks. Ten representative samples were

collected from the least-altered metagabbro-diorite complex, including 6 samples of metagabbros and 4 samples of dioritic rocks. In addition, 18 representative samples were collected from the different alteration zones. Each sample was analyzed for major, trace, and rare earth elements (Tables 2.2 and 2.3).

2.5.1 Geochemistry of the least-altered metagabbro-diorite complex

Geochemical classification using the Na_2O+K_2O versus SiO_2 diagram (Figure 2.11a) suggested by Cox et al. (1979) in shows that metagabbros are in fields of gabbro and gabbro/diorite, whereas diorites fall in the diorite and gabbro/diorite fields. These rocks have calc-alkaline affinities (Figure 2.11b), and are equivalent to calc-alkaline basalt (CAB) (Figure 2.11c). The relationship between Ni and FeO^*/MgO content was used by Miyashiro and Shido (1975) to differentiate volcanic rocks according to different tectonic settings, whereas the plots of the analyzed metagabbro-diorite complex mostly fall in the island arc field (Figure 2.11d).

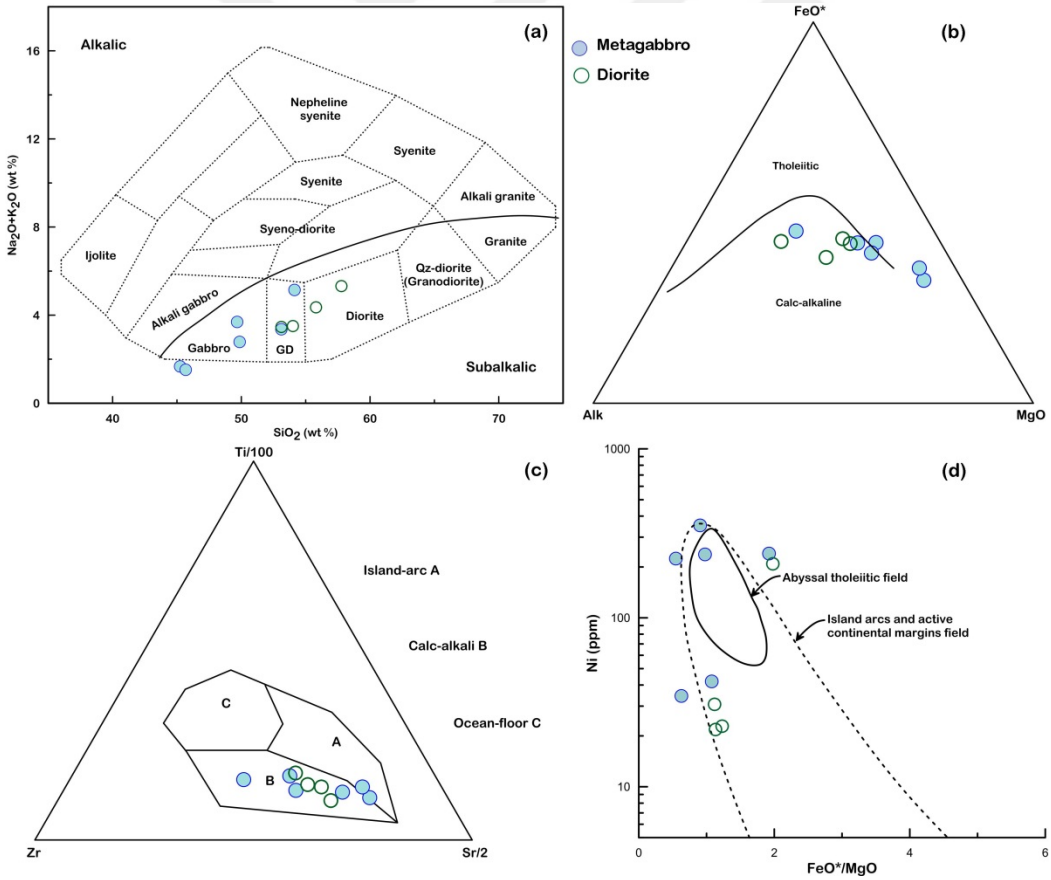

Figure 2.11 : Petrologic discrimination diagrams of metagabbro-diorite rocks: a) TAS diagram after Cox et al. (1979). The dividing line between alkalic and subalkalic after Miyashiro (1978); b) AFM ternary diagram after Irvine and Baragar (1971); c) Ti/100-Zr-Sr/2 ternary diagram after Pearce and Cann (1973); d) FeO*/MgO-Ni diagram after Miyashiro and Shido (1975).

Table 2.2 : Major, Trace, and Rare earth elements (REE) of metagabbro-diorite complex at Atud area.

	Metagabbro							Diorite			
Sample ID	**A 42**	**A105**	**A124**	**A96**	**A124**	**A128**	**AT10.4**	**A14**	**A 103**	**A115**	**A116**
SiO_2	53.11	49.87	54.13	49.67	54.13	45.24	45.68	57.77	53.10	54.00	55.80
Al_2O_3	15.81	16.19	16.79	13.79	16.79	13.96	16.72	16.69	18.33	15.79	16.37
Fe_2O_3	7.83	8.53	7.73	9.00	7.73	6.47	7.05	6.71	7.39	7.43	6.24
MgO	6.94	8.19	3.86	9.43	3.86	11.26	10.45	3.16	5.58	6.34	5.25
CaO	6.99	10.26	5.16	8.57	5.16	15.69	15.09	6.59	8.66	7.18	6.40
Na_2O	2.62	2.43	3.10	2.93	3.10	1.46	1.37	4.39	3.10	2.84	3.53
K_2O	0.74	0.36	2.05	0.76	2.05	0.20	0.14	0.93	0.37	0.67	0.83
TiO_2	0.74	0.65	1.23	1.00	1.23	0.45	0.48	0.92	0.98	0.71	0.63
P_2O_5	0.13	0.11	0.38	0.35	0.38	0.06	0.06	0.26	0.18	0.12	0.11
MnO	0.14	0.14	0.11	0.16	0.11	0.12	0.13	0.11	0.13	0.13	0.11
Cr_2O_3		0.05	0.01	0.09	0.01	0.17	0.05	0.01			
LOI	3.99	3.23	5.45	4.26	5.45	4.91	2.28	2.45	2.28	3.66	3.78
Trace and Rare Earth Elements (ppm)											
Ag	0.9	0.8	1.4	1.1	1.4	0.6	0.3	0.7	0.3	0.8	1.1
As	16.0	3.0	1.0	7.0	1.0	9.0	33.0	8.0	3.0	26.0	10.0
Au (ppb)	35.9	156.2	22.2	27.2	22.2	69.6	8.4	75.1	16.9	49.5	27.7
Ba	167.0	113.0	43.0	131.0	43.0	26.0	41.5	208.0	126.0	160.0	194.0
Be	1.2	1.2	1.8	1.5	1.8	0.9	0.5	1.4	0.7	1.4	1.3
C	349.9	1647.1	6602.0	2461.8	6602.0	3620.0	1096.6	2543.7	100.7	323.2	399.5
Cd	0.4	0.3	0.5	0.7	0.5	0.3	4.0	0.2	0.2	0.6	0.6
Co	31.0	50.0	28.0	44.0	28.0	36.0	45.2	42.0	24.0	31.0	26.0
Cr	0.0	329.8	95.8	604.1	95.8	1132.4		93.7	0.0	0.0	0.0
Cs	32.0	0.3	0.4	0.3	0.4	0.4	0.0	0.9	0.1	0.6	1.3
Cu	15.1	21.8	72.1	22.3	72.1	28.8	12.7	18.5	15.8	22.6	19.5
Ga	0.7	30.9	62.4	32.2	62.4	15.4	10.0	40.8	15.9	33.4	38.4
Hf	1.6	0.8	5.9	3.1	5.9	0.9	0.9	1.2	3.1	2.6	1.2
In	0.1	0.1	0.1	0.1	0.1	0.0	0.0	0.1	0.0	0.1	0.1
Ir	0.0	0.2	0.0	0.0	0.0	0.0	0.0	0.1	0.0	0.0	0.0
Li	10.0	8.6	15.3	12.6	15.3	4.8	4.8	12.2	3.0	9.4	10.1
Ni	42.0	237.4	240.0	352.5	240.0	224.1	34.5	209.3	23.0	31.0	22.0
Pb	3.6	8.1	25.4	16.3	25.4	14.9	21.0	15.8	0.2	3.9	4.8
Pd	1.0	0.7	5.4	2.7	5.4	0.8	1.1	0.9	1.2	0.8	0.8
Pt	0.0	0.0	0.0	0.0	0.0	0.0	0.0	0.0	0.0	0.0	0.0
Rb	29.5	15.0	39.8	19.0	39.8	10.7	1.8	36.5	11.0	60.0	27.0
Rh	0.1	0.1	0.1	0.1	0.1	0.1	0.1	0.1	0.1	0.1	0.1
Ru	0.1	0.2	0.1	0.1	0.1	0.2	0.0	0.1	0.1	0.1	0.2
S	250.0	132.1	99.4	208.2	99.4	104.5	1398.3	235.8	244.3	656.9	213.5
Sb	0.8	4.1	4.6	8.8	4.6	7.9	0.2	5.5	0.5	0.7	1.1
Sn	1.7	1.3	2.9	1.8	2.9	1.6	0.8	2.0	1.7	1.6	1.5
Sr	436.2	362.9	366.0	347.1	366.0	336.5	229.7	454.2	334.0	317.0	443.9
Te		-	-	-	-	0.0	0.0	-	-	-	-
Tl	0.1	0.0	0.1	0.1	0.1	0.0	0.0	0.1	0.0	0.1	0.1
U	0.5	0.2	1.2	0.7	1.2	0.2	0.3	0.5	0.1	0.4	0.4
V	369.7	510.4	486.7	577.6	486.7	443.8		344.4	417.1	442.1	389.4
Zn	101.9	109.7	141.1	189.4	141.1	84.8	20.8	134.6	51.1	105.6	109.2
Zr	80.0	47.0	202.0	115.0	202.0	42.0	73.0	107.0	105.0	86.0	96.0
Sc	245.6	234.4	216.5	220.0	216.5	275.7	123.7	221.5	217.7	213.2	206.5
Y	29.1	22.0	58.0	31.6	58.0	17.0	9.6	36.0	37.5	29.4	24.6
La	11.3	5.5	28.4	25.7	28.4	3.4	2.2	15.0	14.3	11.7	11.0
Ce	25.6	12.9	67.2	58.7	67.2	8.6	5.7	34.0	32.8	26.5	23.3
Pr	3.3	1.8	8.5	7.2	8.5	1.3	0.8	4.4	4.4	3.5	3.0
Nd	15.4	8.9	37.4	30.8	37.4	6.5	3.9	20.7	20.4	15.7	13.6
Sm	6.1	2.6	9.4	6.5	9.4	2.0	1.3	5.5	5.2	4.1	3.5
Eu	3.1	1.4	2.4	2.0	2.4	0.8	0.6	2.1	1.8	1.5	1.4
Gd	4.8	3.3	10.1	6.7	10.1	2.7	1.7	6.2	6.1	4.7	4.0
Tb	0.7	0.5	1.5	0.9	1.5	0.4	0.3	0.9	0.9	0.7	0.6
Dy	4.7	3.4	9.1	5.4	9.1	2.8	1.8	5.7	5.9	4.7	3.9
Ho	1.0	0.7	1.8	1.1	1.8	0.6	0.4	1.2	1.2	0.9	0.8
Er	2.9	2.1	5.4	3.1	5.4	1.6	1.0	3.5	3.6	2.8	2.3
Tm	0.4	0.3	0.7	0.4	0.7	0.2	0.1	0.5	0.5	0.4	0.3
Yb	2.7	2.0	4.6	2.7	4.6	1.4	0.9	3.0	3.1	2.6	2.1
Lu	0.5	0.3	0.7	0.4	0.7	0.2	0.1	0.4	0.5	0.4	0.3
Th	2.1	3.4	5.6	4.0	5.6	0.5	0.3	2.5	1.9	2.1	2.3
Parameters											
FeO*	7.5	8.0	7.4	8.5	7.4	6.2	6.6	6.2	6.8	7.1	5.9
Na_2O+K_2O	3.4	2.8	5.1	3.7	5.1	1.7	1.5	5.3	3.5	3.5	4.4
FeO*/MgO	1.1	1.0	1.9	0.9	1.9	0.5	0.6	2.0	1.2	1.1	1.1
Zr/Y	2.7	2.1	3.5	3.6	3.5	2.5	7.6	3.0	2.8	2.9	3.9
Σ REE	82.4	45.9	187.2	151.6	187.2	32.4	20.8	103.1	100.7	80.1	70.2
Σ LREE	64.8	33.1	153.3	130.9	153.3	22.5	14.4	81.7	78.9	62.9	55.9
Σ HREE	17.6	12.7	33.9	20.7	33.9	9.8	6.4	21.5	21.8	17.2	14.3
Eu/Eu*	1.7	1.4	0.8	0.9	0.8	1.1	1.2	1.1	1.0	1.0	1.2
$(La/Sm)_N$	1.1	1.3	1.9	2.4	1.9	1.0	1.1	1.7	1.7	1.8	1.9
$(Gd/Yb)_N$	1.5	1.3	1.8	2.0	1.8	1.6	1.6	1.6	1.6	1.5	1.5
Sr/Sr*	0.2	0.3	0.1	0.1	0.1	0.4	0.4	0.1	0.1	0.1	0.2

Pearce and Norry (1979) suggested that Zr/Y ratios increase from mid-ocean ridges to within plate basalts due to heterogeneities of the source, whereas the low Zr and Zr/Y ratio of volcanic arc basalts result from a high degree of partial melting of a depleted source. On the other hand, the high Zr and similar Zr/Y ratio of basalts are due to open-system fractional crystallization. Floyd (1993) stated that amphibole and clinopyroxene fractionation significantly increase the abundance of Zr, whereas olivine and plagioclase fractionation does not change the Zr/Y ratio. Based on a Zr versus Zr/Y binary diagram, a significant variation of Zr/Y ratios increase with increasing Zr (Figure 2.12a); their trend closely follows curve I of Drury et al. (1983), indicating fractional crystallization of mafic phases with or without feldspars (Drury et al., 1983). The metagabbro samples reflect clinopyroxene fractionation crystallized from mafic phases from island arcs (Drury et al., 1983), whereas the metadiorite samples reflect amphibole fractionation crystallized from mafic phases from Andean-type arcs (Drury et al., 1983) and are typical of calc-alkaline volcanic arc lavas (Brown et al., 1977). The chondrite-, N-type MORB, and primitive mantle-normalized REE patterns of metagabbro-diorite complex rocks are characterized by concave profiles (Figures 2.12b-d). These patterns are characterized by an enriched LREE, with an average 81.8 for metagabbro and 69.9 for dioritic rocks [$(La/Sm)_N$ = 1.1-2.4 for metagabbro and 1.7-2.0 for dioritic rocks], and a practically flat HREE, with an average 19.3 for metagabbro and 18.7 for dioritic rocks [average $(Gd/Yb)_N$ = 1.6 and 1.5 for metagabbro and dioritic rocks, respectively]. The patterns also show slight positive Eu anomalies (Eu/Eu*= 0.8-1.7 and 1.0-1.2 for metagabbro and dioritic rocks, respectively). The positive Eu anomalies are due to plagioclase accumulations that contributed to Eu and light REE abundances, and led to a dilution of the HREE (Hassanipak et al., 1996). In addition, the Sr/Sr* is used as a comparison with the Eu contents, and positive Eu/Eu* and Sr/Sr* anomalies of analyzed rocks refer to plagioclase accumulations (Nagihara and Casey, 2001) (Figures 2.12c-d).

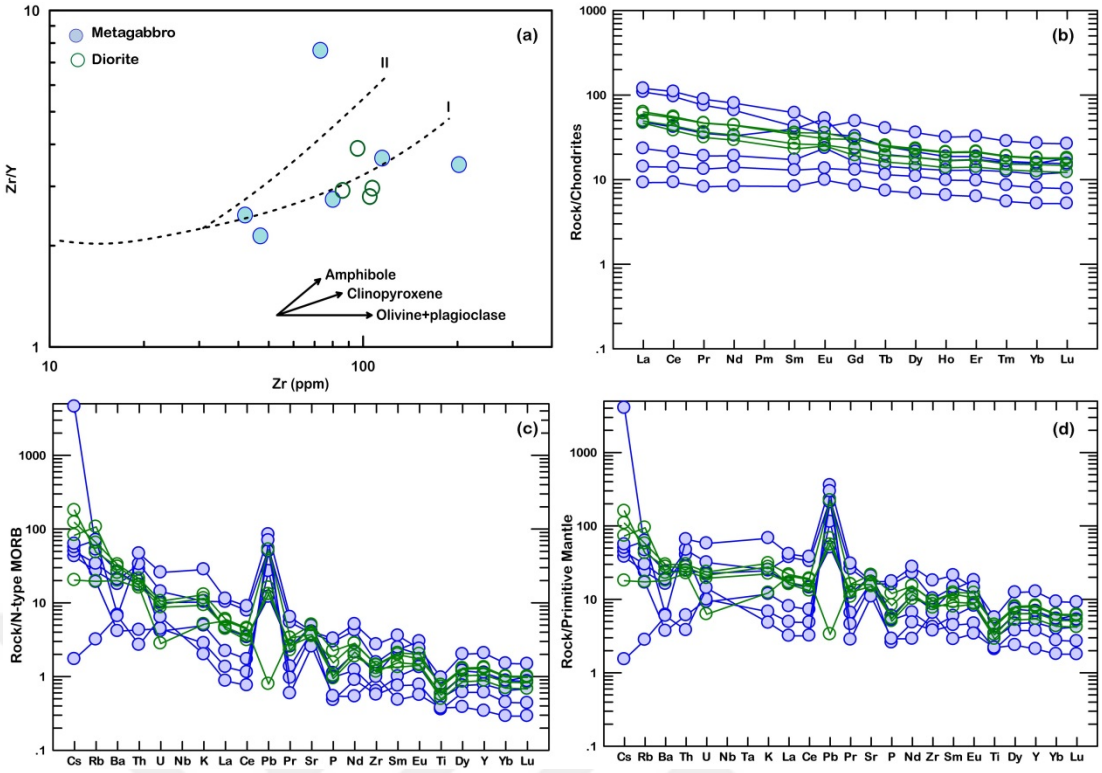

Figure 2.12 : Geochemical diagrams of metagabbro-diorite rocks: a) Zr/Y - Zr binary diagram, vectors for fractional crystallization after Floyd (1993) and melting curves I and II after Drury et al. (1983); b) Chondrite-normalized REE patterns (Sun and McDonough, 1989); c) N-type MORB-normalized patterns (Sun and McDonough, 1989); d) Primitive mantle-normalized trace element patterns (Sun and McDonough, 1989).

2.5.2 Alteration geochemistry

The geochemical characteristics of the hydrothermally altered wall rocks associated with the Atud gold deposit are based on a number of whole-rock geochemical analyses of the samples from the underground levels of the alteration zones (Table 2.3). The major factor responsible for the precipitation of different ores is the chemical interaction between the rocks and the circulating hydrothermal solutions (Rose and Burt, 1979; Susak, 1994). When the hydrothermally altered wall rocks were compared to the least-altered rocks, a higher K_2O content was observed, indicating that sericite, kaolinite, muscovite and chlorite are the main alteration phases in all the alteration zones, with higher loss on ignition (LOI) content referring to more intense alteration. Generally, these altered wall rocks have a large proportion of sulfur representing arsenopyrite and pyrite. Furthermore the model percentages of the arsenopyrite, chalcopyrite, and enargite are changed in the three alteration zones. Zone 1 and 2 which have no enragite contain 5-8 vol. % and 3-5 vol. % arsenopyrite, and 2-3 vol. % and 1-2 vol. % chalcopyrite, respectively. On the other hand, zone 3

Table 2.3 : Major and Trace elements of the median of least altered rocks and the altered rocks from alteration zones 1, 2, and 3.

	Mean	Zone 1										Zone 2			Zone 3			
Sample ID		**A34**	**A39**	**A47**	**A49**	**A53**	**A60**	**A64**	**At68**	**A75**	**A-sh-1**	**A66**	**A67**	**A81**	**A19**	**A40**	**A58**	**AT10.1**
SiO2	52.05	52.57	52.24	50.21	48.71	52.37	42.10	44.44	70.67	42.99	51.86	56.58	57.85	57.85	53.21	53.62	49.13	23.42
Al2O3	16.11	17.39	15.36	15.43	16.48	14.00	18.40	10.78	10.82	17.53	16.30	18.64	13.71	17.51	16.36	17.46	15.21	10.18
Fe2O3	7.46	5.06	4.97	5.60	5.28	6.27	5.61	7.10	3.02	7.32	4.02	3.74	6.09	4.58	7.32	7.39	9.84	3.13
FeOt	6.72	4.55	4.47	5.04	4.75	5.64	5.05	6.39	2.72	6.59	3.62	3.36	5.48	4.12	6.59	6.65	8.85	2.81
MgO	6.76	2.40	3.60	3.89	3.72	3.04	3.35	6.77	1.14	3.59	3.47	1.43	1.48	1.96	4.28	4.90	3.25	4.17
CaO	8.71	4.94	6.08	6.27	6.20	5.81	8.19	7.71	1.65	6.28	7.01	3.98	4.39	4.64	7.89	3.93	5.79	32.56
Na2O	2.81	0.22	0.31	0.84	0.20	0.25	0.25	0.12	0.10	0.54	0.61	3.78	2.40	3.27	3.25	5.10	2.23	0.91
K2O	0.83	4.56	3.83	3.53	4.22	3.63	4.44	2.75	2.54	4.50	3.67	3.03	2.56	2.52	0.59	0.28	2.09	0.14
TiO2	0.82	0.83	0.66	0.65	0.65	1.03	0.63	0.61	0.37	1.13	0.59	0.42	0.82	0.59	0.81	1.01	1.82	0.18
P2O5	0.20	0.20	0.12	0.13	0.11	0.10	0.08	0.11	0.07	0.14	0.06	0.23	0.22	0.15	0.21	0.20	0.17	0.00
MnO	0.13	0.08	0.09	0.09	0.09	0.11	0.12	0.15	0.03	0.13	0.09	0.07	0.08	0.06	0.13	0.09	0.12	0.05
LOI	3.79	10.67	11.75	13.06	12.90	12.10	14.16	17.78	6.34	14.01	12.29	8.09	8.91	6.87	5.93	4.49	8.75	24.69
Trace elements (ppm)																		
Ag	0.8	7.0	1.3	0.7	2.2	10.0	14.0	1.2	69.6	29.4	0.9	0.9	12.3	2.4	0.7	1.2	3.4	1.0
As	10.6	810.7	91.1	3040.2	2522.3	1969.5	1404.0	294.4	4220.0	2697.4	211.0	158.0	1194.5	172.0	6.0	6450.4	4093.9	48.5
Au (ppb)	46.4	275.1	25.0	156.3	237.8	182.6	270.6	28.0	790.2	184.2	159.6	118.6	176.1	48.6	53.9	74.7	90.3	155.4
Ba	113.9	375.2	440.4	131.2	185.6	273.7	25.0	72.0	9.0	259.2	211.0	334.0	188.1	245.0	144.0	80.9	347.9	73.8
C	2340.6	27056.0	19785.0	25364.0	14553.0	4882.4	30903.0	13295.0	5717.3	24749.0	25541.0	12529.0	26180.0	12589.0	7687.8	44681.0	23086.0	52887.0
Co	35.0	13.0	20.7	20.7	16.0	19.1	16.0	25.8	36.0	21.8	13.0	5.0	11.2	31.0	27.0	22.1	22.0	26.2
Cu	29.2	27.9	19.1	6.0	15.6	44.6	46.5	6.3	83.8	35.3	27.2	112.6	118.2	39.6	19.9	32.7	79.0	0.2
Ga	31.1	25.4	22.4	16.8	17.2	20.8	38.4	11.1	20.4	22.1	33.1	52.7	16.4	40.5	33.6	20.7	25.6	9.7
Hf	2.5	0.6	0.8	1.1	0.8	1.0	1.5	0.6	1.0	1.1	1.3	1.5	2.7	1.4	0.9	3.0	1.7	0.4
Ni	150.5	19.4	52.3	25.8	21.0	24.9	360.9	32.5	398.3	25.1	408.9	157.6	6.8	163.4	206.5	47.3	11.2	55.6
Pb	12.7	9.4	7.6	9.3	10.9	10.8	4.0	10.6	23.4	12.8	1.6	5.3	9.2	5.5	35.7	10.3	14.6	22.0
S	331.1	36168.0	20741.0	20427.0	33425.0	5986.8	26186.0	16316.0	21224.0	1091.8	6015.9	9123.3	16301.0	1989.2	70.7	5525.8	28274.0	823.0
Sb	3.5	8.6	26.4	20.0	9.8	21.7	30.4	3.8	143.1	37.6	13.6	7.0	17.5	10.3	14.4	3.9	3.6	0.4
Sn	1.8	1.4	1.2	1.3	0.9	1.3	2.3	1.0	1.6	1.4	2.5	1.9	0.8	1.7	2.0	2.5	2.0	0.5
Sr	363.1	106.5	145.6	114.6	133.8	133.5	131.7	132.5	32.1	142.3	203.7	169.9	88.5	110.6	375.7	197.9	160.4	276.7
V	446.8	113.0	137.0	132.0	124.0	156.0	357.0	142.0	258.2	167.0	264.2	214.7	66.0	275.1	344.3	179.0	337.0	
Y	32.1	10.0	7.5	9.9	8.6	12.6	14.7	8.2	8.0	10.7	12.9	20.1	15.0	18.9	32.1	19.2	21.2	5.2
Zn	108.1	25.3	53.2	72.2	77.3	123.4	82.9	97.0	100.1	79.0	90.8	85.8	24.7	97.5	216.4	65.5	119.3	11.3
Zr	105.0	184.0	74.0	76.0	68.0	90.0	96.0	67.0	74.0	98.0	70.0	163.0	167.0	100.0	90.0	124.0	137.0	15.0
Density (g/cm^3)	2.91	2.85	2.88	2.89	2.91	2.88	2.90	3.00	2.79	2.92	2.87	2.87	2.85	2.86	2.88	2.90	2.97	2.84
Ishikawa AI	39.71	57.43	53.76	51.07	55.37	52.40	47.98	54.87	67.79	54.26	48.38	36.47	37.30	36.14	30.44	36.45	39.97	11.40

has high amount of arsenopyrite (5-8 vol. %) with enargite (1-2 vol. %). Some elements, e.g. Au, Ag, S, and Sb with As, are most common in alteration zone 1 decreasing outward to zone 3. In zone 2, a high amount of SiO_2 reflects silicification, whereas in zone 3, a significant amount of CaO and C with Na_2O indicates carbonatization and albitization. In addition, the relationship between Na_2O and K_2O in the Ishikawa alteration index (AI = [100(K_2O+MgO) / (K_2O+MgO+CaO+Na_2O)]) of Ishikawa et al. (1976) for altered rocks suggests sericite in zone 1 with some chlorite and carbonate, dolomite/ankerite in zones 2 and 3, and albite/calcite in zone 3 (Figures 2.13a-b).

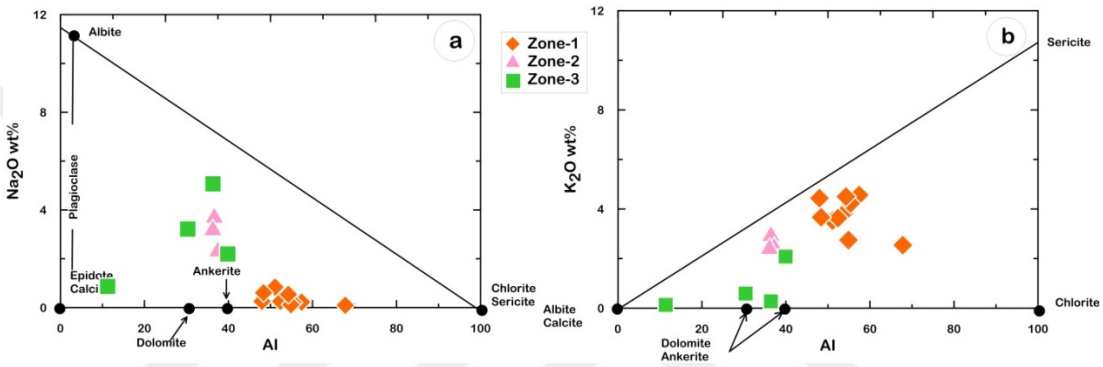

Figure 2.13 : Relationship between alteration index (AI) and (a) Na_2O and (b) K_2O for the altered rocks (Large et al., 2001).

2.5.2.1 Mass balance calculation

During hydrothermal alteration processes, the mass changes of each alteration zone are respected to the unaltered precursor and elemental compositions that experience gains/losses or dilutions are set from the composition-volume comparison of altered and unaltered rocks (Gresens, 1967). The Gresens' equation was improved by Grant (1986); Grant (2005) who suggested that the immobile elements plot along an isocon line that has no mass transfer during alteration processes. GEOISO-Windows (Coelho, 2006) is a recent version of software which determines and plots mass balance/volume changes during alteration processes. The absolute mobility of different elements, which indicates the mass balance/volume change, is defined using Gresens (1967) equations and a best-fit isocon line (Grant, 1986) and requires selection of immobile elements. This enables the determination of mass gains/losses of mobile elements in altered rocks. Al, Ti, and Zr represent high field strength elements and are assumed to be immobile elements (or their mobility is not significant during alteration processes). Furthermore, aluminum is considered to be

an immobile element within greenschist-grade metamorphic conditions under low-to-moderate temperature hydrothermal systems (Barton et al., 1991). Based on mass/volume gains and losses, each of the alteration zones has different additions and depletions of major/trace elements (Tables 2.3 and 2.4).

Table 2.4 : Elements/oxides mass changes in relation to original whole rock mass ((Mfi-Moi)/Mo) and in relation to original elements/oxides mass in original rock ((Mfi-Moi)/Moi) (Data resulted from GEOISO-A Windows™ program).

	Zone 1		Zone 2		Zone 3	
	(Mfi-Moi)/Mo	(Mfi-Moi)/Moi	(Mfi-Moi)/Mo	(Mfi-Moi)/Moi	(Mfi-Moi)/Mo	(Mfi-Moi)/Moi
SiO_2	1.636	0.031	3.618	0.07	-3.241	-0.062
Al_2O_3	0	0	0	0	0	0
Fe_2O_3	-1.724	-0.231	-2.807	-0.376	0.073	0.01
FeO^t	-1.565	-0.233	-2.533	-0.377	0.061	0.009
MgO	-3.063	-0.453	-5.19	-0.768	-2.243	-0.332
CaO	-2.361	-0.271	-4.503	-0.517	4.94	0.567
Na_2O	-2.451	-0.872	0.243	0.087	0.314	0.112
K_2O	3.153	3.798	1.787	2.153	0.019	0.023
TiO_2	-0.07	-0.085	-0.229	-0.279	0.225	0.274
P_2O_5	-0.084	-0.419	-0.006	-0.031	-0.037	-0.184
MnO	-0.024	-0.187	-0.062	-0.478	-0.021	-0.163
LOI	9.425	2.487	3.926	1.036	8.151	2.151
Ag	13.559	16.141	4.21	5.012	0.88	1.047
As	1812.758	170.372	481.917	45.293	2873.594	270.075
Au	197.514	4.252	64.488	1.388	55.402	1.193
Ba	95.528	0.839	133.974	1.177	62.077	0.545
C	17925.864	7.659	14234.031	6.081	32584.856	13.922
Co	-13.66	-0.39	-19.753	-0.564	-8.526	-0.244
Cu	3.751	0.128	58.154	1.99	6.626	0.227
Ga	-7.107	-0.228	4.259	0.137	-6.757	-0.217
Hf	-1.455	-0.587	-0.648	-0.261	-0.847	-0.342
Ni	-5.89	-0.039	-44.593	-0.296	-63.255	-0.42
Pb	-2.063	-0.163	-6.224	-0.491	9.809	0.774
S	19484.857	58.844	8526.297	25.749	9109.961	27.512
Sb	29.726	8.397	7.704	2.176	2.545	0.719
Sn	-0.216	-0.121	-0.355	-0.199	0.137	0.076
Sr	-228.211	-0.629	-243.834	-0.672	-88.036	-0.242
V	-251.304	-0.562	-267.195	-0.598	-134.648	-0.301
Y	-21.179	-0.66	-14.622	-0.456	-10.92	-0.341
Zn	-23.461	-0.217	-40.907	-0.378	4.148	0.038
Zr	-10.242	-0.098	33.932	0.323	-5.401	-0.051

(Mfi-Moi)/Mo: Mass change in relation to original rock mass

(Mfi-Moi)/Moi: Mass change in relation to original element mass

On the x-y plots of least-altered vs. altered samples (calculated using GEOISO-Windows), Al_2O_3 is shown to be an immobile element in all alteration zones during hydrothermal alteration (Figures 2.14a-c). The mass balance calculations and isocon diagrams reveal that the samples from zone 1 are enriched in K_2O, SiO_2, and LOI with Au, Ag, As, Ba, C, Cu, S, and Sb (Figure 2.14a & 2.15a-b). Mass change (MC)

and volume change (VC) of this zone are calculated as 5.6 % and 6.4 %, respectively (Table 2.5). Enrichment of K_2O, Na_2O, and SiO_2 with higher Au, Ag, As, Ba, C, Cu, Ga, S, Sb, and Zr is observed in samples from zone 2 (Figure 2.14b & 2.15a-b), with -3.1 % MC and -1.4 % VC (Table 2.5). Finally, common additions of CaO, Fe_2O_3, K_2O, Na_2O, TiO_2 and LOI with significant Au, Ag, As, Ba, C, Cu, Pb, S, Sb, Sn, and Zn enrichments characterize the chemical changes in the altered rocks in zone 3 (Figure 2.14c & 2.15a-b) with 8.8 % MC and 9.2 % VC (Table 2.5). Zone 3 has the highest amount of MC and VC, because it is rich in iron and titanium which they easily leached from the least altered metagabbro-diorite rocks and concentrated in this zone.

2.6 Chemistry of Alteration Minerals

The alteration minerals, e.g. sericite, carbonate, chlorite, and albite (Figure 2.16a), were analyzed with an electron microprobe. These minerals are distributed in the alteration zones associated with ore minerals and associated with gold mineralization in the underground levels.

Sericite is a very fine-grained white mica of white and yellowish color, and typically forms by the decomposition of feldspars. Sericite is the main secondary and alteration mineral observed in the gold-bearing hydrothermal alteration zone 1 and in mineralized quartz veins. Sericite is associated with kaolinite, muscovite, quartz, and pyrite. Electron microprobe data of sericite (Table 2.6) showed that its muscovite component was high in all analyzed flakes (average $X_{Ms} = 0.89$) and that its phengite content ($Mg+Fe_{a.p.f.u.}$) varied from 0.10 to 0.55 and 0.13 to 0.29 in wall rocks and mineralized veins, respectively. A negative correlation between ($Si+Mg+Fe^{2+}$) and ($Al^{iv}+Al^{vi}$) for sericite minerals (Figure 2.16b) indicates that their chemical compositional variations are controlled by phengitic substitutions of Si for Al ($Fe^{(VI)}$, $Mg^{(VI)} + Si^{(IV)} + Al^{(VI)}+ Al^{(IV)}$) (Muscovite formula calculated by Monier and Robert (1986); Tindle and Webb (1990)).

Carbonate minerals represent the second component of the secondary minerals, after sericite. Carbonate minerals occur either as thin veinlets traversing the silicified and chloritized wall rocks in alteration zones 2 and 3 or as disseminated grains intermingling with the mineralized quartz veins and wall rocks (Figure 2.9l).

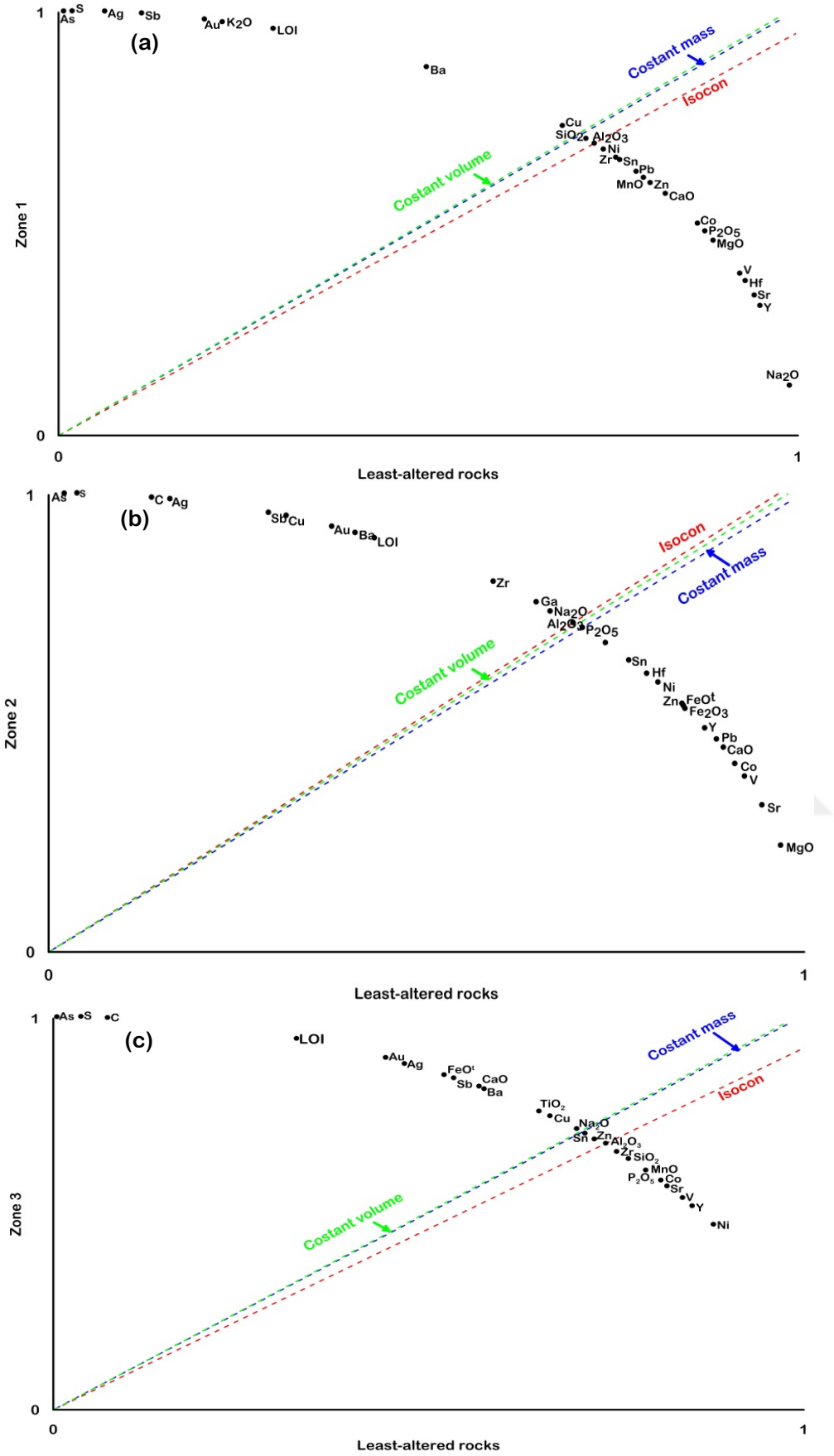

Figure 2.14 : Isocon diagram comparing the mean composition of least-altered samples and altered samples from (a) zone 1; (b) zone 2; (c) zone 3.

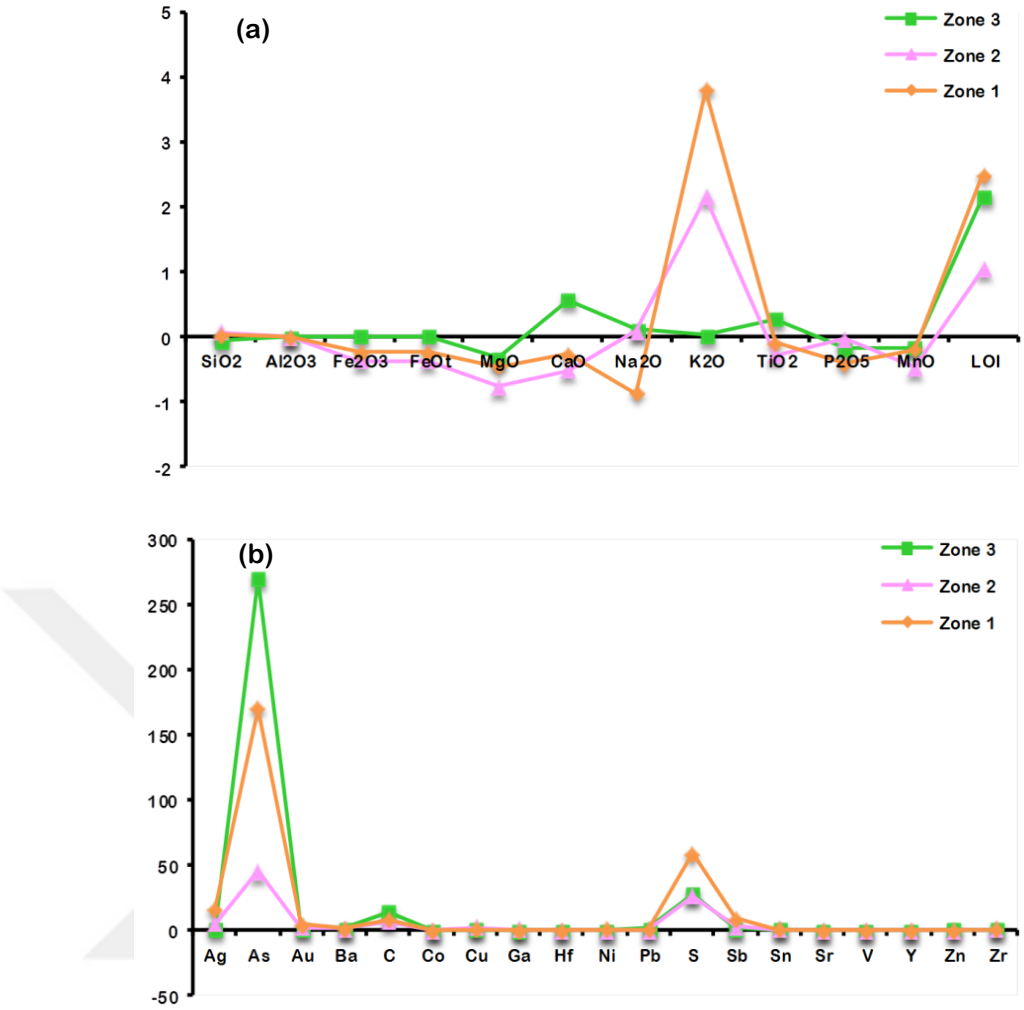

Figure 2.15 : Gain/loss of major oxides (wt.%) and trace elements (ppm) during alteration in the different zones of hydrothermal alteration based on mean data of the least altered samples as a reference for calculations, a) for zone 1; b) for zone 2, (c) for zone 3.

Table 2.5 : Whole rock mass and volume change in different alteration zones around Atud gold mine area.

	zone 1	**zone 2**	**zone 3**
MC: whole rock mass change	5.639	-3.069	8.851
VC: Whole rock volume change	6.37	-1.374	9.227

The electron microprobe data indicate that these carbonate minerals have higher amounts of $CaCO_3$ and lower amounts of $MgCO_3$ and $FeCO_3$ in the quartz veins than in the wall rocks (Table 2.7). Furthermore, in alteration zones 2 and 3, carbonate minerals occur principally as dolomite, iron-dolomite and magnesium-ankerite, whereas in quartz veins the carbonate minerals differentiated into iron-dolomite (Figure 2.16c).

Chlorite occurs as colorless-to-olive green flakes associated with disseminated arsenopyrite in hydrothermal alteration zone 3. Electron microprobe data of chlorite flakes (Table 2.8) revealed that they are generally iron-rich (FeO^t 20.64-20.10 wt. %) and are composed of pycnochlorite or ripidolite ($Al^{(iv)}$ = 2.30-2.36 pfu and 2.41-2.51 pfu, respectively) (Figure 2.17a). The estimated formation temperatures are 289–295°C and 301-312°C for pycnochlorite and ripidolite, respectively, and were calculated using the empirical Si–Aliv substitution geothermometer of Cathelineau (1988).

Table 2.6 : Representative electron microprobe data for sericite from the alteration zones and quartz veins in the Atud gold mine area.

	Sericite from altered rocks										
Spot no.	**3 / 1 .**	**6 / 1 .**	**7 / 1 .**	**9 / 1 .**	**10 / 1 .**	**11 / 1 .**	**12 / 1 .**	**13 / 1 .**	**16 / 1 .**	**18 / 1 .**	**19 / 1 .**
SiO_2	47.44	46.69	48.95	47.86	49.28	47.29	48.69	55.29	48.65	48.23	47.79
TiO_2	0.13	0.15	0.19	0.17	0.02	0.06	0.08	0.08	0.05	0.13	0.10
Al_2O_3	34.13	33.54	31.75	33.53	37.19	35.79	36.41	28.27	34.72	34.96	35.14
FeO	0.55	0.29	0.47	0.50	0.24	0.33	0.27	0.33	0.40	0.32	0.37
MnO	0.02	0.02	0.00	0.00	0.01	0.06	0.01	0.00	0.00	0.00	0.00
MgO	1.13	0.87	0.80	1.16	0.55	0.97	0.54	0.87	0.95	0.88	0.91
CaO	0.13	0.08	0.10	0.08	0.03	0.05	0.16	0.06	0.11	0.04	0.05
Na2O	0.33	0.36	0.35	0.47	2.09	0.61	1.66	0.32	0.31	0.36	0.32
K2O	9.03	8.84	8.14	8.76	6.13	8.17	6.65	7.58	9.01	8.50	8.76
SrO	0.00	0.03	0.00	0.01	0.00	0.00	0.00	0.00	0.00	0.00	0.00
BaO	0.00	0.04	0.06	0.08	0.04	0.09	0.06	0.06	0.07	0.06	0.00
F	0.00	0.00	0.00	0.00	0.00	0.01	0.01	0.02	0.00	0.00	0.00
Cl	0.02	0.02	0.02	0.00	0.01	0.00	0.00	0.01	0.03	0.01	0.01
Cr_2O_3	0.00	0.01	0.00	0.04	0.03	0.02	0.05	0.02	0.00	0.00	0.01
H2O*	4.46	4.37	4.40	4.46	4.67	4.51	4.60	4.55	4.54	4.52	4.51
Total	97.36	95.31	95.22	97.12	100.29	97.96	99.19	97.45	98.83	98.01	97.97
Number of cations on basis of 24 (O, OH, F, Cl)											
Si	6.37	6.40	6.67	6.44	6.33	6.28	6.34	7.26	6.42	6.40	6.35
Al^{iv}	1.63	1.60	1.33	1.56	1.67	1.72	1.66	0.74	1.58	1.60	1.65
Al^{vi}	3.77	3.81	3.76	3.75	3.95	3.88	3.92	3.64	3.82	3.86	3.86
Al total	5.40	5.42	5.10	5.31	5.63	5.60	5.59	4.38	5.40	5.47	5.51
Ti	0.01	0.02	0.02	0.02	0.00	0.01	0.01	0.01	0.00	0.01	0.01
Cr	0.00	0.00	0.00	0.00	0.00	0.00	0.01	0.00	0.00	0.00	0.00
Fe	0.06	0.03	0.05	0.06	0.03	0.04	0.03	0.04	0.04	0.04	0.04
Mn	0.00	0.00	0.00	0.00	0.00	0.01	0.00	0.00	0.00	0.00	0.00
Mg	0.23	0.18	0.16	0.23	0.11	0.19	0.10	0.17	0.19	0.17	0.18
Ca	0.02	0.01	0.01	0.01	0.00	0.01	0.02	0.01	0.02	0.01	0.01
Na	0.09	0.10	0.09	0.12	0.52	0.16	0.42	0.08	0.08	0.09	0.08
K	1.55	1.54	1.41	1.50	1.00	1.38	1.10	1.27	1.52	1.44	1.49
Ba	0.00	0.00	0.00	0.00	0.00	0.00	0.00	0.00	0.00	0.00	0.00
OH*	4.00	4.00	4.00	4.00	4.00	4.00	4.00	3.99	3.99	4.00	4.00
Fe/Fe+Mg	0.21	0.16	0.25	0.19	0.20	0.16	0.22	0.18	0.19	0.17	0.19
X_{MS}	0.95	0.94	0.94	0.92	0.66	0.90	0.72	0.94	0.95	0.94	0.95
Fe+Mg	0.29	0.21	0.22	0.29	0.13	0.23	0.13	0.21	0.23	0.21	0.22
Fe+Mg+Si	6.66	6.61	6.88	6.72	6.46	6.51	6.47	7.47	6.65	6.61	6.57

Table 2.6 (Continuous) : Representative electron microprobe data for sericite from the alteration zones and quartz veins in the Atud gold mine area.

	Sericite from quartz veins																							
Spot no.	**1 / 1 .**	**2 / 1 .**	**6 / 1 .**	**7 / 1 .**	**9 / 1 .**	**10 / 1 .**	**11 / 1 .**	**14 / 1 .**	**15 / 1 .**	**16 / 1 .**	**17 / 1 .**	**18 / 1 .**	**19 / 1 .**	**21 / 1 .**	**23 / 1 .**	**27 / 1 .**	**28 / 1 .**	**29 / 1 .**	**30 / 1 .**	**16 / 1 .**	**17 / 1 .**	**19 / 1 .**	**20 / 1 .**	**27 / 1 .**	**28 / 1 .**
SiO_2	49.06	48.68	48.11	49.18	48.36	49.17	49.58	47.44	47.84	47.97	47.65	47.90	46.79	47.77	48.47	49.01	47.28	47.99	47.91	47.84	55.07	48.30	47.40	46.10	47.28
TiO_2	0.07	0.14	0.07	0.07	0.08	0.10	0.09	0.41	0.07	0.13	0.23	0.33	0.09	0.18	0.13	0.44	0.27	0.22	0.28	0.16	0.06	0.05	0.21	0.42	0.15
Al_2O_3	37.39	33.11	36.38	37.21	37.11	37.12	37.07	34.26	34.61	34.75	33.59	34.90	34.62	32.97	34.09	32.75	33.36	34.68	33.65	33.98	30.46	36.35	32.76	32.78	31.62
FeO	0.28	1.36	1.00	0.54	0.17	0.26	0.46	1.51	0.85	1.15	1.13	1.27	1.25	1.66	0.60	1.44	1.75	1.13	1.41	1.27	0.33	0.27	1.70	1.83	2.22
MnO	0.01	0.00	0.01	0.00	0.01	0.01	0.00	0.02	0.00	0.00	0.03	0.00	0.00	0.00	0.00	0.00	0.04	0.01	0.01	0.02	0.00	0.00	0.01	0.00	0.01
MgO	0.37	1.73	0.62	0.43	0.43	0.52	0.55	1.52	1.15	1.29	1.52	1.18	1.38	1.84	1.43	1.41	1.83	1.27	1.68	1.20	0.83	0.57	1.58	1.21	1.59
CaO	0.06	0.05	0.02	0.05	0.05	0.07	0.14	0.00	0.06	0.05	0.08	0.04	0.08	0.04	0.03	0.03	0.00	0.02	0.01	0.08	0.10	0.05	0.04	0.02	0.00
Na2O	2.00	0.27	0.23	1.48	1.42	1.85	1.69	0.26	0.22	0.21	0.18	0.24	0.23	0.13	0.09	0.23	0.32	0.27	0.17	0.30	3.94	0.46	0.34	0.31	0.25
K2O	6.02	10.01	9.07	6.38	6.94	5.88	6.26	9.91	9.32	8.99	9.95	9.11	9.15	10.04	9.67	9.60	8.83	9.93	9.87	8.87	6.11	7.77	9.19	9.77	9.54
SrO	0.00	0.00	0.00	0.00	0.00	0.00	0.00	0.05	0.00	0.00	0.00	0.01	0.00	0.00	0.00	0.00	0.04	0.05	0.00	0.00	0.00	0.00	0.00	0.00	0.00
BaO	0.14	0.17	0.01	0.10	0.12	0.10	0.00	0.29	0.06	0.12	0.17	0.26	0.17	0.11	0.01	0.55	0.29	0.03	0.18	0.18	0.00	0.10	0.29	0.38	0.18
F	0.00	0.00	0.00	0.00	0.00	0.00	0.00	0.01	0.00	0.00	0.00	0.00	0.00	0.00	0.00	0.00	0.00	0.00	0.00	0.00	0.00	0.00	0.00	0.00	0.00
Cl	0.01	0.00	0.00	0.01	0.00	0.00	0.01	0.00	0.00	0.01	0.00	0.00	0.01	0.02	0.01	0.00	0.01	0.02	0.01	0.01	0.01	0.01	0.00	0.01	0.01
Cr_2O_3	0.00	0.01	0.04	0.06	0.14	0.07	0.09	0.10	0.02	0.00	0.03	0.11	0.00	0.04	0.01	0.03	0.04	0.05	0.07	0.00	0.00	0.04	0.00	0.01	0.00
H2O*	4.66	4.54	4.59	4.66	4.61	4.66	4.68	4.53	4.52	4.54	4.50	4.56	4.47	4.49	4.53	4.54	4.48	4.55	4.52	4.49	4.72	4.56	4.45	4.38	4.39
Total	100.07	100.07	100.15	100.17	99.44	99.81	100.62	100.31	98.72	99.20	99.06	99.91	98.24	99.28	99.07	100.03	98.53	100.22	99.77	98.40	101.63	98.53	97.97	97.22	97.24
Number of cations on basis of 24 (O, OH, F, Cl)																									
Si	6.31	6.43	6.28	6.33	6.28	6.33	6.34	6.27	6.35	6.34	6.35	6.30	6.27	6.37	6.41	6.48	6.33	6.31	6.35	6.38	6.99	6.34	6.39	6.31	6.45
Al^{iv}	1.69	1.57	1.72	1.67	1.72	1.67	1.66	1.73	1.65	1.66	1.65	1.70	1.73	1.63	1.59	1.52	1.67	1.69	1.65	1.62	1.01	1.66	1.61	1.69	1.55
Al^{vi}	3.98	3.58	3.88	3.97	3.97	3.96	3.94	3.61	3.77	3.75	3.63	3.72	3.73	3.56	3.72	3.57	3.60	3.69	3.60	3.72	3.54	3.97	3.60	3.59	3.53
Al total	5.67	5.15	5.60	5.64	5.68	5.63	5.59	5.34	5.42	5.41	5.28	5.41	5.47	5.18	5.31	5.10	5.27	5.38	5.25	5.34	4.55	5.63	5.21	5.29	5.08
Ti	0.01	0.01	0.01	0.01	0.01	0.01	0.01	0.04	0.01	0.01	0.02	0.03	0.01	0.02	0.01	0.04	0.03	0.02	0.03	0.02	0.01	0.00	0.02	0.04	0.02
Cr	0.00	0.00	0.00	0.01	0.01	0.01	0.01	0.01	0.00	0.00	0.00	0.01	0.00	0.00	0.00	0.00	0.00	0.01	0.01	0.00	0.00	0.00	0.00	0.00	0.00
Fe	0.03	0.15	0.11	0.06	0.02	0.03	0.05	0.17	0.09	0.13	0.13	0.14	0.14	0.19	0.07	0.16	0.20	0.12	0.16	0.14	0.04	0.03	0.19	0.21	0.25
Mn	0.00	0.00	0.00	0.00	0.00	0.00	0.00	0.00	0.00	0.00	0.00	0.00	0.00	0.00	0.00	0.00	0.00	0.00	0.00	0.00	0.00	0.00	0.00	0.00	0.00
Mg	0.07	0.34	0.12	0.08	0.08	0.10	0.10	0.30	0.23	0.25	0.30	0.23	0.28	0.37	0.28	0.28	0.37	0.25	0.33	0.24	0.16	0.11	0.32	0.25	0.32
Ca	0.01	0.01	0.00	0.01	0.01	0.01	0.02	0.00	0.01	0.01	0.01	0.01	0.01	0.01	0.00	0.00	0.00	0.00	0.00	0.01	0.01	0.01	0.01	0.00	0.00
Na	0.50	0.07	0.06	0.37	0.36	0.46	0.42	0.07	0.06	0.05	0.05	0.06	0.06	0.03	0.02	0.06	0.08	0.07	0.04	0.08	0.97	0.12	0.09	0.08	0.07
K	0.99	1.69	1.51	1.05	1.15	0.97	1.02	1.67	1.58	1.52	1.69	1.53	1.56	1.71	1.63	1.62	1.51	1.67	1.67	1.51	0.99	1.30	1.58	1.70	1.66
Ba	0.01	0.01	0.00	0.01	0.01	0.01	0.00	0.02	0.00	0.01	0.01	0.01	0.01	0.01	0.00	0.03	0.02	0.00	0.01	0.01	0.00	0.01	0.02	0.02	0.01
OH*	4.00	4.00	4.00	4.00	4.00	4.00	4.00	4.00	4.00	4.00	4.00	4.00	4.00	4.00	4.00	4.00	4.00	4.00	4.00	4.00	4.00	4.00	4.00	4.00	4.00
Fe/Fe+Mg	0.30	0.31	0.48	0.41	0.18	0.22	0.32	0.36	0.29	0.33	0.29	0.38	0.34	0.34	0.19	0.36	0.35	0.33	0.32	0.37	0.18	0.21	0.38	0.46	0.44
X_{MS}	0.66	0.96	0.96	0.74	0.76	0.68	0.71	0.96	0.97	0.97	0.97	0.96	0.96	0.98	0.99	0.96	0.95	0.96	0.97	0.95	0.50	0.92	0.95	0.95	0.96
Fe+Mg	0.10	0.49	0.23	0.14	0.10	0.13	0.15	0.47	0.32	0.38	0.43	0.37	0.42	0.55	0.35	0.44	0.56	0.37	0.49	0.38	0.19	0.14	0.51	0.46	0.58
Fe+Mg+Si	6.41	6.92	6.51	6.47	6.39	6.46	6.50	6.74	6.67	6.72	6.78	6.68	6.68	6.92	6.76	6.91	6.89	6.69	6.84	6.76	7.18	6.48	6.90	6.76	7.02

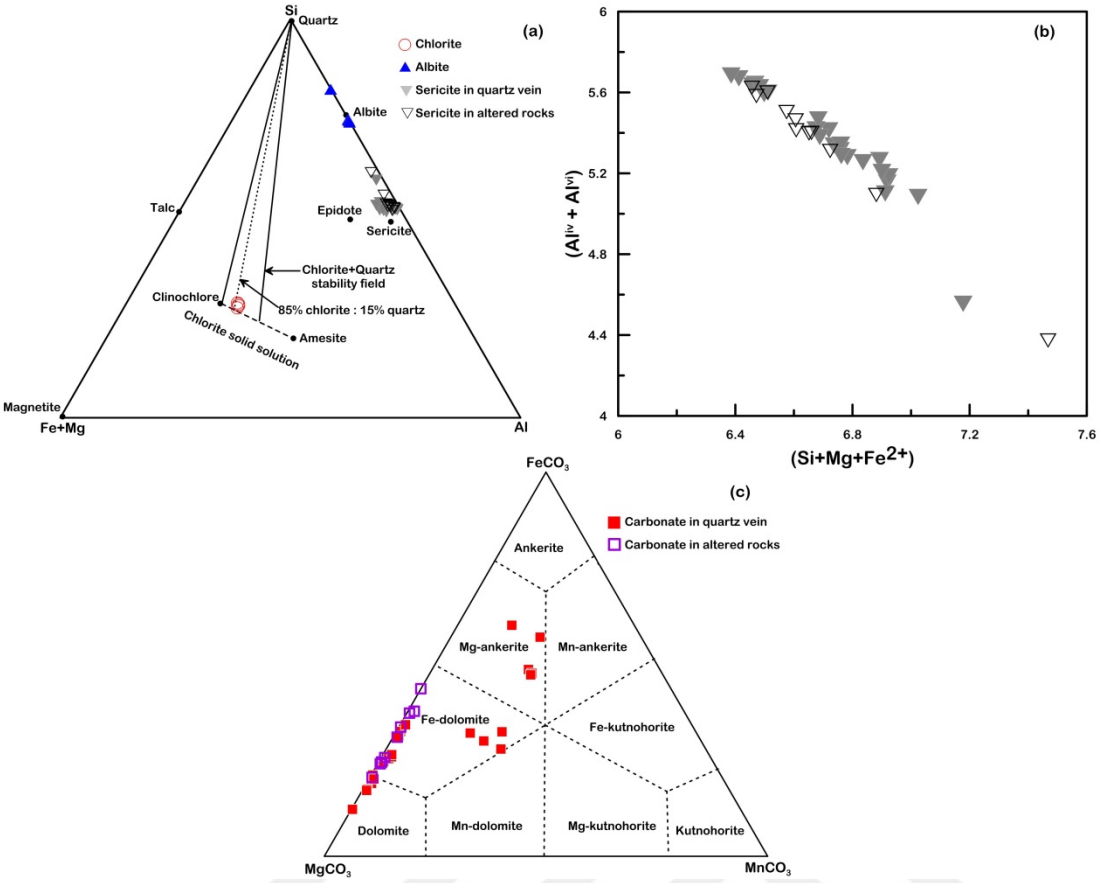

Figure 2.16 : a) Si-Al-(Fe + Mg) cation ternary diagram showing representative composition of different secondary and hydrothermal minerals from Atud gold mine, after Kranidiotis and MacLean (1987); b) $(Si+Mg+Fe^{2+})$ versus $(Al^{iv}+Al^{vi})$ of the sericite minerals from the mineralized quartz vein and altered wall rocks; c) $FeCO_3$-$MgCO_3$-$MnCO_3$ triangular classification diagram of Trdlička and Hoffman (1976) showing compositions of carbonate of the dolomite-ankerite series in samples of the mineralized veins and altered rocks.

Table 2.7 : Representative electron microprobe data for carbonate from the alteration zones and quartz veins in the Atud gold mine area.

	Carbonate from alteration zones								
Spot no.	**1 / 1 .**	**2 / 1 .**	**4 / 1 .**	**5 / 1 .**	**8 / 1 .**	**14 / 1 .**	**15 / 1 .**	**17 / 1 .**	**20 / 1 .**
CaO	29.78	24.51	24.53	20.02	27.76	22.07	26.29	25.06	27.69
MgO	14.25	9.37	16.64	12.12	12.69	19.51	13.08	13.98	14.21
MnO	0.37	0.51	0.39	0.01	0.42	0.32	0.25	0.22	0.31
FeO	11.31	13.25	22.72	21.35	13.15	11.50	9.50	16.22	10.60
BaO	0.04	0.00	0.03	0.01	0.06	0.00	0.00	0.00	0.00
Structural formulae basis on cation per 2 oxygens									
Ca	0.97	0.98	0.72	0.72	0.95	0.70	0.96	0.84	0.94
Mg	0.76	0.62	0.80	0.72	0.72	1.03	0.79	0.77	0.79
Mn	0.01	0.01	0.01	0.00	0.01	0.01	0.01	0.01	0.01
Fe	0.26	0.38	0.48	0.55	0.32	0.26	0.25	0.39	0.26
Ba	0.00	0.00	0.00	0.00	0.00	0.00	0.00	0.00	0.00
C	2.00	2.00	2.00	2.00	2.00	2.00	2.00	2.00	2.00
O	6.00	6.00	6.00	6.00	6.00	6.00	6.00	6.00	6.00
% Molecule									
$CaCO_3$	48.29	49.18	35.78	36.18	47.50	35.19	47.93	41.83	46.97
$MgCO_3$	38.09	30.99	40.01	36.11	35.80	51.28	39.31	38.47	39.74
$MnCO_3$	0.44	0.75	0.41	0.01	0.52	0.37	0.33	0.27	0.38
$FeCO_3$	13.16	19.08	23.78	27.69	16.15	13.16	12.43	19.43	12.90
$BaCO_3$	0.02	0.00	0.01	0.01	0.03	0.00	0.00	0.00	0.00

Table 2.7 (Continuous) : Representative electron microprobe data for carbonate from the alteration zones and quartz veins in the Atud gold mine area.

	Carbonate from quartz veins																								
Spot no.	**3 / 1 .**	**4 / 1 .**	**5 / 1 .**	**8 / 1 .**	**12 / 1 .**	**13 / 1 .**	**20 / 1 .**	**22 / 1 .**	**24 / 1 .**	**25 / 1 .**	**26 / 1 .**	**6 / 1 .**	**7 / 1 .**	**8 / 1 .**	**9 / 1 .**	**10 / 1 .**	**21 / 1 .**	**22 / 1 .**	**23 / 1 .**	**24 / 1 .**	**25 / 1 .**	**26 / 1 .**	**29 / 1 .**	**30 / 1 .**	**31 / 1 .**
CaO	28.46	29.43	29.61	30.91	29.62	28.63	29.61	29.62	29.66	31.19	28.87	57.58	59.05	0.32	62.63	60.76	30.91	52.58	62.27	63.35	31.93	31.02	48.32	31.85	30.95
MgO	12.66	11.65	15.42	15.61	15.68	14.98	15.79	16.11	16.20	18.12	14.43	0.79	0.47	0.01	0.49	0.59	12.45	0.35	0.44	0.50	12.27	11.17	0.08	11.87	10.99
MnO	0.41	0.49	0.16	0.41	0.48	0.50	0.51	0.43	0.44	0.11	0.44	0.59	0.58	0.01	0.62	0.57	0.70	0.58	0.78	0.87	0.86	0.45	0.16	0.74	0.40
FeO	14.19	14.20	9.53	7.57	8.49	8.17	9.27	7.92	7.80	5.81	11.05	1.14	0.80	0.05	0.68	0.83	10.00	1.32	1.64	1.82	10.16	11.91	0.46	10.08	11.58
BaO	0.02	0.00	0.00	0.03	0.00	0.03	0.00	0.00	0.02	0.00	0.01	0.00	0.00	0.00	0.00	0.05	0.02	0.00	0.01	0.07	0.03	0.00	0.02	0.00	0.00
Structural formulae basis on cation per 2 oxygens																									
Ca	0.95	0.99	0.96	0.99	0.96	0.96	0.95	0.95	0.95	0.96	0.95	1.92	1.94	1.69	1.95	1.94	1.05	1.93	1.92	1.92	1.06	1.06	1.98	1.08	1.07
Mg	0.70	0.65	0.82	0.83	0.84	0.83	0.83	0.85	0.86	0.91	0.78	0.04	0.03	0.09	0.03	0.03	0.69	0.02	0.02	0.02	0.67	0.63	0.01	0.66	0.63
Mn	0.01	0.01	0.00	0.01	0.01	0.01	0.01	0.01	0.01	0.00	0.01	0.01	0.01	0.04	0.01	0.01	0.02	0.02	0.02	0.02	0.02	0.01	0.00	0.02	0.01
Fe	0.34	0.34	0.22	0.17	0.20	0.20	0.21	0.18	0.18	0.13	0.26	0.03	0.02	0.19	0.02	0.02	0.24	0.03	0.04	0.04	0.24	0.29	0.01	0.24	0.29
Ba	0.00	0.00	0.00	0.00	0.00	0.00	0.00	0.00	0.00	0.00	0.00	0.00	0.00	0.00	0.00	0.00	0.00	0.00	0.00	0.00	0.00	0.00	0.00	0.00	0.00
C	2.00	2.00	2.00	2.00	2.00	2.00	2.00	2.00	2.00	2.00	2.00	2.00	2.00	2.00	2.00	2.00	2.00	2.00	2.00	2.00	2.00	2.00	2.00	2.00	2.00
O	6.00	6.00	6.00	6.00	6.00	6.00	6.00	6.00	6.00	6.00	6.00	6.00	6.00	6.00	6.00	6.00	6.00	6.00	6.00	6.00	6.00	6.00	6.00	6.00	6.00
% Molecule																									
$CaCO_3$	47.58	49.73	47.77	49.55	47.84	48.07	47.25	47.64	47.61	47.76	47.40	95.76	97.09	84.28	97.28	96.82	52.28	96.43	96.18	95.79	53.14	53.20	98.80	53.81	53.67
$MgCO_3$	34.89	32.45	41.01	41.25	41.75	41.46	41.54	42.71	42.87	45.74	39.05	2.17	1.27	4.34	1.25	1.55	34.71	1.06	1.12	1.25	33.67	31.58	0.27	33.06	31.42
$MnCO_3$	0.50	0.60	0.19	0.48	0.57	0.61	0.59	0.50	0.52	0.12	0.53	0.72	0.70	1.92	0.70	0.66	0.86	0.78	0.88	0.96	1.04	0.56	0.24	0.91	0.51
$FeCO_3$	17.02	17.22	11.03	8.71	9.84	9.84	10.62	9.14	8.99	6.38	13.02	1.36	0.94	9.45	0.76	0.95	12.14	1.74	1.82	1.97	12.14	14.66	0.68	12.22	14.41
$BaCO_3$	0.01	0.00	0.00	0.01	0.00	0.01	0.00	0.00	0.01	0.00	0.00	0.00	0.00	0.00	0.00	0.02	0.01	0.00	0.00	0.03	0.01	0.00	0.01	0.00	0.00

Table 2.8 : Representative electron microprobe data for chlorite from the alteration zones in the Atud gold mine area.

Spot no	3 / 1 .	4 / 1 .	5 / 1 .	11 / 1 .
SiO_2	27.67	27.37	27.00	26.42
TiO_2	0.04	0.02	0.10	0.05
Al_2O_3	19.64	19.99	20.10	20.04
FeO	20.44	20.79	20.35	21.71
MnO	0.28	0.25	0.23	0.25
MgO	18.89	18.67	18.96	18.53
CaO	0.03	0.03	0.03	0.08
Na_2O		0.02	0.01	0.05
K_2O				
Cl				0.01
F		0.01		
TOTAL	86.34	86.50	86.13	86.49
O=F,Cl	0.00	0.00	0.00	0.00
T2	12.40	12.41	12.44	12.51
Cations based on 28 anions (O, F), anhydrous basis				
Si	5.71	5.65	5.59	5.50
Ti	0.01	0.00	0.02	0.01
$Al^{(iv)}$	2.29	2.35	2.41	2.50
$Al^{(vi)}$	2.49	2.52	2.50	2.42
Al	4.78	4.86	4.91	4.92
Fe^2	3.53	3.59	3.52	3.78
Mn	0.05	0.04	0.04	0.04
Mg	5.81	5.75	5.85	5.75
Ca	0.01	0.01	0.01	0.02
Na	0.00	0.01	0.00	0.02
K	0.00	0.00	0.00	0.00
Cl	0.00	0.00	0.00	0.00
F	0.00	0.01	0.00	0.00
Fe/(Fe+Mg)	0.38	0.38	0.38	0.40
$Al^{iv}c$	2.29	2.35	2.41	2.50
T(°C)	288.57	295.40	301.17	312.30

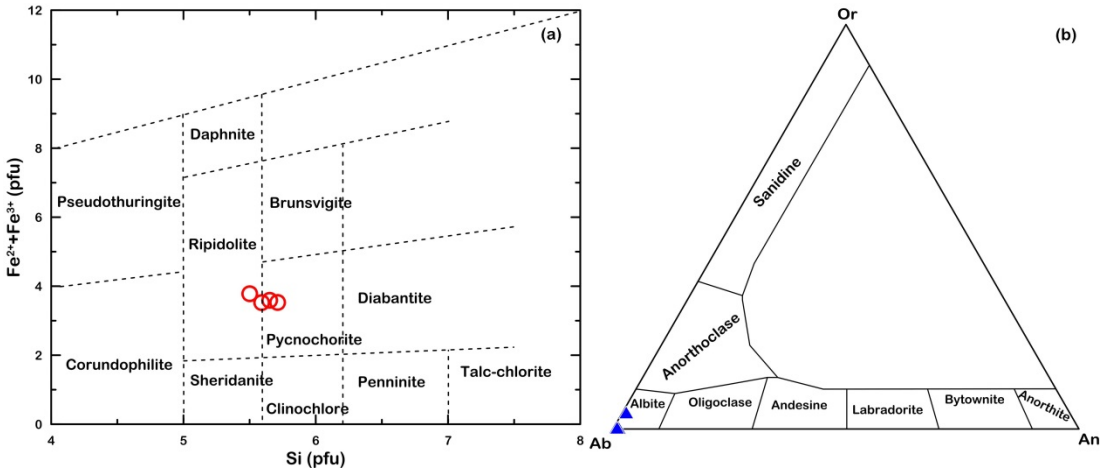

Figure 2.17 : a) Si versus (Fe^{2+}+Fe^{3+}) diagram showing chlorite composition in the alteration zone in the Atud gold mine (Classification of Hey (1954)); b) Feldspars chemistry in the Or-Ab-An diagram of Deer et al. (1992); (Ab: Albite; Or: Orthoclase; An: Anorthite).

Albite represents the main secondary feldspar produced by plagioclase substitution, and is found disseminated in altered wall rocks with chlorite in alteration zone 2. The representative chemical compositions of albite show high SiO_2 (68.2-79.5 wt. %), Al_2O_3 (14.2-19.9 wt. %), and Na_2O (7.3-11.9 wt. %) content and low amounts of CaO (0.1-0.2 wt. %) (Table 2.9). Albite was relatively pure having a high Ab content in all analyzed samples (Ab = 95.08%-99.20%). The triangular diagram of albite (Ab), anorthite (An) and orthoclase (Or) end-members refers to the analyzed samples plotted in the albite field (Figure 2.17b).

Table 2.9 : Representative electron microprobe data for albite from the alteration zones in the Atud gold mine area.

Spot no.	1 / 1 .	12 / 1 .	13 / 1 .	14 / 1 .	18 / 1 .
SiO_2	68.95	69.02	69.31	68.22	79.49
Al_2O_3	19.49	19.50	19.88	19.96	14.20
FeO	0.03	0.08	0.04	0.10	0.09
CaO	0.24	0.11	0.10	0.16	0.11
Na_2O	11.87	11.57	11.73	11.98	7.28
K_2O	0.05	0.05	0.07	0.06	0.48
BaO	0.06	0.03	0.04		
Total	100.69	100.36	101.17	100.48	101.65
Formula					
Si	2.99	3.00	2.99	2.97	3.32
Al	1.00	1.00	1.01	1.02	0.70
Fe^2	0.00	0.00	0.00	0.00	0.00
Ca	0.01	0.01	0.00	0.01	0.00
Na	1.00	0.98	0.98	1.01	0.59
K	0.00	0.00	0.00	0.00	0.03
Ba	0.00	0.00	0.00	0.00	0.00
T2	2.61	2.61	2.59	2.62	2.51
Anorthite	1.10	0.52	0.47	0.73	0.79
Albite	98.62	99.20	99.14	98.94	95.08
Orthoclase	0.27	0.28	0.39	0.33	4.12

2.7 Discussions and Conclusions

In the Atud area, the metagabbro-diorite complex occurred in Gabal Atud in the central part of the Egyptian Eastern Desert. The complex is intruded into serpentinites and their derivatives and metatuffs, and is later intruded by younger olivine gabbro norite. The Atud gold mineralization is considered as a vein-type gold deposit closely associated with intense hydrothermal alteration haloes along the NW-

SE brittle-ductile shear zone. It was genetically related to the metagabbro-diorite complex that was intruded by quartz veins that occupied the pre-existing fractures. These quartz veins that are linked to the shear zone system are younger than the intrusion of olivine gabbro norite, having two generations: a mineralized grayish-to-white old vein (trending N 30°-40° W), and a younger, non-mineralized milky white vein (trending NE-SW). Underground levels were drifting along the NNW-SSE brittle-ductile shear zone that represents the strike of the main lode. The geological, petrographical and XRD analytical studies suggest that there are three main hydrothermal alteration zones of mineral assemblages with gradual boundaries placed around mineralized and non-mineralized quartz veins in these levels. Zone 1 is a zone of sericite/kaolinite, muscovite, quartz, and pyrite with minor amounts of graphite, ankerite, dolomite, and/or albite. Larger amounts of quartz, albite, and sericite/kaolinite are found in zone 2 with minor amounts of pyrite, dolomite, clinochlore, and muscovite. Zone 3 is characterized by significant amounts of carbonate (ankerite/calcite) and chlorite (chamosite/chlinochlore) with albite and arsenopyrite and lower amounts of pyrite, muscovite, and quartz. The ore mineralogy includes mainly arsenopyrite and pyrite, with minor amounts of chalcopyrite, sphalerite, and enargite with goethite, associated with gold mineralization that occurred along the contact of quartz veins with hydrothermal alteration zones as well as within these zones. The first, second (main ore), and third (supergene) phases of mineralization represent the contact relationships of gold with sulfide and gangue minerals in the paragenesis. The geochemical behavior of the least-altered metagabbro-diorite complex rocks reveals that the metagabbros are calc-alkaline gabbro and gabbro/diorite, whereas the diorites are calc-alkaline diorite and gabbro/diorite. These rocks are equivalent to calc-alkaline basalt (CAB) formed in island arc environments indicating clinopyroxene fractionation for metagabbros and amphibole fractionation for dioritic rocks.

GEOISO-Windows calculated the mass/volume gain and loss values, with Al_2O_3 considered as an immobile element. The mass balance calculations and isocon diagrams concluded that K_2O, Au, S, and Sb decrease from alteration zone 1 to zone 2, indicating that gold mineralization is highly related to sericitic, kaolinitic and muscovite alteration. Zone 3, which has a high amount of CaO, Fe_2O_3, and Na_2O with K_2O – indicating carbonatization, chloritization and albitization – is

characterized by a lower amount of gold. Therefore, gold decreases from zone 1 outwards to zone 3.

Sericite exhibited a high muscovite component in all analyzed flakes (average X_{Ms} = 0.89) and a phengite content ranging from 0.10 to 0.55 and 0.13 to 0.29 in wall rocks and mineralized veins, respectively. Carbonate has higher amounts of calcite ($CaCO_3$) and lower amounts of $MgCO_3$ and $FeCO_3$ in wall rocks than in quartz veins. Chlorite flakes are generally iron-rich (FeO^t 20.64–20.10 wt.%) and are composed of pycnochlorite and ripidolite, with $Al^{(iv)}$ = 2.30-2.36 pfu and 2.41-2.51 pfu, respectively and estimated formation temperatures of 289–295°C and 301-312°C, respectively. Albite is accompanied with chlorite but was generally pure in all samples (Ab = 95.08%-99.20%).

3. S, C, O STABLE ISOTOPE AND MINERAL CHEMISTRY CONSTRAINTS ON THE GENESIS OF THE ATUD GOLD DEPOSIT, CENTRAL EASTERN DESERT, EGYPT

3.1 Introduction

The intrusion-related gold deposits represent the most important deposits in the Phanerozoic arc settings which have chalcophile metal-bearing porphyry and non-porphyry types(Sillitoe, 1991). Based on the metal association, the porphyry type ranges from into Cu-Au to Au only which related to calc-alkaline to alkaline, intermediate (diorite-monzonite), and I-type intrusions (Sillitoe, 1991). On the other hand, the non-porphyry type associated with I-type intrusion and characterized by enrichments of Zn, Pb, and Ag rather than Cu (Sillitoe, 1991; Richards and Kerrich, 1993). Their gold mineralization and associated metals have oxidized and metasomatized magmatic source (McInnes and Cameron, 1994) associated with K-silicate alteration assemblages (Sillitoe, 1991).

Stable isotope studies (C, O, H, N, and S isotopes) provide good information on the fluid source of many types of the hydrothermal ore deposits (e.g., Carlin-type, porphyry Cu–Au, volcanic-hosted massive sulfide [VMS] Mississippi-Valley-type, vein-hosted Au, and epithermal Au–Ag deposits) (Groves et al., 1998; Bierlein et al., 2004). Hydrothermal fluid can have the following water sources; meteoric, magmatic, metamorphic, seawater, connate, and juvenile sources (Pirajno, 2009). Most ore-bearing fluids in hydrothermal deposits have a mixed origin.

The intrusion-related gold deposits in the Egyptian Eastern Desert are located in the Precambrian basement rocks of the Arabian-Nubian Shield (ANS). The gold mineralization is mainly confined to quartz-mineralized shear zones. These structures represent the most important host to gold mineralization in Egypt (Klemm et al., 2001). Gabra (1986) stated that during the Pharaonic time [New Kingdom times (1550–1070 BC) and Roman and Byzantine times based on the existence of the old mining tools at Atud area (Klemm et al., 2001)], these deposits were first exploited.

Among these deposits is the Atud gold deposit, which is located in the Central Eastern Desert of Egypt and was re-opened between 1953 and 1969 by the Egyptian Geological Survey and Mining Authorities (EGSMA) (Gabra, 1986). EGSMA studied the surface and subsurface workings in detail, including drilling, mapping, mining, and sampling mineralized and unmineralized quartz veins and altered as well as unaltered rocks (Gabra, 1986). The Atud gold deposit is considered to be a mesothermal vein-type gold deposit hosted in metagabbro-dioritic rocks. The gold mineralization is closely confined to quartz veins and intense hydrothermal alteration along the NW-SE brittle-ductile shear zones peripheral to and crosscutting Atud gabbroic intrusion with intense hydrothermal alterations (Harraz, 1999; Harraz, 2002). Gabra (1986) mentioned that <0.l-31 g/t with an average 16.28 g/t represents the gold grade at the Atud area that has 19,000 tons of rock and 348 kg of pure gold in the principal lode. While Hussein and El Sharkawi (1990) stated that this deposit has 1600 tons of waste dump material from the mining of the Pharaonic age with 12.4 g/t of gold.

This chapter reports new data on the mineralogy and microchemical characteristics of the gold and associated ore minerals at the Atud gold deposit as well as stable isotope studies and aims to gain an understanding of the genesis of this gold deposit. Sulfur, carbon, and oxygen stable isotopic analyses of the sulfide and carbonate minerals were carried out in order to determine the temperature of the ore system and the sources of sulfur and carbon as well as the origin, evolution, and nature of ore-bearing fluids.

3.2 Geologic setting

The Atud area which covers 18 km^2 in the Central Eastern Desert of Egypt (Figure 3.1a) consists of serpentinites and related metasomatized rocks and metatuffs. These rocks were intruded by the so-called metagabbro-diorite complex (Figure 3.1b). At Gabal Atud, which is located in the center of the mapped area, this metagabbro-diorite complex is later intruded by olivine gabbronorite rocks (Figure 3.1b). The serpentinite and related metasomatized rocks cover a vast area around Gabal Atud (Figures 3.1b & 3.2a) and are classified petrographically into serpentinite, talc-carbonate, dolomitic marble, and calc-silicate rocks. The serpentinite rocks are associated with the talc-carbonate at the southern part of the study area, where they

are tectonically incorporated in the metatuffs (Figure 3.2a). They consist mainly of antigorite and chrysotile with fewer amounts of actinolite, tremolite, dolomite, and chromite (Figure 3.2b). Talc-carbonate rocks composed mainly of talc (45-55 vol. %) and dolomite (40-50 vol. %) and smaller amounts of actinolite, antigorite, and chromite (Figure 3.2c). The dolomitic marble occurs as small isolated outcrops along the southern slope of Gabal Atud and is mainly composed of dolomite (90 vol. %) with fewer amounts of magnesite and chromite (Figure 3.2d). The calc-silicate rocks are composed essentially of ankerite, dolomite, and quartz along with minor amounts of calcite, clinochlore, epidote, and chromite (Figure 3.2e) and occur in the northern part of the study area.

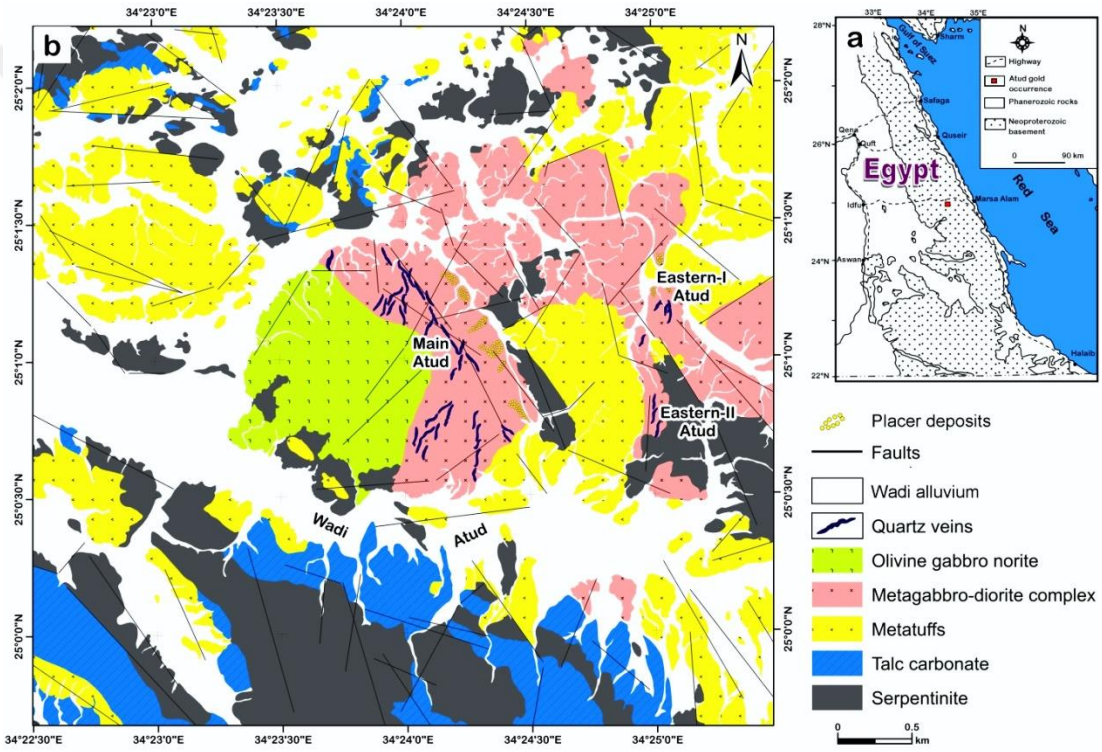

Figure 3.1 : a) Location map of Atud gold mine in the Central Eastern Desert of Egypt; b) Geological map of the study area (modified from Gabra (1986); Harraz (1999); Abdelnasser and Kumral (2016)).

Metatuffs also occur near Gabal Atud in low-lying areas associated with serpentinite rocks (Figures 3.1b and 3.2a). They have been subjected to a low-grade greenschist facies metamorphism and are petrographically differentiated into mafic lapilli metatuffs, intermediate metatuffs, metacherts, and quartz-biotite schists (Abdelnasser and Kumral, 2016). Mafic lapilli metatuffs exposed at Wadi Atud at the southern part of the mapped area with the serpentinites consist of carbonatized plagioclase and microperthite with tremolite, actinolite, dolomite, and epidote in a microcrystalline

tuffaceous matrix (Figure 3.2f). The intermediate metatuffs exposed at the northern part of the study area are composed of kaolinized microperthite, phlogopite, biotite, and quartz set in a much finer tuffaceous matrix (Figure 3.2g). Metacherts occurring small areas positioned along the southern slope of Gabal Atud are composed of irregularly banded quartz- and feldspar-containing laminae (Figure 3.2h). Quartz biotite schists are foliated rocks that consist essentially of quartz, feldspar, and biotite with minor amounts of carbonate, muscovite, and opaque minerals (Figure 3.2i).

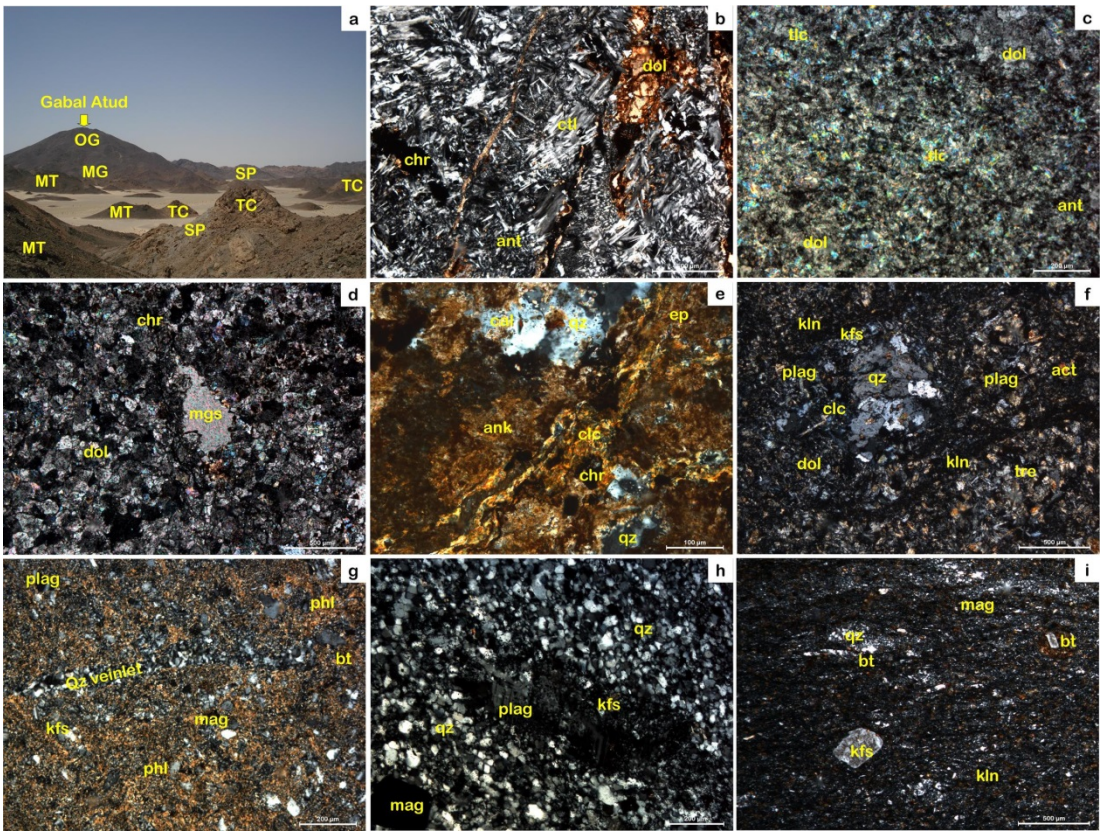

Figure 3.2 : a) Serpentinites (SP) and their derivatives (talc-carbonate; TC) occurred with the metatuffs (MT) around the metagabbro-diorite complex (MG) and olivine gabbro norite (OG) of Gabal Atud; b) Photomicrograph of antigorite (ant) and chrysotile (ctl) with actinolite, tremolite, dolomite (dol), and chromite (chr) in serpentinite rock; c) Talc (tlc) and dolomite (dol) with antigorite (ant) in talc-carbonate rock; d) Mineral compositions of dolomitic marble; e) Ankerite (ank), dolomite, and quartz (qz) with calcite (cal), clinochlore (clc), epidote (ep), and chromite (chr) in the calc-silicate rock; f) Photomicrograph of mineral compositions of mafic lapilli metatuffs; g) Kaolinized microperthite (kfs), phlogopite (phl), biotite (bi), and quartz (qz) in tuffaceous matrix in intermediate metatuffs; h) Quartz (qz)- and feldspar (plagioclase (plag) & microperthite (kfs))-containing laminae in metachert; i) Mineral compositions of quartz-biotite schist.

The metagabbro-diorite complex covers a large proportion of the mapped area and exists as a semicircular body of Gabal Atud (Figure 3.1b). It represents one of the early orogenic gabbro-diorite complexes in the ANS and its age ranges from 987 to

830 Ma (Abdelrahman and Doig, 1987; Hashad, 2015). It was emplaced into the pre-existing rocks on the Atud area (serpentinites and metatuffs) and later intruded by the olivine gabbronorite (Figures 3.1b & 3.2a). This complex is differentiated into metamorphosed gabbro and diorite rocks. It represents the main host rock of Atud gold mineralization, which cut by numerous and dikes and mineralized and unmineralized quartz veins in the northeastern, eastern and southeastern parts of Gabal Atud along the NW-SE brittle-ductile shear zone (Figure 3.1b). The metagabbros consist mainly of plagioclase (labradorite in composition; An_{50-65}), tremolite, and actinolite with fewer amounts of secondary quartz and chlorite as well as relics of clinopyroxene and orthopyroxene with hornblende and magnetite (Figure 3.3a). The diorite is made up of plagioclase (partly altered), chlorite, and hornblende as well as subordinate quartz, chlorite, actinolite, and tremolite with iron oxide (Fig. 3.3b).

Olivine gabbronorites comparable with the younger gabbro of Ghoneim (1989) are emplaced into the metagabbro-diorite complex of Gabal Atud (Ghoneim, 1989) (Figures 3.1b & 3.2a). These rocks are distinct from the metagabbro rocks by being non-deformed and having very little and/or no alteration appearances. They are composed of plagioclase (labradorite to bytownite; 35-40 vol. %), diopside (25-30 vol. % partly altered to tremolite and actinolite; 5 vol. %), hypersthene (15-20 vol. %), cumulate olivine (partly altered into serpentine minerals, 15-20 vol. %), and opaque minerals (~ 3 vol. %), (Figure 3.3c).

3.3 Atud Gold mineralization

The Atud gold mine was historically exploited during Pharaonic times (Gabra, 1986). Three underground levels were developed by the Egyptian Geologic Survey and Mining Authority (EGSMA) between 1953 and 1969 at the northeastern and eastern slope of Gabal Atud (Gabra, 1986). This mining area was called the main Atud. Two further occurrences of gold mineralization in the study area were observed: Atud East-I is located at the NE part of the Atud area, and Atud East-II is located at the SE part of the Atud area (Harraz, 1999) (Figure 3.1b).

3.3.1 Hydrothermal alteration

The Atud gold mineralization is structurally controlled along the NW-SE brittle-ductile shear zone. It also associated with the intense hydrothermal alteration and the

quartz veins that occupied the pre-existing fractures. Its mineralization style can be classified as a mesothermal vein-type gold deposit (Harraz, 1999; Harraz, 2002) showing similarities with Um Eleiga gold deposit of Zoheir (2012a) in the ANS. Three subsurface hydrothermal alteration zones were observed around the mineralized and barren quartz veins (Abdelnasser and Kumral, 2016) (Figure 3.4); (1) sericitic alteration zone has mainly sericite/muscovite with subordinate quartz and kaolinite as well as pyrite (Figure 3.3d). (2) Phyllic alteration zone has high of quartz and sericite with pyrite and subordinate albite (Figure 3.3e). (3) Carbonate propylitic alteration zone has mainly carbonate (ankerite/calcite) and chlorite (chamosite/clinochlore) with albite and arsenopyrite (Figure 3.3f).

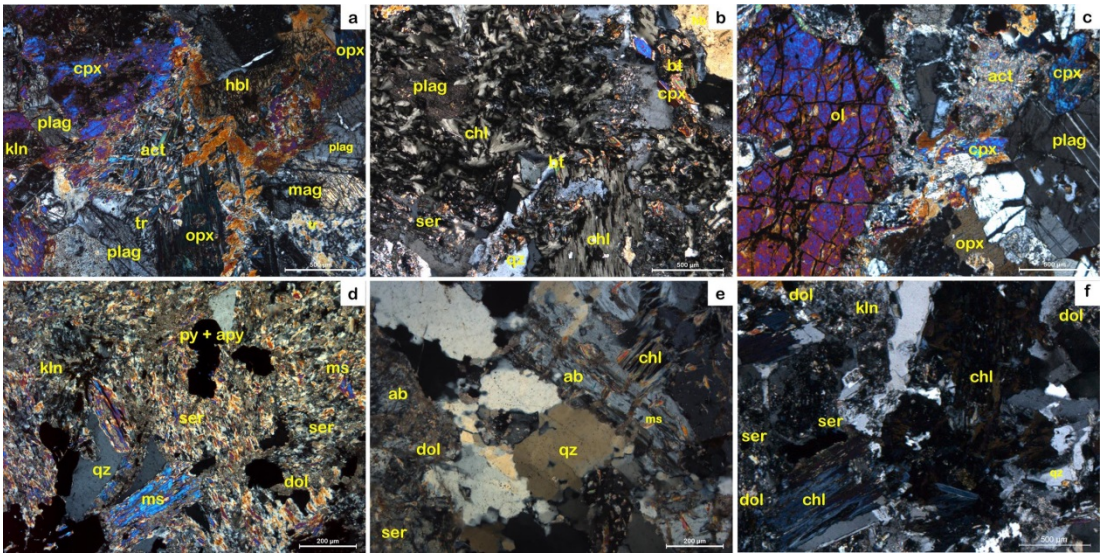

Figure 3.3 : a) Photomicrograph of mineral compositions of metagabbro; b) Plagioclase (plag), chlorite (chl), and hornblende (hb) with subordinate quartz (qz), biotite (bi), sericite (ser), and clinopyroxene (cpx) in dioritic rock; c) Cumulate olivine (ol) with plagioclase (plag), clinopyroxene (cpx), and orthopyroxene (opx) in olivine gabbronorite; d) Sericite (ser)/kaolinite (kln), muscovite (ms), quartz (qz), and pyrite (py)/arsenopyrite (apy) in the alteration zone 1; e) Quartz (qz), albite (ab), and chlorite (chl) with muscovite (ms), sericite (ser), and dolomite (dol) in the alteration zone 2; f) Chlorite (chl) and dolomite (dol) with sericite (ser), kaolinite (kln), and quartz (qz) in the alteration zone 3.

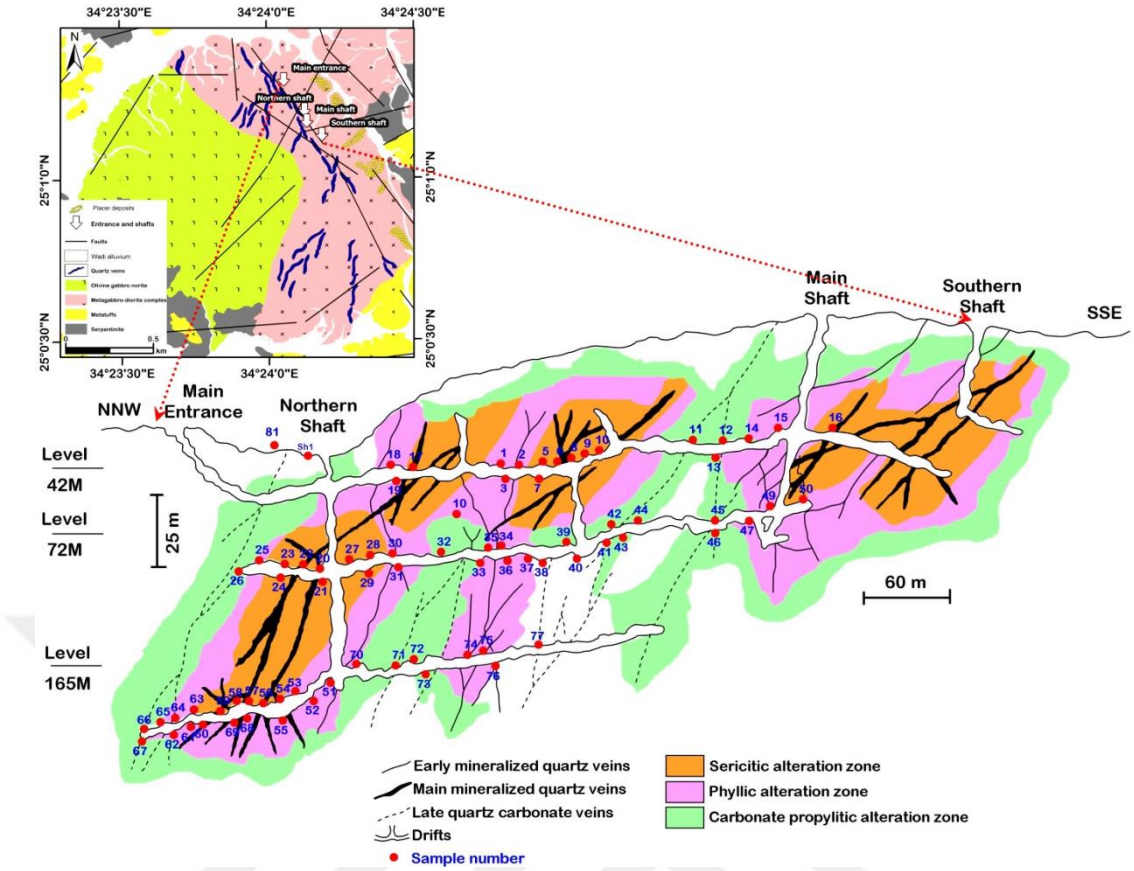

Figure 3.4 : Longitudinal section shows drifting of underground working of the Atud gold mine (traced quartz vein stages and alteration zones, after Gabra (1986); Harraz (1999); Abdelnasser and Kumral (2016)).

3.3.2 Quartz veins and their deformational textures

Three main type of quartz vein formed in three mineralization stage at Atud area suggesting by Harraz (2002) based on the textural relationships. Each quartz vein type has definitive characteristics as well as deformational texture types, as following:

(a) Early mineralized quartz veins are characterized by bluish- to dark-grey colored quartz ranging in thickness from few centimeters to one meter (Fig. 5a). They have subhedral medium to coarse grained quartz crystals with serrated grain boundaries (Figure 3.5b).

(b) Main mineralized quartz veins are closely associated with sericitic alteration zone and locally contain carbonate (Figures 3.4 & 3.5c-d). They are laminated (Figure 3.5d), exhibiting numerous features representative of ductile deformation (Figure 3.5e). Quartz occurs as coarse-grained subhedral crystals, traversed by a network of fine cracks commonly filled with milky quartz (Figure 3.5f). They also display undulate extinction and granulated grain boundaries. This refers to bulging

recrystallization (BLG) deformation with bulged and recrystallized subgrains along the boundaries of the original quartz grain boundaries (Figure 3.5g) that occurred at temperatures of around 280 to 400°C of Stipp et al. (2002): this is compatible with the formation temperature of this quartz type (270-490 °C), as confirmed by the fluid inclusion studies of Harraz (2002). Gold occurs as microscopic inclusions in arsenopyrite and pyrite in vein type.

(c) Late quartz-carbonate veins range in thickness from a few centimeters to 0.6 m thick post-dated all other quartz types, comprising milky quartz and calcite with pyrite (Figures 3.5h-i).

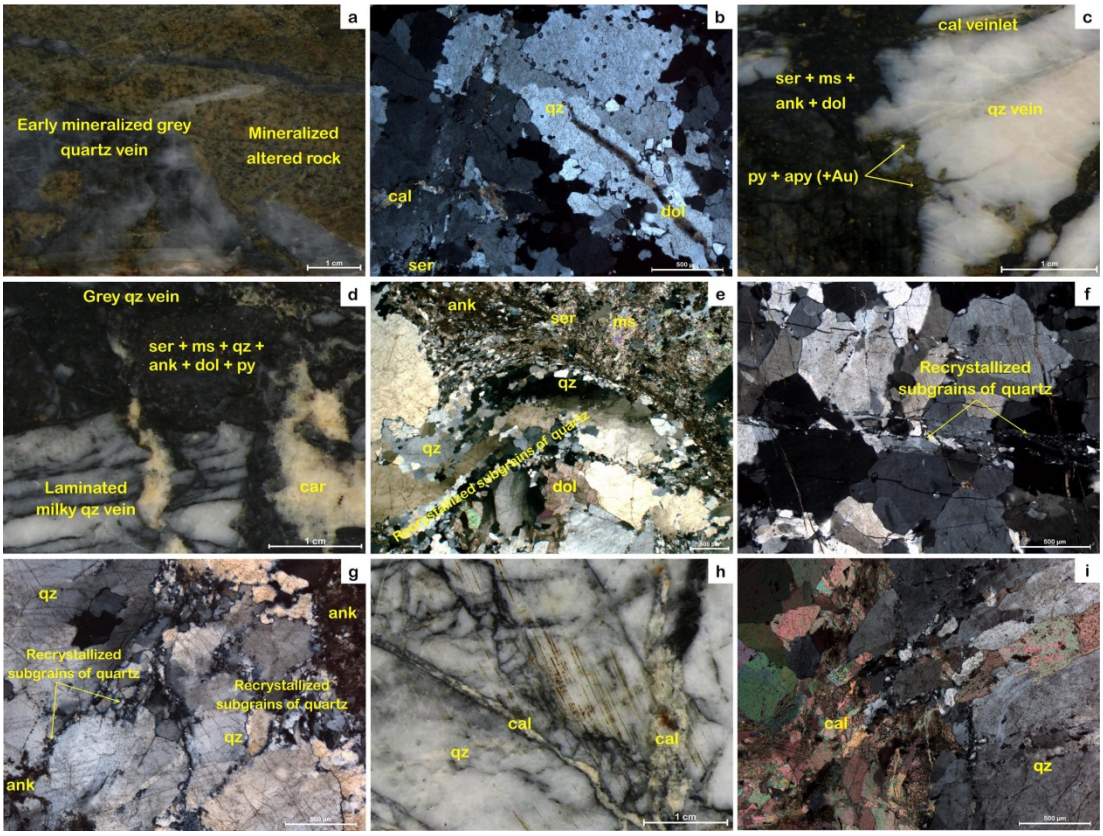

Figure 3.5 : a) Early mineralized grey quartz vein; b) Subhedral medium to coarse grained quartz (qz) crystals with serrated grain boundaries in the early mineralized quartz vein; c) Mineralization (pyrite-arsenopyrite-(±Au) along the contact between the main mineralized quartz vein (qz) and sericite (ser), muscovite (ms), ankerite (ank), and dolomite (dol) alteration types; d) Laminated main mineralized quartz vein; e) Main mineralized quartz vein affected by ductile deformation; f) A network of fine cracks filled with milky quartz cut through coarse-grained quartz crystals; g) Bulged and recrystallized subgrains along the boundaries of the original quartz grain boundaries; h); and i) Late quartz-carbonate vein.

3.4 Analytical methods

Field studies were carried out in order to collect representative samples of the host rocks, mineralized, and unmineralized veins in the Atud area in the Egyptian Eastern Desert. Sixty thin- and polished sections were examined petrographically.

3.4.1 Electron microprobe analyses (EMPA)

A subset of mineralized samples (Ten polished sections) was analyzed by scanning electron microscope (SEM) backscattered electron imaging. The ore mineral chemistry was investigated by wavelength-dispersive X-ray spectrometry at TU-Clausthal, Germany, using a Cameca SX100 four spectrometer and a fully automated electron microprobe. The sulfide minerals were analyzed under conditions of an accelerating voltage of 20 keV, a beam current of 40 nA and 10 sto 60 s counting times using a 2 μm beam diameter. Certified reference materials of natural and synthetic sulfides were used for calibration and quality control. The analyses were corrected for electron beam/matrix effects, instrumental drift, and dead time using a Phi-Rho-Z (CITZAF; Armstrong (1995)) scheme, as supplied with the Cameca SX100 electron microprobe. Based on the comparison between measured and published compositions of standard reference materials, the relative accuracy of the analyses is ~1–2% for concentrations >1 wt. % and ~5–10% for concentrations b1 wt. %.

3.4.2 Stable isotope analyses

Sulfide minerals for sulfur isotope analysis were separated from slightly crushed (40–60 mesh) lode samples. They were washed and hand-picked under a binocular microscope. Calcite also was separated for oxygen and carbon isotope measurements. These analyses were carried out in the SIRFER Stable Isotope Ratio Facility for Environmental Research laboratory at University of Utah by using EA-IRMS (Elemental Analysis-Isotope Ratio Mass Spectrometry) Techniques.

3.5 Results

3.5.1 Microprobe data of the ore mineral associated with gold mineralization

Ore mineralogy studies reported that the gold mineralization is associated with sulfide minerals; including arsenopyrite, pyrite, chalcopyrite, and sphalerite, with tetrahedrite. These minerals disseminated in the metasomatic hydrothermal alteration

zones and along the border of the mineralized quartz veins with the alteration zones within the altered metagabbro-diorite complex. Representative analyses of arsenopyrite, pyrite (type-I and II), chalcopyrite, sphalerite, tetrahedrite, and pyrrhotite are shown in Tables 3.1-3.7.

Arsenopyrite occurs as euhedral to subhedral individual prismatic zoned grains (Figure 3.6a). It is affected by shearing in the altered metagabbro-dioritic wall rocks (Figure 3.6a). Its back-scattered electron images (Figure 3.6b) show the oscillatory growth zoning reflecting variations in the As content. The compositional variations between the different zones seem relatively small (Table 3.1). It also occurs as rhombic grains disseminated in the quartz veins and wall rock associated and intergrown with type-II pyrite (As-bearing) (Figure 3.6c-d).

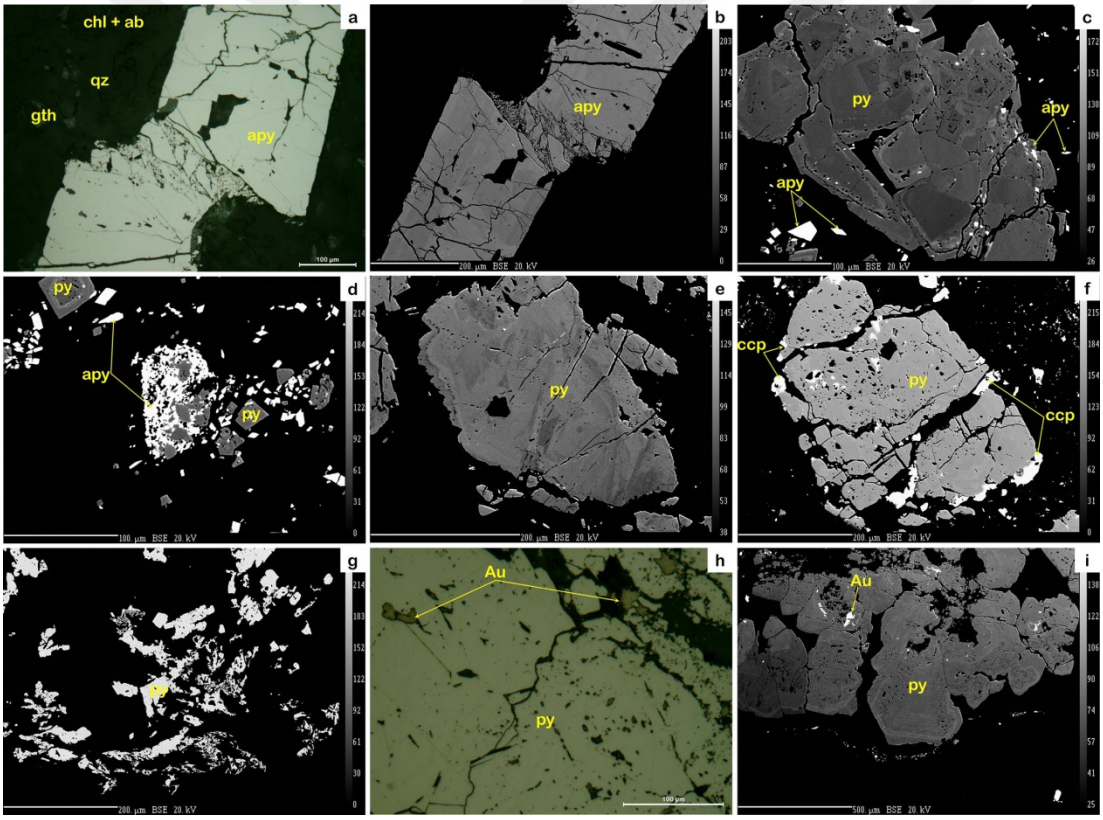

Figure 3.6 : a) Photomicrographs of reflected light microscopy shows shearing of prismatic grains of arsenopyrite (apy); b) Back-scattered electron image shows oscillatory and growth zoning in arsenopyrite (apy); c) and d) Intergrowth between arsenopyrite (apy) and type-I pyrite; e) Subhedral crystal of type-I pyrite (py); f) Type-II pyrite (py) replaced by chalcopyrite (ccp); g) Skeletal pyrite (py); h) and i) Inclusion of gold (Au) in type-II pyrite (py).

Pyrite represents the second mineral after arsenopyrite which carried gold as small inclusion. Based on the As content, two types of pyrite can be distinguished: type-I pyrite that is early pyrite and type-II pyrite that is late pyrite in the Atud gold deposit

distinguished by electron microprobe analyses (Tables 3.2-3.3). Type-I contains very low concentrations of As (Table 3.3), is optically homogeneous, and does not have any inclusions (Figure 3.6e) by contrast type-II pyrite is As-bearing (As contents up to 3.85 wt. %; Table 3.3). Type II pyrite is found associated with arsenopyrite and occurs disseminated in the host rocks and in the mineralized quartz veins (Figures 3.6c-d). Their grains are characterized by coarse-to-microcrystalline subhedral to anhedral zoned crystals replaced by chalcopyrite (Figure 3.6f). It also occurs as skeletal pyrite (Figure 3.6g). This pyrite has inclusions of gold (Figures 3.6h-i). Chalcopyrite, sphalerite, tetrahedrite, and pyrrhotite minerals occur associated with As-bearing pyrite and arsenopyrite (Tables 3.4-3.6 & Figures 3.7a-f).

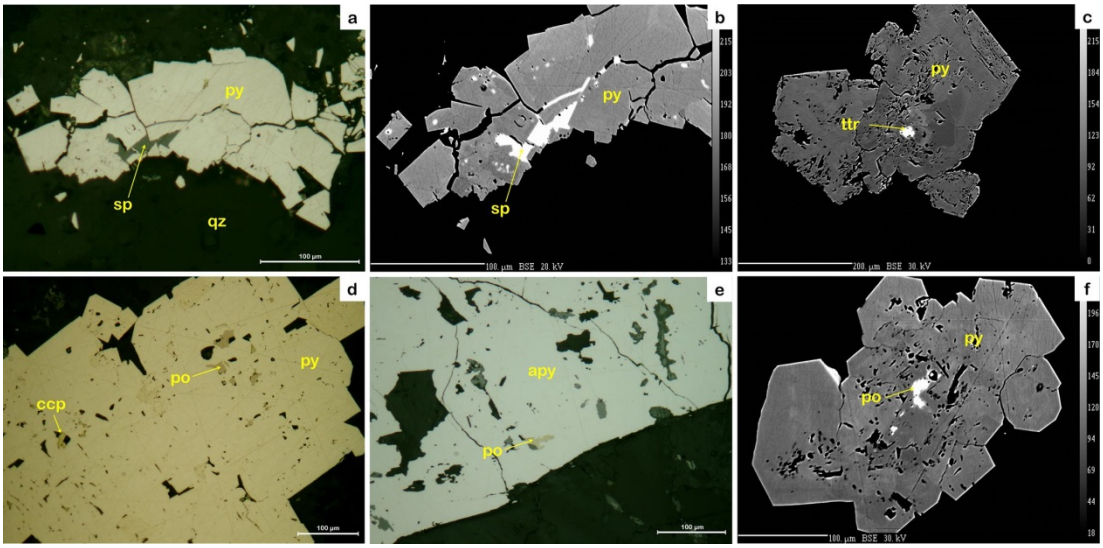

Figure 3.7 : a) and b) Inclusion of sphalerite (sp) in type-II pyrite (py); c) Tetrahedrite (ttr) inclusion in type-II pyrite (py); d) Inclusions of pyrrhotite (po) and chalcopyrite (ccp) in type-II pyrite (py); e) Pyrrhotite (po) inclusion in arsenopyrite (apy); f) Pyrrhotite (po) inclusion in type-II pyrite (py).

The paragenetic relationships between ore minerals and associated alteration minerals reveal three phases of the mineralization at Atud gold deposit (Figure 3.8). The first mineralization phase is characterized by the presence of euhedral arsenopyrite and type-I pyrite as well as large anhedral crystals of quartz in the early mineralized quartz veins. The second mineralization phase, which is considered to be the main mineralization phase, is characterized by the presence of chalcopyrite, sphalerite, tetrahedrite, and pyrrhotite associated with gold-bearing type-II pyrite (As-rich) and arsenopyrite. Recrystallized small polygonal subgrains of the secondary quartz were deposited with some carbonate minerals along the original quartz grain boundaries, forming thin veinlets during this stage. The third phase

seems to be a supergene overprint rather than a mineralization phase as a result of forming goethite minerals.

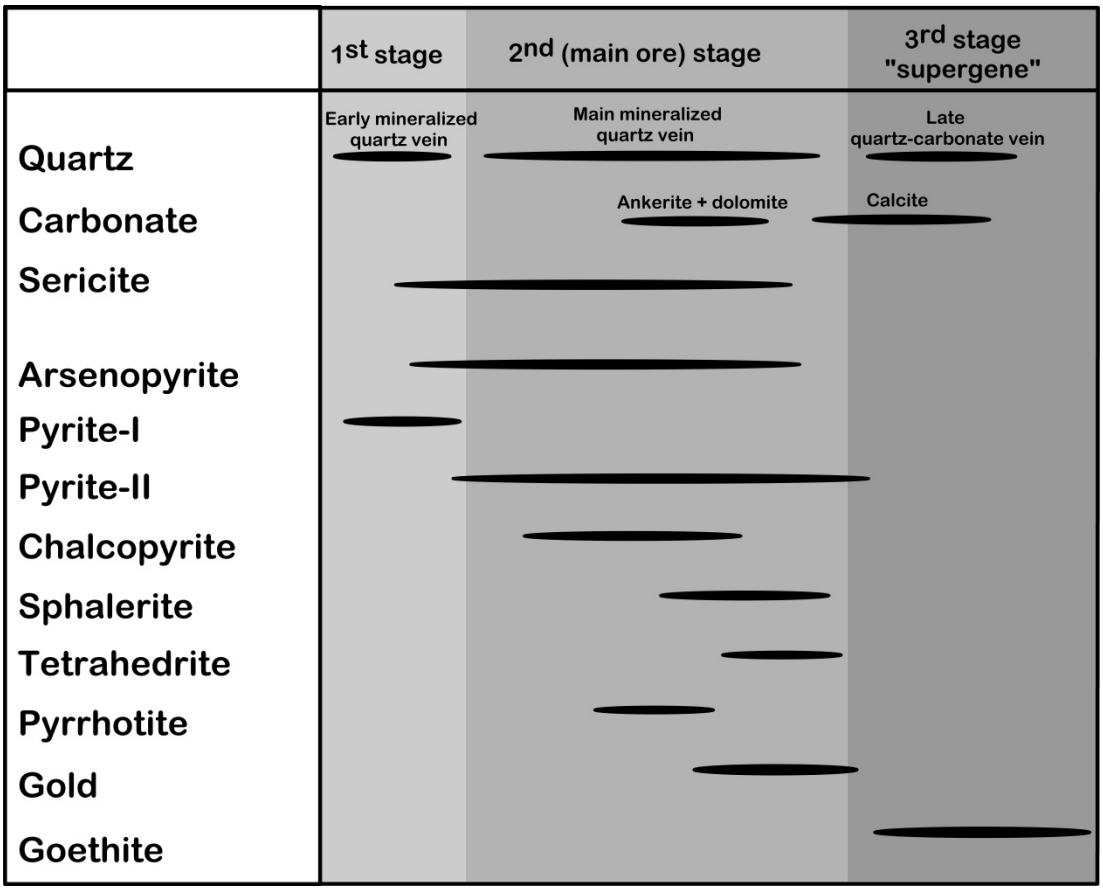

Figure 3.8 : Paragenetic sequence of quartz, carbonate, and sericite with sulfide minerals and supergene minerals as defined by mineral assemblages.

The chemical compositions of arsenopyrite (Table 3.1) reveal that their sulfur contents are negatively correlated with the arsenic contents (Figure 3.9a). It is considered to be a carrier of gold having Au content ranges from 0.04 to 0.21 wt. % (Table 3.1). Also, there is a negative correlation between Fe (Atomic %) and Au (Atomic %) revealing that the gold is substituted by Fe in the arsenopyrite (Wu and Delbove, 1989) (Figure 3.9b). The (Fe+S) versus As binary diagram (Yan et al., 2014) (Figure 3.9c) reveals that the samples of type-I pyrite minerals are plotted in the magmatic- and volcanic- hydrothermal gold deposits, while the type-II pyrite (late and As-rich) are mostly distributed in the fields of magmatic-, volcanic-, and metamorphic- hydrothermal gold deposits.

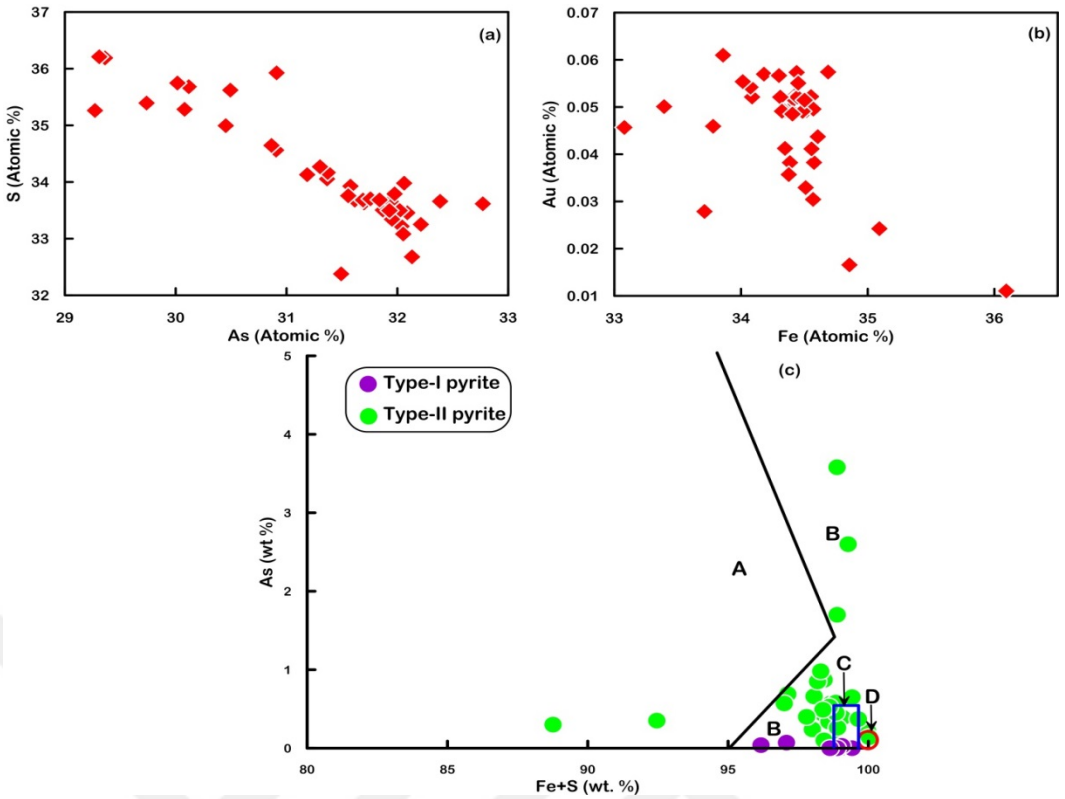

Figure 3.9 : a) Correlation between S (Atom. %) and As (Atom. %) in arsenopyrite in the altered wallrock in Atud area; b) Correlation between Fe (Atom. %) and Au (Atom. %) in arsenopyrite; c) Diagram of (Fe+S) versus As characteristics of pyrite in Atud gold deposits; A: Carlin-type gold deposits, B: magmatic hydrothermal gold deposits, C: volcanic hydrothermal gold deposits, and D: metamorphic hydrothermal gold deposits (after Yuan et al. (2012)).

Table 3.1 : Representative electron microprobe data for arsenopyrite from Atud gold deposit

Spot no.	**7 / 1 .**	**13 / 1 .**	**14 / 1 .**	**15 / 1 .**	**16 / 1 .**	**18 / 1 .**	**20 / 1 .**	**24 / 1 .**	**25 / 1 .**	**26 / 1 .**	**27 / 1 .**	**28 / 1 .**
wt. %			*Bright core*	*Less bright rim*	*Dark rim*							
S	19.66	20.74	20.04	19.98	20.31	19.70	20.22	19.80	19.79	19.83	19.46	20.08
Fe	34.02	35.73	35.89	35.71	35.78	35.65	35.70	35.44	35.37	35.42	35.42	35.36
Te	0.15	0.00	0.07	0.06		0.23	0.04	0.10	0.05	0.14	0.49	0.13
Cu	0.03	0.08										
Au	0.18	0.21	0.14	0.15	0.18	0.12	0.14	0.18	0.18	0.15	0.11	0.19
As	44.79	43.34	44.14	43.83	43.37	44.40	43.98	44.26	44.36	44.30	44.06	43.22
Ni	0.05	0.05	0.01	0.05	0.09	0.09	0.02	0.03	0.04	0.03	0.03	0.04
Ag	0.01	0.04	0.02	0.02	0.01	0.02	0.01	0.03	0.02		0.01	0.02
Sb	0.01	0.05		0.02	0.05		0.02				0.01	
Zn	0.03	0.17	0.01	0.02	0.01	0.01	0.03		0.01	0.01	0.02	
Total	98.93	100.41	100.32	99.84	99.80	100.22	100.16	99.84	99.82	99.88	99.61	99.04
atom %												
S	33.62	34.56	33.63	33.68	34.13	33.22	33.93	33.47	33.46	33.50	33.08	34.05
Fe	33.39	34.18	34.58	34.56	34.52	34.51	34.39	34.39	34.33	34.35	34.57	34.43
Te	0.06		0.03	0.03		0.10	0.02	0.04	0.02	0.06	0.21	0.06
Cu	0.03	0.07										
Au	0.05	0.06	0.04	0.04	0.05	0.03	0.04	0.05	0.05	0.04	0.03	0.05
As	32.77	30.91	31.70	31.62	31.19	32.04	31.58	32.01	32.09	32.02	32.05	31.37
Ni	0.05	0.05	0.01	0.05	0.08	0.08	0.02	0.03	0.04	0.03	0.03	0.04
Ag	0.01	0.02	0.01	0.01	0.005	0.01	0.005	0.02	0.01		0.01	0.01
Sb	0.005	0.02		0.01	0.02		0.01				0.004	
Zn	0.03	0.14	0.01	0.02	0.01	0.01	0.02		0.01	0.01	0.02	
Formula												
S	1.34	1.38	1.35	1.35	1.37	1.33	1.36	1.34	1.34	1.34	1.32	1.36
Fe	1.34	1.37	1.38	1.38	1.38	1.38	1.38	1.38	1.37	1.37	1.38	1.38
As	1.31	1.24	1.27	1.26	1.25	1.28	1.26	1.28	1.28	1.28	1.28	1.25

Table 3.1 : Continuous

Spot no.	7 / 1 .	8 / 1 .	9 / 1 .	10 / 1 .	13 / 1 .	14 / 1 .	14 / 1 .	15 / 1 .	18 / 1 .	1 / 1 .	4 / 1 .	7 / 1 .	8 / 1 .	9 / 1 .	10 / 1 .	11 / 1 .	20 / 1 .	21 / 1 .	22 / 1 .	29 / 1 .	33 / 1 .	37 / 1 .	39 / 1 .	40 / 1 .	1 / 1 .	3 / 1 .	5 / 1 .
wt. %																										
S	21.07	20.86	21.17	20.74	21.32	19.05	19.93	19.84	19.71	20.37	19.28	19.99	19.98	19.67	19.84	20.44	19.99	20.11	19.97	21.76	21.47	21.46	19.87	19.77	21.83	21.87	21.21
Fe	35.97	35.76	35.23	35.89	36.96	36.99	35.62	35.64	35.60	35.67	35.82	35.59	35.48	35.50	34.29	35.66	35.85	35.91	35.50	34.90	35.65	35.45	34.84	34.64	36.04	36.20	36.13
Te	0.00	0.01	0.03		0.02		0.03	0.02	0.16	0.13	0.04	0.02	0.00	0.01	0.13	0.07			0.10	0.05			0.01	0.00	0.01		0.03
Cu	0.09		0.01		0.05						0.06											0.02		0.02	0.01	0.01	
Au	0.21	0.21	0.19	0.19	0.09	0.04	0.19	0.19	0.18	0.18	0.06	0.19	0.19	0.20	0.10	0.18	0.18	0.16	0.13	0.17	0.20	0.17	0.20	0.22	0.21	0.18	0.19
As	41.37	42.42	41.76	43.18	41.36	43.30	43.82	44.10	44.14	43.71	44.30	44.02	44.31	44.53	43.75	43.63	44.53	43.93	44.11	43.75	42.13	42.93	43.94	44.45	41.39	41.37	42.26
Ni	0.01				0.04						0.05	0.01	0.03	0.01	0.14	0.01	0.01	0.01		0.01				0.01	0.03	0.01	0.00
Ag	0.00	0.01	0.03	0.01	0.07	0.01	0.01	0.00	0.01	0.02	0.02	0.02	0.01		0.03		0.03	0.01	0.04	0.01		0.02					0.02
Sb	0.07	0.09	0.02	0.02	0.47	0.02		0.01	0.01	0.01	0.41	0.01			0.04			0.03		0.01	0.23	0.06	0.30		0.10	0.02	0.12
Zn	0.01	0.01	0.02	0.01	0.03	0.01		0.01	0.01	0.00	0.01	0.01	0.01	0.02		0.02	0.02	0.01			0.01	0.01	0.03	0.01	0.01		0.01
Total	98.80	99.37	98.46	100.04	100.41	99.42	99.60	99.81	99.82	100.09	100.05	99.86	100.01	99.94	98.32	100.01	100.61	100.17	99.85	100.66	99.69	100.12	99.19	99.12	99.63	99.66	99.97
atom %																											
S	35.39	34.99	35.68	34.64	35.26	32.38	33.68	33.51	33.34	34.17	32.68	33.70	33.66	33.25	33.98	34.27	33.50	33.76	33.69	35.93	35.75	35.62	33.79	33.66	36.19	36.21	35.28
Fe	34.69	34.44	34.09	34.42	35.09	36.09	34.56	34.55	34.57	34.34	34.86	34.45	34.31	34.45	33.71	34.32	34.49	34.61	34.38	33.08	34.07	33.78	34.01	33.86	34.30	34.41	34.50
Te		0.004	0.01		0.01		0.01	0.01	0.07	0.05	0.02	0.01		0.004	0.06	0.03			0.04	0.02			0.004		0.004		0.01
Cu	0.08		0.01		0.04						0.05											0.02	0.00	0.02	0.01	0.01	
Au	0.06	0.06	0.05	0.05	0.02	0.01	0.05	0.05	0.05	0.05	0.02	0.05	0.05	0.06	0.03	0.05	0.05	0.04	0.04	0.05	0.05	0.05	0.06	0.06	0.06	0.05	0.05
As	29.74	30.45	30.12	30.87	29.27	31.49	31.69	31.87	31.95	31.37	32.13	31.76	31.94	32.21	32.06	31.30	31.93	31.56	31.84	30.91	30.02	30.49	31.98	32.39	29.36	29.31	30.08
Ni	0.01				0.04						0.05	0.01	0.03	0.01	0.13	0.01	0.01	0.01	0.00	0.01				0.01	0.03	0.01	
Ag		0.005	0.02	0.005	0.03	0.01	0.01		0.01	0.01	0.01	0.01	0.01		0.02		0.01	0.005	0.02	0.005		0.01					0.01
Sb	0.03	0.04	0.01	0.01	0.20	0.01		0.004	0.004	0.004	0.18	0.004			0.02			0.01		0.004	0.10	0.03	0.13	0.00	0.04	0.01	0.05
Zn	0.01	0.01	0.02	0.01	0.02	0.01		0.01	0.01		0.01	0.01	0.01	0.02	0.00	0.02	0.02	0.01			0.01	0.01	0.03	0.01	0.01		0.01
Formula																											
S	1.42	1.40	1.43	1.39	1.41	1.30	1.35	1.34	1.33	1.37	1.31	1.35	1.35	1.33	1.36	1.37	1.34	1.35	1.35	1.44	1.43	1.42	1.35	1.35	1.45	1.45	1.41
Fe	1.39	1.38	1.36	1.38	1.40	1.44	1.38	1.38	1.38	1.37	1.39	1.38	1.37	1.38	1.35	1.37	1.38	1.38	1.38	1.32	1.36	1.35	1.36	1.35	1.37	1.38	1.38
As	1.19	1.22	1.20	1.23	1.17	1.26	1.27	1.27	1.28	1.25	1.29	1.27	1.28	1.29	1.28	1.25	1.28	1.26	1.27	1.24	1.20	1.22	1.28	1.30	1.17	1.17	1.20

This refers to the sulfide minerals in the Atud gold deposit sulfide minerals deviate from juvenile magmatic and/or upper mantle sulfur to a likely metamorphic fluid source. Based on electron microprobe analyses, gold can be classified as electrum having Au ranging from 52.17-60.71 atom % and Ag ranging from 36.72-39.06 atom % (Table 3.7).

Table 3.2 : Representative electron microprobe data for type-I pyrite from Atud gold deposit

Spot no.	**4 / 1 .**	**1 / 1 .**	**2 / 1 .**	**4 / 1 .**	**5 / 1 .**	**3 / 1 .**	**9 / 1 .**	**19 / 1 .**	**20 / 1 .**
wt %									
S	52.02	52.84	52.03	51.89	52.16	52.40	52.34	52.17	51.98
Fe	47.26	46.61	47.32	47.05	47.26	47.33	47.22	47.20	46.90
Te	0.01	0.05				0.01	0.01	0.02	0.01
Cu	0.01			0.02				0.09	
Au	0.03	0.03							0.03
As	0.04					0.03	0.07		
Ni	0.01				0.01				
Ag	0.02	0.02	0.03	0.03	0.02	0.02	0.03	0.03	0.04
Sb				0.06					
Zn	0.02	0.02	0.01		0.01	0.01		0.02	
Total	99.42	99.57	99.39	99.05	99.46	99.80	99.67	99.53	98.96
atom %									
S	65.68	66.36	65.69	65.74	65.77	65.83	65.85	65.76	65.86
Fe	34.26	33.60	34.30	34.22	34.21	34.14	34.10	34.15	34.11
Te	0.003	0.02				0.003	0.003	0.01	0.00
Cu	0.01			0.01				0.06	
Au	0.01	0.01							0.01
As	0.02					0.02	0.04		
Ni	0.01				0.01				
Ag	0.01	0.01	0.01	0.01	0.01	0.01	0.01	0.01	0.02
Sb				0.02					
Zn	0.01	0.01	0.01	0.00	0.01	0.01	0.00	0.01	
Formula									
S	2.63	2.65	2.63	2.63	2.63	2.63	2.63	2.63	2.63
Fe	1.37	1.34	1.37	1.37	1.37	1.37	1.36	1.37	1.36

Table 3.3 : Representative electron microprobe data for type-II pyrite from Atud gold deposit

Spot no.	5/1.	6/1.	30/1.	3/1.	12/1.	15/1.	2/1.	7/1.	10/1.	16/1.	3/1.	12/1.	13/1.	16/1.	25/1.	26/1.	27/1.	28/1.	34/1.	35/1.	36/1.	38/1.	1/1.	2/1.	4/1.	5/1.	6/1.	7/1.	8/1.	9/1.	10/1.	2/1.	4/1.	6/1.	10/1.
wt %																																			
S	49.95	51.75	51.48	51.88	51.72	51.18	52.16	51.79	50.40	52.05	51.81	51.53	51.67	51.48	51.96	52.19	49.36	51.06	52.03	51.72	52.63	51.79	52.12	51.81	52.39	47.59	51.12	51.19	50.71	51.05	53.10	51.60	51.50	51.24	51.29
Fe	46.22	47.13	47.46	47.12	47.16	46.82	46.73	47.26	46.68	47.23	46.82	46.88	46.99	46.83	46.63	47.23	43.10	46.07	47.04	47.00	47.01	47.11	46.72	47.03	46.22	41.17	46.94	47.19	46.29	46.75	46.93	46.82	46.92	46.95	47.01
Te							0.01					0.01	0.01	0.03	0.02						0.02	0.05					0.01	0.02					0.02	0.02	
Cu	0.06		0.01				0.16				0.22	0.01		0.17	0.23	0.08	2.84	1.28			0.01	0.00	0.45	0.06	0.17	3.61		0.01	0.34	0.06	0.18				
Au	0.03	0.02	0.05	0.01	0.01	0.04	0.02	0.01	0.02		0.01	0.03		0.02	0.02	0.06	0.03	0.00	0.02			0.01	0.06	0.03	0.01	0.00	0.10	0.09	0.01	0.03	0.01	0.05	0.02	0.02	0.04
As	3.58	0.38	0.18	0.36	0.24	1.70	1.00	0.75	2.60	0.43	0.43	0.57	0.96	0.34	0.65	0.35	0.69	0.39	0.11	0.37	0.26	0.58	0.45	0.53	0.30	0.66	0.49	0.57	0.40	0.14	0.10	0.87	0.85	0.98	0.93
Ni	0.01		0.01	0.01							0.02	0.01	0.01	0.01	0.01		0.01	0.01	0.01		0.01		0.01	0.01	0.01	0.02		0.01	0.01			0.02			0.04
Ag	0.02	0.03	0.03	0.05	0.01	0.03	0.04	0.04	0.04	0.01	0.03	0.05	0.04	0.04	0.05	0.03	0.14	0.30	0.02	0.04	0.03	0.04	0.08	0.04	0.03	0.25	0.03	0.04	0.03	0.03	0.04	0.03	0.01	0.03	0.04
Sb										0.01	0.17	0.01		0.12	0.34	0.04	2.31	0.79					0.26	0.02	0.04	3.49			0.07	0.08	0.06				
Zn	0.02	0.02	0.02	0.02		0.01	0.01		0.01	0.03	0.06		0.01	0.04	0.03	0.02	0.35	0.31	0.01	0.02	0.01		0.07	0.02	0.03	0.41	0.01	0.01	0.06	0.04	0.03	0.03		0.01	0.01
Total	99.89	99.33	99.24	99.45	99.14	99.78	100.13	99.85	99.75	99.76	99.57	99.10	99.69	99.08	99.94	100.00	98.83	100.21	99.24	99.15	99.98	99.58	100.22	99.55	99.20	97.20	98.70	99.13	97.92	98.18	100.45	99.42	99.32	99.25	99.36
atom %																																			
S	63.98	65.51	65.30	65.57	65.55	64.94	65.60	65.35	64.34	65.58	65.52	65.46	65.34	65.43	65.56	65.62	64.39	64.82	65.78	65.57	65.99	65.47	65.56	65.50	66.17	63.85	65.28	65.15	65.27	65.42	66.19	65.41	65.35	65.16	65.15
Fe	33.99	34.25	34.56	34.19	34.31	34.11	33.74	34.23	34.21	34.16	33.99	34.19	34.11	34.17	33.78	34.09	32.27	33.57	34.14	34.20	33.84	34.19	33.74	34.13	33.51	31.71	34.41	34.48	34.20	34.39	33.58	34.07	34.18	34.28	34.28
Te							0.00					0.00	0.00	0.01	0.01						0.01	0.02					0.00	0.01					0.01	0.01	
Cu	0.04		0.01				0.10				0.14	0.01		0.11	0.15	0.05	1.87	0.82			0.01		0.29	0.04	0.11	2.44		0.01	0.22	0.04	0.11				
Au	0.01	0.00	0.01	0.00	0.00	0.01	0.00	0.00	0.00		0.00	0.01		0.00	0.00	0.01	0.01		0.00			0.00	0.01	0.01	0.00		0.02	0.02	0.00	0.01	0.00	0.01	0.004	0.00	0.01
As	1.96	0.21	0.10	0.19	0.13	0.92	0.54	0.40	1.42	0.23	0.23	0.31	0.52	0.18	0.35	0.19	0.39	0.21	0.06	0.20	0.14	0.31	0.24	0.29	0.16	0.38	0.27	0.31	0.22	0.08	0.05	0.47	0.46	0.53	0.51
Ni	0.01		0.01	0.01							0.01	0.01	0.01	0.01	0.01		0.01	0.01	0.01		0.01		0.01	0.01	0.01	0.01		0.01	0.01			0.01			0.03
Ag	0.01	0.01	0.01	0.02	0.00	0.01	0.01	0.02	0.02	0.004	0.01	0.02	0.02	0.02	0.02	0.01	0.05	0.11	0.01	0.02	0.01	0.02	0.03	0.02	0.01	0.10	0.01	0.02	0.01	0.01	0.01	0.01	0.00	0.01	0.02
Sb										0.003	0.06	0.00		0.04	0.11	0.01	0.79	0.26					0.09	0.01	0.01	1.23			0.02	0.03	0.02				
Zn	0.01	0.01	0.01	0.01		0.01	0.01		0.01	0.02	0.04		0.01	0.02	0.02	0.01	0.22	0.19	0.01	0.01	0.01		0.04	0.01	0.02	0.27	0.01	0.01	0.04	0.03	0.02	0.02		0.01	0.01
Formula																																			
S	2.56	2.62	2.61	2.62	2.62	2.60	2.62	2.61	2.57	2.62	2.62	2.62	2.61	2.62	2.62	2.62	2.58	2.59	2.63	2.62	2.64	2.62	2.62	2.62	2.65	2.55	2.61	2.61	2.61	2.62	2.65	2.62	2.61	2.61	2.61
Fe	1.36	1.37	1.38	1.37	1.37	1.36	1.35	1.37	1.37	1.37	1.36	1.37	1.36	1.37	1.35	1.36	1.29	1.34	1.37	1.37	1.35	1.37	1.35	1.37	1.34	1.27	1.38	1.38	1.37	1.38	1.34	1.36	1.37	1.37	1.37
As	0.08	0.01	0.00	0.01	0.01	0.04	0.02	0.02	0.06	0.01	0.01	0.01	0.02	0.01	0.01	0.01	0.02	0.01	0.00	0.01	0.01	0.01	0.01	0.01	0.01	0.02	0.01	0.01	0.01			0.02	0.02	0.02	0.02

Table 3.4 : Representative electron microprobe data for chalcopyrite from Atud gold deposit

Spot no.	1/1.	2/1.	3/1.	22/1.	31/1.	6/1.	11/1.	1/1.	4/1.	5/1.	6/1.	8/1.	11/1.	12/1.	13/1.	23/1.
wt %																
S	33.49	33.93	33.53	32.98	33.67	32.94	33.36	33.11	33.79	32.11	34.72	33.78	33.67	33.70	33.51	35.21
Fe	32.42	32.49	36.07	32.25	32.92	34.72	32.29	32.46	32.77	33.64	32.99	32.78	32.07	32.96	32.05	32.50
Te	0.01								0.01	0.02				0.01		
Cu	33.10	32.69	30.44	33.65	32.18	32.80	33.74	32.36	33.20	32.85	32.35	33.46	33.11	33.55	33.49	32.95
Au	0.03				0.02	0.01		0.04			0.03	0.02	0.03	0.04	0.02	0.01
As				0.03	0.03			0.14		0.03	0.05		0.03			1.11
Ni						0.01		0.03			0.01					0.02
Ag	0.01		0.03			0.01	0.05	0.08	0.01	0.02	0.03	0.04	0.03	0.03	0.02	1.28
Sb					0.04			0.51								14.15
Zn	0.01	0.04	0.01		0.03	0.06	0.03	0.03	0.01	0.02	0.03	0.02	0.02	0.03	0.03	1.96
Total	99.07	99.15	100.08	98.91	98.89	100.55	99.47	98.76	99.79	98.69	100.21	100.10	98.96	100.32	99.12	119.19
atom %																
S	48.66	49.11	48.17	48.16	48.91	47.42	48.38	48.46	48.71	47.20	49.57	48.60	48.92	48.43	48.68	46.30
Fe	27.04	26.99	29.75	27.03	27.45	28.69	26.88	27.27	27.12	28.39	27.04	27.07	26.75	27.19	26.73	24.53
Te	0.004								0.00	0.01				0.00		
Cu	24.27	23.87	22.06	24.79	23.58	23.83	24.69	23.90	24.15	24.36	23.31	24.29	24.27	24.33	24.55	21.86
Au	0.01				0.005	0.002		0.01			0.01	0.005	0.01	0.01	0.005	0.002
As				0.02	0.02			0.09		0.02	0.03		0.02			0.62
Ni						0.01		0.02			0.01					0.01
Ag	0.004		0.01			0.004	0.02	0.03	0.004	0.01	0.01	0.02	0.01	0.01	0.01	0.50
Sb					0.02			0.20								4.90
Zn	0.01	0.03	0.01		0.02	0.04	0.02	0.02	0.01	0.01	0.02	0.01	0.01	0.02	0.02	1.26
Formula																
S	1.95	1.96	1.93	1.93	1.96	1.90	1.94	1.94	1.95	1.89	1.98	1.94	1.96	1.94	1.95	1.85
Fe	1.08	1.08	1.19	1.08	1.10	1.15	1.08	1.09	1.08	1.14	1.08	1.08	1.07	1.09	1.07	0.98
Cu	0.97	0.95	0.88	0.99	0.94	0.95	0.99	0.96	0.97	0.97	0.93	0.97	0.97	0.97	0.98	0.87

Table 3.5 : Representative electron microprobe data for sphalerite and pyrrhotite from Atud gold deposit

	Sphalerite					**Pyrrhotite**		
Spot no.	**12/1.**	**19/1.**	**17/1.**	**3/1.**	**8/1.**	**17/1.**	**21/1.**	**23/1.**
wt %								
S	31.13	32.60	33.50	31.30	32.77	38.98	39.10	38.57
Fe	8.78	5.73	6.35	7.15	3.93	59.00	58.78	59.38
Te	0.03			0.01	0.01			
Cu	0.46	0.01	1.52	0.88	0.33			
Au	0.05	0.04	0.03		0.03	0.02	0.01	
As	1.03					0.03		0.03
Ni	0.01					0.56	0.16	0.09
Ag	0.02		0.05	0.04		0.03		
Sb	0.01		0.09					
Zn	59.12	61.20	58.35	60.06	62.00	0.02	0.01	0.01
Total	100.64	99.58	99.89	99.44	99.07	98.64	98.06	98.08
atom %								
S	47.26	49.46	50.32	47.92	49.95	53.26	53.61	53.04
Fe	7.65	4.99	5.48	6.28	3.44	46.28	46.26	46.87
Te	0.01			0.00	0.00			
Cu	0.35	0.01	1.15	0.68	0.25			
Au	0.01	0.01	0.01		0.01	0.00	0.00	
As	0.67					0.02		0.02
Ni	0.01					0.42	0.12	0.07
Ag	0.01		0.02	0.02		0.01		
Sb	0.00		0.04					
Zn	44.02	45.54	42.99	45.10	46.35	0.01	0.01	0.01
Formula								
S	1.89	1.98	2.01	1.92	2.00	2.13	2.14	2.12
Fe	0.31	0.20	0.22	0.25	0.14	1.85	1.85	1.87
Zn	1.76	1.82	1.72	1.80	1.85			

Table 3.6 : Representative electron microprobe data for tetrahedrite from Atud gold deposit

Spot no.	**8 / 1 .**	**11 / 1 .**	**29 / 1 .**	**2 / 1 .**	**5 / 1 .**	**6 / 1 .**	**14 / 1 .**	**17 / 1 .**	**18 / 1 .**	**19 / 1 .**	**30 / 1 .**	**31 / 1 .**	**32 / 1 .**	**1 / 1 .**	**3 / 1 .**	**4 / 1 .**	**5 / 1 .**
wt %																	
S	39.41	44.05	23.50	35.40	18.69	18.11	19.74	42.08	19.72	19.35	19.70	26.88	31.66	19.17	20.37	20.70	21.18
Fe	33.90	39.45	18.42	21.97	2.55	3.99	5.94	28.26	7.55	2.75	4.27	14.72	22.81	3.07	3.48	2.34	3.56
Te	0.02	0.03		0.01													
Cu	10.40	5.79	24.71	20.36	32.54	37.63	33.59	15.23	30.71	32.65	32.10	21.50	15.97	29.66	30.80	31.95	31.09
Au	0.01		0.01	0.09	0.03	0.03	0.06		0.03		0.01	0.02	0.02		0.03	0.05	
As	1.63	0.30	1.48	2.69	4.71	0.43	0.65	1.28	3.80	3.44	3.33	0.67	0.32	0.62	4.13	3.51	0.66
Ni	0.03	0.01	0.02	0.01				0.02					0.03				
Ag	0.05	0.06	0.07	1.54	2.04	2.81	2.23	0.54	1.42	2.86	2.63	2.08	1.69	3.38	3.45	2.19	4.77
Sb	13.22	7.60	27.16	14.84	33.73	32.14	33.89	9.53	33.47	33.24	32.18	31.32	18.35	32.48	32.67	33.32	32.83
Zn	1.67	0.91	3.10	2.40	5.33	4.53	3.66	1.84	3.50	4.74	4.63	3.33	2.53	4.75	4.52	5.02	5.74
Total	100.34	98.20	98.47	99.31	99.62	99.67	99.76	98.78	100.20	99.03	98.85	100.52	93.38	93.13	99.45	99.08	99.83
atom %																	
S	56.99	60.99	42.05	54.46	36.87	35.44	38.13	60.01	37.83	38.09	38.40	47.19	53.17	39.90	39.53	40.15	40.68
Fe	28.14	31.36	18.92	19.40	2.89	4.48	6.59	23.14	8.31	3.11	4.78	14.83	21.99	3.67	3.88	2.61	3.92
Te	0.01	0.01		0.00													
Cu	7.59	4.04	22.31	15.80	32.39	37.16	32.74	10.96	29.72	32.43	31.57	19.04	13.53	31.15	30.16	31.27	30.13
Au	0.00	0.00	0.00	0.02	0.01	0.01	0.02	0.00	0.01		0.00	0.01	0.01	0.00	0.01	0.02	
As	1.01	0.18	1.13	1.77	3.98	0.36	0.54	0.78	3.12	2.90	2.78	0.50	0.23	0.55	3.43	2.91	0.54
Ni	0.02	0.01	0.02	0.01				0.02					0.03				
Ag	0.02	0.02	0.04	0.70	1.20	1.63	1.28	0.23	0.81	1.67	1.52	1.09	0.84	2.09	1.99	1.26	2.72
Sb	5.03	2.77	12.80	6.01	17.52	16.56	17.24	3.58	16.91	17.23	16.52	14.48	8.12	17.80	16.70	17.02	16.60
Zn	1.18	0.62	2.72	1.81	5.16	4.35	3.47	1.29	3.29	4.58	4.43	2.87	2.08	4.85	4.30	4.77	5.41
Formula																	
S	2.28	2.44	1.68	2.18	1.47	1.42	1.53	2.40	1.51	1.52	1.54	1.89	2.13	1.60	1.58	1.61	1.63
Fe	1.13	1.25	0.76	0.78	0.12	0.18	0.26	0.93	0.33	0.12	0.19	0.59	0.88	0.15	0.16	0.10	0.16
Cu	0.30	0.16	0.89	0.63	1.30	1.49	1.31	0.44	1.19	1.30	1.26	0.76	0.54	1.25	1.21	1.25	1.21
As	0.04	0.01	0.05	0.07	0.16	0.01	0.02	0.03	0.12	0.12	0.11	0.02	0.01	0.02	0.14	0.12	0.02
Ag	0.0009	0.001	0.001	0.03	0.05	0.07	0.05	0.01	0.03	0.07	0.06	0.04	0.03	0.08	0.08	0.05	0.11
Sb	0.20	0.11	0.51	0.24	0.70	0.66	0.69	0.14	0.68	0.69	0.66	0.58	0.32	0.71	0.67	0.68	0.66
Zn	0.05	0.02	0.11	0.07	0.21	0.17	0.14	0.05	0.13	0.18	0.18	0.11	0.08	0.19	0.17	0.19	0.22

Table 3.7 : Representative electron microprobe data for gold (electrum) grains from Atud gold deposit

Spot no.	15 / 1 .	24 / 1 .	2 / 1 .
wt %			
S	0.20	0.07	0.04
Fe	2.67	1.88	0.80
Cu	0.01	0.01	0.01
Au	63.63	70.52	74.29
As	0.01	0.01	0.02
Ag	26.09	26.64	24.61
Total	92.61	99.13	99.77
atom %			
S	1.01	0.34	0.20
Fe	7.72	5.25	2.31
Cu	0.03	0.02	0.03
Au	52.17	55.84	60.71
As	0.02	0.02	0.04
Ag	39.06	38.52	36.72
Formula			
Au	2.09	2.23	2.43
Ag	1.56	1.54	1.47

3.5.1.1 The arsenopyrite geothermometer

Although arsenopyrite commonly displays zoning, its composition is indicative of the initial formation temperature (Kretschmar and Scott, 1976; Sharp et al., 1985). Therefore, these minerals can be used as a sliding-scale geothermometer to determine the temperature and activities of sulfur during the ore formation (Kretschmar and Scott, 1976). In the Fe-As-S system, the temperature and sulfur fugacity (f_{S2}) ranges are determined from the phase relations as well as sulfide mineral compositions (Figure 3.10) (Kretschmar and Scott, 1976). In the Atud gold deposit, the studied arsenopyrite coexists with Fe-sulfide minerals (pyrite-II and pyrrhotite) disseminated in the quartz veins and altered host rocks. It indicates the arsenic contents 29.3-32.7 atom % deposited with pyrite - based on the application of geothermometer of Kretschmar and Scott (1976) – under approximately 305-450 °C and Log f_{S2} values of -10.5 to -5.5 (Figure 3.10).

3.5.2 S, C, and O isotopic studies

The main aim of the stable isotope studies was to gain information on the source(s) of the hydrothermal fluid that caused the gold mineralization at Atud. The calculated fluid compositions will be compared to typical compositions from the

literature. Nesbitt (1991) and McCuaig and Kerrich (1998) stated that the sulfur and carbon have a wide range of isotopic data in the lode gold deposits referring to the interactions between the ore-forming fluids and the different types of host rocks. These interactions occurred along the pathways of the fluids where the fluid travels from their sources to the deposition of the gold-bearing ore systems (Ridley and Diamond, 2000; Dubé and Gosselin, 2007).

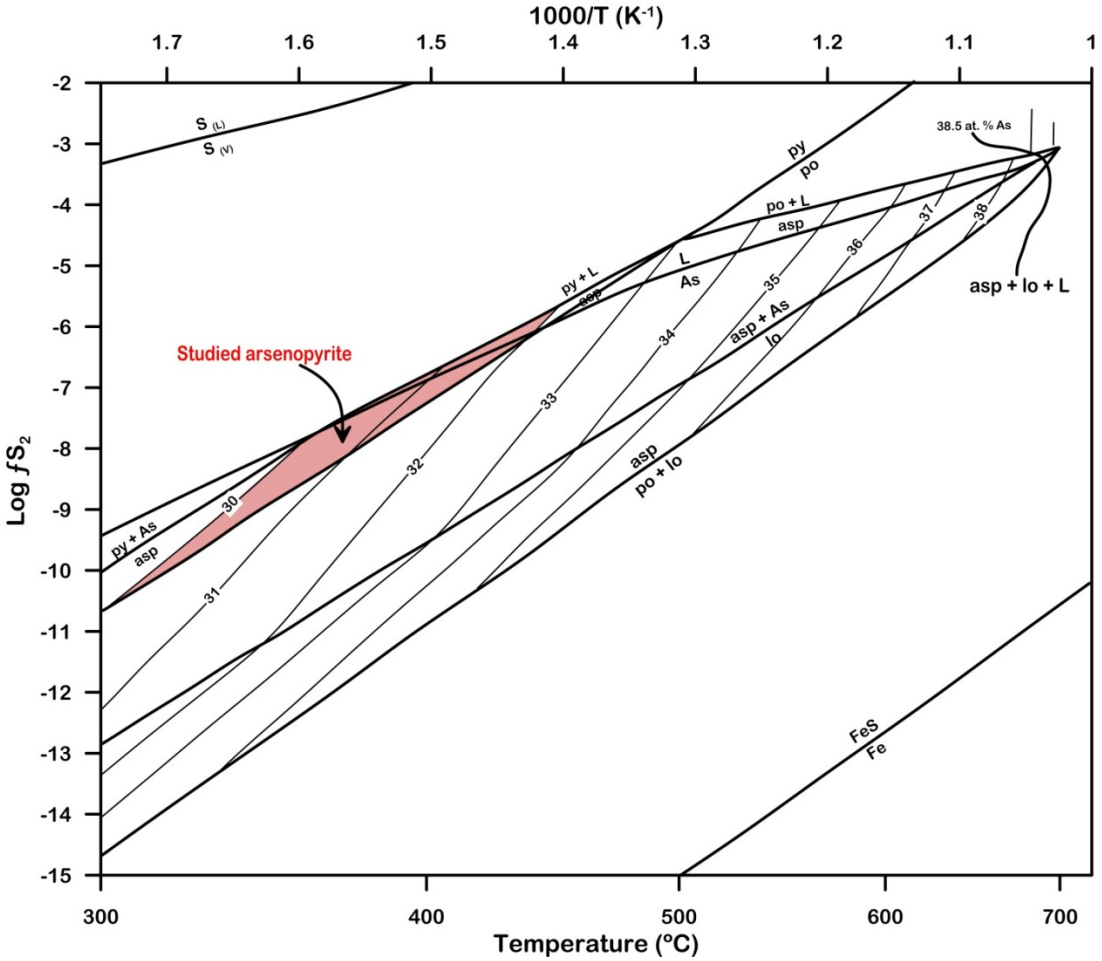

Figure 3.10 : Log fS_2-T projection of the stability of arsenopyrite contoured in at. % of As (Kretschmar and Scott, 1976). Stability field of arsenopyrite after Barton (1969) and arsenopyrite buffered curves from Kretschmar and Scott (1976), lines of pyrite-pyrrhotite after Scott and Barnes (1971), S_L-S_V after Braune and Peter (1951), and Fe-FeS after Robie and Waldbaum (1968).

3.5.2.1 $\delta^{34}S$ isotope of sulfides

The application of $\delta^{34}S$ isotope of the hydrothermal ore deposits reveals the origin of the sulfur in the sulfides and sulfates, the source of the ore-bearing hydrothermal fluid (Ohmoto and Rye, 1979), the formation temperature of the ore-forming fluids, water/rock ratio effective, and the ore deposition mechanism (Rollinson, 1993). The isotopic composition of hydrothermal sulfides is affected by some factors; the

isotopic composition of fluid that deposited these sulfides, their depositional temperature, and the pH and $f_{(O2)}$ values of the dissolved elements (Hoefs, 2008).

Ten samples of As-bearing pyrite (type-II) and arsenopyrite from the main mineralization phase were analyzed for $\delta^{34}S$ isotopes that are reported in Table 3.8. The $\delta^{34}S$ values of As-bearing pyrite (pyrite-II) in the altered wall rocks range 0.7 to 3.9 ‰$_{VCDT}$ and around 2.8 ‰$_{VCDT}$ in the mineralized quartz veins. While, the $\delta^{34}S$ values of arsenopyrite vary from 6.2 to 7.8 ‰$_{VCDT}$ and 8.3 to 9.5 ‰$_{VCDT}$ in the altered wall rocks and quartz veins, respectively (Figure 3.11a). By assuming the sulfur was mainly H_2S in the ore-forming fluids, the $\delta^{34}S$ values of the fluid were calculated from the $\delta^{34}S$ value of sulfide minerals based on fractionation equations of Czamanske and Rye (1974) and Ohmoto and Rye (1979) at depositional temperatures estimated from the chlorite thermometry (300 °C) (Abdelnasser and Kumral, 2016). The calculated $\delta^{34}S$ values of H_2S in the hydrothermal fluids range from -0.5 to 8.3‰ with an average 4.0 ‰ $_{VCDT}$ (Table 3.8 & Figure 3.11b) that represents the bulk sulfur isotope composition of the hydrothermal fluid ($\delta^{34}S_{\Sigma S}$).

Table 3.8 : Sulfur isotope values of sulfides from Atud gold deposit

Sample ID	Host	Mineral	Measured $\delta^{34}S$ (‰)	T (°C)[1)]	$\delta^{34}S_{H2S}$ (‰)[2)]
A34	wallrock	Pyrite	3.9	300.5	2.6
A47	wallrock	pyrite	2.4	300.5	1.2
ASh-1	wallrock	Pyrite	3.0	300.5	1.8
A53	wallrock	Pyrite	0.7	300.5	-0.5
AT68	quartz vein	Pyrite	2.8	300.5	1.5
A33	wallrock	Arsenopyrite	7.8	300.5	6.6
A39	wallrock	Arsenopyrite	7.5	300.5	6.3
A40	wallrock	Arsenopyrite	6.2	300.5	5.0
A60	quartz vein	Arsenopyrite	8.3	300.5	7.1
A66	quartz vein	Arsenopyrite	9.5	300.5	8.3

[1)] Based on the chlorite thermometry (Abdelnasser and Kumral, 2016)

[2)] Calculated by using the sulfur isotope fractionation equations in Czamanske and Rye (1974) and Ohmoto and Rye (1979)

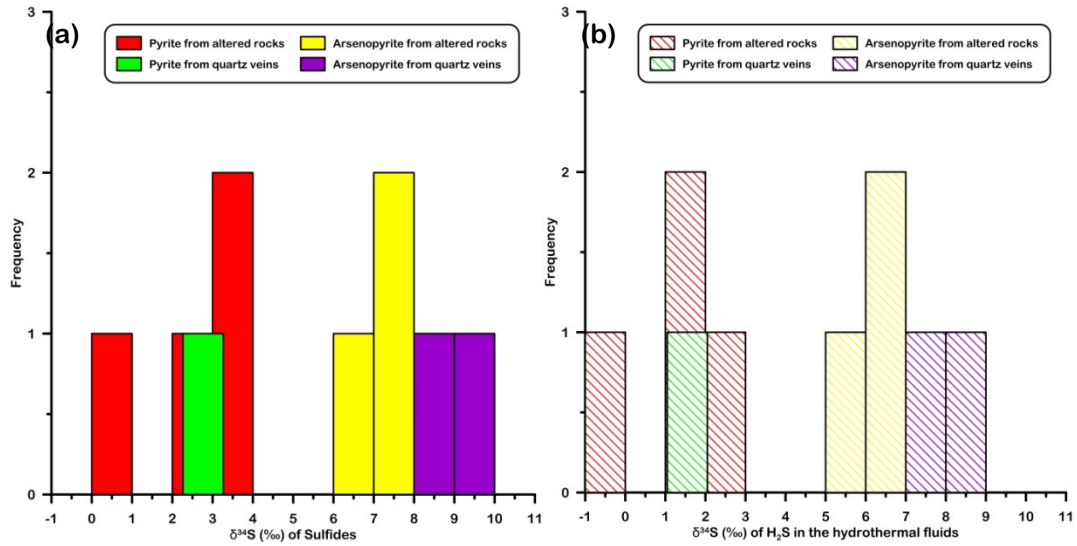

Figure 3.11 : Histograms showing the distributions of: a) the $\delta^{34}S$ isotopic compositions for sulfide minerals (pyrite and arsenopyrite); and (b) the $\delta^{34}S_{H2S}$ of the fluid that formed the sulfides of the Atud gold deposits.

3.5.2.2 $\delta^{13}C$ and $\delta^{18}O$ isotope compositions of carbonate minerals

Three calcite samples that are separated from the late-quartz carbonate vein formed during the mineralization stage at Atud area are analyzed for $\delta^{13}C$ and $\delta^{18}O$ isotope reported in Table 3.9. Their $\delta^{13}C$ values range from -10.6 to -8.0 $‰_{VPDB}$ with an average -8.9 $‰_{VPDB}$. Using the calcite-CO_2 fractionation equation of Ohmoto and Rye (1979), the fluid $\delta^{13}C_{CO2}$ values that are calculated at 300 °C (chlorite thermometry) range from -7.8 to -5.4 ‰. The $\delta^{18}O$ values for calcite range from 13.1 to 14.5 $‰_{SMOW}$ with an average 13.8 $‰_{SMOW}$. The fluid $\delta^{18}O_{H2O}$ values that are calculated based on the equation of oxygen isotopic fractionation of calcite-water of O'Neil et al. (1969) at 300 °C range from 12.8 to 14.1$‰_{SMOW}$ with an average 13.4 $‰_{SMOW}$.

Table 3.9 : Carbon and oxygen isotope values of calcite from Atud gold deposit

Sample ID	$\delta^{13}C_{VPDB}$ (‰)	$\delta^{18}O_{V\text{-}SMOW}$ (‰)	$\delta^{13}C_{CO2}$ (‰)[1)]	$\delta^{18}O_{H2O}$ (‰)[2)]
A60	-8.2	13.1	-5.4	12.8
AT68	-8.0	14.5	-5.2	14.1
A75	-10.6	13.7	-7.8	13.4

[1)] *Calculated based on Ohmoto and Rye (1979)*

[2)] *Equation of oxygen isotopic fractionation of calcite-water (O'Neil et al., 1969)*

3.6 Discussion

3.6.1Mechanism of Atud Au-precipitation

The wide range of depositional temperature (305-450 °C) and very low sulfur fugacity (Log f_{S2}) (-10.5 to -5.5) that resulted from the diagram of Kretschmar and Scott (1976), explain the hydrothermal fluid caused the intense wallrock sulfidation at the mineralization phase where high Au-concentration. Thereby S is removed from the fluid and Log f_{S2} decreases. The residual fluids that depleted in S have less capacity to form the hydrosulphide complexes AuHS° and $Au(HS)^-_2$ that responsible for transporting gold in the hydrothermal fluid, therefore the gold is precipitated due to increasing lack of the complexing ligands.

3.6.2 The geological implications of the S isotopic compositions

Many sources of sulfur in the ore-forming fluids with a definite $\delta^{34}S$ were identified by many authors; (a) a mantle or magmatic source having 0 ± 3 ‰ $\delta^{34}S$ value (Chaussidon and Lorand, 1990), (b) 0 to +9 ‰ $\delta^{34}S$ refers to the magmatic sources due to the dissolution or desulfidation of magmatic sulfides (McCuaig and Kerrich, 1998), (c) a seawater source having about +20 ‰ $\delta^{34}S$ value, and (d) strongly reduced sulfur in the sedimentary rocks having a large negative $\delta^{34}S$ values (Rollinson, 1993).

In the Atud gold deposit, the $\delta^{34}S$ values of the sulfides from the mineralized quartz veins that ranging from 2.8 – 9.5 ‰ are slightly closer to those from the altered metagabbro-dioritic rocks (0.7 – 7.8 ‰) suggesting uniform sulfur source having magmatic signatures. These magmatic signatures are further expected as most regional rocks are of igneous origin and the S could have been remobilized from sulfide minerals in these rocks during a metamorphic event. Furthermore, the S could originate from an igneous intrusion (gabbro-diorite intrusion at Gabal Atud) which must then be contemporaneous with the Atud gold mineralization. They are also comparable with sulfides derived from the magmatic and magmatic-hydrothermal fluids (–7.9 to +5.5‰ (Richards, 1995); 0 to +5 ‰ (Ohmoto and Goldhaber, 1997)) (Figure 3.12).

As well, the $\delta^{34}S$ values of H_2S (-0.5 to 8.3 ‰, average 4.0 ‰) in the ore fluids have a magmatic (mantle) source in which the sulfur is either sourced directly from a magma, remobilized from the magmatic rocks, or has an involvement of fluid with

an average crustal sulfur composition (Lambert, 1984). $\delta^{34}S$ signatures of the Atud gold deposit are comparable to the other intrusion-related gold deposits in Egypt (e.g., Um Eleiga deposit; Zoheir (2012a)) a light uniform sulfur source based on the $\delta^{34}S$ values of sulfide minerals indicating a magmatic source (Zoheir, 2012a) (Figure 3.12).

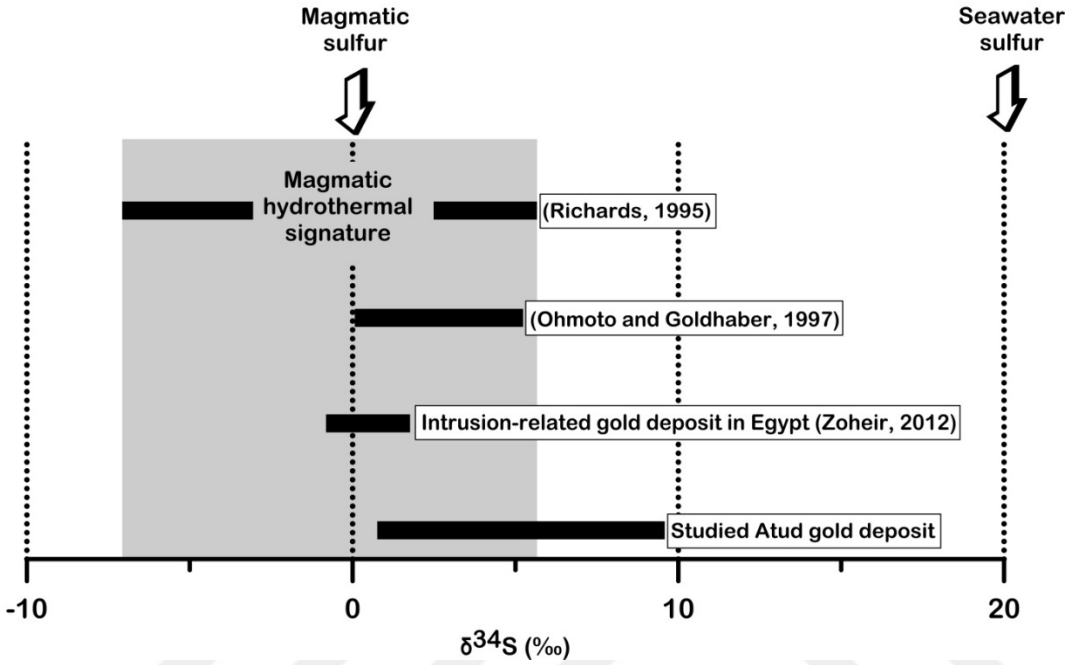

Figure 3.12 : $\delta^{34}S$ values of the Atud gold deposit and comparison with the magmatic-hydrothermal deposits.

3.6.3 Sources of carbon and hydrothermal fluid for the carbonate minerals

Carbon in hydrothermal fluids can have different sources depending on the following factors: (1) the isotopic composition of the fluid, (2) the equilibrium temperature, and (3) the Eh and pH functions of the carbon species in the source rocks and fluids (Bierlein et al., 2004). Exley et al. (1986) stated that the magmatic fluid $\delta^{13}C_{CO2}$ values typically range from -7.5‰ to -5.5‰ at which isotopic equilibrium fractionation between carbon dioxide and calcite occurred at ~270 °C. Also, Hoefs (1997) indicated the magmatic/mantle carbon dioxide has $\delta^{13}C$ value of -5 ‰. The calculated fluid $\delta^{13}C_{CO2}$ values (-7.8 to -5.4, for the temperature 300 °C of associated hydrothermal chlorite) consistent with a magmatic source for carbon.

The calculated fluid $\delta^{18}O_{H2O}$ values range between 12.8 and 14.1 $‰_{SMOW}$ indicating mixed magmatic and metamorphic sources of the hydrothermal fluid (Figure 3.13). This refers to the calcite at Atud area was formed hydrothermal fluids having mainly

magmatic mixed with variably metamorphic origin that is comparable with the intrusion-related gold deposits in Egypt of Zoheir (2012a); Zoheir and Moritz (2014).

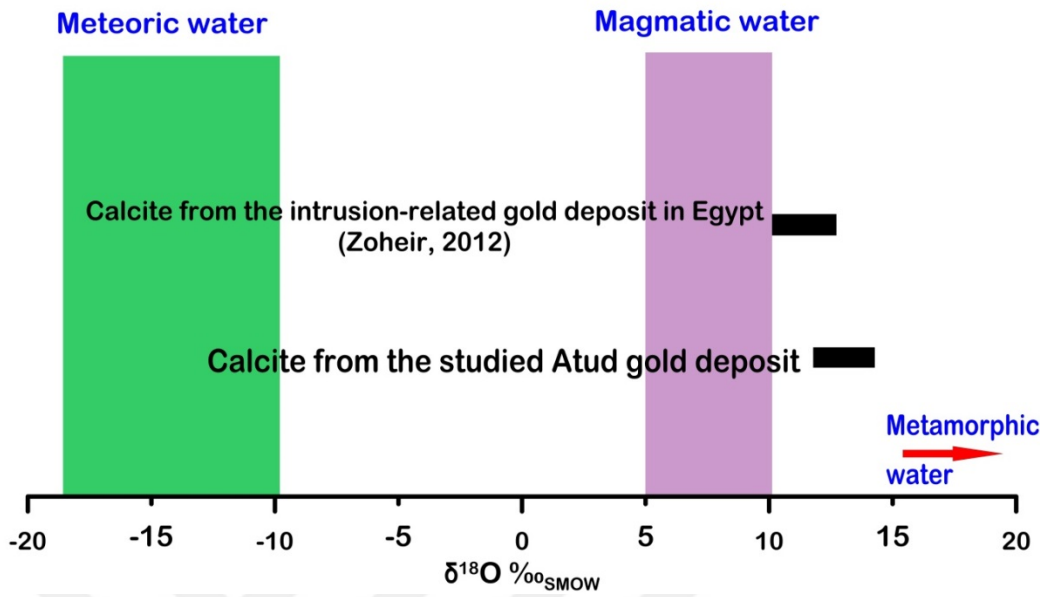

Figure 3.13 : $\delta^{18}O$ values of calcite from Atud gold deposit in comparison with some selected different fluid sources after Hoefs (1997).

3.7 Conclusions

The Atud gold deposit represents a mesothermal orogenic vein-type gold deposit hosted in the metagabbro-dioritic rocks in the Central block of the Egyptian Eastern Desert in the Arabian-Nubian Shield (ANS). The area around the Atud gold deposit is made up of a metagabbro-diorite complex that intruded serpentinites and their derivatives as well as metatuffs. This complex was later intruded by the olivine gabbronorite rocks. The auriferous quartz veins, which are younger than the intrusion of the olivine gabbronorite rocks, are linked to the system of NW-SE shear zones. Early mineralized quartz veins, main mineralized quartz veins, and late quartz-carbonate veins represent the different types of quartz veins in the study area formed during three mineralization stages. Deformational textural studies of the main mineralized quartz veins suggested that these veins were formed under temperatures of 280 to 400°C, as suggested by Stipp et al. (2002).

Euhedral arsenopyrite and type-I pyrite formed together with large anhedral quartz crystal within the early mineralized quartz veins and altered host rocks in the first phase of mineralization. Gold-bearing type-II pyrite (As-rich) is associated with subordinate chalcopyrite, sphalerite, tetrahedrite, and pyrrhotite with recrystallized

small polygonal quartz subgrains were deposited along the original quartz grain boundaries during the second phase of mineralization. Under supergene conditions, the goethite was formed. Gold is classified as electrum (52.2 to 60.7 atom % Au & 36.7 to 39.1 atom % Ag). Based on the application of geothermometer of Kretschmar and Scott (1976), As-contents (29.3-32.7 at. %) in arsenopyrite point to deposition in the f_{S2} and T ranges of -10.5 to -5.5 and 305-450 °C, respectively during the main mineralization phase. This indicates that the gold is transported and precipitated due to increasing lack of the hydrosulphide complexes AuHS° and $Au(HS)^-_2$.

The $\delta^{34}S$ values of the sulfides indicate they are formed from magmatic fluids in which the sulfur is either sourced directly from magma, remobilized from the magmatic rocks or has an involvement of fluid with an average crustal sulfur composition. While the carbon and oxygen isotopic compositions of calcite reveal that this calcite formed from fluids having magmatic mixed with metamorphic signatures.

4. REE GEOCHEMICAL BEHAVIOR AND ASTER-BASED IMAGE PROCESSING OF THE HYDROTHERMAL ALTERATION ASSOCIATED WITH ATUD GOLD DEPOSIT, CENTRAL EASTERN DESERT OF EGYPT

4.1 Introduction

The geochemical behavior of rare earth elements (REEs) in igneous and metamorphic rocks in is significantly affected by the different types of hydrothermal alteration and ore formation (Lottermoser, 1992). The extent to which the rock chemistry is changed is dependent on factors including fluid-rock interaction, pressure-derived percolation, variations in physicochemical condition of the fluid and chemical activity of the rock (Lottermoser, 1992). Distributions of the REE in the hydrothermal minerals are also influenced by the destabilization of the REE complexes and by their concentrations in the host rocks. The study of the REE patterns in altered rocks is commonly regarded as an efficient index in referring to the fluid source and to understand the hydrothermal alteration evolution.

Remote sensing imagery processing can use the spectral signatures of hydrous, iron oxides and carbonate minerals for detecting hydrothermal alteration haloes associated with hydrothermal ore deposits. Detection of iron oxides (e.g. hematite, goethite, jarosite) and greisen associated with some rare earth elements (REEs) are possible in the three VNIR (Hunt et al., 1973; Rowan et al., 1986). On the other hand, Al-OH, Fe, Mg-OH, Si-O-H, and CO_3 absorption features are best visualized in the six SWIR bands (1.65-2.45 lm region; Abrams and Hook (1995)). Alunite, kaolinite, calcite, dolomite, chlorite, talc, muscovite, and many other mineral groups can be detected in arid regions by processing the ASTER SWIR bands (Rowan et al., 2003; Rowan and Mars, 2003; Ducart et al., 2006; Mars and Rowan, 2006; Rowan et al., 2006; Di Tommaso and Rubinstein, 2007; Sanjeevi, 2008).

Intrusion-associated gold occurrences in Egypt are related to silicified shear zones cutting the Neoproterozoic basement rocks (Klemm et al., 2001). The Atud gold deposit in the Central Eastern Desert of Egypt is related to mesothermal quartz-

sulfide veins cutting a gabbroic-dioritic intrusion and are controlled by NW-SE brittle-ductile shear zones (Harraz, 1999; Harraz, 2002). Gold contents vary from traces up to 31g/t in the quartz-sulfide veins (Gabra, 1986). In the mine area, 1600 t of dump @ 12.4 g/t are left behind when the mining activity ceased in the mid-20th century (Hussein and El Sharkawi, 1990).

In this chapter, a new whole-rock geochemical data set and ASTER imagery data processing are integrated to delineate the hydrothermal alteration haloes associated with gold-bearing quartz veins in Atud gold mine. A little more detail, this chapter also deals with REE geochemical behavior of the different alteration types associated with the Au-mineralization at the study area. In addition, the ASTER image processing includes different methods; ASTER-imagery band rationing (BR), relative absorption band depth (RBD), principal component analysis (PCA), false-color composite (FCC), and some mineral indices [e.g. OH-bearing minerals (OHI), kaolinite (KLI), sericite (SRL), and calcite (CLI) indices].

4.2 Materials and methods

Samples of the host rocks and ore bodies were collected during a number of field trips to the mine area. Major elements analysis by XRF and trace and rare earth elements by ICP-MS were carried out on 41 samples in the Geochemistry Research Laboratories of Istanbul Technical University (ITU/JAL), Istanbul, Turkey. The used instruments are BRUKER S8 TIGER model X-ray fluorescence spectrometer (XRF) with a wavelength range from 0.01–12 nm, and an ELAN DRC-e Perkin Elmer model-Inductively Coupled Plasma/Mass Spectrometry (ICP-MS).

For mapping hydrothermal alteration types and mineral assemblages, ubsets of ASTER level 1B and cloud-free images (Granules ID: AST_L1B 00304012005082957 and 20120119100432 acquired on 01/04/2005) were processed by using ENVI software v.4.8. The image processing techniques applied include band rationing (BR), relative absorption band depth (RBD), principal component analysis (PCA), False-Color Composite (FCC) images, and various mineral indices (OHI, KLI, SRI, and CLI).

4.3 Geological setting

Field and petrographic studies reveal that the Atud mine area (Figure 4.1a) is made up of a metagabbro-diorite intrusion intruded into serpentinite and metatuffs and is cut by a younger intrusion of olivine gabbronorite (Figure 4.1b).

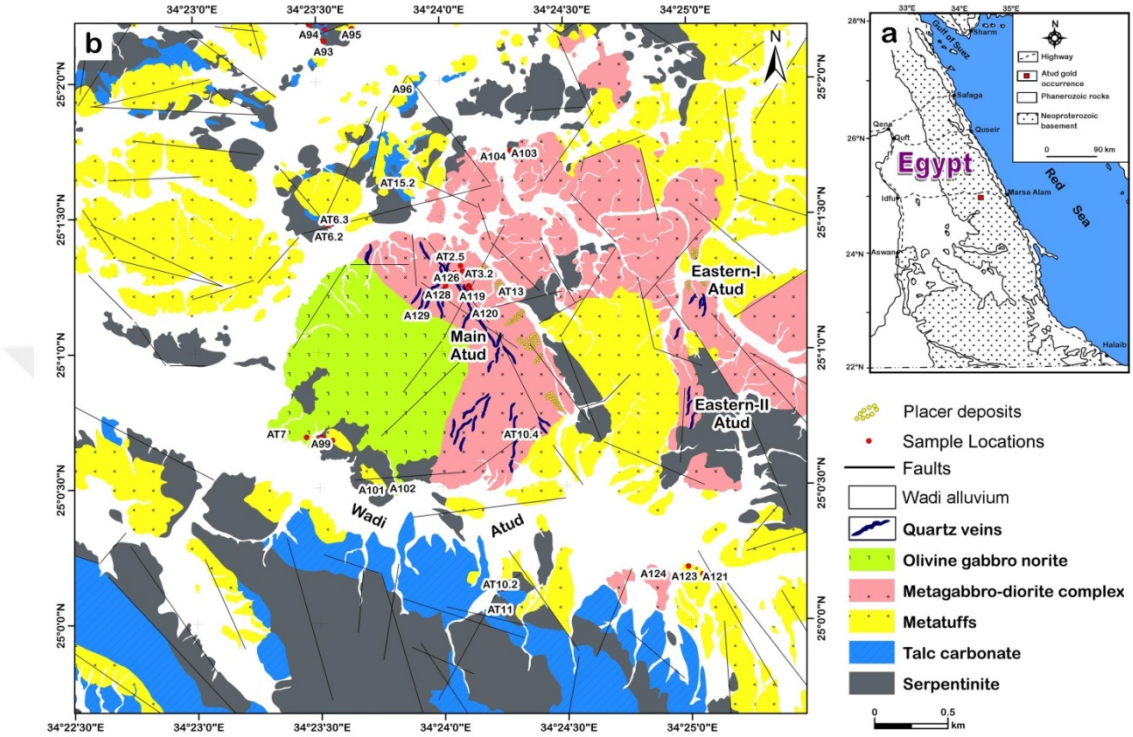

Figure 4.1 : a) Location map of Atud gold mine in the Central Eastern Desert of Egypt; b) Geological map of the study area (modified from Gabra (1986); Harraz (1999); Abdelnasser and Kumral (2016)).

The dispersed talc-carbonate, dolomitic marble, and calc-silicate rocks are derivatives of serpentinite around Gabal Atud (Figures 4.1b & 4.2a). The large serpentinite masses crop out south and southeast of Gabal Atud and are associated with the talc serpenitintes and talc carbonate rocks (Figure 4.2b). Serpentinite is tectonically incorporated in the metatuffs (Figure 4.2c). It is composed mainly of antigorite with subordinate amounts of tremolite, actinolite, graphite, and chromite (Figure 4.2d). Talc-carbonate (Figure 4.2e) covers a vast area in the southern part of the study area and occurs in association with metatuffs and serpentinite (Figures 4.1b & 4.2b-c). At the southern slope of Gabal Atud, small isolated masses of dolomitic marble occurred with the metagabbro-diorite rocks (Figure 4.2f). These marble blocks contain mainly dolomite with disseminated chromite and goethite (Figure 4.2g). On the other hand, calc-silicate rocks are associated with metatuffs at the

northern part of the mine area (Figure 4.2h). These rocks consist mainly of ankerite, calcite, and quartz with minor amounts of clinochlore, epidote, and chromite (Figure 4.2i).

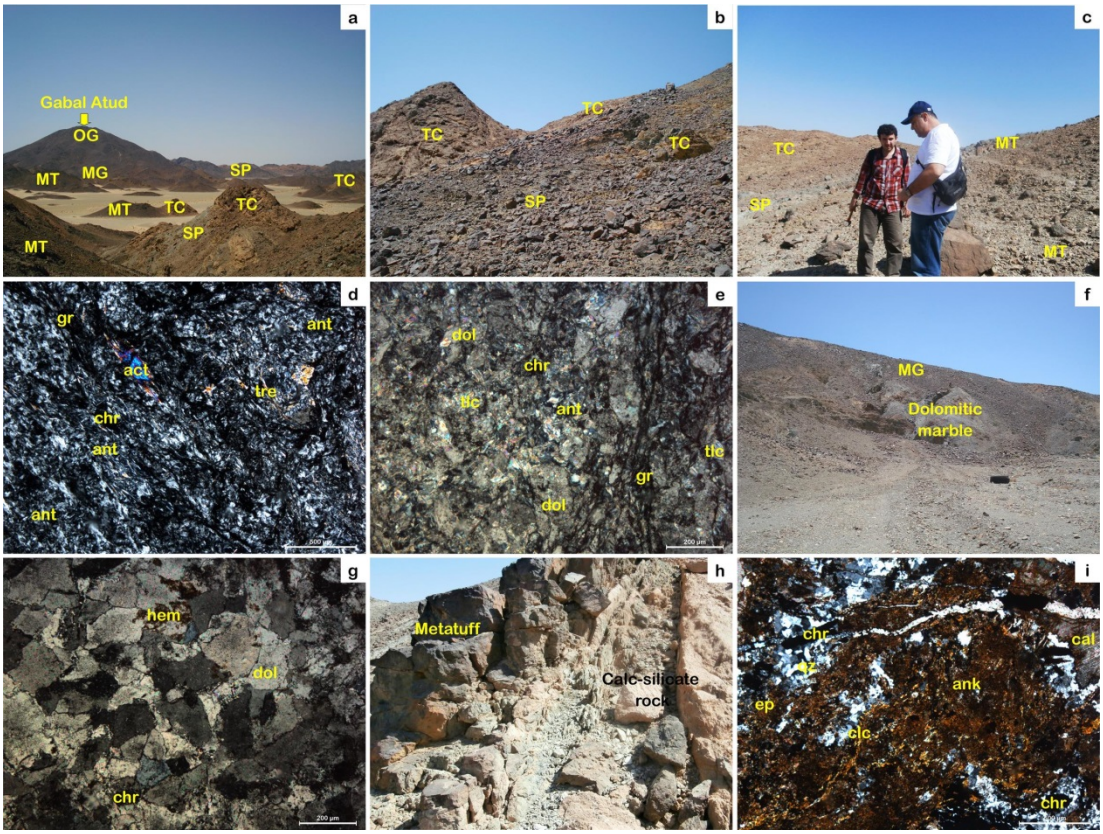

Figure 4.2 : a) Serpentinites (SP) and their derivatives (talc-carbonate; TC) occurred with the metatuffs (MT) around the metagabbro-diorite complex (MG) and olivine gabbro norite (OG) of Gabal Atud; b) Serpentinites (SP) associated with talc carbonate rocks (TC); c) Serpentinites (SP) and talc carbonate rocks (TC) incorporated with metatuffs at the southern part of the study area; d) Photomicrograph of antigorite (ant) with subordinate tremolite (tre), actinolite (act), graphite (gr), and chromite (chr) in serpentinite rock; e) Talc (tlc) and dolomite (dol) with less amount of antigorite (ant), graphite (gr) and chromite (chr) in talc-carbonate rock; f) Dolomitic marble at the southern slope of Gabal Atud; g) Mineral composition of dolomitic marble; h) Calc-silicate rocks associated with intermediate metatuffs at the northern part of the study area; i) Ankerite (ank), and quartz (qz) with calcite (cal), clinochlore (clc), epidote (ep), and chromite (chr) in the calc-silicate rock.

Metatuffs cover a vast area of the area around Gabal Atud where they form low-relief terrane (Figure 4.1b). These rocks are fine-grained mafic lapilli metatuffs, intermediate metatuffs, metacherts, and quartz-biotite schists (Abdelnasser and Kumral, 2016). Mafic lapilli metatuffs occur in Wadi Atud at the southern part of the study area and are associated with talc-carbonate and serpentinite (Figure 4.3a). They are composed mainly of plagioclase and microperthite, tremolite, clinopyroxene,

clinozoisite, and magnetite phenoblasts in a microcrystalline tuffaceous matrix (Figure 4.3b). The intermediate metatuffs occur in the northern part of the study area, where these rocks are associated with the calc-silicate rocks (Figure 4.2h). These tuffs are composed of microperthite, phlogopite, and quartz with biotite and magnetite embedded in a very fine groundmass (Figure 4.3c). Metachert is observed at the southern slope of Gabal Atud, where it forms alternated quartz- and feldspar-rich laminations (Figure 4.3d). Quartz-biotite schists form strongly foliated outcrops at the southern slope of Gabal Atud and are dissected by NW-trending faults (Figure 4.3e). It is made up of quartz and biotite with K-feldspar and minor amounts of muscovite, carbonate, and magnetite (Figure 4.3f).

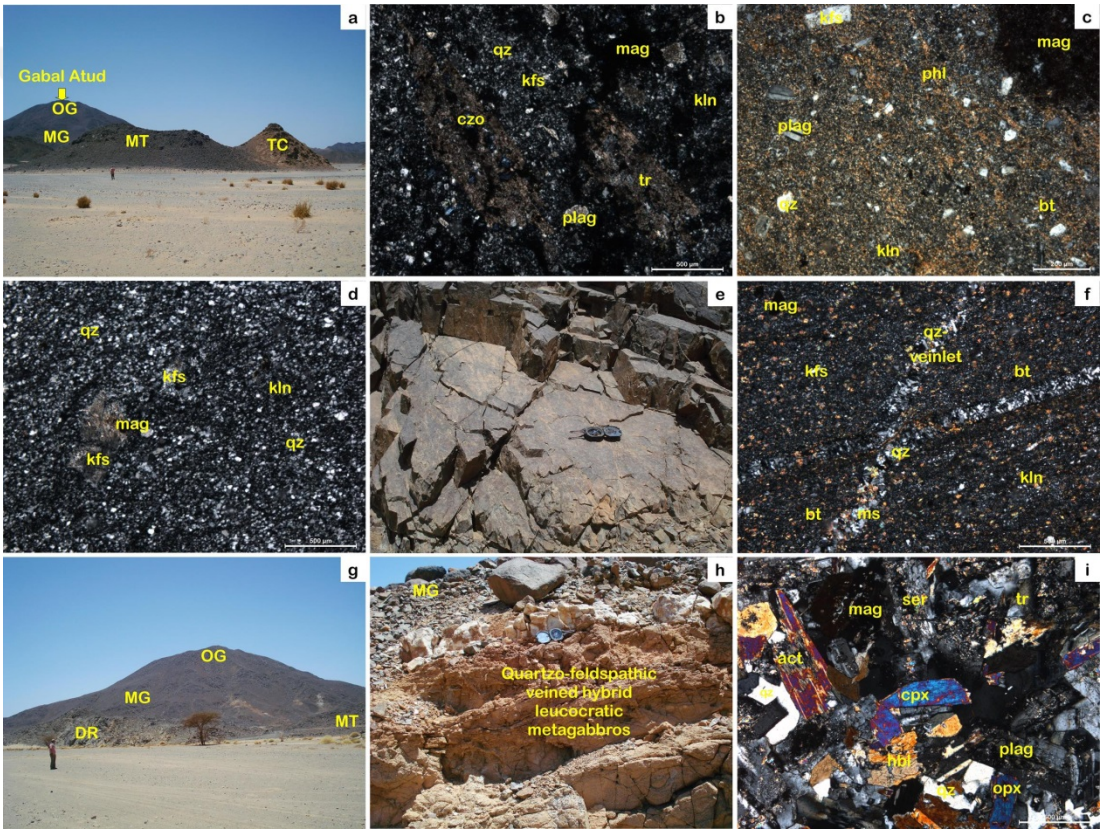

Figure 4.3 : a) Mafic lapilli metatuffs occurred with the talc-carbonate and serpentinite rocks at Wadi Atud; b) Kaolinitized plagioclase (plag) and microperthite (kfs) with clinozoisite (szo) and magnetite (mag) in a microcrystalline tuffaceous matrix in mafic lapilli metatuffs; c) Photomicrograph of mineral compositions of intermediate metatuffs; d) Irregularly quartz-rich and feldspar-rich banded laminae in metachert; e) Faulting (N 30° W dipping 20° toward SE) affected on quartz biotite schists at the southern slope of Gabal Atud; f) Quartz veinlets cut through the quartz biotite schists; g) Metagabbro (MG) and dioritic rocks (DR) were intruded by olivine gabbronorite (OG) at Gabal Atud; h) Quartzo-feldspathic veined hybrid leucocratic metagabbros occurred in-between metagabbro (MG) and dioritic rocks at Gabal Atud; i) Mineral composition of metagabbro.

The main body of Gabal Atud is made up of gabbro-diorite intrusion assumed to belong to the Neoproterozoic island arc assemblage in the Egyptian basement complex. It forms a semicircular body cuts the pre-existing country rocks serpentinite and metatuff and shows a sharp intrusive contact against them. This intrusion is in turn cut by a late-tectonic olivine gabbronorite (Figures 4.1b & 4.2a). Slightly metamorphosed gabbro and diorite rocks and hybrid leucocratic gabbro zone in between are exposed at Gabal Atud (Figures 4.3g-h). The gabbro-diorite complex intrusion forming Gebel Atud is cut by numerous mineralized and barren quartz veins and dikes at its eastern and southeastern slopes, where NW-SE brittle-ductile shear zone cuts through this complex (Figure 4.1b). The metagabbroic rocks are composed essentially of calcic plagioclase (variably sericitized, and kaolinitized), actinolite, and tremolite with subordinate amounts of chlorite and quartz. Relicts of clinopyroxene and orthopyroxene, hornblende, and magnetite are still preserved in some samples (Figure 4.3i). Diorite occurs as a grayish, medium to coarse-grained rock with hypidiomorphic texture of plagioclase, quartz, chlorite, hornblende, and iron oxides (Figures 4.4a-b).

Olivine gabbronorite forms a small intrusion cutting the gabbro-diorite complex of Gabal Atud (Figures 4.1b & 4.2a). It is suggested that this intrusion pertains to the younger gabbro of Ghoneim (1989). It shows no ductile or brittle deformation, implying a post-tectonic setting. It is composed of coarse-to-medium-grained crystals of plagioclase (labradorite to bytownite; 35-40 vol. %), diopside (25-30 vol. %; partly altered to actinolite and tremolite), hypersthene (15-20 vol. %), cumulate olivine (partly altered into antigorite, 15-20 vol. %), and iron oxide (3 vol. %) (Figures 4.4c-d).

There are different types of dykes cut through the country rocks in the mine area, trend mainly in two directions. The oldest one is NNE-SSW and the youngest is NW-SE. Lamprophyre dykes occupy commonly the old direction (NNE-SSW) and cut through the serpentinite rocks, while porphyritic andesite and aplitic dykes occupy the NW-SE direction and cut through the gabbro-diorite intrusion (Figure 4.1b).

4.4 Gold mineralization and associated hydrothermal alteration

Gold-bearing quartz veins are associated with intense hydrothermal alteration along a NW-SE brittle-ductile shear zone in the eastern slope of Gabal Atud (Figure 4.1b). Gold mining though now abandoned from the mine area, remains of active mining refer to long lasting significant mining in the area. The ore zones include three locations, namely: main Atud (at the northeastern, eastern, and southern eastern slope of Gabal Atud), Atud East-I (at NE of Atud mine area), and Atud East-II (at SE of Atud mapped area) (Gabra, 1986; Harraz, 1999) (Figure 4.1b).

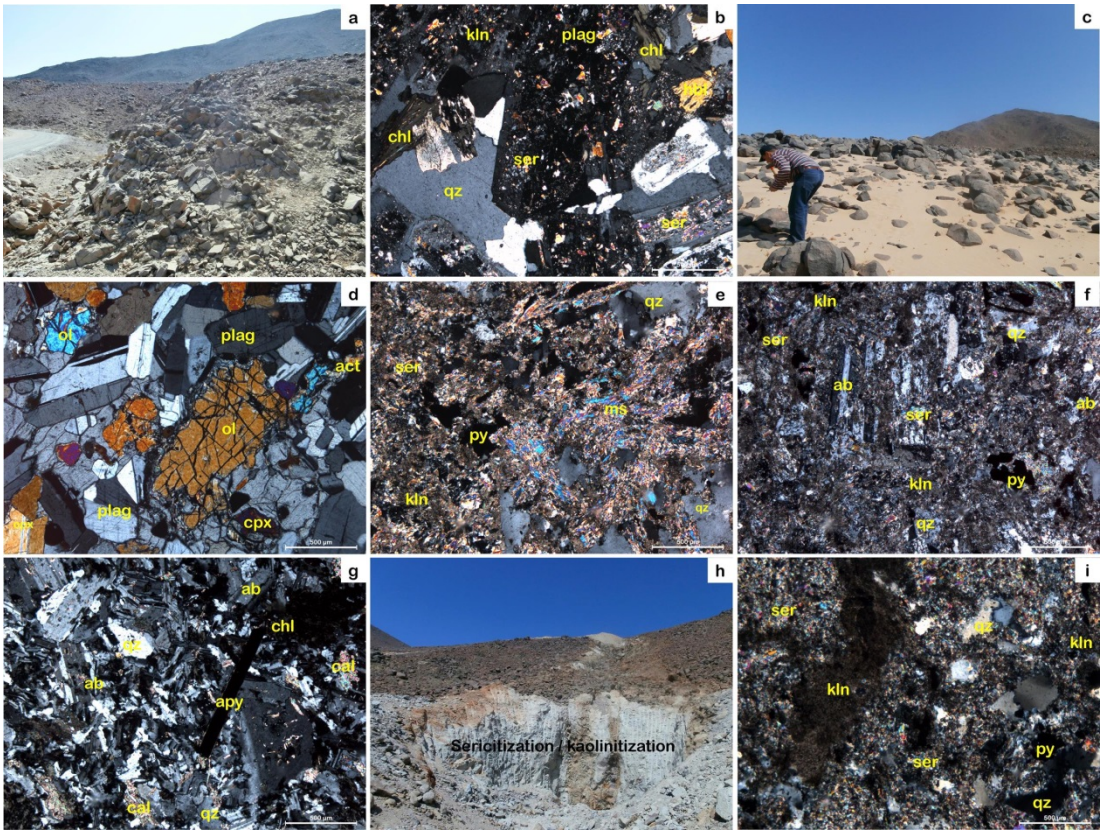

Figure 4.4 : a) Diorite at the eastern slope of Gabal Atud; b) Sericitized plagioclase (ser-plag), chlorite (chl), and hornblende (hbl) with a significant amount of quartz (qz); c) Massive boulder of olivine gabbronorite (OG) at the western slope of Gabal Atud; d) Olivine (ol) and plagioclase (plag) with diopside (cpx), hypersthene (opx), and actinolite (act) in olivine gabbronorite; e) Muscovite (ms), sericite (ser), and kaolinite (kln) with quartz (qz) and pyrite (py) in hydrothermal alteration zone-1; f) Quartz (qz), albite (ab), sericite (ser), and kaolinite (kln) with pyrite (py) in zone-2; g) Chlorite (chl), albite (ab), calcite (cal) with arsenopyrite (apy) and quartz (qz) in zone-3; h) Sericitization/kaolinitization alteration occurred at the eastern side of Gabal Atud, i) Sericite (ser) and kaolinite (kln) with quartz (qz) and pyrite (py) represent the surface alteration products at Gabal Atud.

In the subsurface levels, three main hydrothermal alteration zones were observed bounding the quartz veins in the main Atud area; zone 1: quartz-sericite-pyrite (Figure 4.4e), zone 2: quartz-chlorite-carbonate (Figure 4.4f), and zone 3: calcite-albite-chlorite (Figure 4.4g & Figure 4.5). On the surface, the main alteration types are sericitization and kaolinitization (Figures 4.4h-i). Carbonate alteration and ferrugination are confined to the southern part of Gabal Atud and surrounding serpentinite and tuffacous rocks (Figures 4.6a-f). Ore minerals disseminated the quartz veins and adjacent alteration zones, especially in the vein-wallrock contact. The common ore minerals observed are pyrite, arsenopyrite, and subordinate amounts of chalcopyrite, sphalerite, enargite, and goethite with gold (Figures 4.6g-i).

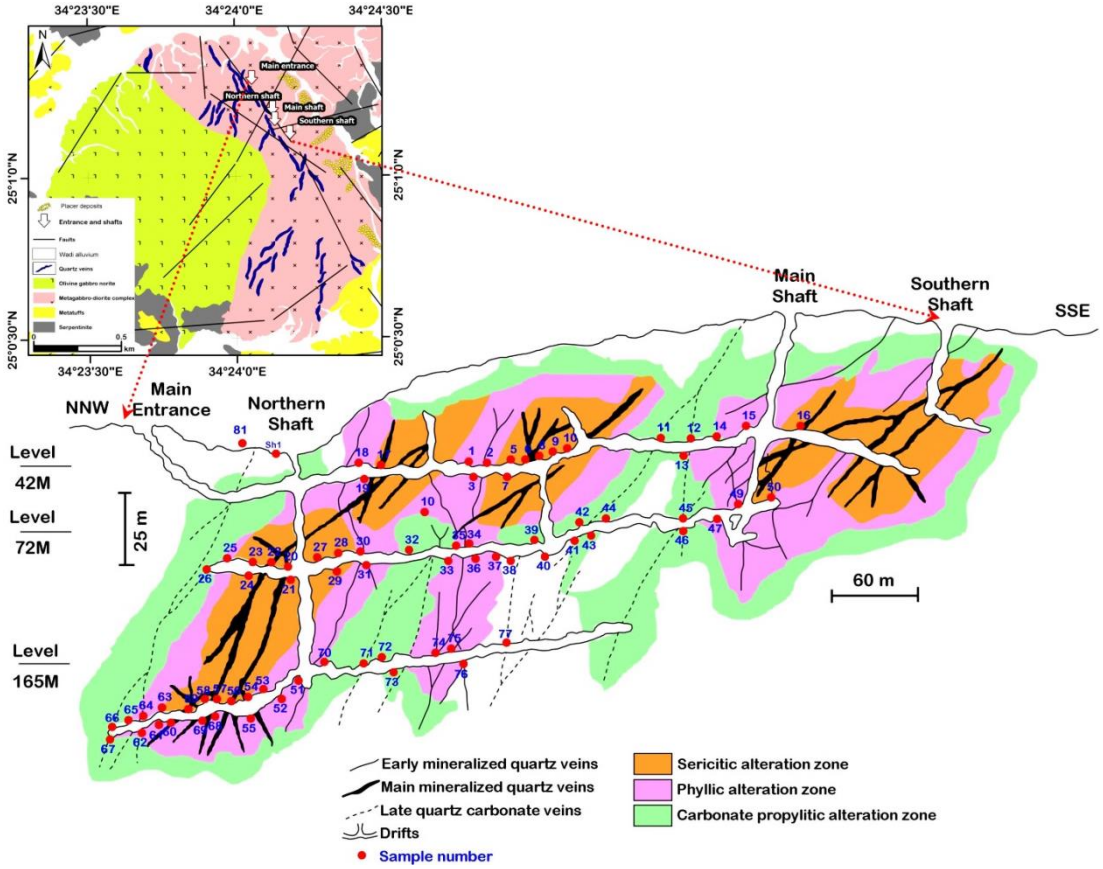

Figure 4.5 : Drifting of underground working of the Atud gold mine (traced quartz vein stages and alteration zones, after Gabra (1986); Harraz (1999); Abdelnasser and Kumral (2016)).

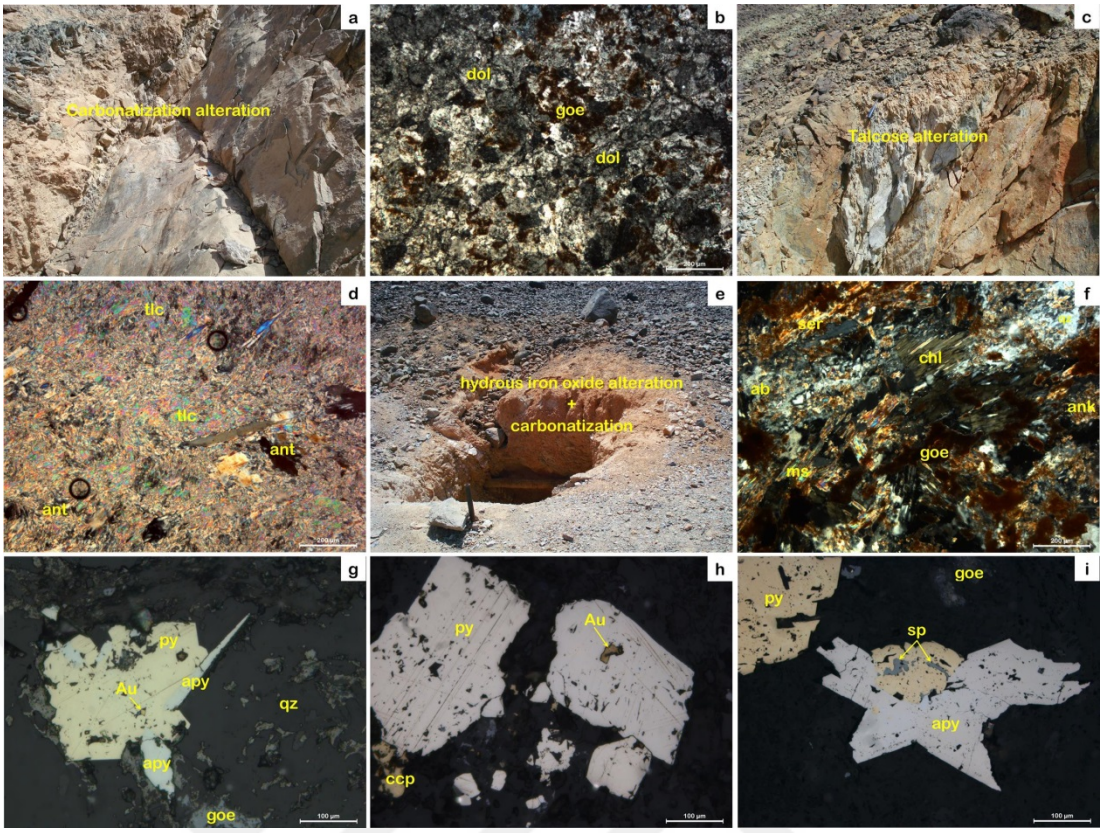

Figure 4.6 : a) & b) Carbonatization at the southern part of the study area; c) & d) talcose and serpentinization alteration at the northern part of the study area; e) & f) Hydrous iron oxide (goethite and limonite) alteration types at the northeastern slope of Gabal Atud; g) & h) Reflected light microscopy photomicrographs show gold (Au) inclusion in pyrite (py) with arsenopyrite (apy) and chalcopyrite (ccp); h) Sphalerite (sp) inclusion in pyrite (py) with arsenopyrite (apy).

4.5 Result and discussion

4.5.1 Whole rock lithogeochemistry

Major, trace, and rare earth elements (REE) data of the different rock units in the Atud area that are represented by serpentinites and their derivatives, metatuffs, and olivine gabbronorite rocks are shown in Table 4.1 and 4.2. As well as, the Major and REEs analyses of the different alteration zones are shown in Table 4.3.

4.5.1.1 Lithogeochemistry of serpentinites and their derivatives

The analyzed samples of the serpentinite, talc-carbonate, and calc-silicate rocks belong mostly to the metamorphic peridotites of Coleman (1977) and comparatively to the mafic-ultramafic cumulate ophiolitic rocks of Coleman (1977) (Figures 4.7a-b). The serpentinite rocks were derived from metamorphic harzburgite, olivine websterite, and orthopyroxenite, while the talc-carbonate rocks from dunite and websterite, and the calc-silicate rocks from the pyroxenite rocks (Figure 4.7c).

Table 4.1 : Major, trace, and rare earth elements (REEs) contents of the serpentinites, talc-carbonate and calc-silicate rocks

	Serpentinite rocks							Talc-carbonate rocks			Calc-silicate rocks		
Sample ID	A89	AT6.1	AT6.2	AT9.1	AT11.1	AT12.1	AT15	A97	AT8.1	A90	14.2	AT2.1	AT15.2
SiO_2	52.33	44.48	27.77	58.89	39.36	40.10	30.53	24.27	2.53	50.05	51.34	52.21	54.42
Al_2O_3	1.48	0.83	21.25	1.35	1.10	1.00	16.56	0.68	0.40	0.92	1.17	9.24	0.40
$Fe_2O_3^{(T)}$	5.67	8.70	9.88	6.54	5.28	5.24	12.12	0.46	0.95	4.92	5.75	6.96	7.93
MgO	26.36	30.68	27.88	26.69	27.89	39.94	25.94	14.29	19.55	24.30	7.24	19.69	26.89
CaO	2.37	2.68	0.45	0.13	5.35	0.72	2.14	27.46	30.43	4.80	16.93	4.52	0.70
Na_2O								0.04			0.04	0.07	
K_2O	0.01	0.03	0.01	0.01		0.01	0.01	0.00	0.03	0.01	0.04	0.01	0.02
TiO_2	0.01	0.02	0.22	0.01	0.01		0.76	0.03	0.02	0.01		0.39	
P_2O_5		0.00	0.17				0.11	1.84	0.08	0.01	0.02	0.09	
MnO	0.06	0.12	0.28	0.04	0.08	0.05	0.23	0.03	0.09	0.06	0.30	0.14	0.07
Cr_2O_3	0.52	0.30	0.00	0.57	0.28	0.27	0.18	0.02	0.00	0.27	0.58	0.08	0.38
L.O.I	11.19	11.68	11.96	5.49	20.36	12.32	11.23	30.89	45.76	14.65	16.04	6.40	8.51
Trace and rare earth elements (ppm)													
Ag	0.3	0.2	2.0	0.3	-0.4	0.7	0.3	0.2	0.3	0.2	0.2	0.7	1.4
As	2.0	33.9	33.3	53.0	69.9	43.1	48.4	4.0	32.1		106.5	31.3	68.2
Au (ppb)	184.7	66.6	41.2	4.0	11.1	25.5	6.0	14.9	6.9	49.4	19.8	25.5	20.9
Ba	3.0	37.8	55.7	17.2	8.2	35.2	16.3		10.2	5.0	72.8	6.4	34.2
Be	0.8	0.5	0.5	0.6	0.3	0.2	0.9	0.5	0.5	0.6	0.7	0.7	0.5
C	347.5	8095.6	584.9	1337.1	42574.0	2673.3	3204.0	74469.0	131000.0	1500.8	37658.0	0.0	1443.8
Cd	0.1	0.1	0.6	4.6	3.7	0.1	3.0	0.7	3.6	0.2	4.6	0.5	3.1
Co	92.0	92.7	15.0	32.2	64.6	80.9	53.8		19.0	68.0	161.7	39.6	79.5
Cr	3562.6	2041.7	0.0	3925.3	1897.3	1846.7	1238.4	122.5	23.9	1817.9	3958.1	565.1	2584.2
Cu	11.5	13.4	2.3	51.8	32.4	5.8	-4.7	96.4	50.4	76.3	25.9	6.9	17.1
Ga	5.6	3.6	18.0	2.0	1.1	1.8	16.3	2.2	0.6	4.4	5.8	7.6	2.2
Hf	0.1	0.1	9.1	0.1	0.0	0.1	2.8	0.3	0.1	0.1	0.1	2.7	0.1
Li	0.5	4.9	60.3	10.0	1.5	3.6	35.7	21.8	3.8	0.9	47.1	23.3	8.1
Ni	0.5	1878.9	61.7	1022.1	1256.5	1992.4	403.5	296.0	31.3	0.5	1385.1	574.4	1526.9
Pb	1.9	7.1	24.1	22.3	16.4	15.3	16.6	1.5	12.4	2.3	27.4	5.2	29.5
Pd	0.3	0.2	0.1	0.1	0.2	0.1	0.2	0.5	0.5	0.2	0.8	0.1	0.2
Pt	0.05	0.01	0.1	0.02	0.03	0.01	0.02	0.01	0.01	0.01	0.01	0.02	0.01
Rb	7.0	0.9	0.8	0.9	0.8	0.9	1.3	4.5	0.9	7.3	3.7	0.8	2.3
Ru	0.1	0.04	0.01	0.1	0.1	0.04	0.03	0.1	0.03	0.1	0.1	0.04	0.1
S	76.4	419.5	87.5	76.7	117.7	144.3	59.5	102.9	177.9	104.2	409.6	55.5	1280.6
Sb	1.3	0.9	0.3	0.4	1.2	3.3	0.4	9.6	0.7	4.4	159.1	0.5	0.9
Sn	0.8	0.9	1.6	0.8	1.1	0.6	1.8	0.8	0.6	0.8	1.5	1.5	1.2
Sr	4.1	28.4	20.8	7.8	26.6	12.3	13.0	86.3	107.9	8.2	176.0	16.2	11.5
Te	0.2	0.1	0.1	0.2	0.1	0.1	0.0	0.1	0.0	0.1	0.3	0.1	0.2
Tl	0.0	0.0	0.0	-0.1	-0.1	0.0	-0.1	0.0	0.0	0.0	0.1	0.0	0.0
U	0.0	0.5	1.3	0.1	0.0	0.4	0.8	2.5	2.7	0.1	0.7	1.2	0.7
Zn	86.7	15.2	163.3	15.1	16.7	54.2	71.9	63.5	48.5	49.5	15.5	48.1	4.9
Zr	14.0	3.0	372.0				82.0	24.0	7.0	14.0	1.0	80.0	
Sc	185.0	81.7	60.5	101.7	74.8	81.6	97.3	85.5	13.1	192.8	100.4	111.6	122.4
Y	2.1	1.9	39.4	0.7	1.4	0.5	31.8	50.4	11.2	2.3	3.0	24.5	2.5
La	0.1	1.2	53.6	0.2	0.9	0.2	5.1	12.0	2.5	0.3	1.4	11.7	1.2
Ce	0.5	2.5	144.8	0.9	1.8	0.5	15.1	24.5	4.8	1.1	2.8	25.9	1.9
Pr	0.1	0.3	13.2	0.1	0.2	0.04	2.2	3.6	0.7	0.2	0.3	3.4	0.2
Nd	0.6	1.2	41.6	0.3	0.8	0.2	10.6	17.1	3.2	0.9	1.5	14.3	0.9
Sm	0.2	0.3	10.9	0.1	0.2	0.05	3.4	3.9	0.8	0.3	0.4	3.5	0.2
Eu	0.03	0.1	4.8	0.02	0.1	0.01	1.9	0.8	0.1	0.0	0.2	1.0	0.1
Gd	0.3	0.4	12.2	0.1	0.2	0.1	4.9	5.0	1.1	0.3	0.5	4.5	0.3
Tb	0.1	0.1	1.5	0.02	0.03	0.01	0.8	0.7	0.2	0.0	0.1	0.7	0.0
Dy	0.3	0.3	7.9	0.1	0.2	0.1	5.2	4.9	1.1	0.3	0.3	4.1	0.2
Ho	0.1	0.1	1.4	0.03	0.05	0.02	1.1	1.1	0.3	0.1	0.1	0.9	0.1
Er	0.2	0.2	4.4	0.1	0.1	0.04	3.3	3.7	0.9	0.2	0.2	2.6	0.2
Tm	0.04	0.03	0.6	0.01	0.02	0.01	0.5	0.5	0.1	0.03	0.03	0.4	0.02
Yb	0.2	0.2	4.3	0.1	0.1	0.05	3.1	3.2	0.8	0.2	0.2	2.4	0.1
Lu	0.03	0.03	0.7	0.02	0.02	0.01	0.5	0.5	0.1	0.0	0.03	0.4	0.02
Th	1.9	0.1	27.1	0.1	0.03	0.03	1.5	1.5	0.3	0.1	0.02	3.4	0.1
Parameters													
FeO^t	5.8	9.0	10.2	6.3	6.0	5.4	12.5	0.6	1.6	5.2	6.2	6.8	7.9
Na2O+K2O	0.0	0.0	0.0	0.0	0.0	0.0	0.0	0.0	0.0	0.0	0.1	0.1	0.0
Σ REE	2.9	6.9	302.0	2.1	4.6	1.2	57.6	81.6	16.6	4.0	7.9	75.5	5.5
Σ LREE	1.6	5.6	269.0	1.6	3.8	0.9	38.3	61.9	12.0	2.9	6.5	59.7	4.5
Σ HREE	1.3	1.3	33.1	0.5	0.8	0.2	19.3	19.7	4.5	1.2	1.4	15.8	1.0
Eu/Eu*	0.3	0.9	1.3	0.8	1.3	0.8	1.4	0.5	0.5	0.4	1.3	0.7	1.6
(La/Sm)n	0.4	2.5	3.0	1.4	3.2	2.3	0.9	1.9	2.0	0.7	2.2	2.0	3.4
(Gd/Yb)n	1.6	1.5	2.2	1.0	1.5	1.0	1.3	1.3	1.0	1.2	2.0	1.5	1.8
Diopside	6.9	10.1	0.0	0.0	23.4	0.8	0.0	0.0	0.0	19.6	60.3	0.0	2.1
Hypersthene	77.1	57.5	14.7	78.0	36.7	30.1	15.2	0.0	0.0	67.1	0.0	59.6	83.5
olivine		26.7	56.3		32.8	63.0	52.7	34.7	61.0				

Bucher and Frey (1994) suggested the chemography of the SiO_2-MgO-CaO-H_2O-CO_2 (CMS-HC) system that discussed the metamorphism of the ultramafic rocks. At this system, the studied serpentinites plot in the antigorite-enstatite-talc-tremolite

joins (Figure 4.7d), while the talc carbonate rocks fall around talc, tremolite, diopside, and dolomite (Figure 4.7d). On the other hand, the calc-silicate rocks plot in the tremolite-talc-quartz joins (Figure 4.7d).

The chondrite-normalized REE patterns of these rocks are characterized by light REE-enrichments with an average 25.8, 25.6, and 23.6 for serpentinite, talc-carbonate, and calc-silicate rocks, respectively [$(La/Sm)_N$=0.4-3.2 for serpentinite, 0.7-2.0 for talc-carbonate, and 2.0-3.4 for calc-silicate rocks] (Figure 4.7e). They also show significantly flat heavy REE with an average 8.1, 8.5, and 6.1 for serpentinite, talc-carbonate, and calc-silicate rocks, respectively [$(Gd/Yb)_N$=1.0-2.2 for serpentinite, 1.0-1.3 for talc-carbonate, and 1.5-2.0 for calc-silicate rocks] (Fig. 7e). Positive Eu-anomaly distinguishes the serpentinite [Eu/Eu*=1.0] and calc-silicate rocks [Eu/Eu*=1.2] (Fig. 7e) referring to their developement during the oceanic serpentinization that assigned the plagioclase dissolution and/or circulation of the hydrothermal fluids (Douville et al., 2002; Paulick et al., 2006; Debret et al., 2013). The primitive mantle normalized spider diagram (Figure 4.7f) for these rocks is represented by depletion of Th, Ti, and Rb with an enrichment of U, Pb, and Eu referring to the occurrence of carbonate in these rocks (Deschamps et al., 2010).

4.5.1.2 Lithogeochemistry of metatuffs

The analyzed samples of the studied metatuffs have high K/Rb (up to 596) (Table 4.2) referring to derivations from magmatic suites having mostly basic composition and some samples have acidic/intermediate characteristics in the field of the metavolcanic tuffs (Floyd and Leveridge, 1987) (Figure 4.8a). This is also comparable with the petrographic studies of the metaffs that have mainly basic with intermediate and acidic compositions. Figure (4.8b) shows the F1–F2 classification diagram that investigates the compositional properties of the different provenances which classified based on the geochemistry of the sedimentary rocks into four provenances; P1-mafic and less intermediate igneous provenance; P2-intermediate igneous provenance, P3-Felsic igneous provenance, and P4-quartoze sedimentary provenance (Roser and Korsch, 1986).

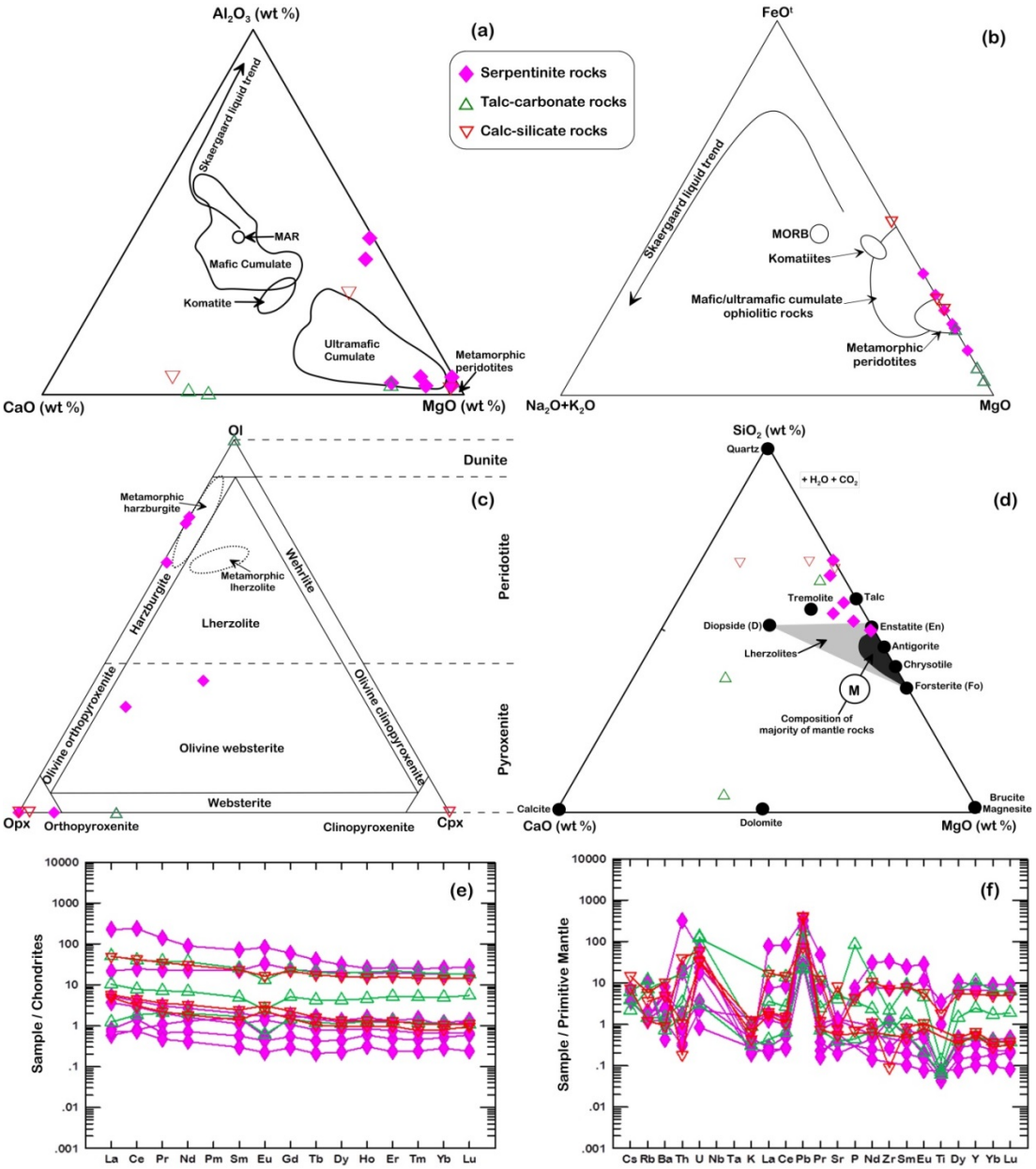

Figure 4.7 : Geochemical diagrams of the serpentinites and their derivatives (talc-carbonate and calc-silicate rocks): a) CaO-Al2O3-MgO diagram after Coleman (1977); b) AFM diagram after Coleman (1977); c) Classification and nomenclature diagram after Streckeisen (1976), field of metamorphic harzburgite and metamorphic lherzolite after Coleman (1977); d) Chemography of the SiO_2-MgO-CaO-H_2O-CO_2 (CMS-HC) system of ultramafic rocks after Bucher and Frey (1994); e) Chondrite-normalized RRE patterns; f) Primitive mantle-normalized trace element patterns (Normalizing values from Sun and McDonough (1989)).

Table 4.2 : Major, trace, and rare earth elements (REEs) contents of the metatuffs and olivine gabbronorite.

	Metatuffs						Olivine gabbronorite					
Sample ID	A95	A100	A101	A122	AT6.3	AT12.2	A44	A98	A102	A126	A129	AT7
SiO_2	58.58	97.78	69.89	68.87	61.63	44.53	45.55	47.19	47.33	46.55	45.55	44.80
Al_2O_3	16.40	0.74	13.07	12.48	16.27	12.07	16.12	16.15	19.99	19.35	18.14	19.02
$Fe_2O_3^{(T)}$	7.12	0.57	4.70	2.68	6.57	16.17	7.88	5.93	5.25	5.31	6.79	7.00
MgO	3.24	0.09	1.20	0.63	2.36	7.97	11.22	11.82	9.78	10.02	12.96	11.08
CaO	5.52	0.11	1.40	8.58	1.74	10.22	13.70	15.69	15.59	15.49	13.41	13.32
Na_2O	4.25	0.19	4.39	2.10	6.22	1.89	1.53	0.94	1.21	1.05	1.00	1.62
K_2O	1.09	0.11	2.14	0.40	2.43	0.45	0.18	0.07	0.08	0.11	0.09	0.14
TiO_2	0.78	0.03	0.56	0.42	0.90	1.97	0.61	0.29	0.27	0.24	0.20	0.45
P_2O_5	0.19	0.03	0.08	0.17	0.18	0.22	0.07	0.03	0.03	0.04	0.04	0.07
MnO	0.13	-	0.12	0.24	0.15	0.24	0.13	0.10	0.08	0.09	0.11	0.11
Cr_2O_3	0.02	0.06	0.02	0.03	0.01	0.00	0.07					0.11
LOI	2.68	0.29	2.43	3.40	1.35	3.92	2.93	1.21	1.36	1.68	2.16	1.85
Trace and rare earth elements (ppm)												
Ag	0.6	0.1	0.2	0.9	1.2	0.8	0.7	0.2	0.3	0.6	0.5	0.2
As	5.0	45.0	12.0	2.0	30.8	25.5	2.0	5.0	5.0	6.0	4.0	23.2
Au (ppb)	27.3	46.5	33.3	19.0	26.4	14.0	34.3	171.3	17.1	133.9	20.5	19.8
Ba	211.0	320.0	19.0	51.0	312.0	52.9	32.0	24.0	38.0	29.0	27.0	38.8
Be	1.8	0.5	1.1	1.2	2.1	0.6	0.8	0.6	0.4	0.9	0.8	0.5
C	4437.2	2137.9	2017.7	4418.7	1979.5	1034.8	1143.3	75.7	110.2	113.0	112.8	1265.5
Cd	0.2	0.2	0.1	0.4	0.5	4.1	0.3	0.2	0.2	0.3	0.3	0.5
Co	14.0	438.0	8.0	2.0	29.8	41.0	56.0	49.0	41.0	41.0	56.0	66.9
Cr	139.6	404.4	112.2	231.3	47.9	0.0	500.2	0.0	0.0	0.0	0.0	729.4
Cs	0.7	0.1	0.7	0.1	1.1	0.5	0.1	0.0	0.0	0.3	0.4	0.1
Cu	11.8	40.7	36.6	13.2	8.1	55.2	50.2	62.0	55.0	41.0	10.1	43.7
Ga	42.6	4.6	19.5	22.2	32.4	14.5	21.0	8.5	8.9	16.9	15.2	11.1
Hf	1.8	0.4	1.8	2.3	4.4	2.0	1.3	0.7	1.1	0.5	0.4	1.0
In	0.1	0.0	0.0	0.1	0.0	0.0	0.0	0.0	0.0	0.0	0.0	0.0
Ir	0.0	0.1	0.0	0.0	0.0	0.0	0.0	0.2	0.0	0.1	0.0	0.0
Li	17.7	0.4	3.3	1.9	10.7	8.6	3.1	1.3	0.7	2.0	3.0	25.3
Ni	164.4	164.5	273.5	338.3	30.2	37.8	304.2	67.0	74.0	384.8	352.4	126.0
Pb	7.5	0.3	2.0	3.1	13.9	54.3	40.5	-0.4	-0.3	2.0	1.1	14.6
Pd	1.1	0.4	1.6	1.5	0.3	0.5	1.1	0.6	0.5	0.6	0.4	1.0
Pt	0.0	0.0	0.0	0.0	0.0	0.0	0.0	0.0	0.0	0.0	0.0	0.0
Rb	22.3	13.5	36.4	15.3	33.9	8.4	11.7	5.8	7.0	7.8	8.2	2.0
Rh	0.1	0.0	0.1	0.0	0.0	0.0	0.1	0.1	0.1	0.1	0.05	0.04
Ru	0.1	0.2	0.2	0.1	0.0	0.0	0.1	0.1	0.2	0.2	0.2	0.04
S	69.6	902.9	213.3	374.8	139.3	230.5	159.2	2392.1	2043.1	1436.7	158.9	902.3
Sb	1.0	0.4	0.3	4.0	0.4	0.5	13.9	0.3	0.3	0.2	0.2	0.2
Sn	2.5	1.3	2.4	2.1	3.0	1.8	1.3	0.9	0.9	0.9	0.9	0.8
Sr	298.4	8.0	201.3	320.8	82.5	81.2	399.6	269.0	327.0	363.3	350.0	256.4
Te	-	0.1	-	-	0.1	0.1	0.0	0.2	0.2	0.1	0.0	0.1
Tl	0.2	0.0	0.1	0.03	0.3	0.0	0.0	0.0	0.0	0.0	0.0	0.0
U	1.5	0.2	0.3	0.4	1.7	0.2	0.1	0.0	0.0	0.1	0.1	0.2
V	397.5	237.8	293.5	183.7			400.0	392.3	315.9	367.0	315.0	
Zn	133.9	35.1	57.2	91.5	65.8	81.8	132.9	40.0	31.1	52.7	57.0	39.9
Zr	181.0	24.0	159.0	96.0	279.0	131.0	48.0	30.0	31.0	28.0	27.0	108.0
Sc	195.3	222.7	200.3	176.1	114.3	110.8	268.1	237.0	214.7	227.5	209.8	99.5
Y	49.2	15.9	55.5	60.3	37.2	46.6	19.7	11.7	10.5	9.7	8.2	7.9
La	23.5	3.6	22.3	13.0	18.7	5.2	4.4	2.2	2.4	2.2	2.3	2.0
Ce	57.4	6.6	53.8	33.3	44.3	14.9	11.4	5.5	5.8	8.0	5.3	5.1
Pr	7.5	1.2	6.9	4.8	5.8	2.5	1.7	0.8	0.9	0.8	0.8	0.7
Nd	33.5	5.9	30.9	23.7	25.4	13.4	8.6	4.5	4.4	4.1	3.8	3.6
Sm	8.0	1.4	7.7	6.6	6.3	4.7	2.6	1.4	1.3	1.2	1.1	1.1
Eu	2.1	0.3	1.8	1.8	1.5	1.6	1.1	0.7	0.7	0.7	0.6	0.5
Gd	8.6	1.8	8.8	8.2	7.4	7.2	3.2	1.9	1.8	1.6	1.3	1.5
Tb	1.3	0.3	1.4	1.3	1.1	1.2	0.5	0.3	0.3	0.3	0.2	0.2
Dy	7.8	1.8	8.6	8.8	6.3	8.3	3.3	2.0	1.8	1.6	1.4	1.4
Ho	1.6	0.4	1.8	1.9	1.3	1.8	0.7	0.4	0.4	0.4	0.3	0.3
Er	4.7	1.2	5.2	5.8	4.0	5.2	2.0	1.2	1.0	1.0	0.8	0.9
Tm	0.6	0.2	0.7	0.8	0.6	0.7	0.3	0.2	0.1	0.2	0.1	0.1
Yb	3.8	1.1	4.1	5.4	3.7	4.5	1.7	1.0	0.9	0.8	0.7	0.7
Lu	0.5	0.2	0.5	0.8	0.6	0.6	0.2	0.1	0.1	0.1	0.1	0.1
Th	5.6	0.5	4.7	1.9	4.8	0.4	0.5	7.7	0.3	3.1	0.3	0.2
Parameters												
Na_2O+K_2O							1.7	1.0	1.3	1.2	1.1	1.8
FeO^t/MgO							0.7	0.5	0.5	0.5	0.5	0.6
K/Rb	403.6	70.6	488.3	215.8	595.6	440.3						
F1	4.3	-8.4	0.1	4.7	1.9	1.8						
F2	-0.6	-6.5	1.9	0.2	3.7	-10.4						
Σ REE	160.8	26.1	154.5	116.2	126.9	71.8	41.5	22.2	21.8	23.1	18.8	18.4
Σ LREE	131.9	19.1	123.5	83.2	102.1	42.2	29.7	15.1	15.5	17.1	13.9	13.1
Σ HREE	28.9	7.0	31.0	33.0	24.8	29.6	11.8	7.1	6.4	6.0	5.0	5.3
Sr_N	3.3	0.1	2.2	3.6	0.9	0.9	4.4	3.0	3.6	4.0	3.9	2.8
Ce_N	66.4	7.6	62.2	38.5	51.2	17.2	13.2	6.4	6.7	9.2	6.2	5.9
Sm_N	39.4	7.1	37.9	32.7	31.1	23.3	12.6	7.0	6.6	6.1	5.4	5.4
$(La/Yb)_N$	4.1	2.2	3.6	1.6	3.4	0.8	1.7	1.5	1.8	1.8	2.2	1.8
$(Gd/Yb)_N$	1.8	1.3	1.7	1.2	1.6	1.3	1.5	1.6	1.6	1.6	1.6	1.6
Eu/Eu*	0.8	0.6	0.7	0.7	0.7	0.8	1.2	1.2	1.4	1.4	1.5	1.3
Sr/Sr*	0.1	0.0	0.0	0.1	0.0	0.0	0.3	0.4	0.5	0.5	0.6	0.5
Zr/Zr*	0.1	0.0	0.0	0.0	0.1	0.1	0.0	0.1	0.1	0.1	0.1	0.3

Most of the investigated metatuffs fall in P2-field that refers to intermediate igneous provenance with some samples fall in the mafic and felsic igneous provenances (P1 and P3) (Figure 8b). On the basis of the nature of the crust, Bhatia (1983) classified the continental margins and oceanic basins into four types; (1) oceanic island arcs which correspond to the sedimentary basins adjacent to the oceanic island arcs and their sediments are derived either from the calc-alkaline or tholeiitic arc, (2) continental island arcs that are comparable with the sedimentary basins adjacent to island arcs formed on a well-developed continental crust and their sediments are mainly derived from the felsic volcanic rocks and deposited in the fore-arc, back-arc, and inter-arc basins. (3) Active continental margins include the sedimentary basins which were developed on or adjacent to a thick continental crust and their sediments are mainly derived from granite-gneisses and siliceous volcanics of the uplifted basement in the Andean type setting. (4) Passive margins which comprise the rifted continental margins of the Atlantic type occurred along the edges of the continents and the edges of the remnant ocean basins adjacent to the inactive convergent margins and the collision orogens and their sediments were formed from the recycling of the older sedimentary and metamorphic rocks of platforms or recycled orogens. Figure (4.8c) shows that the studied metatuffs are mostly tendency to be similar to the metasediments of the oceanic island arc that derived from the calc-alkaline and tholeiitic rocks with some samples plotted in the passive and active continental margins that derived by the recycling of the old metamorphic/sedimentary rocks of the recycled orogens.

The chondrite-normalized REE patterns of the metatuffs stated that these rocks are enriched in the light REE [$(La/Yb)_N$ = 2.6] relative to the heavy REE [$(Gd/Yb)_N$ = 1.5] with negative Eu-anomaly [Eu/Eu* = 0.7] (Figure 4.8d). The REE profile of the studied metatuffs is comparable to that of the continental arc basin (CAB) of McLennan et al. (1990) (Figure 4.8e). While, based on the primitive mantle-normalized incompatible element spider diagram of the analyzed metatuffs, Cs, U, K, La, Pb, Nd, and Y are enriched-, and Ba, Sr, Zr, Eu, Ti, and Yb are depleted relative to the primitive mantle (Figure 4.8f). Negative Eu- [Eu/Eu* = 0.7], negative Sr- [Sr/Sr* = 0.04], and negative Zr- [Zr/Zr* = 0.06] anomalies suggested that the source rocks of these metatuffs had crystallized plagioclase and formed from a magma

contaminated by components added to the mantle source by subduction zone fluids (Wilson, 2007).

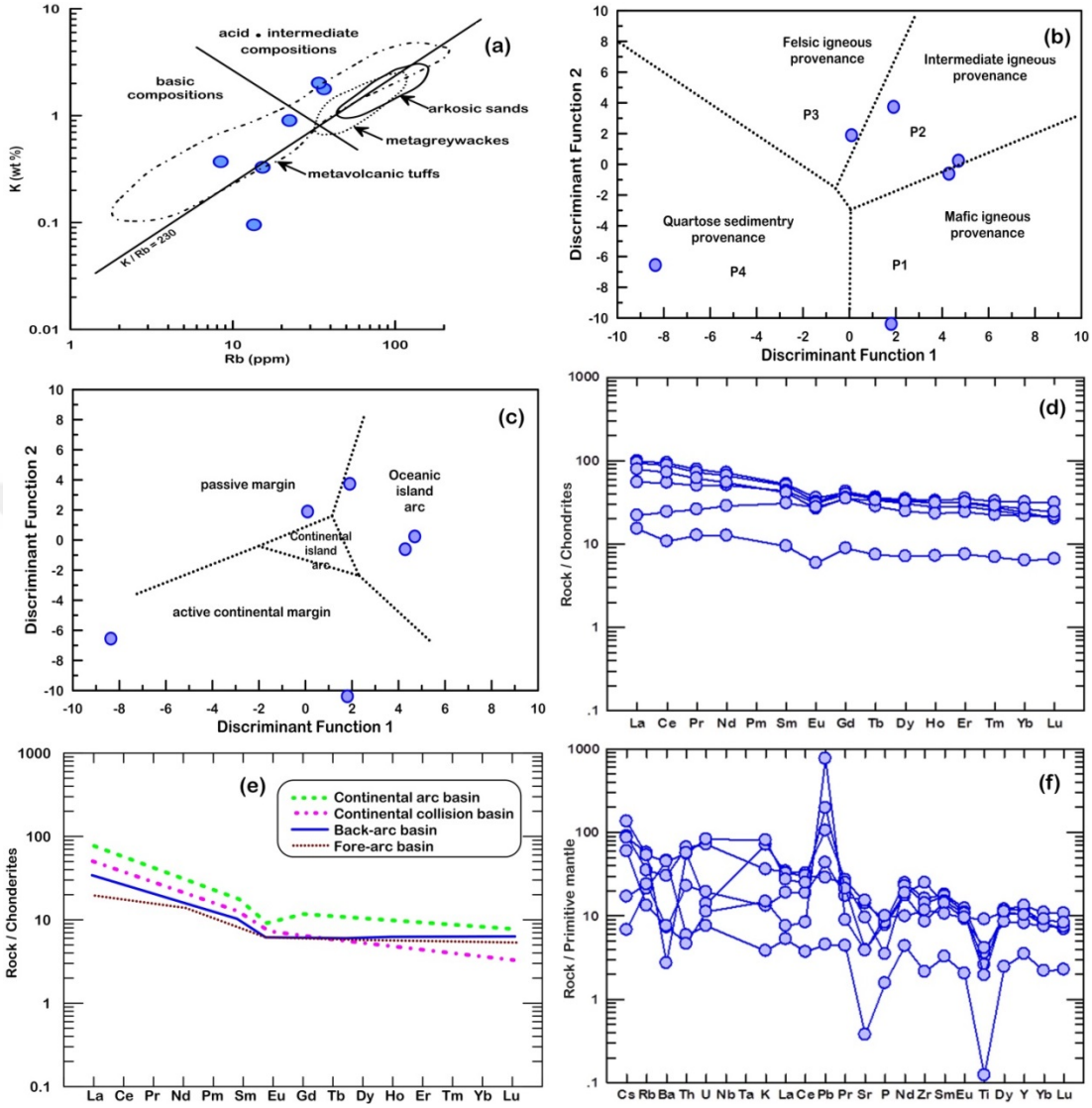

Figure 4.8 : Geochemical diagrams of the metatuffs: a) K-Rb diagram after Floyd and Leveridge (1987), fields of unmetamorphosed arkosic sands after van de Kamp et al. (1976), low grade metagreywackes after Condie et al. (1970); Caby et al. (1977), and higher grade metavolcanic tuffs after van de Kamp (1968); b) Plot of discriminant functions F1 and F2, provenance fields are after Roser and Korsch (1986); c) Plot of discriminant scores along Function 1 versus II after Bhatia (1983); d) Chondrite-normalized REE patterns (Sun and McDonough, 1989); e) Typical chondrite-normalized REE profiles for clastic rocks in arc-related basins after McLennan et al. (1990); f) Primitive mantle-normalized trace element patterns (Sun and McDonough, 1989).

4.5.1.3 Lithogeochemistry of metagabbro-diorite complex

This metagabbro-diorite complex that represents the host rock of the gold mineralization at Atud area is studied geochemically at the 2.chapter. The metagabbros are classified as calc-alkaline gabbro and gabbro/diorite as well as are

comparable to the calc-alkaline basalt (CAB) formed in the island arc environments having clinopyroxene fractionation. On the other hand, the dioritic rocks are calc-alkaline diorite and gabbro/diorite formed in the island arc environments that had amphibole fractionation. The REE profiles of these rocks have LREE-enriched and HREE-depleted with positive Eu- and Sr-anomalies referring to plagioclase accumulations (Abdelnasser and Kumral, 2016).

4.5.1.4 Lithogeochemistry of olivine gabbronorite

Based on the geochemical data of the olivine gabbronorite rocks that appear in Table 4.2, they prove to have low-K tholeiitic magmatic affinities (Figure 4.9a), classified as gabbroic rocks (Figure 4.9b), and correspond to the island-arc tholeiites (IAT) of Ikeda (1990) (Figure 4.9c). They also are similar to the intrusive rocks that evolved in the stable continent and oceanic islands environments of Miyashiro and Shido (1975) (Figure 4.9d).

The chondrite-normalized REE patterns of the olivine gabbronorite rocks suggest LREE-enrichment [average $(La/Yb)_N$=1.8] and nearly flat HREE [average $(Gd/Yb)_N$=1.6] with positive Eu-anomalies [average Eu/Eu*=1.3] (Figure 4.9e). The primitive mantle-normalized incompatible element spider diagram of the analyzed rocks reveals positive anomalies of Th, Pb, Sr, Zr, and Eu with negative P- and Ti-anomalies (Figure 4.9f) suggesting low-pressure fractionation of plagioclase and olivine (Hawkesworth et al., 1977).

4.5.1.5 REE Geochemistry of different alteration zones associated with Atud gold mineralization

The hydrothermal alteration zones are divided into three main types in the subsurface levels; zone 1: mainly quartz-sericite-pyrite, zone 2: mainly quartz-chlorite-calcite, and zone 3: mainly calcite-albite-chlorite alteration (Abdelnasser and Kumral, 2016).

The chondrite - and primitive mantle-normalized REE pattern of the altered rocks from the different alteration types reveal that the behavior of the REE of these altered rocks has nearly the same behavior of the least altered rocks. High LREE, low HREE, and positive Eu-anomalies relative to chondrite and primitive mantle are common features (Figures 4.10a-f).

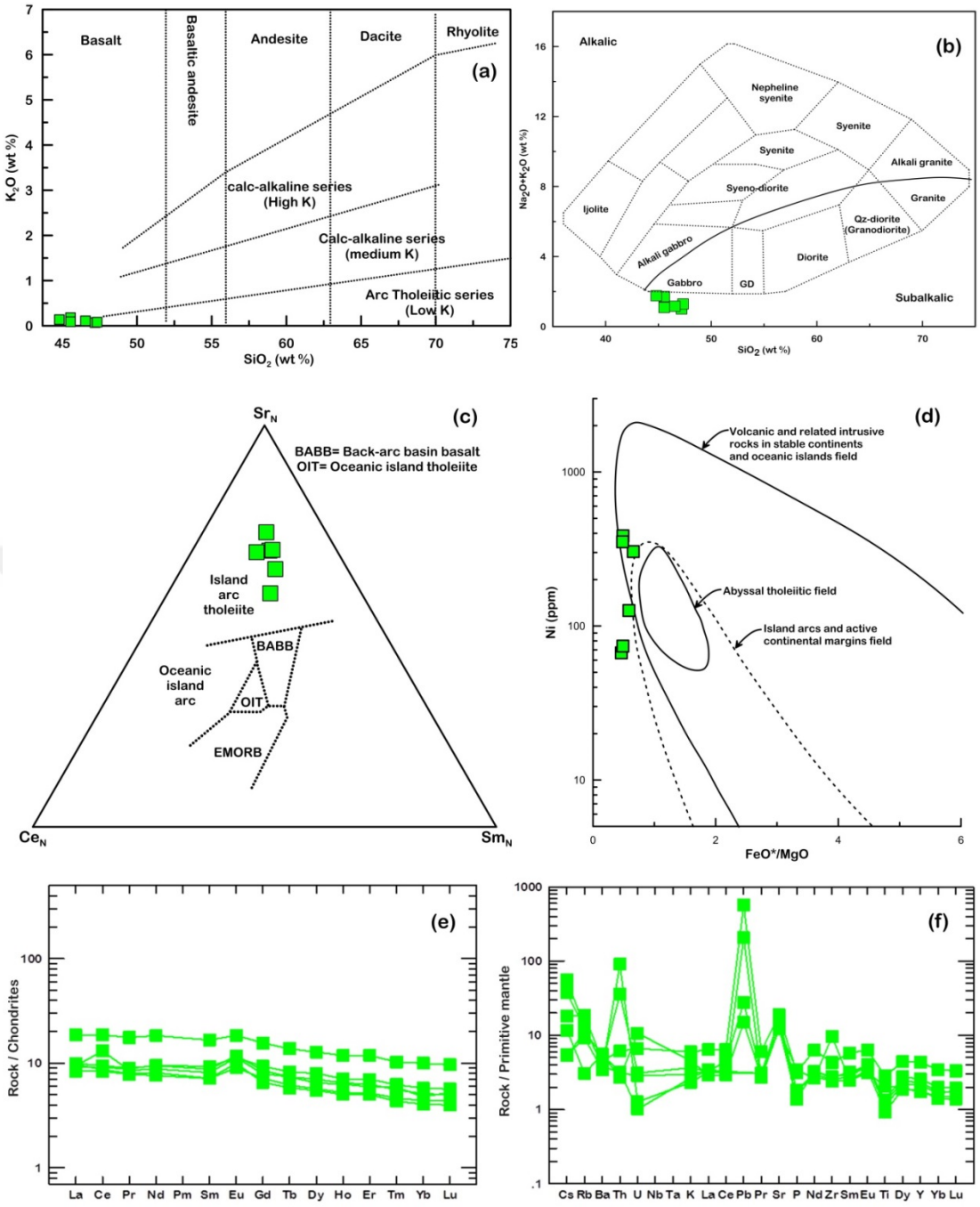

Figure 4.9 : Geochemical diagrams of olivine gabbronorite: a) K_2O - SiO_2 diagram; subdivisions between series after Le Maitre et al. (1989), b) TAS diagram after Cox et al. (1979), the dividing line between alkalic and subalkalic after Miyashiro (1978), c) Ce_N-Sr_N-Sm_N diagram after Ikeda (1990), d) FeO^t/MgO-Ni diagram after Miyashiro and Shido (1975), e) & f) Chondrite- and primitve mantle-normalized REE pattern. Normalization values from Sun and McDonough (1989).

When normalized to the least altered gabbro-dioritic rocks, The LREE patterns of samples collected from these alteration zones reveal slight enrichments compared to significant ones in HREE associated with sericite alteration in zones (1) and (2) (Figures 4.10g-h). The alteration zone 3 shows a different pattern of strong

anomalies of LREE and weak anomalies of HREE associated with calcite and chlorite alteration (Figure 4.10i).

Table 4.3 : Major, rare earth elements (REEs), and some trace elements contents of the different alteration zones.

	Zone 1										Zone 2			Zone 3		
Sample ID	A34	A39	A47	A49	A53	A60	A64	At68	A75	A-sh-1	A66	A67	A81	A19	A40	A58
SiO_2	52.57	52.24	50.21	48.71	52.37	42.10	44.44	70.67	42.99	51.86	56.58	57.85	57.85	53.21	53.62	49.13
Al_2O_3	17.39	15.36	15.43	16.48	14.00	18.40	10.78	10.82	17.53	16.30	18.64	13.71	17.51	16.36	17.46	15.21
$Fe_2O_3^{(T)}$	5.06	4.97	5.60	5.28	6.27	5.61	7.10	3.02	7.32	4.02	3.74	6.09	4.58	7.32	7.39	9.84
MgO	2.40	3.60	3.89	3.72	3.04	3.35	6.77	1.14	3.59	3.47	1.43	1.48	1.96	4.28	4.90	3.25
CaO	4.94	6.08	6.27	6.20	5.81	8.19	7.71	1.65	6.28	7.01	3.98	4.39	4.64	7.89	3.93	5.79
Na_2O	0.22	0.31	0.84	0.20	0.25	0.25	0.12	0.10	0.54	0.61	3.78	2.40	3.27	3.25	5.10	2.23
K_2O	4.56	3.83	3.53	4.22	3.63	4.44	2.75	2.54	4.50	3.67	3.03	2.56	2.52	0.59	0.28	2.09
TiO_2	0.83	0.66	0.65	0.65	1.03	0.63	0.61	0.37	1.13	0.59	0.42	0.82	0.59	0.81	1.01	1.82
P_2O_5	0.20	0.12	0.13	0.11	0.10	0.08	0.11	0.07	0.14	0.06	0.23	0.22	0.15	0.21	0.20	0.17
MnO	0.08	0.09	0.09	0.09	0.11	0.12	0.15	0.03	0.13	0.09	0.07	0.08	0.06	0.13	0.09	0.12
Cr_2O_3						0.03				0.03	0.02		0.01	0.02		
LOI	10.67	11.75	13.06	12.90	12.10	14.16	17.78	6.34	14.01	12.29	8.09	8.91	6.87	5.93	4.49	8.75
Rare earth elements and some trace elements (ppm)																
Ag	7.0	1.3	0.7	2.2	10.0	14.0	1.2	69.6	29.4	0.9	0.9	12.3	2.4	0.7	1.2	3.4
As	810.7	91.1	3040.2	2522.3	1969.5	1404.0	294.4	4220.0	2697.4	211.0	158.0	1194.5	172.0	6.0	6450.4	4093.9
Au (ppb)	275.1	25.0	156.3	237.8	182.6	270.6	28.0	790.2	184.2	159.6	118.6	176.1	48.6	53.9	74.7	90.3
C	27056.0	19785.0	25364.0	14553.0	4882.4	30903.0	13295.0	5717.3	24749.0	25541.0	12529.0	26180.0	12589.0	7687.8	44681.0	23086.0
Cd	1.1	0.1	0.4	0.3	0.5	0.4	0.2	1.3	0.7	0.3	0.4	0.1	0.6	0.5	0.1	0.1
Cu	27.9	19.1	6.0	15.6	44.6	46.5	6.3	83.8	35.3	27.2	112.6	118.2	39.6	19.9	32.7	79.0
Li	3.7	4.3	5.2	3.2	2.4	3.3	5.3	5.3	3.9	2.3	2.6	2.7	7.0	12.1	14.9	15.6
Ni	19.4	52.3	25.8	21.0	24.9	360.9	32.5	398.3	25.1	408.9	157.6	6.8	163.4	206.5	47.3	11.2
Pb	9.4	7.6	9.3	10.9	10.8	4.0	10.6	23.4	12.8	1.6	5.3	9.2	5.5	35.7	10.3	14.6
Pd	0.3	0.4	0.4	0.4	0.4	1.0	0.4	1.0	0.5	1.0	1.2	0.3	0.9	0.8	0.5	0.5
Pt	0.0	0.0	0.0	0.0	0.0	0.0	0.0	0.0	0.0	0.0	0.0	0.0	0.0	0.0	0.0	0.0
Rb	123.8	86.6	88.5	102.8	98.8	112.0	74.0	82.4	121.7	135.9	73.8	68.1	50.6	24.6	6.1	46.8
Rh	0.0	0.1	0.1	0.0	0.1	0.0	0.1	0.0	0.1	0.1	0.0	0.1	0.0	0.1	0.1	0.1
Ru	0.0	0.0	0.0	0.0	0.0	0.1	0.0	0.2	0.0	0.1	0.1	0.0	0.1	0.1	0.0	0.0
S	36168.0	20741.0	20427.0	33425.0	5986.8	26186.0	16316.0	21224.0	1091.8	6015.9	9123.3	16301.0	1989.2	70.7	5525.8	28274.0
Sb	8.6	26.4	20.0	9.8	21.7	30.4	3.8	143.1	37.6	13.6	7.0	17.5	10.3	14.4	3.9	3.6
Sn	1.4	1.2	1.3	0.9	1.3	2.3	1.0	1.6	1.4	2.5	1.9	0.8	1.7	2.0	2.5	2.0
Sr	106.5	145.6	114.6	133.8	133.5	131.7	132.5	32.1	142.3	203.7	169.9	88.5	110.6	375.7	197.9	160.4
Zn	25.3	53.2	72.2	77.3	123.4	82.9	97.0	100.1	79.0	90.8	85.8	24.7	97.5	216.4	65.5	119.3
Zr	184.0	74.0	76.0	68.0	90.0	96.0	67.0	74.0	98.0	70.0	163.0	167.0	100.0	90.0	124.0	137.0
Sc	54.3	59.0	57.8	56.5	66.8	185.9	63.1	213.9	59.0	217.2	195.4	64.8	193.3	229.7	63.0	70.9
Y	10.0	7.5	9.9	8.6	12.6	14.7	8.2	8.0	10.7	12.9	20.1	15.0	18.9	32.1	19.2	21.2
La	4.9	7.7	6.5	7.3	7.3	9.7	6.6	8.6	8.1	11.2	18.8	13.2	13.9	11.9	11.7	11.3
Ce	10.2	13.8	13.4	14.3	15.4	21.3	14.0	19.0	18.0	23.3	41.0	24.0	31.0	27.6	22.3	22.9
Pr	2.5	2.0	2.2	2.2	2.6	2.7	2.2	2.4	3.2	2.8	4.9	4.2	3.9	3.7	3.9	4.1
Nd	11.7	7.4	8.5	8.6	10.4	12.2	8.8	10.2	12.8	11.9	20.7	16.6	17.4	17.8	15.0	16.8
Sm	2.7	2.0	2.2	2.1	2.9	3.4	2.2	2.2	3.1	3.0	4.7	4.4	4.1	4.8	3.6	4.8
Eu	0.9	1.0	0.7	0.8	1.0	1.2	0.7	0.6	1.0	1.3	1.6	1.2	1.0	1.7	1.1	1.7
Gd	2.8	2.2	2.5	2.3	3.0	3.6	2.3	2.2	3.0	3.0	4.4	5.1	4.2	5.6	4.3	5.4
Tb	0.4	0.3	0.4	0.4	0.5	0.5	0.4	0.3	0.5	0.4	0.6	0.9	0.6	0.9	0.8	1.0
Dy	2.1	1.6	2.2	1.9	2.1	2.8	1.7	1.5	2.4	2.3	3.3	4.5	3.3	5.3	3.9	5.1
Ho	0.5	0.4	0.5	0.4	0.6	0.5	0.4	0.3	0.6	0.5	0.7	1.1	0.7	1.1	0.9	1.2
Er	1.0	1.0	1.3	1.1	1.5	1.6	1.0	0.9	1.4	1.3	1.9	2.8	2.0	3.2	2.4	3.2
Tm	0.2	0.2	0.2	0.2	0.3	0.2	0.2	0.1	0.2	0.2	0.3	0.5	0.3	0.4	0.4	0.5
Yb	1.1	1.0	1.2	1.0	1.5	1.7	1.0	0.8	1.1	1.4	1.8	2.6	1.9	2.8	2.2	3.0
Lu	0.2	0.2	0.2	0.2	0.3	0.3	0.2	0.1	0.3	0.2	0.3	0.5	0.3	0.4	0.4	0.5
Th	1.9	2.1	1.2	1.7	2.0	4.6	1.1	1.4	0.7	7.8	3.5	2.9	2.4	2.3	2.7	2.5
Parameters																
Σ REE	41.2	40.8	42.2	42.9	49.4	61.8	41.7	49.3	55.7	62.7	104.9	81.4	84.5	87.1	72.8	81.6
Σ LREE	32.9	34.0	33.6	35.3	39.7	50.6	34.5	43.1	46.2	53.5	91.7	63.5	71.3	67.4	57.6	61.6
Σ HREE	8.2	6.8	8.6	7.5	9.7	11.2	7.2	6.2	9.5	9.2	13.2	17.9	13.2	19.7	15.2	20.0
LREE ratio	0.8	0.8	0.8	0.8	0.8	0.8	0.8	0.9	0.8	0.9	0.9	0.8	0.8	0.8	0.8	0.8
HREE ratio	0.2	0.2	0.2	0.2	0.2	0.2	0.2	0.1	0.2	0.1	0.1	0.2	0.2	0.2	0.2	0.2
Eu/Eu*	1.1	1.5	0.9	1.2	1.1	1.1	1.0	0.9	1.0	1.4	1.1	0.8	0.8	1.0	0.9	1.0
Alteration index	57.4	53.8	51.1	55.4	52.4	48.0	54.9	67.8	54.3	48.4	36.5	37.3	36.1	30.4	36.5	40.0
K_2O index	37.6	27.7	24.3	29.4	28.5	27.3	15.9	46.8	30.2	24.8	24.8	23.6	20.3	3.7	2.0	15.6
MgO index	19.8	26.0	26.8	25.9	23.9	20.6	39.0	21.0	24.1	23.5	11.7	13.7	15.8	26.7	34.5	24.3

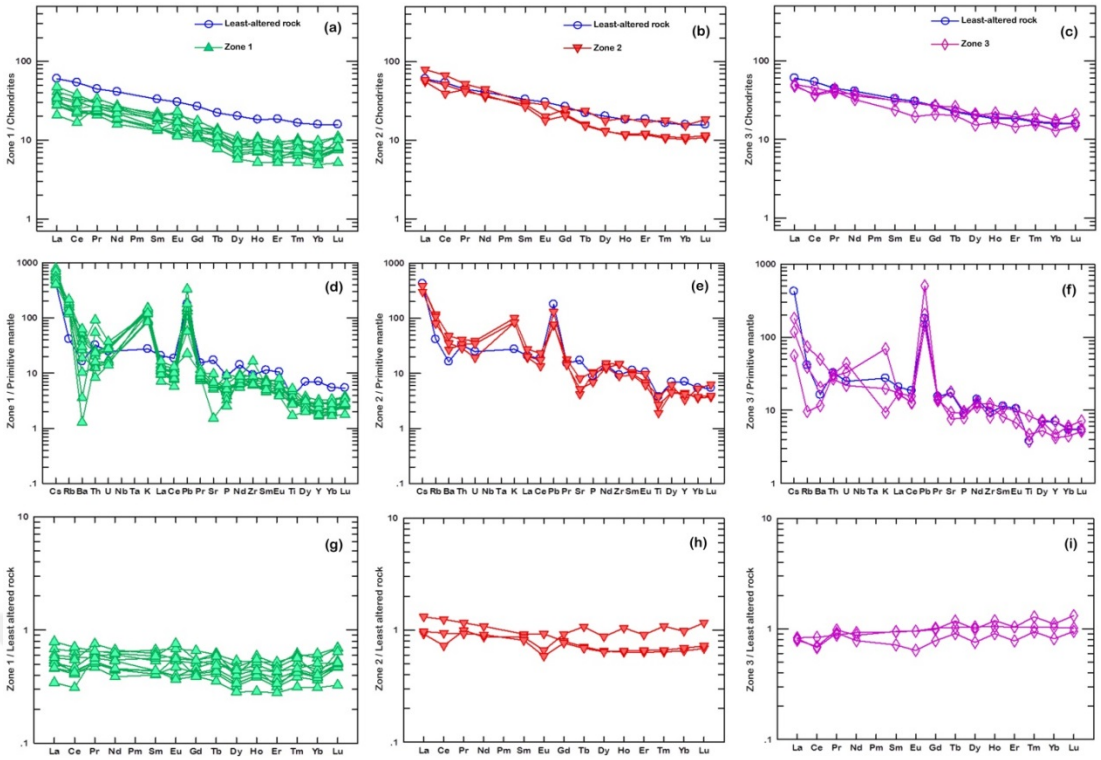

Figure 4.10 : a), b) & c) Chondrite-normalized REE patterns (Sun and McDonough, 1989) for zones 1, 2, and 3, respectively; d), e) & f) Primitive mantle-normalized trace element patterns (Sun and McDonough, 1989) for zones 1, 2, and 3, respectively; g), h) & i) Least altered rock-normalized REE patterns for zones 1, 2, and 3, respectively.

The parameters of REE of the altered rocks [LREE ratio (∑LREE/∑REE), HREE ratio (∑HREE/∑REE), and Eu-anomaly (Eu/Eu*)] are compared with the geochemical exploration indices in order to figure out the behavior of the REE during the different alteration types. The alteration index (A.I.) of Ishikawa et al. (1976), K_2O index (K.I.), and MgO index (M.I.) are calculated as follows (Shikazono et al., 2008):

$$A.I. = (MgO+K_2O) / (Na_2O+K_2O+CaO+MgO) \times 100$$

$$K.I. = K_2O / (Na_2O+K_2O+CaO+MgO) \times 1\ 00$$

$$M.I. = MgO / (Na_2O+K_2O+CaO+MgO) \times 1\ 00$$

In the hydrothermal alteration zones 1 and 2, where sericite and quartz prevail, the A.I. and K.I. show a positive correlation with LREE ratio and Eu/Eu*, and show a negative correlation with HREE ratio (Figures 4.11a-f). This refers to La, Eu, and K added to the rocks from hydrothermal solution during the alteration processes in these zones (LREE mobility in K-rich hydrothermal fluids). On the other hand, in alteration zone 3, where chlorite and calcite are common, the LREE ratio shows a

positive correlation with M.I. and negative one with A.I. and K.I. (Figures 4.11a-i) referring the and LREE were probably partially re-deposited during the chloritization alteration with Mg-enrichments. On the other hand, HREE anomalies with increasing M.I. in this zone 3 may suggest low solubility of these elements in alkaline hydrothermal solutions during chlorite and carbonate alterations.

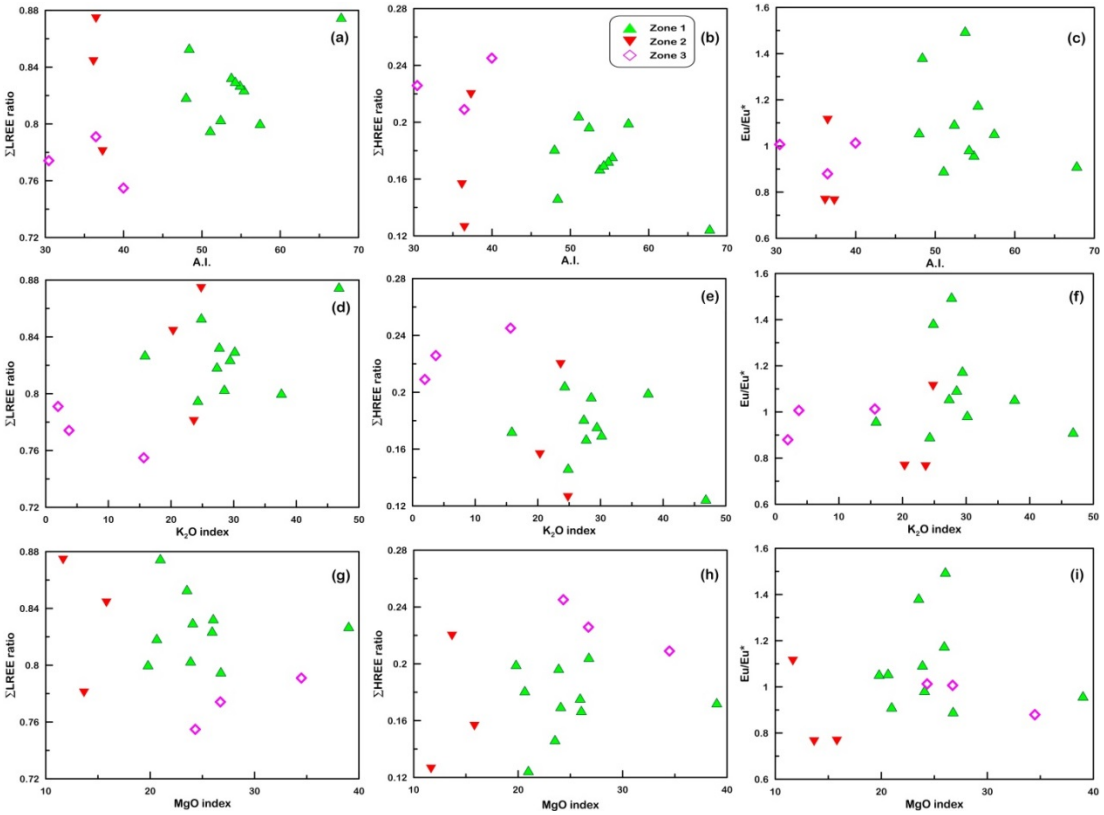

Figure 4.11 : Alteration index (A.I.) versus a) ∑LREE, b) ∑HREE, and c) Eu/Eu* for different alteration zones; K2O index (K.I.) versus d) ∑LREE, e) ∑HREE, and f) Eu/Eu* for different alteration zones; MgO index (M.I.) versus g) ∑LREE, h) ∑HREE, and i) Eu/Eu* for different alteration zones.

4.5.2 ASTER image processing

Abrams and Hook (1995) claimed ASTER as the multispectral space-borne sensor which discriminates and identifies the hydrothermal alteration minerals in the region of the shortwave infrared (SWIR) of the electromagnetic spectrum. The thermal infrared (TIR) bands provide the possibility of mapping silicate and carbonate minerals (Bedell, 2001; Ninomiya, 2003; Rockwell and Hofstra, 2008).

Cloud free ASTER level 1B (AST_L1B 00304012005082957 and 20120119100432) images of the Atud mine area are processed to produce band ratios (BR) and relative absorption band depth (RBD), principal component analysis (PCA), false-color

composite (FCC), and different mineral indices for deducing the distribution of the hydrothermal mineral phase in the mine area.

The minimum noise fraction transformation (MNF) is applied to the SWIR and VNIR bands of ASTER to reduce the computational requirements for subsequent processing by separating and balancing the noise in the data (Boardman and Kruse, 1994).

4.5.2.1 ASTER band ratios (BR) and relative absorption band depth (RBD) method

The band ratio transformation (BR) of ASTER data is powerful technique in visualizing the anomalies and quantitative detection of hydrothermal minerals (Abrams et al., 1983; Di Tommaso and Rubinstein, 2007). ASTER BR and Relative absorption Band Depth images (RBD; Crowley et al. (1989)) methods are useful in lithological mapping and classification depending on the spectral absorption characters of Al-OH and Fe^{2+}-mineral groups in felsic rocks, and Fe3+, Mg-OH-mineral groups in the mafic–ultramafic rocks (Rowan et al., 2005). The spectral features of Si-O commonly best explored in the TIR region to discriminate felsic from mafic rocks.

In this study, the composite color image of band ratios 4/5, 4/6, and 4/7 in RGB channels (He et al., 2010) give the Al-OH-bearing minerals in yellow and green (Figures 4.12a-b), while the Fe-OH-bearing minerals appear as blue in Figure (4.12a) and red in Figure (4.12c). Argillic alteration (kaolinite and sericite/muscovite; Al-OH-bearing minerals) is delineated by a combination of band ratios; 5/ 6, 7/ 6, 7/ 5 in RGB (Hewson et al., 2004) by characteristic yellowish and light bluish color (Figure 4.12d). The relative absorption band depth (RBD) method used to delineate the argillic alteration as well (Rowan and Mars, 2003), where argillic alteration assemblage appear as yellow or green color in 4+7/6, 5+7/6, and 7+9/8 in RGB channels (Figure 4.12e).

4.5.2.2 ASTER principal component analysis (PCA)

Principal Component Analysis (PCA; Singh and Harrison (1985)) is a multivariate statistical technique applied on VNIR and SWIR bands of ASTER to descriminate the different lithological units and alteration zones in metallogenic provinces (Ruiz-Armenta and Prol-Ledesma, 1998; Tangestani and Moore, 2001; Gomez et al.,

2005). In the study area, the first three principal components (PCA 1, PCA 2, PCA 3) in RGB are found efficient in mapping the different lithological units (Amer et al., 2012). Serpentinite and talc carbonate rocks appear as dark green; metasediments as bluish green; metavolcanics as blue, and gabbroic rocks as yellowish green, while the pink is alluvium (Figure 4.12f).

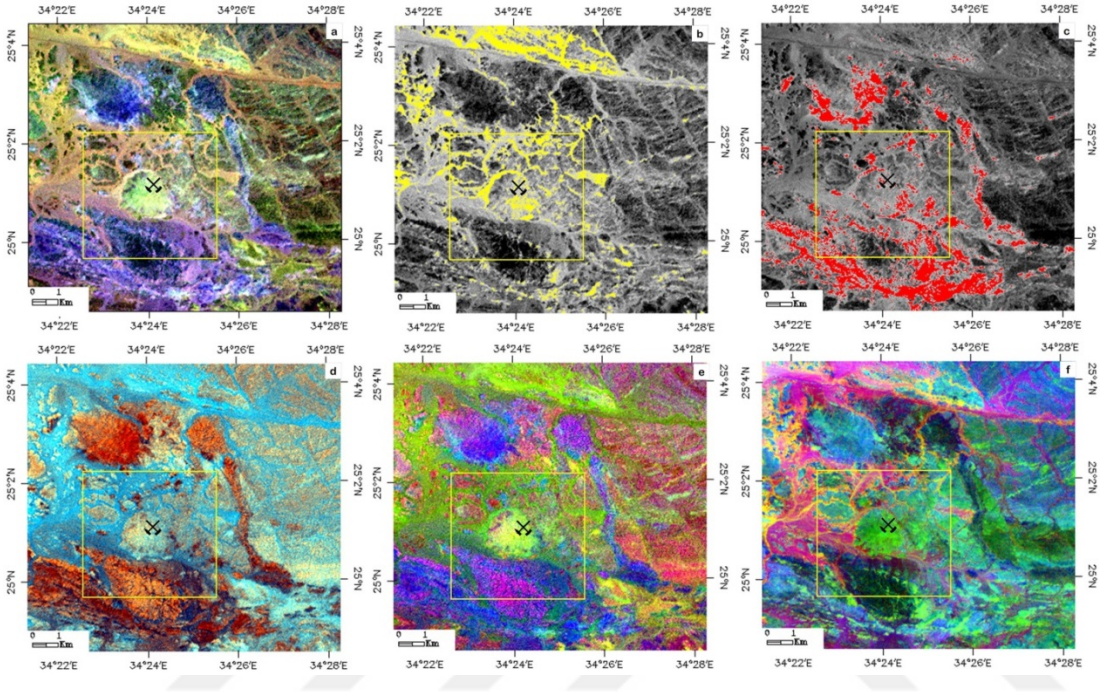

Figure 4.12 : a), b) & c) ASTER band ratio (4/5, 4/6, 4/7) in RGB, Al-OH-bearing minerals have yellow and green color (4.12a-b), Fe-OH-bearing minerals have bluish color (4.12a) and reddish color (4.12c); d) ASTER band ratio (5/6, 7/6, 7/5 in RGB), the argillic alteration show light yellowish and light bluish color; e) Relative absorption band depth (RBD) method of ASTER SWIR band ratios of [(4+7)/6] : [(5+7)/6] and [(7+9)/8] images in RGB, the argillic alteration shows yellowish to greenish color; f) Principal component analyses on ASTER data (PCA1, PCA2, PCA2 in RGB).

4.5.2.3 ASTER False-Color Composite (FCC) method

The False Color Composite (FCC) method is used to discriminate the different geologic units by the SWIR bands (Moghtaderi et al., 2007). The FCC image of [4/ 7, 2/ 4, and 6/ 8] in RGB (Zoheir and Emam, 2012) recognizes the different rock units in the Atud area; where the serpentinite rocks appear in yellowish green, the talc-carbonate rocks in light rose, the metagabbros show in brownish/pinkish green, and the metatuffs appear in purple (Figure 4.13a). ASTER bands 8, 5, and 6 are chosen to indicate the presence of calcite mineral because its strong absorption feature in band 8, and weak absorption in both bands 5 and 6 (Moghtaderi et al.,

2007). In the study area, the ASTER FCC image 856 in RGB shows calcite as pale to dark blue (Figure 4.13b-c).

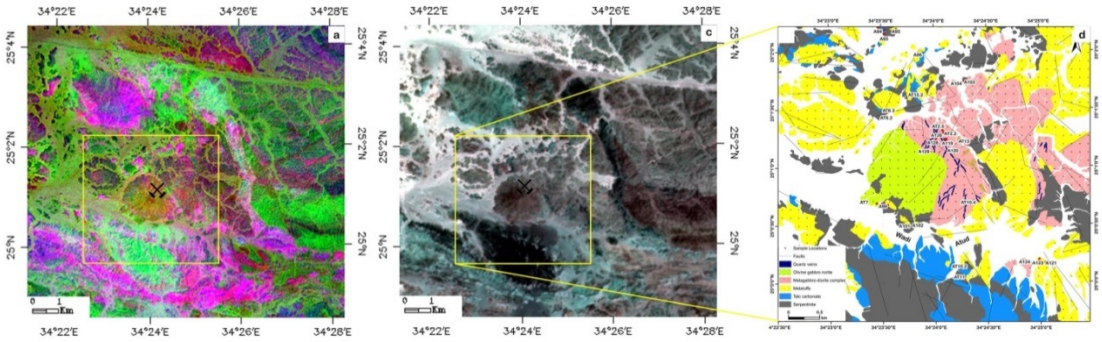

Figure 4.13 : a) FCC image of (4/7), (2/4), (6/8) in RGB differentiate the rock units in the Atud area (the serpentinite rocks in yellowish green, the talc-carbonate rocks in light rose, the metagabbros in brownish/pinkish green, and the metatuffs appear in purple color); b) FCC image of 8, 5, and 6 in RGB, calcite shows greenish to dark cyanic color; c) Geologic map of Atud area.

4.5.2.4 ASTER spectral indices for hydrothermal alteration zones

The Aster spectral mineralogical indices are useful in the discriminations of the lithological and hydrothermal alteration types (Ninomiya, 2003; Ninomiya and Fu, 2003; Ninomiya et al., 2005; Di Tommaso and Rubinstein, 2007; Zhang et al., 2007; Khan and Mahmood, 2008; Aboelkhair et al., 2010; Zoheir and Emam, 2014). The VNIR and SWIR band ratios are used to identify the mineral indices by using absorption features of the different minerals in the spectral range of ASTER (Ninomiya, 2003). For example, mineral indices (Ninomiya, 2003) including OH-bearing minerals (OHI), kaolinite (KLI), sericite (SRI), and calcite (CLI) are derived from the (VNIR + SWIR) bands by calculating given equations in ENVI 4.8^{TM} as follows :

OH-bearing altered minerals index (OHI) = ASTER bands (7 /6) x (4 /6)

Kaolinite index (KLI) = ASTER bands (4 /5) x (8 /6)

Sericite index (SRI) = ASTER bands (5 + 7 /6)

Calcite index (CLI) = ASTER bands (6 /8) x (9 /8)

The OH-mineral alteration and kaolinite- and sericite-rich zones are concentrated in the Main-Atud, Atud East-I, and Atud East-II areas. Identification of these alteration types is made by the miner indices of OH-bearing minerals (OHI), kaolinite (KLI), and sericite (SRI) (Figures 4.14a-c). These three indices refer to the argillic/sericitization alteration which is the main alteration type in the mine area.

Calcite index as pale blue shows high concentrations in the serpentinites and talc-carbonate rocks around Gabal Atud (Figure 4.14d). Three gray scale mineralogical indices – OHI, KLI, and CLI –are combined in the false-color composite (FCC) image in RGB channels (Zoheir and Emam, 2014) show that the carbonate-bearing rocks have blue image signature and OH-bearing rocks appear as yellow to orange (Figures 4.14e-f).

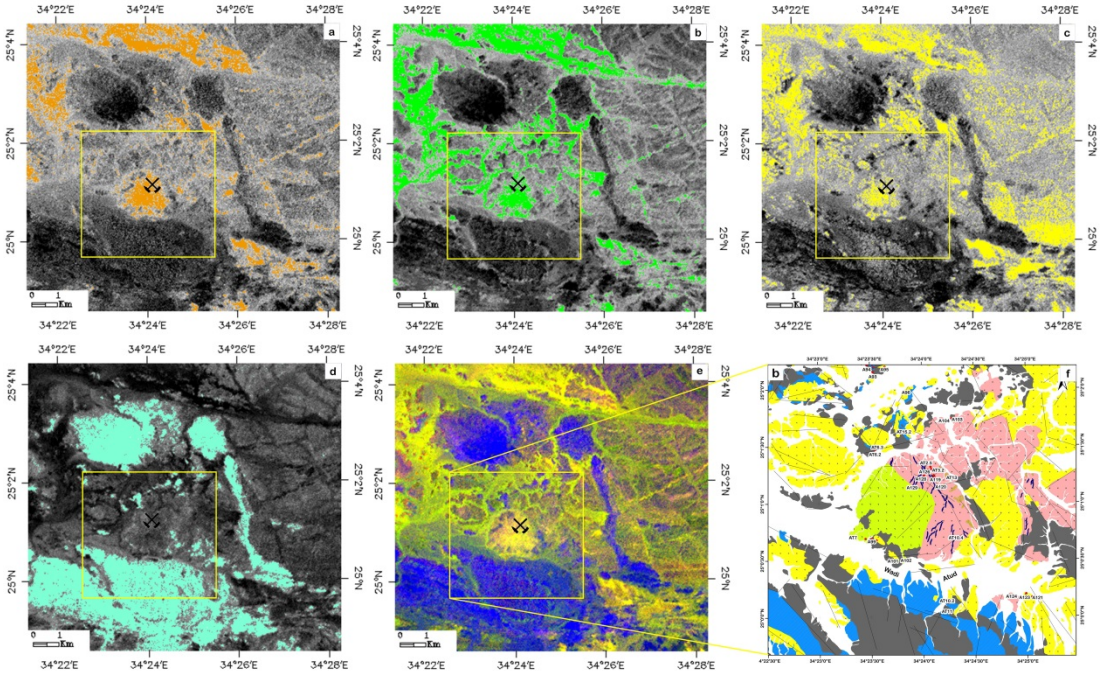

Figure 4.14 : a) Aster spectral mineralogical indices for alteration mineral mapping: a) OH-bearing minerals index (OHI); b) Kaolinite index (KLI); c) Sericite index (SRI); d) Calcite index (CLI); e) RGB FCC image (OHI, KLI, CLI), carbonate-bearing rocks have blue image signature and OH-bearing rocks appear as yellow to orange tones; f) Geological map of Atud mine area (Abdelnasser and Kumral, 2016).

4.6 Conclusions

Atud gold deposit represents a mesothermal vein-type gold deposit related to the gabbroic intrusion at the Central part of the Egyptian Eastern Desert. This gold-bearing quartz veins are associated with the intense greenschist facies hydrothermal alteration assemblages along the NW-SE brittle-ductile shear zones at the northeastern, eastern, southeastern slope of Gabal Atud.

The Atud mine area is made up of a metagabbro-diorite intrusion intruded into the serpentinites and metatuffs and was later intruded by olivine gabbronorite rocks. These rocks units were analyzed for major, trace, and rare earth elements (REE) geochemistry revealing that the following;

1) The serpentinites and their derivatives (talc-carbonate and calc-silicate rocks) are mostly metamorphic peridotites. The serpentinites have mainly antigorite-enstatite-talc-tremolite, while the talc-carbonate rocks have talc, tremolite, diopside, and dolomite, and calc-silicate rocks have tremolite-talc-quartz based on CMS-HC system of Bucher and Frey (1994). Light REE-enrichments and flat heavy REE, and positive Eu-anomaly characterize these rocks suggesting the oceanic serpentinization occurred with the plagioclase dissolution and/or circulation of the hydrothermal fluids.
2) The highest K/Rb ratio of the metatuffs reveals that these rocks were derived from magmatic suites with mostly basic, intermediate and rarely acidic affinities. They are mostly comparable with the metasediments of the oceanic island arc from calc-alkaline and tholeiitic rocks. Their REE pattern is similar to that of the continental arc basin (CAB) of McLennan et al. (1990) having LREE-enriched, HREE-depleted, and negative Eu-anomalies. In addition, their negative Eu-, Sr-, and Zr- anomalies refers to their source rocks had been formed from a magma contaminated by components added to the mantle source by subduction zone.
3) The olivine gabbronorite rocks are classified as gabbroic rocks having low-K tholeiitic magmatic affinities and compatible with the island-arc tholeiites (IAT) of Ikeda (1990). Their REE patterns reveal LREE-enrichment and nearly flat HREE with positive Eu-, Th-, Pb-, Sr-, and Zr-anomalies and negative P- and Ti-anomalies implying low-pressure fractionation of plagioclase and olivine.

Three subsurface hydrothermal alteration zones were occurred around the mineralized and barren quartz veins at the main Atud area; zone 1: quartz-sericite-pyrite, zone 2: quartz-chlorite-carbonate, and zone 3: calcite-albite-chlorite. Their REE pattern suggested that the sericite alteration in zones (1) and (2) companied with slight enrichments of LREE compared to HREE, referring to La, Eu, and K added to the rocks from hydrothermal solution during the alteration processes, while calcite and chlorite alterations are associated with Mg-enrichment with anomalies of HREE in zone 3, showing the HREE solubility occurred in alkaline hydrothermal solutions during these alterations.

On the other hand, the sericite/kaolinite alterations are the main alteration on the surface at Atud mine area with subordinate ferrugination and carbonate alteration. These alteration types were delineated using ASTER-image processing techniques [e.g. band ratios (BR), relative absorption band depth (RBD), principal component analysis (PCA), false-color composite (FCC), and mineral index method (OH-bearing minerals (OHI), kaolinite (KLI), sericite (SRL), and calcite (CLI) indices)] as followings;

1) Al-OH and Fe-OH bearing minerals were detected at the main Atud area using ASTER BR [(4 / 5), (4 / 6), and (4 / 7)] in RGB, and argillic alteration by ASTER BR [(5 / 6), (7 / 6), and (7 / 5)] in RGB and ASTER RBD [(4 + 7) / 6, (5 + 7) / 6, and (7+ 9) / 8] images in RGB.
2) The rock unit discriminations at the study area were noticed with ASTER PCA (PCA-1, PCA-2, PCA-3 in RGB) and ASTER FCC image of [(4 / 7), (2 / 4), (6 / 8) in RGB.
3) The ASTER spectral mineralogical indices reveal that sericitic and argillic (kaolinite) alterations have been successfully detected associated with the gold mineralization at the Atud mine areas (Main-Atud, Atud East-I, and Atud East-II), while carbonate (calcite and dolomite) alterations and ferrugination are exposed with the serpentinites and talc-carbonate rocks around Gabal Atud.

5. CONCLUSIONS

- Atud gold deposit represents a mesothermal orogenic vein-type gold deposit related to the gabbroic intrusion at the Central part of the Egyptian Eastern Desert in the Arabian-Nubian Shield (ANS). This gold-bearing quartz veins are associated with the intense greenschist facies hydrothermal alteration assemblages along the NW-SE brittle-ductile shear zones at the northeastern, eastern, southeastern slope of Gabal Atud and the eastern part of the study area.
- The Field relationships, geologic, and petrographic studies reveal that the Atud mine area is made up of a metagabbro-diorite intrusion intruded into the pre-existing rocks; serpentinite and metatuffs, and is cut by a younger intrusion of olivine gabbronorite.
- The dispersed talc-carbonate, dolomitic marble, and calc-silicate rocks are derivatives of serpentinite around Gabal Atud. The large serpentinite masses crop out south and southeast of Gabal Atud and are associated with the talc serpenitintes and talc carbonate rocks. Serpentinite is tectonically incorporated in the metatuffs and is composed mainly of antigorite with subordinate amounts of tremolite, actinolite, graphite, and chromite. In the southern part of the study area, talc-carbonate covers a vast area association with metatuffs and serpentinite, and composed mainly of talc and dolomite with minor amount of antigorite, actinolite, and chromite. Dolomitic marble occur as small isolated masses at the southern slope of Gabal Atud associated with the metagabbro-dioritic rocks. It consists mainly of dolomite with disseminated chromite and goethite. On the other hand, at the northern part of the study calc-silicate rocks are associated with metatuffs and composed mainly of ankerite, calcite, and quartz with minor amounts of clinochlore, epidote, and chromite. Geochemically, these rocks - serpentinites and their derivatives (talc-carbonate and calc-silicate rocks) - are mostly metamorphic peridotites. Based on CMS-HC system of Bucher and Frey (1994), the serpentinites have mainly antigorite-enstatite-talc-tremolite assemlages, talc-carbonate rocks have an assemblage of talc, tremolite, diopside, and dolomite, while, calc-silicate

rocks have tremolite-talc-quartz assemblages. These rocks, based on the REE pattern, are characterized by light REE-enrichments and flat heavy REE, and positive Eu-anomaly revealing the oceanic serpentinization occurred with the plagioclase dissolution and/or circulation of the hydrothermal fluids.

- Metatuffs cover a vast area of the area around Gabal Atud forming low-relief terrane. These rocks are differentiated into fine-grained mafic lapilli metatuffs, intermediate metatuffs, metacherts, and quartz-biotite schists. Mafic lapilli metatuffs are associated with talc-carbonate and serpentinite in Wadi Atud at the southern part of the study area consisting mainly of plagioclase and microperthite, tremolite, clinopyroxene, clinozoisite, and magnetite phenoblasts in a microcrystalline tuffaceous matrix. While, the intermediate metatuffs occur in the northern part of the study area associated with the calc-silicate rocks and composed mainly of microperthite, phlogopite, and quartz with biotite and magnetite embedded in a very fine groundmass. Metachert is observed at the southern slope of Gabal Atud associated with the sepentinite rocks forming alternated quartz- and feldspar-rich laminations. On the other hand quartz-biotite schists form strongly foliated outcrops at the southern slope of Gabal Atud consisting of quartz and biotite with K-feldspar and minor amounts of muscovite, carbonate, and magnetite. The geochemical data of these rocks reveal that based on the K/Rb ratio, they were derived from magmatic suites with mostly basic, intermediate and rarely acidic affinities that are compatible with metasediments of the oceanic island arc from calc-alkaline and tholeiitic rocks. The REE geochemical data suggested that their REE pattern is similar to that of the continental arc basin (CAB) of McLennan et al. (1990). They are characterized by LREE-enrichments, HREE-depletions, and negative Eu-, Sr-, and Zr- anomalies revealing their source rocks had been formed from a magma contaminated by components added to the mantle source by subduction zone.
- The metagabbro-diorite complex represents the main body of Gabal Atud that formed by the gabbro-diorite intrusion. This intrusion is assumed to belong to the Neoproterozoic island arc assemblage in the Egyptian basement complex cut the serpentinite and metatuff at Atud area showing a sharp intrusive contact against them. It is later intruded by the late-tectonic olivine gabbronorite. This complex is differentiated into slightly metamorphosed gabbro and diorite rocks with hybrid leucocratic gabbro zone in between at Gabal Atud. It is also cut by numerous

mineralized and non-mineralized quartz veins and dikes at the eastern and southeastern slopes of Gabal Atud, where NW-SE brittle-ductile shear zone occurred. The metagabbroic rocks are composed mainly of calcic plagioclase (variably sericitized, and kaolinitized), actinolite, and tremolite with subordinate amounts of chlorite and quartz. Relicts of clinopyroxene and orthopyroxene, hornblende, and magnetite are still preserved in some samples. While, the diorite occurs as a grayish, medium to coarse-grained rock with hypidiomorphic texture of plagioclase, quartz, chlorite, hornblende, and iron oxides. The geochemical data of these rocks shows that metagabbros are classified as calc-alkaline gabbro and gabbro/diorite as well as are comparable to the calc-alkaline basalt (CAB) formed in the island arc environments having clinopyroxene fractionation. While, the dioritic rocks are calc-alkaline diorite and gabbro/diorite formed in the island arc environments that had amphibole fractionation. Their REE geochemical data and profiles revealed that they are characterized by LREE-enrichments and HREE-depletions with positive Eu- and Sr-anomalies referring to plagioclase accumulations.

- The olivine gabbronorite rocks which form a small intrusion cutting the gabbro-diorite complex of Gabal Atud, pertain to the younger gabbro of Ghoneim (1989). They show no ductile or brittle deformation, implying a post-tectonic setting, and consist mainly of coarse-to-medium-grained crystals of plagioclase (labradorite to bytownite), diopside (partly altered to actinolite and tremolite), hypersthene, cumulate olivine (partly altered into antigorite), and iron oxide. Geochemically, these rocks are classified as gabbroic rocks having low-K tholeiitic magmatic affinities and compatible with the island-arc tholeiites (IAT) of Ikeda (1990). Their REE patterns reveal LREE-enrichment and nearly flat HREE with positive Eu-, Th-, Pb-, Sr-, and Zr-anomalies and negative P- and Ti-anomalies implying low-pressure fractionation of plagioclase and olivine.
- There are different types of dykes cut through the country rocks in the mine area, trend mainly in two directions. The oldest one is NNE-SSW and the youngest is NW-SE. Lamprophyre dykes occupy commonly the old direction (NNE-SSW) and cut through the serpentinite rocks, while porphyritic andesite and aplitic dykes occupy the NW-SE direction and cut through the gabbro-diorite intrusion. The aplite dyke samples are yellowish, fine-grained rocks with porphyritic textures consisting mainly of phenocrysts of carbonatized plagioclase, biotite and/or

phlogopite (partly altered to chlorite) in a carbonate-rich groundmass with K-feldspar, quartz, sericite, and iron oxide.

- The Gold mineralization at Atud area occurred in three areas: the main Atud occurring on the eastern and northeastern slopes of Gabal Atud, Atud East-I (NE of the Atud area), and Atud East-II (SE of the Atud area). The main Atud mineralization was genetically related to the metagabbro-diorite complex that was intruded by quartz veins. The mineralization was associated with a NNW-SSE brittle-ductile shear zone within hydrothermal alteration zones and quartz veins that occupy the pre-existing fractures. The Atud gold mine is one of many in the Egyptian Eastern Desert that was exploited during Pharaonic times (New Kingdom times) and Roman and Byzantine times, but no ore has been produced since then (Gabra, 1986). At the mid-20 century the Egyptian Geologic Survey and Mining Authority (EGSMA) worked in detail at the Atud gold mine, including surface and subsurface geological studies, drilling, mapping, mine workings and sampling of the altered rocks, quartz veins and country rocks.
- In the subsurface levels, according to the geological, petrographical and XRD analytical studies, three main hydrothermal alteration zones were observed around the quartz veins in the main Atud area; zone 1: quartz-sericite-pyrite, zone 2: quartz-chlorite-carbonate, and zone 3: calcite-albite-chlorite. The ore mineralogy includes mainly arsenopyrite and pyrite, with minor amounts of chalcopyrite, sphalerite, and enargite with goethite, associated with gold mineralization. These ore minerals disseminated the quartz veins and adjacent alteration zones, especially in the vein-wallrock contact.
- GEOISO-Windows calculated the mass/volume gain and loss values, with Al_2O_3 considered as an immobile element. The mass balance calculations and isocon diagrams concluded that K_2O, Au, S, and Sb decrease from alteration zone 1 to zone 2, indicating that gold mineralization is highly related to sericitic, kaolinitic and muscovite alteration. Zone 3, which has a high amount of CaO, Fe_2O_3, and Na_2O with K_2O – indicating carbonatization, chloritization and albitization – is characterized by a lower amount of gold. Therefore, gold decreases from zone 1 outwards to zone 3. The LREE patterns of samples collected from these alteration types reveal slight enrichments compared to significant ones in HREE associated with sericite alteration in zone (1) and (2). The alteration zone 3 shows a different pattern of strong anomalies of LREE and weak anomalies of HREE. The LREE

and Eu enrichment is correlated with the Alteration index (A.I.) and K_2O index (K.I.) in types 1 and 2, suggesting LREE mobility in K-rich hydrothermal fluids. On the other hand, HREE anomalies with increasing MgO index (M.I.) in zone 3 may imply low solubility of these elements in alkaline hydrothermal solutions during chlorite and carbonate alterations.

- The geologic, petrographic and structural features of quartz veins reveal that they extended for 305 m in metagabbro-diorite rocks in the main Atud mine area with a few centimeters to 2 meters. These veins were formed in three stages of mineralization subdivided into; (1) early mineralized quartz veins having bluish- to dark-grey colored and subhedral medium to coarse grained quartz crystals with serrated grain boundaries; (2) main mineralized quartz veins are laminated veins exhibiting numerous features representative of ductile deformation and characterized by euhedral to subhedral, coarse-grained crystals with undulate extinction and granulated grain boundaries (refering to bulging recrystallization (BLG) deformation with bulged and recrystallized subgrains along the boundaries of the original quartz grain boundaries occurred at temperatures of around 280 to 400°C of Stipp et al. (2002)); and (3) late quartz-carbonate veins ranging from a few centimeters to 0.6 m thick post-dated all other quartz types, comprising milky quartz and calcite with pyrite.
- The microprobe data of the alteration minerals revealed that the sericite has a high muscovite component in all analyzed flakes (average X_{Ms} = 0.89) and a phengite content ranging from 0.10 to 0.55 and 0.13 to 0.29 in wall rocks and mineralized veins, respectively. Carbonate has higher amounts of calcite ($CaCO_3$) and lower amounts of $MgCO_3$ and $FeCO_3$ in wall rocks than in quartz veins. Chlorite flakes are generally iron-rich (FeO^t 20.64–20.10 wt.%) and are composed of pycnochlorite and ripidolite, with $Al^{(iv)}$ = 2.30-2.36 pfu and 2.41-2.51 pfu, respectively and estimated formation temperatures of 289–295°C and 301-312°C, respectively. Albite is accompanied with chlorite but was generally pure in all samples (Ab = 95.08%-99.20%).
- While, the microprobe data of the ore minerals associated with gold mineralization concluded that in the first phase of mineralization, arsenopyrite and type-I pyrite formed together with early mineralized quartz veins and altered host rocks. On the other hand, during the second phase of mineralization type-II pyrite (As-rich) associated with gold and other sulfides and recrystallized small polygonal quartz

subgrains. Under supergene conditions, the goethite was formed during the last stage of mineralization. Gold is classified as electrum (52.2 to 60.7 atom % Au & 36.7 to 39.1 atom % Ag). Based on the application of geothermometer of Kretschmar and Scott (1976), As-contents (29.3-32.7 at. %) in arsenopyrite point to deposition in the f_{S2} and T ranges of -10.5 to -5.5 and 305-450 °C, respectively during the main mineralization phase. This indicates that the gold is transported and precipitated due to increasing lack of the hydrosulphide complexes AuHS° and $Au(HS)^-_2$.

- $\delta^{34}S$ isotope data of the sulfide minerals from the main mineralized quartz veins (As-bearing pyrite: +2.8 $‰_{VCDT}$ and arsenopyrite: 8.3-9.5 $‰_{VCDT}$) show slightly similar values to those from the altered host rocks (As-bearing pyrite: 0.7-3.9 $‰_{VCDT}$ and arsenopyrite: 6.2-7.8 $‰_{VCDT}$) suggesting a uniform sulfur source. This indicates that they are formed from magmatic fluids, in which the sulfur is either sourced directly from magma or remobilized from the magmatic rocks. While, $\delta^{13}C$ and $\delta^{18}O$ isotope data of the calcite range from -10.6 to -8.0 $‰_{VPDB}$ and from 13.1 to 14.5 $‰_{SMOW}$, respectively, revealing that this calcite formed from fluids having mainly magmatic mixed with variable metamorphic signatures.
- The surface main alteration types are sericite and kaolinite alteration are observed at the main Atud area with subordinate carbonate alteration and ferrugination at the southern part of Gabal Atud. ASTER-image processing was done in order to delineate these alteration types and discriminate the different rock units at the study area. By using ASTER band ratio (BR) and relative absorption band depth (RBD) detect the Al-OH and Fe-OH bearing minerals at the main Atud area. ASTER principal component analysis (PCA) and ASTER FCC image discriminate the different rock units at the study area. OH-bearing minerals (OHI), kaolinite (KLI), sericite (SRL) indices reveal that the sericitic and argillic (kaolinite) alterations have been successfully detected associated with the gold mineralization at the Atud mine areas (Main-Atud, Atud East-I, and Atud East-II), while calcite alteration and ferrugination are exposed with the serpentinites and talc-carbonate rocks around Gabal Atud.

REFERENCES

Abdelnasser, A. and Kumral, M. 2016. Mineral chemistry and geochemical behavior of hydrothermal alterations associated with mafic intrusive-related Au deposits at the Atud area, Central Eastern Desert, Egypt. *Ore Geology Reviews, 77*: 1-24.

Abdelnasser, A., Kumral, M., Zoheir, B.A., Weihed, P., Budakoglu, M. and Gumus, L. 2014a. Micro-Analytical Data of Au Mineralization at Atud Gold Deposit, Eastern Desert, Egypt, International Conference on Earth Science and Climate Change (ICESCC 2014).

Abdelnasser, A., Kumral, M., Zoheir, B.A., Weihed, P., Yildrim, D.K. and Karaman, M. 2014b. Hydrothermal alteration geochemistry of Atud gold deposits at the central block of the Egyptian Eastern Desert, Egypt: Insights provided by mass-balance calculations, Goldschmidt 2014 (Gold2014), Sacramento, California, USA.

Abdelrahman, A.M. and Doig, R. 1987. The Rb-Sr geochronological evolution of the Ras Gharib segment of the northern Nubian Shield. *Journal of the Geological Society, 144*(4): 577-586.

AbdelTawab, M. 1992. Gold exploration in Egypt from Pharoanic to modern times. *Zentralbl Geol Paläont Teil, 1*(1991): 2721-2733.

Aboelkhair, H., Ninomiya, Y., Watanabe, Y. and Sato, I. 2010. Processing and interpretation of ASTER TIR data for mapping of rare-metal-enriched albite granitoids in the Central Eastern Desert of Egypt. *Journal of African Earth Sciences, 58*(1): 141-151.

Abrams, M. and Hook, S.J. 1995. Simulated ASTER data for geologic studies. *Geoscience and Remote Sensing, IEEE Transactions on, 33*(3): 692-699.

Abrams, M.J., Brown, D., Lepley, L. and Sadowski, R. 1983. Remote sensing for porphyry copper deposits in southern Arizona. *Economic Geology, 78*(4): 591-604.

Amer, R., Kusky, T. and El Mezayen, A. 2012. Remote sensing detection of gold related alteration zones in Um Rus area, Central Eastern Desert of Egypt. *Advances in Space Research, 49*(1): 121-134.

Armstrong, J.T. 1995. Citzaf-a package of correction programs for the quantitative Electron Microbeam X-Ray-Analysis of thick polished materials, thin-films, and particles. *Microbeam Analysis, 4*(3): 177-200.

Barton, M.D., Staude, J.-M., Snow, E.A. and Johnson, D.A. 1991. Aureole systematics. *Reviews in Mineralogy and Geochemistry, 26*(1): 723-847.

Barton, P.B. 1969. Thermochemical study of the system Fe-As-S. *Geochimica et Cosmochimica Acta, 33*(7): 841-857.

Bedell, R. 2001. Geological mapping with ASTER satellite: new global satellite data that is a significant leap in remote sensing geologic and alteration mapping. *Special Publication Geology Society of Nevada, 33*: 329-334.

Bertrand, J. and Caby, R. 1978. Geodynamic evolution of the Pan-African orogenic belt: a new interpretation of the Hoggar Shield (Algerian Sahara). *Geologische Rundschau, 67*(2): 357-388.

Bhatia, M.R. 1983. Plate tectonics and geochemical composition of sandstones. *The Journal of Geology*: 611-627.

Bierlein, F.P., Arne, D.C. and Cartwright, I. 2004. Stable isotope (C, O, S) systematics in alteration haloes associatedwith orogenic gold mineralization in the Victorian gold province, SE Australia. *Geochemistry: Exploration, Environment, Analysis, 4*(3): 191-211.

Boardman, J.W. and Kruse, F.A. 1994. Automated spectral analysis: a geological example using AVIRIS data, north Grapevine Mountains, Nevada, Proceedings of the Thematic Conference on Geologic Remote Sensing. *Environmental Research Institute of Michigan*, pp. I-407.

Botros, N.S. 2004. A new classification of the gold deposits of Egypt. *Ore Geology Reviews, 25*(1): 1-37.

Braune, v.H. and Peter, S. 1951. Die Dissoziation des Schwefeldampfes. *Zeitschrift für Naturforschung A, 6*(1): 32-37.

Brown, L.D., Reilinger, R.E., Holdahl, S.R. and Balazs, E.I. 1977. Postseismic crustal uplift near Anchorage, Alaska. *Journal of Geophysical Research, 82*(23): 3369-3378.

Bucher, K. and Frey, M. 1994. Petrogenesis of metamorphic rocks. 6th edn and complete revision of Winkler's textbook. *Springer-Verlag, New York*.

Burke, K. and Sengör, C. 1986. Tectonic escape in the evolution of the continental crust. *Reflection seismology: the continental crust*: 41-53.

Caby, R., Dostal, J. and Dupuy, C. 1977. Upper Proterozoic volcanic graywackes from northwestern Hoggar (Algeria)—geology and geochemistry. *Precambrian Research, 5*(3): 283-297.

Carr, M. 2007. Igpet 2007 for Windows XP or Vista. *Terra Softa Inc*.

Cathelineau, M. 1988. Cation site occupancy in chlorites and illites as function of temperature. *Clay minerals, 23*(4): 471-85.

Chaussidon, M. and Lorand, J.-P. 1990. Sulphur isotope composition of orogenic spinel lherzolite massifs from Ariege (North-Eastern Pyrenees, France): An ion microprobe study. *Geochimica et Cosmochimica Acta, 54*(10): 2835-2846.

Coelho, J. 2006. GEOISO—a Windows™ program to calculate and plot mass balances and volume changes occurring in a wide variety of geologic processes. *Computers & Geosciences, 32*(9): 1523-1528.

Coleman, R. 1977. Ophiolites Springer-Verlag. *New York, NY*.

Condie, K.C., Macke, J.E. and Reimer, T.O. 1970. Petrology and geochemistry of early Precambrian graywackes from the Fig Tree Group, South Africa. *Geological Society of America Bulletin, 81*(9): 2759-2776.

Cox, K.G., Bell, J.D. and Pankhurst, R.J. 1979. The Interpretation of Igneous Rocks. *George Allen & Unwin*.

Crowley, J.K., Brickey, D.W. and Rowan, L.C. 1989. Airborne imaging spectrometer data of the Ruby Mountains, Montana: mineral discrimination using relative absorption band-depth images. *Remote Sensing of Environment, 29*(2): 121-134.

Czamanske, G.K. and Rye, R.O. 1974. Experimentally determined sulfur isotope fractionations between sphalerite and galena in the temperature range 600 degrees to 275 degrees C. *Economic Geology, 69*(1): 17-25.

Debret, B., Andreani, M., Godard, M., Nicollet, C., Schwartz, S. and Lafay, R. 2013. Trace element behavior during serpentinization/de-serpentinization of an eclogitized oceanic lithosphere: A LA-ICPMS study of the Lanzo ultramafic massif (Western Alps). *Chemical geology, 357*: 117-133.

Deer, W., Howie, R. and Zussman, J. 1992. An Introduction to the Rock Forming Minerals. *Longman, London*.

Deschamps, F., Guillot, S., Godard, M., Chauvel, C., Andreani, M. and Hattori, K. 2010. In situ characterization of serpentinites from forearc mantle wedges: timing of serpentinization and behavior of fluid-mobile elements in subduction zones. *Chemical geology, 269*(3): 262-277.

Di Tommaso, I. and Rubinstein, N. 2007. Hydrothermal alteration mapping using ASTER data in the Infiernillo porphyry deposit, Argentina. *Ore Geology Reviews, 32*(1): 275-290.

Douville, E., Charlou, J., Oelkers, E., Bienvenu, P., Colon, C.J., Donval, J., Fouquet, Y., Prieur, D. and Appriou, P. 2002. The rainbow vent fluids (36 14′ N, MAR): the influence of ultramafic rocks and phase separation on trace metal content in Mid-Atlantic Ridge hydrothermal fluids. *Chemical geology, 184*(1): 37-48.

Drury, S., Holt, R., Van Clasteren, P. and Beckinsale, R. 1983. Sm-Nd and Rb-Sr ages for Archaean rocks in western Karnataka, south India.

Dubé, B. and Gosselin, P. 2007. Greenstone-hosted quartz-carbonate vein deposits. *Mineral Deposits of Canada: A synthesis of major deposit-types, district metallogeny, the evolution of geological provinces, and exploration methods: Geological Association of Canada, Mineral Deposits Division, Special Publication, 5*: 49-73.

Ducart, D.F., Crósta, A.P., Souza Filho, C.R. and Coniglio, J. 2006. Alteration mineralogy at the Cerro La Mina epithermal prospect, Patagonia, Argentina: Field mapping, short-wave infrared spectroscopy, and ASTER images. *Economic Geology, 101*(5): 981-996.

EGSMA 1981. Geologic Map of Egypt, Scale 1:2,000,000. *Egyptian Geological Survey and Mining Authority*.

El-Bouseily, A., El-Dahhar, M. and Arslan, A. 1985. Ore-microscopic and geochemical characteristics of gold-bearing sulfide minerals, El Sid Gold Mine, Eastern Desert, Egypt. *Mineralium Deposita, 20*(3): 194-200.

El-Gaby, S., List, F. and Tehrani, R. 1988. Geology, evolution and metallogenesis of the Pan-African Belt in Egypt. *The Pan-African belt of Northeast Africa and adjacent areas*: 17-68.

El-Taher, A., Kratz, K.-L., Nossair, A. and Azzam, A. 2003. Determination of gold in two Egyptian gold ores using instrumental neutron activation analysis. *Radiation physics and chemistry, 68*(5): 751-755.

Exley, R., Mattey, D., Clague, D. and Pillinger, C. 1986. Carbon isotope systematics of a mantle "hotspot": a comparison of Loihi Seamount and MORB glasses. *Earth and planetary science letters, 78*(2): 189-199.

Floyd, P. 1993. Geochemical discrimination and petrogenesis of alkalic basalt sequences in part of the Ankara melange, central Turkey. *Journal of the Geological Society, 150*(3): 541-550.

Floyd, P. and Leveridge, B. 1987. Tectonic environment of the Devonian Gramscatho basin, south Cornwall: framework mode and geochemical evidence from turbiditic sandstones. *Journal of the Geological Society, 144*(4): 531-542.

Gabra, S. 1986. Gold in Egypt: A commodity package, minerals, petroleum and groundwater assessment program: USAID project 363-0105. *Geological Survey of Egypt*.

Garson, M. and Shalaby, I.M. 1976. Precambrian-Lower Paleozoic plate tectonics and metallogenesis in the Red Sea region.

Ghoneim, M. 1989. Mineral chemistry of some gabbroic rocks of the central Eastern Desert, Egypt. *Journal of African Earth Sciences (and the Middle East), 9*(2): 289-295.

Gomez, C., Delacourt, C., Allemand, P., Ledru, P. and Wackerle, R. 2005. Using ASTER remote sensing data set for geological mapping, in Namibia. *Physics and Chemistry of the Earth, Parts A/B/C, 30*(1): 97-108.

Grant, J.A. 1986. The isocon diagram; a simple solution to Gresens' equation for metasomatic alteration. *Economic Geology, 81*(8): 1976-1982.

Grant, J.A. 2005. Isocon analysis: a brief review of the method and applications. *Physics and Chemistry of the Earth, Parts A/B/C, 30*(17): 997-1004.

Gresens, R.L. 1967. Composition-volume relationships of metasomatism. *Chemical geology, 2*: 47-65.

Groves, D.I., Goldfarb, R.J., Gebre-Mariam, M., Hagemann, S. and Robert, F. 1998. Orogenic gold deposits: a proposed classification in the context of their crustal distribution and relationship to other gold deposit types. *Ore Geology Reviews, 13*(1): 7-27.

Harraz, H.Z. 1999. Wall rock alteration, Atud gold mine, Eastern Desert, Egypt: processes and P-T-XCO2 conditions of metasomatism. *Journal of African Earth Sciences, 28*(3): 527-551.

Harraz, H.Z. 2002. Fluid inclusions in the mesozonal gold deposit at Atud mine, Eastern Desert, Egypt. *Journal of African Earth Sciences, 35*(3): 347-363.

Harraz, H.Z. and Ashmawy, M. 1994. Structural and lithogeochemical constraints on the localization of gold deposits at the El Sid-Fawakhir gold mine area, Eastern Desert, Egypt. *Egyptian Journal Geology, 38*: 629-648.

Harraz, H.Z., Hassanen, M. and El Dahhar, M. 1992. Fluid inclusions and stable isotopic studies at El-Sid gold mine, Eastern Desert, Egypt. *Egyptian Journal of Geology, 36*(1-2): 243-332.

Harrell, J.A. and Brown, V.M. 1992. The World's oldest surviving geological map: the 1150 BC Turin Papyrus from Egypt. *The Journal of Geology*: 3-18.

Hashad, A. 2015. Present status of geochronological data on the Egyptian basement complex. *Evolution and mineralization of the Arabian-Nubian shield, 1*: 31-46.

Hassaan, M. and El Mezayen, A. 1995. Genesis of gold mineralization in Eastern Desert, Egypt. *Al-Azhar Bulletin of Science, 6*: 921-939.

Hassanipak, A., Ghazi, A.M. and Wampler, J. 1996. Rare earth element characteristics and K-Ar ages of the Band Ziarat ophiolite complex, southeastern Iran. *Canadian Journal of Earth Sciences, 33*(11): 1534-1542.

Hawkesworth, C., O'nions, R., Pankhurst, R., Hamilton, P. and Evensen, N. 1977. A geochemical study of island-arc and back-arc tholeiites from the Scotia Sea. *Earth and planetary science letters, 36*(2): 253-262.

He, Z., He, B. and Cui, Y. 2010. Hydrothermal alteration mapping using aster data in East Kunlun Mountains, China, Geoscience and Remote Sensing Symposium (IGARSS), 2010 IEEE International. *IEEE*, pp. 4514-4517.

Hewson, R., Cudahy, T., Burtt, A., Okada, K. and Mauger, A. 2004. Assessment of ASTER imagery for geological mapping within the Broken Hill and Olary domains, Proceedings of the 12-th Australasian Remote Sensing and Pho togrammetric Conference, pp. 12.

Hey, M.H. 1954. A new review of the chlorites. *Mineralogical Magazine, 30*: 277-292.

Hilmy, M.E. and Osman, A. 1989. Remobilization of gold from a chalcopyrite-pyrite mineralization Hamash gold mine, Southeastern Desert, Egypt. *Mineralium Deposita, 24*(4): 244-249.

Hoefs, J. 1997. Stable isotope geochemistry, *201*. *Springer*.

Hoefs, J. 2008. Stable isotope geochemistry. *Springer Science & Business Media*.

Hunt, G.R., Salisbury, J.W. and Lenhoff, C.J. 1973. Visible and near infrared spectra of minerals and rocks. VI. Additional silicates. *Modern geology, 4*: 85-106.

Hussein, A. and El Sharkawi, M. 1990. Mineral deposits. *The Geology of Egypt. Balkema, Rotterdam*: 511-566.

Ikeda, Y. 1990. CeN/SrN/SmN-Atrace-element discriminant for basaltic rocks from different tectonomagmatic environments. *NEUES JAHRBUCH FUR MINERALOGIE-MONATSHEFTE*(4): 145-158.

Irvine, T. and Baragar, W. 1971. A guide to the chemical classification of the common volcanic rocks. *Canadian Journal of Earth Sciences, 8*(5): 523-548.

Ishikawa, Y., Sawaguchi, T., Iwaya, S. and Horiuchi, M. 1976. Delineation of prospecting targets for Kuroko deposits based on modes of volcanism of underlying dacite and alteration halos. *Mining Geology, 26*: 105-117.

Khan, S.D. and Mahmood, K. 2008. The application of remote sensing techniques to the study of ophiolites. *Earth-Science Reviews, 89*(3): 135-143.

Klemm, D., Klemm, R. and Murr, A. 2001. Gold of the Pharaohs–6000 years of gold mining in Egypt and Nubia. *Journal of African Earth Sciences, 33*(3): 643-659.

Kochine, G. and Bassyuni, F. 1968. Mineral Resources of the UAR, Part I, Metallic Minerals. *Int. Rep. Geol. Surv. Egypt*.

Kranidiotis, P. and MacLean, W. 1987. Systematics of chlorite alteration at the Phelps Dodge massive sulfide deposit, Matagami, Quebec. *Economic Geology, 82*(7): 1898-1911.

Kretschmar, U. and Scott, S. 1976. Phase relations involving arsenopyrite in the system Fe-As-S and their application. *Canadian Mineralogist, 14*(3): 364-386.

Kroeper, K. and Wildung, D. 1994. Minshat Abu Omar. *Ein vor-und frühgeschichtlicher Friedhof im Nildelta, 2*: 115-204.

Kröner, A. 1979. Pan African plate tectonics and its repercussions on the crust of northeast Africa. *Geologische Rundschau, 68*(2): 565-583.

Lambert, I. 1984. Sulfur isotope composition and genesis of Archean gold mineralization, Australia and Zimbabwe. *Gold'82*.

Large, R.R., Gemmell, J.B., Paulick, H. and Huston, D.L. 2001. The alteration box plot: A simple approach to understanding the relationship between alteration mineralogy and lithogeochemistry associated with volcanic-hosted massive sulfide deposits. *Economic Geology, 96*(5): 957-971.

Le Maitre, R.W.B., Dudek, P., Keller, A., Lameyre, J., Le Bas, J., Sabine, M., Schmid, P., Sorensen, R., Streckeisen, H. and Woolley, A. 1989. A classification of igneous rocks and glossary of terms: Recommendations of the International Union of Geological Sciences, Subcommission on the Systematics of Igneous Rocks. *International Union of Geological Sciences*.

Leitch, C. and Lentz, D.R. 1994. The Gresens approach to mass balance constraints of alteration systems: methods, pitfalls, examples. *Alteration and alteration processes associated with ore-forming systems: Geological Association of Canada, Short Course Notes, 11*: 161-192.

Lindgren, W. 1894. Characteristic features of California gold-quartz veins. *Geological Society of America Bulletin, 6*(1): 221-240.

Lottermoser, B. 1992. Rare earth elements and hydrothermal ore formation processes. *Ore Geology Reviews, 7*(1): 25-41.

Mars, J.C. and Rowan, L.C. 2006. Regional mapping of phyllic-and argillic-altered rocks in the Zagros magmatic arc, Iran, using Advanced Spaceborne Thermal

Emission and Reflection Radiometer (ASTER) data and logical operator algorithms. *Geosphere, 2*(3): 161-186.

McCuaig, T.C. and Kerrich, R. 1998. P—T—t—deformation—fluid characteristics of lode gold deposits: evidence from alteration systematics. *Ore Geology Reviews, 12*(6): 381-453.

McInnes, B.I. and Cameron, E.M. 1994. Carbonated, alkaline hybridizing melts from a sub-arc environment: Mantle wedge samples from the Tabar-Lihir-Tanga-Feni arc, Papua New Guinea. *Earth and planetary science letters, 122*(1-2): 125-141.

McLennan, S., Taylor, S., McCulloch, M. and Maynard, J. 1990. Geochemical and Nd-Sr isotopic composition of deep-sea turbidites: crustal evolution and plate tectonic associations. *Geochimica et Cosmochimica Acta, 54*(7): 2015-2050.

Meyer, C. and Hemley, J.J. 1967. Wall rock alteration. *Geochemistry of hydrothermal ore deposits, 1*: 166.

Meyer, C. and Heidorn, L. 1998. Three seasons at Bir Umm Fawakhir in the Central Eastern Desert. *Life on the Fringe. Research School CNWS, Leiden*: 197-209.

Middelburg, J.J., van der Weijden, C.H. and Woittiez, J.R. 1988. Chemical processes affecting the mobility of major, minor and trace elements during weathering of granitic rocks. *Chemical geology, 68*(3): 253-273.

Miyashiro, A. 1978. Nature of alkalic volcanic rock series. *Contributions to mineralogy and petrology, 66*(1): 91-104.

Miyashiro, A. and Shido, F. 1975. Tholeiitic and calc-alkalic series in relation to the behaviors of titanium, vanadium, chromium, and nickel. *American Journal of Science, 275*(3): 265-277.

Moghtaderi, A., Moore, F. and Mohammadzadeh, A. 2007. The application of advanced space-borne thermal emission and reflection (ASTER) radiometer data in the detection of alteration in the Chadormalu paleocrater, Bafq region, Central Iran. *Journal of Asian Earth Sciences, 30*(2): 238-252.

Mond, R. and Winkler, H.A. 1940. ROCK DRAWINGS OF SOUTHERN UPPER EGYPT. II. *JSTOR*.

Monier, G. and Robert, J. 1986. Muscovite solid solutions in the system K2O-MgO-FeO-Al2O3-SiO2-H2O: an experimental study at 2 kbar PH2O and comparison with natural Li-free white micas. *Mineral. Mag, 50*: 257-266.

Murray, G.W. 1925. The Roman roads and stations in the Eastern Desert of Egypt. *The Journal of Egyptian Archaeology, 11*(3/4): 138-150.

Nagihara, S.S. and Casey, J.F. 2001. 10. Whole-Rock Geochemistry of Amphibolites and Metagabbros from the West Iberia Margin, Leg 173.

Nesbitt, B. 1991. Phanerozoic gold deposits in tectonically active continental margins, Gold metallogeny and exploration. *Springer*, pp. 104-132.

Newberry, P. 1893. Beni Hassan II: archaeological survey of Egypt. *London: Kegan Paul*.

Ninomiya, Y. 2003. A stabilized vegetation index and several mineralogic indices defined for ASTER VNIR and SWIR data, Geoscience and Remote Sensing Symposium, 2003. IGARSS'03. Proceedings. 2003 IEEE International. *IEEE*, pp. 1552-1554.

Ninomiya, Y. and Fu, B.-h. 2003. Extracting lithologic information from ASTER multispectral thermal infrared data in the northeastern Pamirs. *新疆地質, 21*(1): 22-30.

Ninomiya, Y., Fu, B. and Cudahy, T.J. 2005. Detecting lithology with Advanced Spaceborne Thermal Emission and Reflection Radiometer (ASTER) multispectral thermal infrared "radiance-at-sensor" data. *Remote Sensing of Environment, 99*(1): 127-139.

O'Neil, J.R., Clayton, R.N. and Mayeda, T.K. 1969. Oxygen isotope fractionation in divalent metal carbonates, Univ. of Chicago.

Ohmoto, H. and Rye, R. 1979. Isotopes of sulfur and carbon. *Geochemistry of Hydrothermal Ore Deposits (ed*: 509-567.

Ohmoto, H. and Goldhaber, M. 1997. Sulfur and carbon isotopes. *Geochemistry of hydrothermal ore deposits, 3*: 517-611.

Paulick, H., Bach, W., Godard, M., De Hoog, J., Suhr, G. and Harvey, J. 2006. Geochemistry of abyssal peridotites (Mid-Atlantic Ridge, 15 20′ N, ODP Leg 209): implications for fluid/rock interaction in slow spreading environments. *Chemical geology, 234*(3): 179-210.

Pearce, J.A. and Cann, J. 1973. Tectonic setting of basic volcanic rocks determined using trace element analyses. *Earth and planetary science letters, 19*(2): 290-300.

Pearce, J.A. and Norry, M.J. 1979. Petrogenetic implications of Ti, Zr, Y, and Nb variations in volcanic rocks. *Contributions to mineralogy and petrology, 69*(1): 33-47.

Pirajno, F. 2009. Hydrothermal processes associated with meteorite impacts. *Springer*.

Pohl, W. 1982. Large-scale metallogenetic features of the Precambrian in Northeast Africa and Arabia. *Precambrian Research, 16*(4): A32-A33.

Reed, M.H. 1997. Hydrothermal alteration and its relationship to ore fluid composition. *Geochemistry of hydrothermal ore deposits, 3*: 303-365.

Richards, J.P. 1995. Alkalic-type epithermal gold deposits—a review. *Magmas, Fluids, and Ore Deposits, Mineralogical Association of Canada Short Course, 23*: 367-400.

Richards, J.P. and Kerrich, R. 1993. The Porgera gold mine, Papua New Guinea; magmatic hydrothermal to epithermal evolution of an alkalic-type precious metal deposit. *Economic Geology, 88*(5): 1017-1052.

Ridley, J.R. and Diamond, L.W. 2000. Fluid chemistry of orogenic lode gold deposits and implications for genetic models, Gold in, pp. 141-162.

Robie, R.A. and Waldbaum, D.R. 1968. Thermodynamic properties of minerals and related substances at 298.15 K (25.0 C) and one atmosphere (1.013 bars) pressure and at higher temperatures. 1259.

Rockwell, B.W. and Hofstra, A.H. 2008. Identification of quartz and carbonate minerals across northern Nevada using ASTER thermal infrared emissivity data—Implications for geologic mapping and mineral resource investigations in well-studied and frontier areas. *Geosphere, 4*(1): 218-246.

Rollinson, H. 1993. Using geochemical data, 352 pp. *Longman, London*.

Rose, A.W. and Burt, D.M. 1979. Hydrothermal alteration. In: H.L. Barnes (Editor), Geochemistry of hydrothermal ore deposits,. *John Wiley & Sons*, New York, pp. 173-227.

Roser, B. and Korsch, R. 1986. Determination of tectonic setting of sandstone-mudstone suites using content and ratio. *The Journal of Geology*: 635-650.

Roubet, C. 1989. The grinding stones of site E-78-3 Wadi Kubbaniye. *The Prehistory of Wadi Kubbaniye, 3*: 473-489.

Rowan, L.C. and Mars, J.C. 2003. Lithologic mapping in the Mountain Pass, California area using advanced spaceborne thermal emission and reflection radiometer (ASTER) data. *Remote Sensing of Environment, 84*(3): 350-366.

Rowan, L.C., Kingston, M.J. and Crowley, J.K. 1986. Spectral reflectance of carbonatites and related alkalic igneous rocks; selected samples from four North American localities. *Economic Geology, 81*(4): 857-871.

Rowan, L.C., Mars, J.C. and Simpson, C.J. 2005. Lithologic mapping of the Mordor, NT, Australia ultramafic complex by using the Advanced Spaceborne Thermal Emission and Reflection Radiometer (ASTER). *Remote Sensing of Environment, 99*(1): 105-126.

Rowan, L.C., Schmidt, R.G. and Mars, J.C. 2006. Distribution of hydrothermally altered rocks in the Reko Diq, Pakistan mineralized area based on spectral analysis of ASTER data. *Remote Sensing of Environment, 104*(1): 74-87.

Rowan, L.C., Hook, S.J., Abrams, M.J. and Mars, J.C. 2003. Mapping hydrothermally altered rocks at Cuprite, Nevada, using the Advanced Spaceborne Thermal Emission and Reflection Radiometer (ASTER), a new satellite-imaging system. *Economic Geology, 98*(5): 1019-1027.

Ruiz-Armenta, J. and Prol-Ledesma, R. 1998. Techniques for enhancing the spectral response of hydrothermal alteration minerals in Thematic Mapper images of Central Mexico. *International Journal of Remote Sensing, 19*(10): 1981-2000.

Sabet, A. and Bordonosov, V. 1984. The gold ore formations in the Eastern Desert of Egypt. *Ann. Geol. Surv. Egypt, 16*: 35-42.

Sabet, A., Tscgoev, V., Bordonosov, V., Babourin, L., Zalata, A. and Francis, M. 1976. On gold mineralization in the Eastern Desert of Egypt. *Ann Geol Surv Egypt, 6*: 201-212.

Sanjeevi, S. 2008. Targeting limestone and bauxite deposits in southern India by spectral unmixing of hyperspectral image data. *The International Archives of the Photogrammetry, Remote Sensing and Spatial Information Sciences, 37*: 1189-1194.

Scott, S. and Barnes, H. 1971. Sphalerite geothermometry and geobarometry. *Economic Geology, 66*(4): 653-669.

Sharp, Z.D., Essene, E.J. and Kelly, W.C. 1985. A re-examination of the arsenopyrite geothermometer: pressure considerations and applications to natural assemblages. *Journal of the Mineralogical Association of Canada, 23*(Part 4).

Shikazono, N., Ogawa, Y., Utada, M., Ishiyama, D., Mizuta, T., Ishikawa, N. and Kubota, Y. 2008. Geochemical behavior of rare earth elements in hydrothermally altered rocks of the Kuroko mining area, Japan. *Journal of Geochemical Exploration, 98*(3): 65-79.

Sillitoe, R. 1991. Intrusion-related gold deposits, Gold metallogeny and exploration. *Springer*, pp. 165-209.

Singh, A. and Harrison, A. 1985. Standardized principal components. *International Journal of Remote Sensing, 6*(6): 883-896.

Stern, R.J. 1994. Arc-assembly and continental collision in the Neoproterozoic African orogen: implications for the consolidation of Gondwanaland. *Annual Review of Earth and Planetary Sciences, 22*: 319-351.

Stipp, M., Stünitz, H., Heilbronner, R. and Schmid, S.M. 2002. Dynamic recrystallization of quartz: correlation between natural and experimental conditions. *Geological Society, London, Special Publications, 200*(1): 171-190.

Streckeisen, A. 1976. To each plutonic rock its proper name. *Earth-Science Reviews, 12*(1): 1-33.

Sun, S.-S. and McDonough, W. 1989. Chemical and isotopic systematics of oceanic basalts: implications for mantle composition and processes. *Geological Society, London, Special Publications, 42*(1): 313-345.

Susak, N.J. 1994. Alteration factors affecting ore deposition. *DR Lenz*: 115-130.

Tangestani, M. and Moore, F. 2001. Comparison of three principal component analysis techniques to porphyry copper alteration mapping: a case study, Meiduk area, Kerman, Iran. *Canadian Journal of Remote Sensing, 27*(2): 176-182.

Tindle, A.G. and Webb, P.C. 1990. Estimation of lithium contents in trioctahedral micas using microprobe data: application to micas from granitic rocks. *European Journal of Mineralogy*: 595-610.

Trdlička, Z. and Hoffman, V. 1976. Untersuchungen der chemischen Zusammensetzung der Gangkarbonate von Kutná Hora (ČSSR). *Freib. Forschungshefte C, 321*: 29-81.

Vail, J. 1988. Tectonics and evolution of the Proterozoic basement of NE Africa. *The Pan-African belts of NE Africa and Adjacent areas. Friedr Vieweg and Sohn*: 185-226.

van de Kamp, P.C. 1968. Geochemistry and origin of metasediments in the Haliburton-Madoc area, southeastern Ontario. *Canadian Journal of Earth Sciences, 5*(6): 1337-1372.

van de Kamp, P.C., Leake, B.E. and Senior, A. 1976. The petrography and geochemistry of some Californian arkoses with application to identifying gneisses of metasedimentary origin. *The Journal of Geology*: 195-212.

Wilson, B.M. 2007. Igneous petrogenesis a global tectonic approach. *Springer Science & Business Media*.

Wu, X. and Delbove, F. 1989. Hydrothermal synthesis of gold-bearing arsenopyrite. *Economic Geology, 84*(7): 2029-2032.

Yan, Y., Zhang, N., Li, S. and Li, Y. 2014. Mineral chemistry and isotope geochemistry of pyrite from the Heilangou gold deposit, Jiaodong Peninsula, Eastern China. *Geoscience Frontiers, 5*(2): 205-213.

Zhang, X., Pazner, M. and Duke, N. 2007. Lithologic and mineral information extraction for gold exploration using ASTER data in the south Chocolate Mountains (California). *ISPRS Journal of Photogrammetry and Remote Sensing, 62*(4): 271-282.

Zoheir, B.A. 2012a. Microchemistry and stable isotope systematics of gold mineralization in a gabbro–diorite complex, SE Egypt. *Microchemical Journal, 103*: 148-157.

Zoheir, B.A. 2012b. Controls on lode gold mineralization, Romite deposit, South Eastern Desert, Egypt. *Geoscience Frontiers, 3*(5): 571-585.

Zoheir, B.A. and Emam, A. 2012. Integrating geologic and satellite imagery data for high-resolution mapping and gold exploration targets in the South Eastern Desert, Egypt. *Journal of African Earth Sciences, 66*: 22-34.

Zoheir, B.A. and Emam, A. 2014. Field and ASTER imagery data for the setting of gold mineralization in Western Allaqi–Heiani belt, Egypt: A case study from the Haimur deposit. *Journal of African Earth Sciences, 99*: 150-164.

Zoheir, B.A. and Moritz, R. 2014. Fluid evolution in the El-Sid gold deposit, Eastern Desert, Egypt. *Geological Society, London, Special Publications, 402*(1): 147-175.

CURRICULUM VITAE

Name Surname : Amr Abdelnasser Ali Khalil

Place and Date of Birth : Sharkia / Egypt – 20/11/1982

E-Mail :amrkhalil@itu.edu.tr & abdelnasser82@gmail.com

EDUCATION :

- **B.Sc.** : 2003, Benha University, Faculty of Science, Geology Department
- **M.Sc.** : 2009, Benha University, Faculty of Science, Geology Departments (Rocks, Minerals, and Ore deposits)

PROFESSIONAL EXPERIENCE AND REWARDS:

- **Feb. 2005 - Now:** Teaching Assistant at geology department, Faculty of Science, Benha University, Egypt.

PUBLICATIONS, PRESENTATIONS AND PATENTS ON THE THESIS:

JOURNAL PUBLICATION

- **Amr Abdelnasser,** Mustafa Kumral, 2016: Mineral chemistry and geochemical behavior of hydrothermal alterations associated with mafic intrusive-related Au deposits at the Atud area, Central Eastern Desert, Egypt. *Ore Geology Reviews; 77:1-24.* DOI:10.1016/j.oregeorev.2016.01.011.

CONFERENCE PROCEEDINGS

- **Amr Abdelnasser**, Mustafa Kumral, 2016: Rare earth elements geochemistry of the hydrothermal alterations associated with the intrusion related gold deposits at Atud area, Egypt. *7th Geochemistry Symposium with International Participation: 16-18 May 2016, Side/Antalya, Turkey.*

- **Amr Abdelnasser,** Mustafa Kumral, 2015: Deformational quartz textures and mineralogy of hydrothermal alteration associated with intrusion-related gold deposits: a case study from the Atud area, Central Eastern Desert, Egypt. *2015 GSA Annual Meeting in Baltimore, Maryland, USA (1-4 November 2015).*

- **Amr Abdelnasser**, Mustafa Kumral, 2015: Oxygen, carbon and sulphur isotope studies in the intrusion-related Au deposits at Atud area, Egypt. *12th International Congress for Applied Mineralogy (ICAM 2015), Istanbul/Turkey, 10-12 August 2015*.

- **Amr Abdelnasser**, Muhittin Karaman, Mustafa Kumral, Basem Zoheir, Pär Weihed, 2015: Detection of hydrothermal alteration associated with intrusion related gold mineralization at Central Eastern Desert of Egypt by using ASTER-based image processing. *12th International Congress for Applied Mineralogy (ICAM 2015), Istanbul/Turkey, 10-12 August 2015*.

- **Amr Abdelnasser**, Kumral M., Zoheir B., Weihed P., Budakoglu M., Gumus L., 2015: Microchemical data of the Atud gold deposit, Eastern Desert, Egypt. *ICESCC 2014: International Conference on Earth Science and Climate Change, Cape Town, South Africa; 11/2014.*

- **Amr Abdelnasser,** M. Kumral, Basem Ahmed Zoheir, P. Weihed, D. Kiran Yildrim, M. Karaman, 2015: Hydrothermal alteration geochemistry of Atud gold deposits at the central block of the Egyptian Eastern Desert, Egypt: Insights provided by mass-balance calculations. *Goldschmidt 2014 (Gold2014), 8-13 June 2014, Sacramento, California, USA; 06/2014.*

OTHER PUBLICATIONS, PRESENTATIONS AND PATENTS:

JOURNAL PUBLICATIONS

- Mustafa Kumral, Amr Abdelnasser, Murat Budakoglu: Geochemistry of Hydrothermal Alteration Associated with Cenozoic Intrusion-Hosted Cu-Pb-Zn Mineralization at Tavşanlı Area, Kütahya, NW Turkey. 02/2016; 6(1: 13):1-23. DOI:10.3390/min6010013

- Murat Budakoglu, **Amr Abdelnasser**, Muhittin Karaman, Mustafa Kumral, 2015: The rare earth element geochemistry on surface sediments, shallow cores and lithological units of Lake Acıgöl basin, Denizli, Turkey. *Journal of Asian Earth Sciences; 111*. DOI:10.1016/j.jseaes.2015.05.016

- Nedal Qaoud**, Amr Abdelnasser**, 2012: Geochemistry and petrogenesis of El-Fringa metagabbro-diorite rocks, Wadi Sa'al area, south Sinai, Egypt. *Journal of Al Azhar University-Gaza (Natural Sciences), 2012, 14: 111-138.*

CONFERENCE PROCEEDINGS

- **Amr Abdelnasser**, Demet Kiran Yildirim, Zeynep Doner, Mustafa Kumral, 2016: Geochemical element mobility during the hydrothermal alteration in the Tepeoba porphyry Cu-Mo-Au deposits at Balikesir, NW Turkey. *EGU General Assembly 2016, Vienna, Austria; 04/2016.*

- Mustafa Kumral, **Amr Abdelnasser**, Muhittin Karaman, Murat Budakoglu, 2016: Using the concentration–volume (C–V) fractal model in the delineation of gold mineralized zones within the Tepeoba porphyry Cu-Mo-Au, Balikesir, NW Turkey. *EGU General Assembly 2016, Vienna, Austria; 04/2016.*

- Demet Kiran Yildirim, **Amr Abdelnasser**, Zeynep Doner, Mustafa Kumral: Mass change calculations of hydrothermal alterations within the volcanogenic metasediments hosted Cu-Pb (-Zn) mineralization at Halilar area, NW Turkey. *EGU General Assembly 2016, Vienna, Austria; 04/2016.*

- Zeynep Doner, **Amr Abdelnasser**, Demet Kiran Yildirim, Mustafa Kumral, 2016: Geochemical behavior of rare earth elements of the hydrothermal alterations within the Tepeoba porphyry Cu-Mo-Au deposits at Balikesir, NW Turkey. *EGU General Assembly 2016, Vienna, Austria; 04/2016.*

- Cihan Yalçin, Nurullah Hanilçi, Mustafa Kumral, **Amr Abdelnasser**, 2016: Geology of the Göçükdibi Cu-Pb-Zn Mineralization, Gökçedogan, Çorum (Turkey): Preliminary Findings on Its Formation. *EGU General Assembly 2016, Vienna, Austria; 04/2016.*

- Sercan Ozturk, Lokman Gumus, **Amr Abdelnasser**, Cihan Yalçin, Mustafa Kumral, Nurullah Hanilçi, 2016: Alteration geochemistry of the volcanic-hosted Dedeninyurdu, Yergen and Fındıklıyar Cu-Fe mineralization, Northern part of Gökçedogan Village, Çorum-Kargi Region, Turkey: Implications for the rare earth elements geochemical characteristics. *EGU General Assembly 2016, Vienna, Austria; 04/2016*

- Lokman Gumus, Sercan Öztürk, Cihan Yalçın, **Amr Abdelnasser**, Nurullah Hanilçi, Mustafa Kumral, 2016: Alteration geochemistry of the volcanic-hosted Dedeninyurdu, Yergen and Fındıklıyar Fe-Cu mineralization at Gökçedogan, Çorum-Kargi region, Turkey. *EGU General Assembly 2016, Vienna, Austria; 04/2016.*

- M.Sezai Kırıkoglu, Huseyin Kocaturk, Ali Tugcan Unluer, Murat Budakoglu, Zeynep Doner, **Amr Abdelnasser**, Emin Ciftci, 2015: The Mantle Derived Potassic and Ultrapotassic Rocks Related Enrichments of Rare Earth Elements (REE) on Peneplains of Golcuk District (Southern Turkey). *35th International Geological Congress, Cape Town (South Africa); 08/2016.*

- M. Sezai Kirikioğlu, Ali Tuğcan Ünlüer, Hüseyin Kocatürk, Emin Çiftçi, **Amr Abdelnasser**, Zeynep Döner, Murat Budakoğlu, 2016: Study of Rare Earth Elements (REE) Potentials in Residual Formations Occurring at Bucak Region, Isparta (Southwest Turkey). *7th Geochemistry Symposium with International Participation: 16-18 May 2016, Side/Antalya, Turkey*.

- Demet Kiran Yildirim, **Amr Abdelnasser**, Zeynep Doner, Mustafa Kumral, 2015: Mineralogy and geochemistry of base-metal deposits at Halilar area, NW Turkey. *2015 AGU Fall Meeting Program in San Francisco, USA (14-18 December 2015).*

- Mustafa Kumral, **Amr Abdelnasser**, Demet Kiran Yildirim, Muhittin Karaman, Zeynep Doner, Murat Budakoglu, 2015: Quantitative mass transfer analysis during hydrothermal alteration of intrusion-related Cu-Pb-Zn mineralization in SW Kütahya, Turkey. *12th International Congress for Applied Mineralogy (ICAM 2015), Istanbul, Turkey; 08/2015.*

- Hamza Samast, Mustafa Kumral, Nurullah Hanilçi, Cihan Yalçin, **Amr Abdelnasser**, Murat Budakoğlu, 2015: Investigation of the nature of volcanic-hosted massive sulfide deposits at the north of Gökçedoğan, Corum-Kargiregion, Turkey. *12th International Congress for Applied Mineralogy (ICAM 2015), Istanbul, Turkey; 08/2015.*

- Mustafa Kaya, Mustafa Kumral, Nurullah Hanilçi, Mustafa Selman Aydoğan, Cihan Yalçin, **Amr Abdelnasser**, 2014: Characteristics of ophiolite-hosted massive sulfide deposits: A case study from Corum-Kargi region (North Gökçedoğan village), Turkey. *12th International Congress for Applied Mineralogy (ICAM), Istanbul/Turkey; 08/2015*

- Budakoglu M., Karaman M., **Abdelnasser A**., Kiran D., Kumral M., 2014: Geochemical Approach of Rare Earth Element Distribution: A Case Study from Lake Acigol, Denizli, Turkey. *ICESCC 2014: International Conference on Earth Science and Climate Change, Cape Town, South Africa; 11/2014*

- Budakoglu M., Karaman M., **Abdelnasser A**., Kumral M., 2014: Spatial REE Geochemical Modeling at Lake Acıgöl, Denizli, Turkey: Analytical Approaches on Spatial Interpolation and Spatial Correlation. *ICESCC 2014: International Conference on Earth Science and Climate Change, Cape Town, South Africa; 11/2014*

- Kumral M., **Abdelnasser A**., Budakoglu M., Karaman M., Yildirim D. K., Doner Z., Bostanci A., 2014: Porphyry Cu-Mo-(Au) Mineralization at Parağa Area, Nakhchivan District, Azerbaijan: Evidence from Mineral Paragenesis, Hyrothermal Alteration and Geochemical Studies. *ICESCC 2014: International Conference on Earth Science and Climate Change, Cape Town, South Africa; 11/2014*

- M Kumral, **Amr Abdelnasser**, A K Bostanci, Z Doner, M Budakoglu, M Karaman, 2014: Geochemical investigations of Eğrigöz granitoid-hosted Cu-Pb-Zn mineralization at the northern margin of Tauride-Anatolide platform: A case study from Tavşanli zone, Kütahya, Turkey. *Goldschmidt 2014 (Gold2014), 8-13 June 2014., Sacramento, California, USA; 06/2014.*

- D K Yildirim, A K Akay, T T Bonab, **Amr Abdelnasser**, M Kumral, And M Budakoğlu, 2014: Investigation of geochemistry and subsurface modeling of porphyry Cu- Mo deposit in Tepeoba-Havran, NW Turkey. *Goldschmidt 2014 (Gold2014), 8-13 June 2014., Sacramento, California, USA; 06/2014.*

- Murat Budakoğlu, Muhittin Karaman, Serpil Geredeli, **Amr Abdelnassar**, Demet Kıran Yıldırım, 2014: Clay Mineralogy of Shallow Core Sediments of Lake Acıgöl, Denizli,Turkey. *EGU2014, Vienna; 04/2014.*

- A M Mehanna, A A Rashwan, M H Abu Farh, **Amr Abdelnasser,** 2008: Petrography, geochemistry and petrogensis of the Pan-African basement rocks in the area around Gabal Hamrat Salma-Wadi Shait terrain, South Eastern Desert, Egypt. *9thInternational Conference on Geological Arab World (GAW 9), Cairo University, Cairo, Egypt; 01/2008.*